Pore Engineered Carbons for Enhanced Electrochemical Performance

A Thesis Submitted for the Degree of

Doctor of Philosophy

By

Dheeraj Kumar Singh

Chemistry and Physics of Materials Unit

Jawaharlal Nehru Centre for Advanced Scientific Research

(A Deemed University)

Bengaluru, India

March 2018

Pore Engineered Carbons for Enhanced Electrochemical Performance

A Thesis Submitted for the Degree of

Doctor of Philosophy

By

Dheeraj Kumar Singh

Under the Supervision of

Prof. Muthusamy Eswaramoorthy

Chemistry and Physics of Materials Unit

Jawaharlal Nehru Centre for Advanced Scientific Research

(A Deemed University)

Bengaluru, India

March 2018

Everything for My Mother
Sunita

DECLARATION

I hereby declare that the thesis entitled "**Pore Engineered Carbons for Enhanced Electrochemical Performance**" is an authentic record of research work carried out by me at the Chemistry and Physics of Materials Unit, Jawaharlal Nehru Centre for Advanced Scientific Research, Bangalore, India under the supervision of **Prof. M. Eswaramoorthy** and that it has not been submitted elsewhere for the award of any degree or diploma.

In keeping with the general practice in reporting scientific observations, due acknowledgment has been made whenever the work described is based on the findings of other investigators. Any omission that might have occurred due to oversight or error in judgment is regretted.

Dheeraj Kumar Singh

Jawaharlal Nehru Centre for Advanced Scientific Research

Prof. M. Eswaramoorthy
Chemistry and Physics of Materials Unit
Jawaharlal Nehru Centre for Advanced Scientific Research (JNCASR)
Bangalore-560064, India
Phone : +91 80 2208 2870
Fax: + 91 80 22082766
E-mail: eswar@jncasr.ac.in

Date
March 9, 2018

CERTIFICATE

I hereby certify that the work described in this thesis titled "**Pore Engineered Carbons for Enhanced Electrochemical Performance**" has been carried out by **Dheeraj Kumar Singh** at the Chemistry and Physics of Materials Unit, Jawaharlal Nehru Centre for Advanced Scientific Research, Bangalore, India under my supervision and it has not been submitted elsewhere for the award of any degree or diploma.

M. Eswaramoorthy

(Research Supervisor)

Acknowledgements

The journey of Ph.D. is no less than an adventure which not only enables us to realize our own inner strength but also the joy of discovering and devising things. As they say, we ride on the shoulders of the giants; mine too was not an exception and I would like to acknowledge the people who have contributed greatly towards the pursuit of 'My journey' called Science and Self.

My life is the blessing of my mother, **Smt. Sunita Devi** and no amount of word is capable enough to describe her sacrifice and love for me. The person with her immense and entire concentration focused on me with only one thought of my well-being.

My guru, **Prof. Muthusamy Eswaramoorthy**, for shaping me with the sacred thoughts with which the knowledge must be pursued to greater depths for human advancement. I would be ever grateful to him for introducing me to the field of materials science (Electrochemistry in particular) and providing me with the opportunity to think independently while guiding me all through. His love and patience has been humbling and made me emulate him in the deepest of my thinkings with belief that highest form of knowledge must nourish character. And above all, for being a family to me.

My teacher, **Prof. Sundaresan Neelakantan**, at SSSIHL (Sri Sathya Sai Institute of Higher Learning) for inspiring and introducing me to the field of alchemy (chemistry). His unconditional love towards me is relentless and prodigious.

I would like to express my gratitude to **Prof. C. N. R. Rao, FRS** for being a constant source of inspiration and creating such a vibrant research atmosphere to carry out my work.

I thank the past and present chairmen of **CPMU**, **Prof. Balasubramanian Sundaram** and **Prof. Chandrabhas Narayana** for providing world-class facilities at the center.

My course instructors: **Prof. A. Sundaresan**, **Prof. S. Balasubramanian**, **Prof. Subi George**, **Prof. N. Ravishankar,** and **Prof. S. Sampath** for their informative and insightful courseworks.

I am thankful to my collaborators: **Prof. Srinivasan Sampath (IISc.)**, **Dr. Harish Srinivasan**, **Ramesh Naidu Jenjeti**, **Dr. Aninda Jiban Bhattacharya (IISc.)**, **Dr.**

Subhra Gope and **Dr. Subi George (JNCASR)** for sharing their expertise with me.

My heartfelt thanks to my labmates: **Amrit**, **Piyush**, **Pavan**, **Sai Krishna**, **KKR Datta**, **Sisir**, **Sonu**, **Suchi**, **Soumita**, **Momin**, **Arunava**, **Divya**, **Nijita**, **Surishi**, **Shivanna**, **Subramaniam**, **Himani**, **Sushummna,** and **Mehraj** for their immense love and affection.

I am thankful to the academic and administrative staff of JNCASR for their assistance.

Untiring support of technical staffs is greatly appreciated: **Mrs. Usha** (TEM), **Mr. Srinath**, **Mr. Anil** (PXRD), **Mrs. Selvi** (FESEM), **Dr. Jay Ghatak** (TEM), **Mr. Kannan (TEM)**, **Mr. Vasu** (FTIR, TGA, UV-Vis, and Raman) and **Mr. Shiva** (CHNS analyses).

I thank all my friends from **JNCASR** and **IISc.** for their company in various activities. My special thanks are due to **Rajat** and **Dr. V Anju**.

My Alma Mater, **Sri Sathya Sai Institute of Higher learning** for everything which I possess.

Besides the research life, I am thankful to **Prof. M. Eswaramoorthy** and his family members for their hospitality and affection.

Financial assistance from **Council of Scientific and Industrial Research (CSIR)** is gratefully acknowledged.

My Sister, **Sai Jagriti Singh,** for her immense love and support.

Preface

The present investigation deals with the synthesis of pore engineered carbons from microporous to macroporous regime for a wide spectrum of electrochemical applications viz. supercapacitors, Li/Na-S batteries, and electrocatalysts. Additionally it has been shown that how interface engineering between conducting (graphene) and non-conducting (redox-active covalent organic polymers) phases leads to efficient pseudocapacitive energy storage.

Chapter 1. briefly introduces the implications of porosity towards an electrochemical interface and how mass transfer affects the performances of electrochemical devices. It involves a short discussion on various techniques used for the synthesis of ordered mesoporous carbons. Besides, it also includes a brief note on carbons for various electrochemical applications viz. supercapacitors, Li/Na-S batteries, and electrocatalytic performance and their mechanistic insights.

Chapter 2. deals with the templated synthesis of high surface area ordered micro-mesoporous carbons (JNC-1 and JNC-2) using Teflon as a silica removal agent. It discusses the mechanism of silica removal by Teflon via elaborate control experiments. Gas storage capabilities of JNC-1 were tested and were compared with activated carbon (AC) and CMK-3. Finally, supercapacitor measurements were performed to evaluate electrochemical performance.

Chapter 3. involves the utilization of above-synthesized carbon i.e. JNC-1 for application in Li-S and intermediate temperature Na-S batteries. The electrochemical performance in such host is accounted in terms of its high surface area and beneficial hierarchical micro-mesoporous structure. Mass transport and electron transfer kinetics are also elaborated upon.

Chapter 4. describes the synthesis of N-doped wider mesopore (> 30 nm) carbons (NDCs) from a clay template (halloysite), for hydrogen evolution reaction (HER) and oxygen reduction reaction (ORR). The study discusses the effect of nitrogen doping and the conductivity of NDCs (tuned by varying pyrolysis temperature) on HER and ORR performance.

Chapter 5. introduces a new technique for the ultrafast synthesis of highly interconnected 3D meso-macroporous carbon containing highly dispersed, low amounts of CoO/Co for oxygen evolution reaction (OER) using simple combustion technique. Oxygen evolution kinetics are discussed in terms of

enhanced mass transport effects along with charge transfer kinetics in conducting carbon matrix.

Chapter 6. presents interface engineering between conducting (graphene) and non-conducting (viologen containing redox active polymers) for efficient charge transfer kinetics for better pseudocapacitive energy storage. It discusses how sequential two-electron reduction in an otherwise difficult system can be achieved by intimate contact between graphene and redox active networks.

Table of Contents

Table of Contents

Chapter-1

An Introduction to Pore Engineered Carbons and Their Electrochemical Applications

Summary:

Present chapter gives a short introduction to different types of carbons, their band structure and electrochemical applications (viz. supercapacitors, batteries, and electrocatalysts) of porous carbons.

1.1 Electrochemical implications of porous electrodes:

Electrochemistry deals with the study of electrified interfaces usually involving electronation and de-electronation reactions, aiding the mutual transformation of electrical and chemical energies. It encompasses a wide spectrum of electrochemical processes involving energy storage to conversion devices viz. batteries, supercapacitors, fuel cells etc.(*1*) Since, in an electrochemical transformation, current density (*j*) is a measure of the rate of the reaction which in turn is proportional to the number of active sites.(*2*) Therefore, it is imperative that porous electrode is expected to show much higher *j* compared to planar systems of similar dimensions on account of its higher number of active sites aiding in the practical development of such prototypes **(Scheme 1)**. Therefore porous electrodes are technologically important.(*3, 4*)

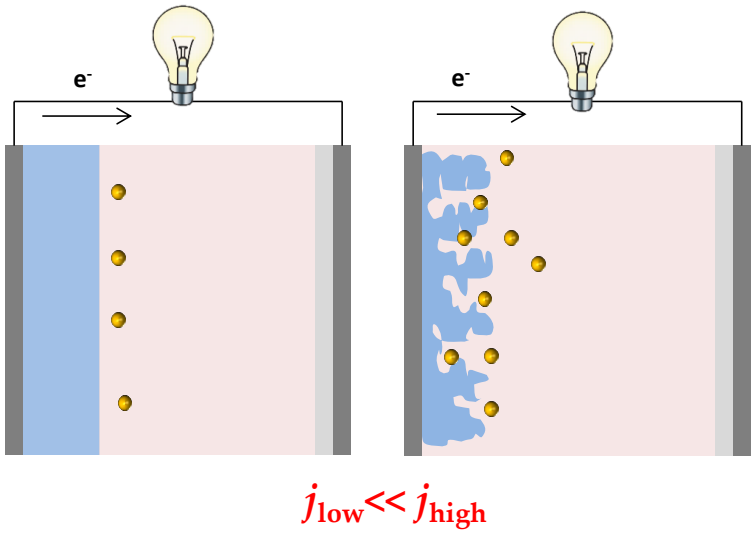

Scheme 1. Schematic comparing the effect of porosity over the current densities of electrochemical devices; subscripts to *j* indicate low and high surface areas. (Left: planar electrode. Right: high surface area porous electrode).

Apart from their role in devising high surface area electrodes, the geometry of the pores plays a dominant role in determining the ease of accessibility of those active sites. Therefore it is essential to understand the mass transport effects in the pores of different geometries.(*5-7*)

1.2 Effect of pore geometries on mass transport:

A material is said to be porous when it is deeper than wider. IUPAC classifies three kinds of porous materials based on their pore diameters.(*8*) Microporous compounds are those materials whose pore diameters are less than 2 nm while

mesoporous compounds have pore dimensions in the range of 2-50 nm whereas macroporous systems have pore diameters more than 50 nm. It is to be noted that each of the above porous materials can be either ordered or disordered which in turn again affects mass transport through them in a different way.

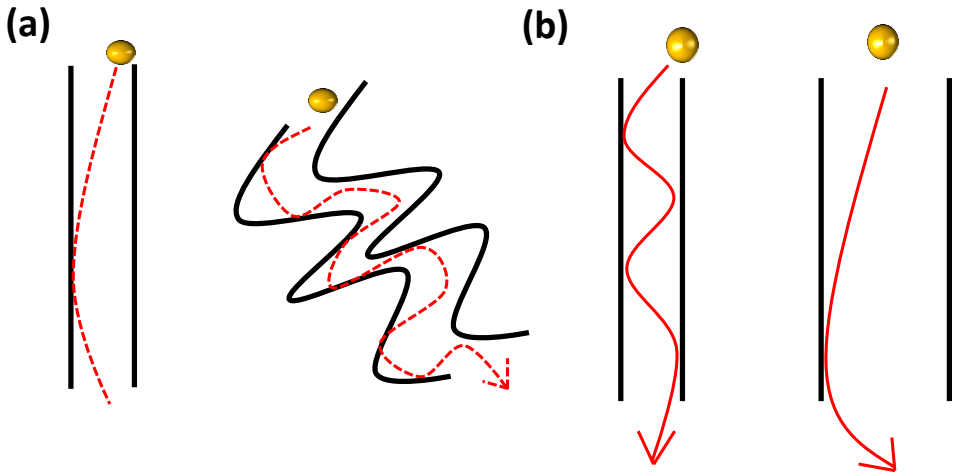

Scheme 2. (a) Comparison of mass transport of a species through the pores of regular and irregular geometries and (b) through the pores of similar geometry but of different dimensions.

Let us compare the transport of a species through the pore of a regularly ordered geometry (cylindrical) with a tortuous one **(Scheme 2a)**. It is apparent that the time taken to travel the same distance is greater in tortuous pore than in a pore of regular geometry because of the multitudes of the collision in the former, thereby impeding ion flux.(*9*) Apart from the pore's geometrical heterogeneity, ion flux is closely related to its dimensions. For example, ion transport is faster in wider pores (meso-macropores) than in smaller ones (micropores) of similar geometry as the pore dimensions are greater than mean free path of the particles in the former **(Scheme 2b)**.(*9-13*)

Therefore, it is clear that porosity plays a central role in the performance of an electrochemical device as it determines the ease of accessibility (pore dimensions) of the active sites apart from creating them (porous electrodes). Few examples are given below to underline the importance of pore engineering in obtaining enhanced electrochemical performances.

1.3 Enhanced electrochemical performance through pore engineering-few examples:

The first example **(Figure 1)** pertains to engineering of porous Pt_3Ni nanoframes with exposed Pt-skin faces as cathode material in polymer electrolyte membrane fuel cells.(*14, 15*) The synthesized material showed excellent oxygen reduction

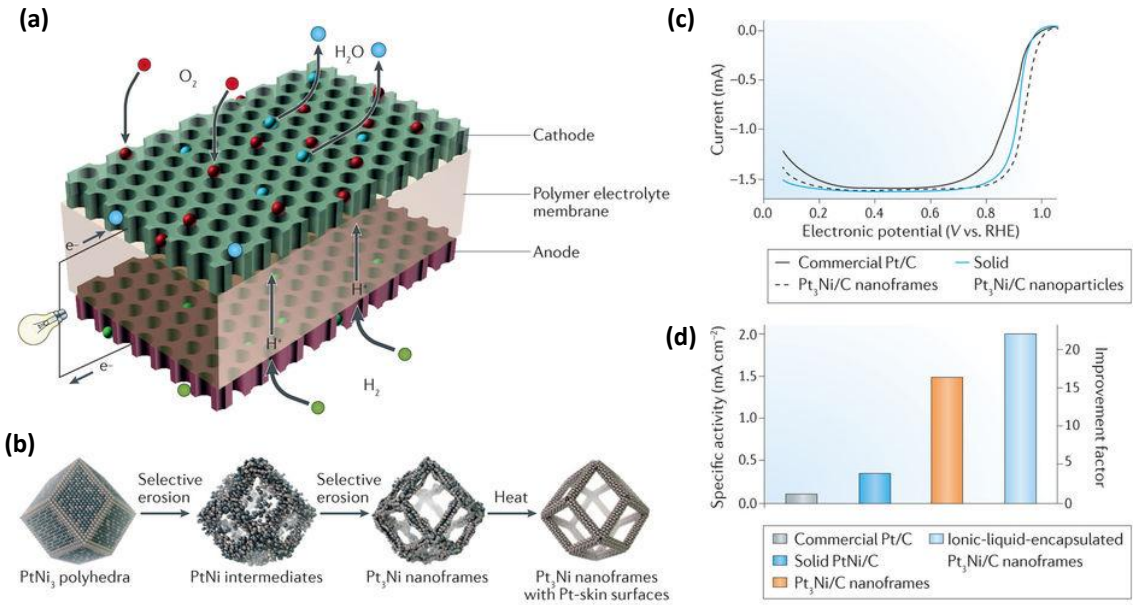

Figure 1. (a-b) Schematic illustrating the advantage of implementing mesoporous Pt_3Ni nanoframes with Pt-skin surfaces as cathode in polymer electrolyte membrane fuel cells leading to superior (c) oxygen reduction performance and as well as (d) higher specific activity compared to $PtNi_3$ nanocrystals and state-of-the-art catalyst i.e. Pt/C. Reproduced with permission from reference (*14, 15*).

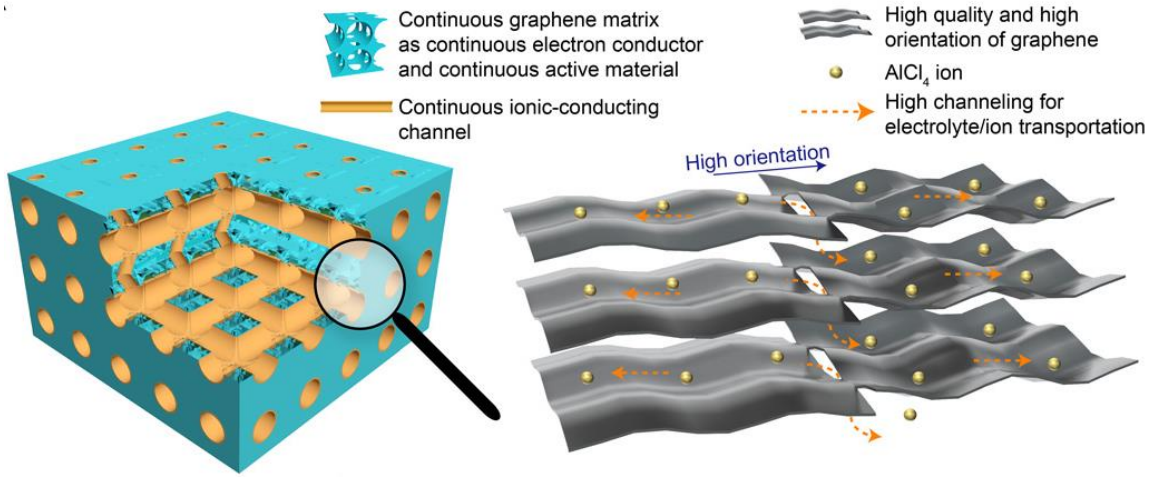

Figure 2. Illustration depicting the fabrication of highly conducting 3D graphene matrix with well-defined oriented channels leading to excellent electrolyte permeability and ion-flux resulting in the fabrication of ultrafast Al-graphene battery with quarter-million cycle life. Reproduced with permission from reference (*16*).

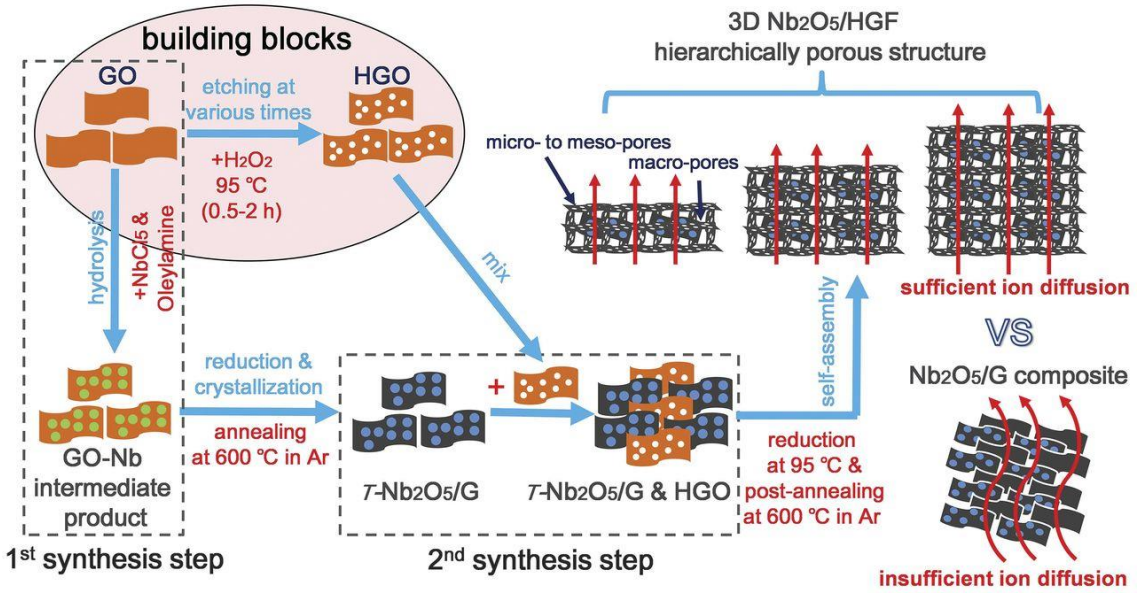

Figure 3. Schematic indicating fabrication of highly interconnected 3D holey-graphene/niobia architecture for enhanced ion diffusion and electron transfer kinetics resulting in excellent battery performance. Adapted with permission from reference (*17*).

performance compared to $PtNi_3$ nanocrystals and state-of-the-art catalyst i.e. Pt/C. Pt_3Ni exhibited ORR activity 22 times and specific activity 16 order higher compared to the commercial catalyst. Such performance metric can be attributed to the ease of accessibility of enhanced catalytically active sites via local porous structures. The second example shows **(Figure 2)** how oriented channeling of local structures in graphene architectures can mitigate internal polarization by supporting high electrolyte permeability and ion-flux.(*16*) Additionally, such architectures on account of their highly conducting interfaces, equally aided by porous structure leads to rapid redox reactions resulting in superior Al-graphene battery performance with quarter a million cycle life. In the next instance **(Figure 3)** it was shown that nanostructuring in 3D holey-graphene/niobia composites leads to ultrahigh-rate energy storage devices at higher loadings (>10 mg cm^{-2}).(*17*) The origin of the activity can be attributed to the presence of hierarchical porous (micro-meso) structure leading to excellent ion diffusion equally aided by fast electron transfer kinetics via conducting carbon phase. Thus, it is apparent that well-developed porosity and conductivity are heart to the functioning of any electrochemical devices and are synergistic in nature. Also, it is to be noted that the last two examples indicate towards the fact that carbon possesses some 'special' properties which deems it to be an ideal material for electrochemical applications. The following sections

will discuss briefly about different aspects of carbons which makes them particularly interesting from above perspective.

1.4 Carbon as an electrode material and technological implications:

Widespread technological applications of carbon electrodes/systems owes much credit to Sir Humphry Davy who first utilized graphite electrodes for alkali metal production. Since then, carbon has found extensive industrial applications ranging from metal production, energy storage (supercapacitors and battery), electrocatalysts etc.(*18-20*) The success of carbons in such applications can be attributed to its low cost, earth-abundance, rich surface chemistry, inert and wide electrochemical window, electrochemical response to a variety of redox systems, predictable interaction dynamics at the electrode-electrolyte interface, tailored properties (glassy carbon, carbon black, graphite etc.) etc.(*18, 21*)

1.5 Advanced carbon materials:

In this endeavor, our ability to manipulate the existing properties with newer, exciting ones would strengthen our fundamental understanding of interaction dynamics at the molecular level. For example, our expertise in designing precisely controlled porous materials have greatly contributed to the understanding of the adsorption behavior of the gases, behavior of the dielectrics and environment of the ions near porous electrode etc. at the nanoscale level. In the following discussions, the existing properties of the various allotropes of the carbon will be discussed and thereafter focus would be paid upon the strategies employed to synthesize mesoporous carbon-based materials.(*22, 23*)

1.6 Carbon (allotropes, electronic structure, and electrochemistry):

The versatility of chemical bonding (sp^3, sp^2, and sp) in carbon endows its existence in different allotropic forms viz. graphite, diamond, fullerenes, carbon nanotubes (CNTs), glassy carbons, carbon fibers, amorphous carbon etc.(*18, 24, 25*) Such variations in chemical bonding have resulted in a diverse physical properties even among different allotropes of carbon which are rarely found in any other single element of the periodic table.(*26*) For example, the energy difference between graphite (thermodynamically stable phase of carbon at NTP) and diamond is ~0.02 eV per atom, with the latter being more isotropic than the former (as a consequence of their bonding nature), results in vastly different electronic, optical, mechanical, thermal etc. properties.(*24*) Graphite, for instance, composed of single layer 2D sheets of sp^2 bonded hexagonal carbon

arrays (graphene), has an electron mobility of ~20 × 10^3 cm^2/Vs (in-plane) with the band gap of -0.04 eV. On the other hand, diamond is composed entirely of sp^3 bonded 3D network resulting in a cubic lattice, with an electron mobility of 1800 cm^2/Vs and the band gap of 5.47 eV.(*27, 28*) The properties of graphene are much more anisotropic than that of diamond and usually, two sets of parameters (in-plane and through plane) are usually employed to describe such phenomena (Debye temperature, charge mobility, thermal conductivity, etc.).(*24*) Other allotropic forms of carbon like fullerenes (0D), CNTs (1D) etc. can be obtained from graphene via appropriate lattice manipulation of the latter **(Figure 4)**.(*29*) As a corollary, the derived physicochemical properties of these materials are closer to that of graphene along with the generation of newer ones. For instance, CNTs can be prepared either in semiconducting or metallic form depending on the dimensions and chirality of the tubes.(*30*) More complex, hierarchical structures can be engineered (3D) by appropriate choice of allotropic building blocks (CNTs, graphene etc.) which inherits the properties of the starting components and additionally opens up exciting textural properties. A composite of CNTs and graphene, on account of its unique 3D structure, results in excellent mass transport properties and when coupled with their electrically conducting nature leads to the synthesis of synergistic smart materials.(*31, 32*)

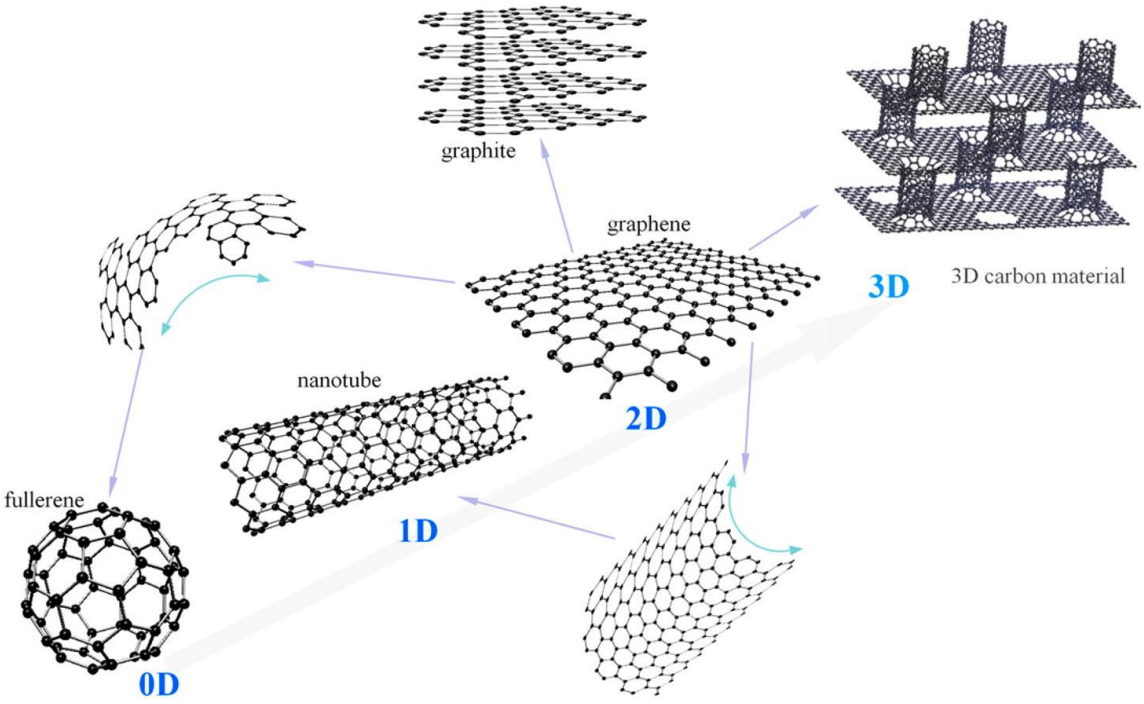

Figure 4. Schematic illustrating 2D graphene is the building block for other carbon nanomaterials viz. fullerenes (0D), carbon nanotubes (1D) and 3D carbon nanomaterials. *Adapted from reference (29).*

1.7 Band structure (DOS) in carbon materials:

Fundamental understanding of an interface involves detailed knowledge about the density of electronic states (DOS) of the system around the Fermi level under investigation as it governs the interfacial charge transfer kinetics. The DOS distribution functions of carbons are strongly correlated to their structures and are more tunable both in magnitude and shape compared to their metal counterparts.(*33, 34*) Although, the graphene exhibit no band gaps in electronic DOS like metals but the surface chemistry of the former is much more complex (governed by the method of preparation, annealing temperature etc.) than metals.(*35*) For instance, DOS of CNTs contains many van Hove singularities compared to that of graphene **(Figure 5)** and an absence of DOS near Fermi level for the latter deems it to be a semi-metal or zero-gap semiconductor whereas CNTs are metallic in nature **(Figure 6)**.(*36*) The electron transfer usually occurs at the Fermi level and the applied potential modifies it without any change in the occupation states around it. The current density (j) which is determined by the overlap integral of the Fermi level and DOS of the redox species must be optimum along with appropriate symmetry matching of frontier orbitals for facile electron transfer and ideally be elastic according to Gerischer-Marcus(*2*) model. Doping with heteroatom provides another useful pathway for tailoring the electronic properties of the carbon (discussed later).

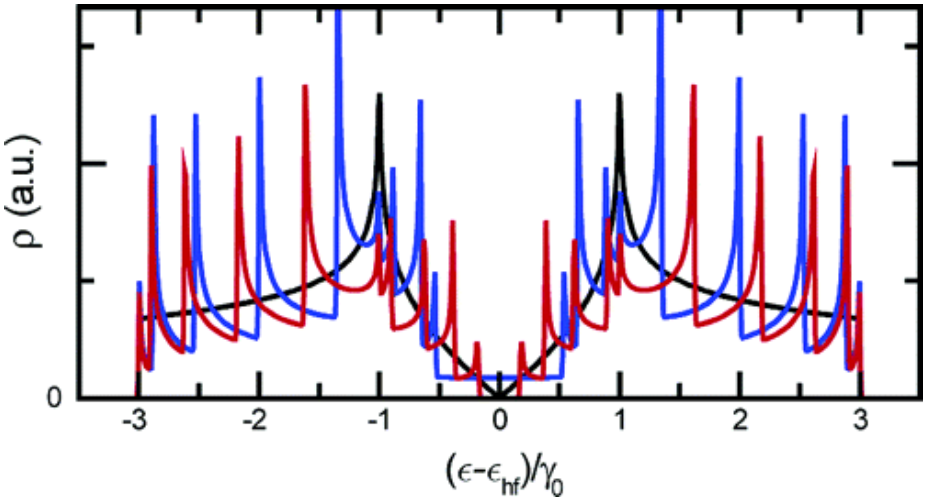

Figure 5. Comparison of DOS distribution for different carbons; metallic CNT (blue), semiconducting CNT (red) and graphene (black). van Hove singularities are prominent for CNTs and are typical for 1D structures (quantum wire) due to circumferential quantization of size-dependent electronic wave function. Zero of energy scale corresponds to Fermi level. *Adapted from reference (36).*

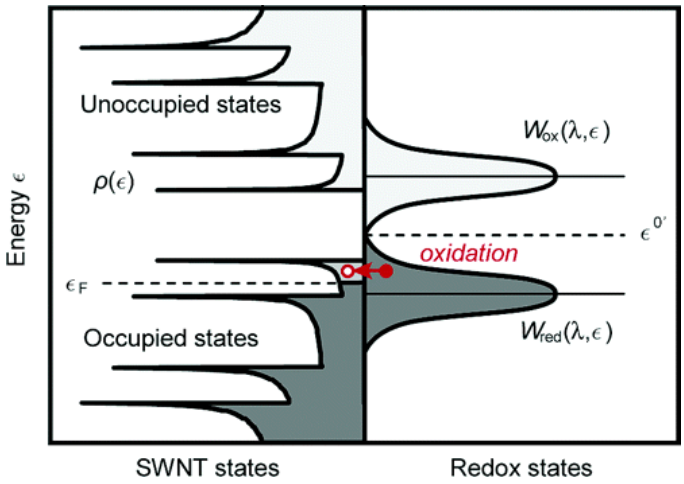

Figure 6. The condition for favorable electron transfer between semiconducting single-walled carbon nanotube, SWCNT (left) and redox species (right) in the solution phase by appropriate overlap of the electronic states. Arrow indicates the direction of charge transfer to an empty state of SWCNT. Dark and light shaded regions indicate filled and vacant states respectively. *Adapted from reference (36).*

1.8 Heteroatom doping for band tuning (DOS) in carbons:

Apart from pore engineering, subtle changes in the physicochemical properties of carbons can be brought about by heteroatom (N, P, B etc.)-doping in the carbon framework.(*36, 37*) Such dopants significantly alters the electronic properties of the adjacent carbon atoms which otherwise is not possible in pristine form. For example, nitrogen doping in CNTs significantly enhances the DOS at the Fermi level (E_F) thereby remarkably improving electronic conductivity and electron transfer rates of such doped systems. One such example **(Figure 7)** is shown here for band gap tuning and p-type transport properties in graphene obtained via graded boron doping.(*38*) This maneuverability opens up newer paradigms in technological advancements as well as the fundamental insights into the development of materials with tailor-made properties. Additionally, it was shown that not only does doping can dictate the electronic/chemical properties of carbon but can also considerably increase the thermal stability of such materials.(*39*)

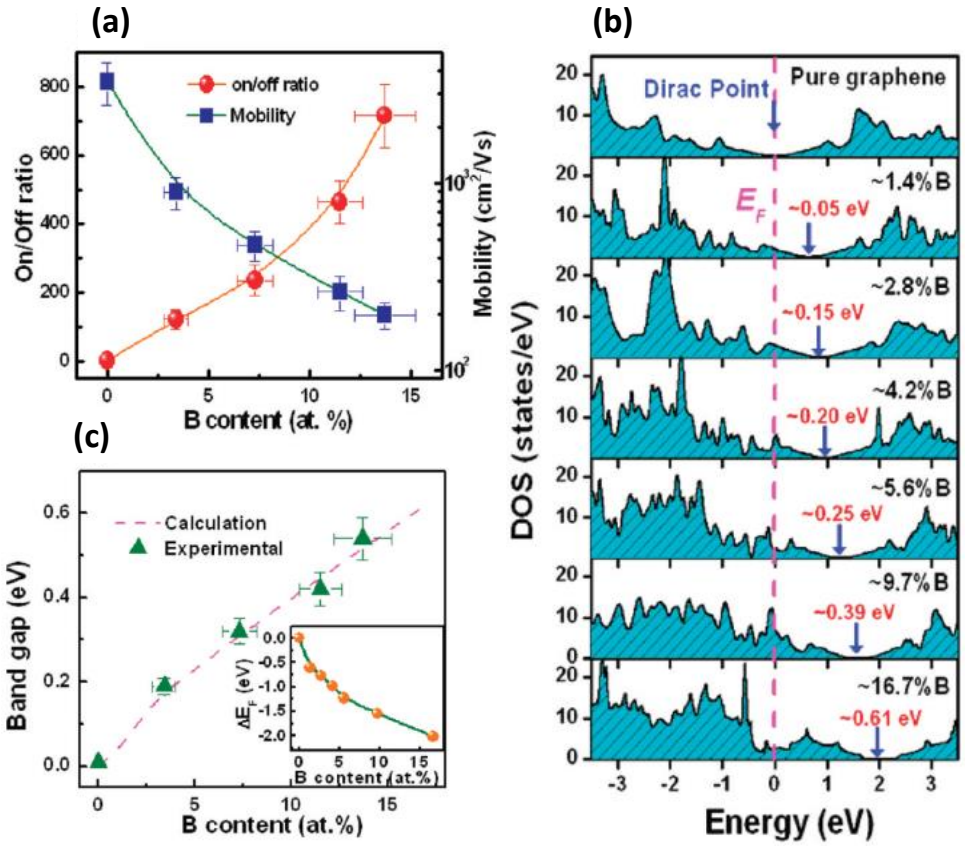

Figure 7. (a) Variation of on/off current and carrier mobility of graphene with B-doping. (b) Comparison of theoretically calculated band gap with experimentally obtained values of B-doped graphene as a function of B content. (c) Shows changes in DOS distribution with varying amounts of B. *Adapted from reference (38).*

1.9 Porous carbons:

Syntheses of pore engineered carbons pose an upfront scientific challenge and hold immense technological promise in terms of materials design and implications in practical archetypes. Tailored properties based solely upon the amount/nature of dopant with dimensions and as well as hierarchy of pores would one to enable molecular level control of desired properties.(*13, 40*) Micropores (<2 nm), pose serious mass transport issues associated with confined/limited space and exert diffusional limitation on reaction rates leave alone selectivity as a catalyst in industrial processes (zeolites).(*41*) It has been realized that such processes are even slower than Knudsen diffusion thereby mass transport to and fro from active sites located inside the micropores becomes rate limiting. Not only does the pore size plays an important role in selectivity/permeability of the molecules across the former but also pore geometry exerts a significantly vital effect on diffusion, as discussed earlier.(*41*)

Pore size and tortuosity plays an important role in the diffusion kinetics of the electrolytes at the electroactive interface and such engineering holds technological importance to the development of advanced energy storage systems.

Understanding the fundamental electrochemical processes occurring at the nanoscopic electrified interfaces would aid our ability to design materials with predictable properties. The behavior of the dielectrics in the confined spaces is different than what is observed in the bulk phases. The precise knowledge of the influence of confined pores upon the electrical double layer, more precisely solvation/desolvation effects would allow one to zero down the optimum performing materials for a given set of the dielectrics.(*42*)

Generally, the synthesis of ordered microporous carbon is not straightforward whereas it is easier to synthesize ordered mesoporous counterparts. **Figure 8** shows two predominant routes to synthesize ordered mesoporous carbons.(*15*) The first strategy involves mesoporous silica (SBA-15)(*43*) as a hard template. Subsequent precursor filling and pyrolysis at elevated temperatures followed by silica etching results in ordered mesoporous carbon.(*44*) The other approach uses self-assembly of thermosetting reagents with pore forming polymers. Further heating leads to the decomposition of porogens along with the carbon generation.(*45*)

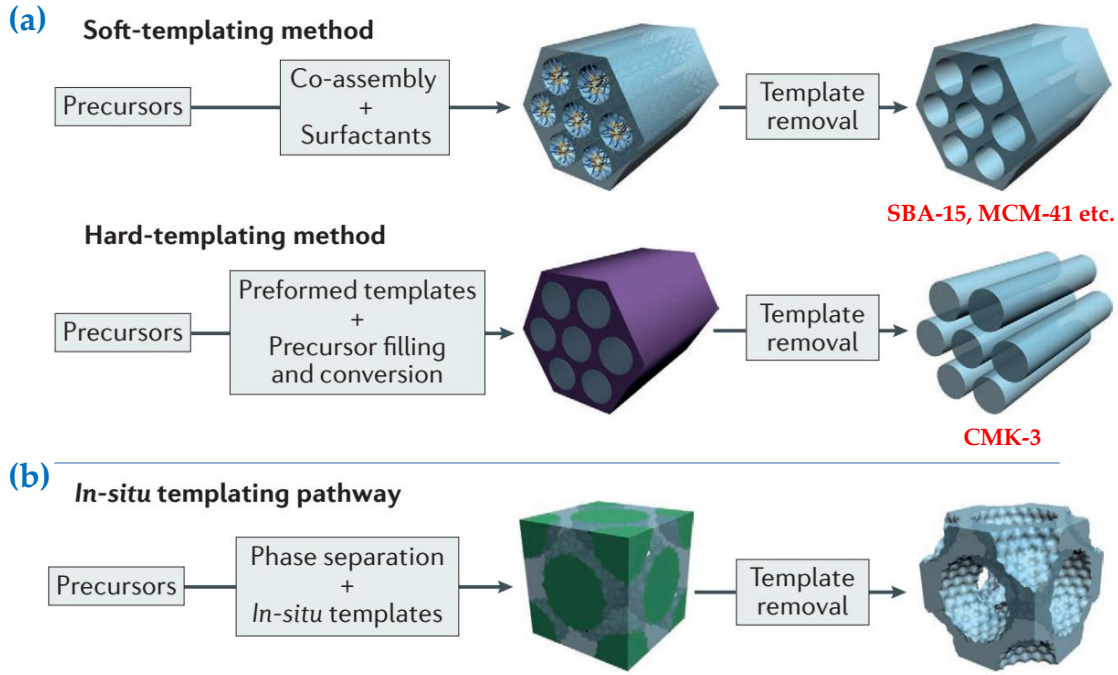

Figure 8. Strategies employed in the syntheses of ordered mesoporous compounds: (a) hard templating approach and (b) self-assembly route. Adapted with permission from reference (*15*).

1.10 Electrochemical applications of carbons:

1.10.1 Supercapacitors: The choice of carbon for electrical double layer capacitors

Capacitors are energy storing devices wherein the reversible electrosorption of ions onto the electrode surface is utilized to store electrical energy in an electrostatic field (unlike batteries which stores energy in chemical form) in response to an applied potential.(*46*) Electrochemical capacitors (ECs), also known as supercapacitors store energy either via charge accumulation at electrochemically inert, high specific surface area porous carbon (~2000 m^2 g^{-1}) electrode-electrolyte interface (electrical double layer capacitors, *EDLCs)* or by surface-bound rapid reversible redox processes occurring in certain metal oxides, electronically conducting polymers etc. (*pseudo-capacitors*).(*46, 47*) The polarization of electrodics results in accumulation/separation of charges at the interfaces leading to what is referred to as double layer capacitance (C) as enunciated by Helmholtz (*vide infra*). If an electrochemical interface is modeled as a parallel plate capacitor then its capacitance 'C' can be defined as follows:

$$C = \varepsilon A/d.$$

Clearly, the above equation states that charge storage capacity of a material goes up with surface area (A), explaining the natural choice of high surface area carbon for such applications. Pore tailoring in carbons ranging from mesopores to micropores allows to control d precisely, which is often of the order of few angstroms (Å). Therefore, decreasing the double layer thickness (d), further boosts the capacitance of such electrodes. ε is the dielectric constant of the electrolyte at the electrode-electrolyte interface.(*48-50*)

EDLCs implementing molecularly thick dielectric to store electrical energy in an electrostatic field via interfacial electrosorption of ions onto high surface area carbon with tailored pores have fundamental consequences on energy storage capability, power delivery ability and cyclability of the materials.(*47*) Pore dimensions of carbons significantly influence the double layer thickness d and the mass transport properties through it (rate capability). Electrochemical capacitors based either on EDLCs or pseudocapacitors tremendously enhance the capacitance and consequently energy density of the materials (often by a factor of 10000 as compared to conventional capacitors) with superior cycle life (100000 cycles).(*46*)

1.10.2 Mechanisms of double layer formation:

Fundamental insights to the electrical double layer (EDL) formation was first put forward by Hermann von Helmholtz while studying the stability of colloidal suspensions. He proposed that the surface charges on the colloidal particles are exactly balanced by a layer of counterions of opposite charge, behaving much like a parallel plate capacitor **(Figure 9)**.(*47*) Thus, any electrode/electrolyte interface was envisaged to contain two layers of opposite charges, their loci (passing through the center of ions) being equidistant and hence the name "double layer". Potential across the double layer was described by 1D form Poisson's equation relating charge density to potential. However, the model failed to account for potential dependence behavior of the capacitance.(*47*)

Later, Gouy and Chapman introduced Boltzmann factor to account for the thermal motion of the ions near an electrode surface contrary to the Helmholtz

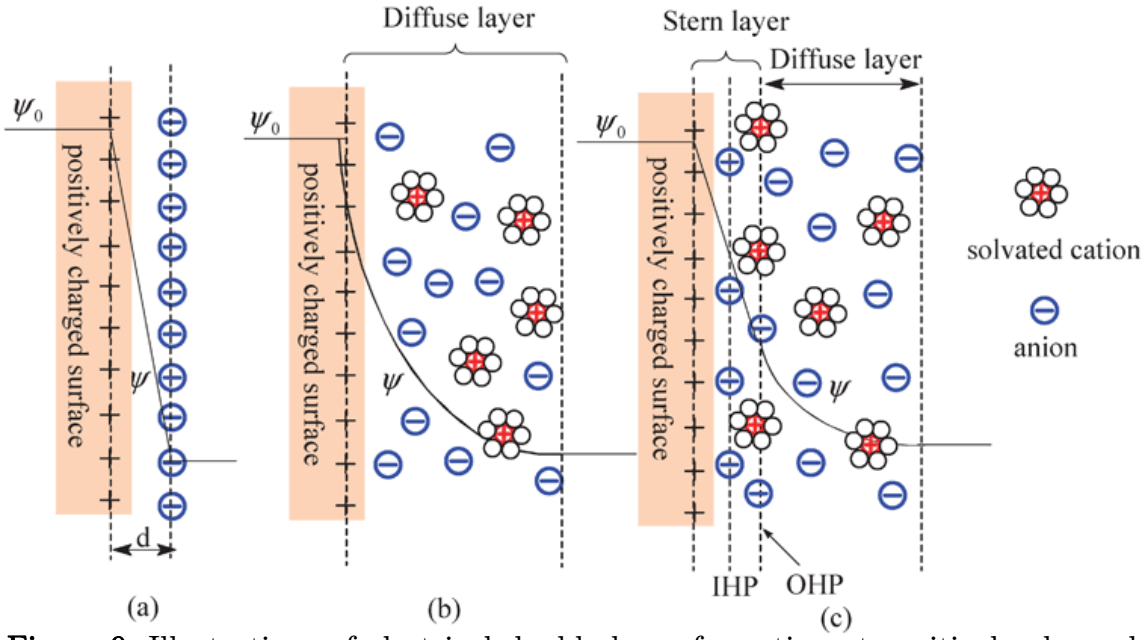

Figure 9. Illustrations of electrical double layer formation at positively charged surface according to (a) the Helmholtz model, (b) the Gouy-Chapman model and (c) the Gouy-Chapman-Stern model. The Gouy-Chapman-Stern model shows the existence of inner Helmholtz plane (IHP) referring to loci (drawn through the center of ions) of closest approach of specifically adsorbed anions and outer Helmholtz plane (OHP) refers to that of non-specifically adsorbed ions. Diffuse layer starts at the OHP. Ψ_o is the potential at the electrode surface whereas Ψ is the potential variation with distance at the electrode/electrolyte interface. Reproduced with permission from The Royal Society of Chemistry (*50*).

model, leading to the concept of diffuse double layer compared to static one of the latter. Such potential distributions were described by the Poisson-Boltzmann equation **(Figure 9)**. However, the theory failed to predict the observed behavior in highly ionic solutions.(*50*)

Stern introduced a hybrid model based on Helmholtz and as well as Gouy-Chapman ideas. It states that close to the electrode, the compact double layer is formed much like Helmholtz behavior followed by a diffuse layer of counter ions **(Figure 9)**, accounting for the thermal factor as proposed by Gouy-Chapman model.(*47, 50*) Consequently, the total capacitance of any surface arises from a series combination of Helmholtz (C_H) and Gouy-Chapman (C_D) contributions. Therefore,

$$\frac{1}{C} = \frac{1}{C_H} + \frac{1}{C_D}$$

The capacitance in series is dictated by smaller of C_H or C_D.

1.10.3 Differences between battery and supercapacitor:

Supercapacitors occupy a strategic position in terms of power and as well as energy densities when compared with other energy storage and conversion devices in what is referred to as "Ragone plot or chart" **(Figure 10)**.*(51)* Even though the energy density of the supercapacitors (5 Wh kg^{-1}) is much lower compared to batteries (180 Wh kg^{-1}), supercapacitors occupy niche position in the energy domain because of their ability to deliver exceptionally higher amount of energy in a very short span of time i.e. pulse power capability (~15 kW kg^{-1}).(*47, 49*) The higher power capability of the supercapacitors compared to batteries stems from the fundamental difference in the charge storage mechanism between the two. Batteries involve faradaic charge transfer reactions across the electrodes resulting in chemical phase transformation of the materials and are associated with kinetic limitations/polarizations.(*1*) Such processes involve irreversibility of the involved chemistries resulting in poor cyclability (few 100 cycles). Whereas, supercapacitors store energy in an electrostatic field due to reversible sorption of ions at the electrode-electrolyte interface. Since such reversible electrosorption processes do not involve any chemical/physical transformation of the chemical species; they are highly reversible in nature resulting in higher cycle life (>10000 cycles) compared to batteries. The above discussed fundamental difference between the charge storage mechanisms also explains why batteries have higher energy storage capabilities than supercapacitors.(*46*)

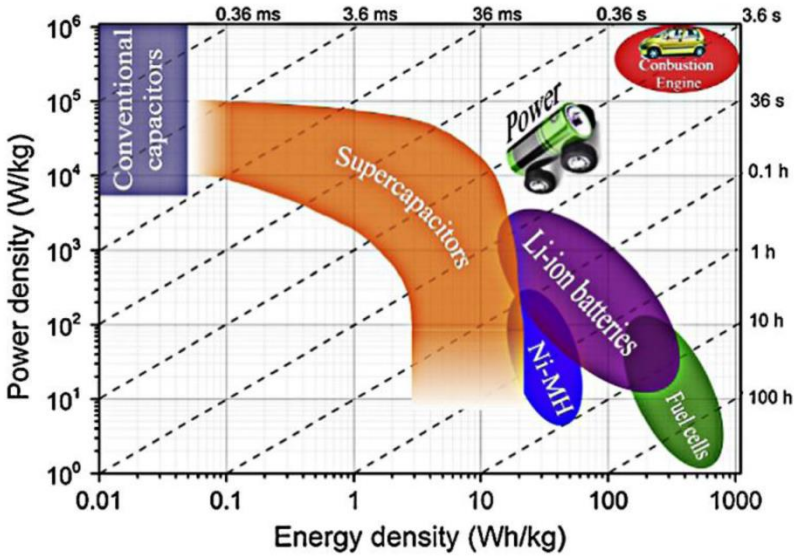

Figure 10. Ragone plot comparing specific power with specific energy of various electrochemical energy storage devices. *Adapted from reference (51).*

1.10.4 Influence of pores on carbon-based EDLCs:

Our recent fundamental understanding of double layers have greatly contributed towards the growth of the enormous amount of literature utilizing different carbons such as activated carbons, templated porous carbons, CNTs, graphene, carbon fibers, carbon aerogels etc. as EDLCs with high surface area and well-developed porosity.(*52*) It has been realized that pore dimensions play a primary role in the double layer formation and dictates the solvation environment of ions in the micropores. Mesoporous carbon allows double layer formation within the cylindrical pores **(Figure 11a)** thereby establishing electric double-cylinder capacitors (EDCCs).(*53, 54*) However, unusual enhancement in specific capacitances was observed in the subnanometer regime when the ion size matched with the pore diameter (0.7 nm) of the micropores, which previously were thought to be inaccessible, indicating the ripping of solvation sheath in confined spaces **(Figure 11b-c)**. Such capacitance was referred to as an electric wire in a cylinder model, EWCCs **(Figure 11b)**.(*53, 54*)

The anomalous dielectric behavior in micropores and the resultant unusual enhancement in the storage capacity throws up interesting electrified interfacial phenomena at the nanoscales. Micropores inherit strong local electric field due to sharp tips arising due to curvature effect.(*47, 55*) Therefore, it is clear that hierarchical porous structures (micro-meso) would result in enhanced energy density and as well as power capability of the materials. One such strategy was used by Juan et al. to obtain hierarchical (micro-meso) carbon from CMK-3 by

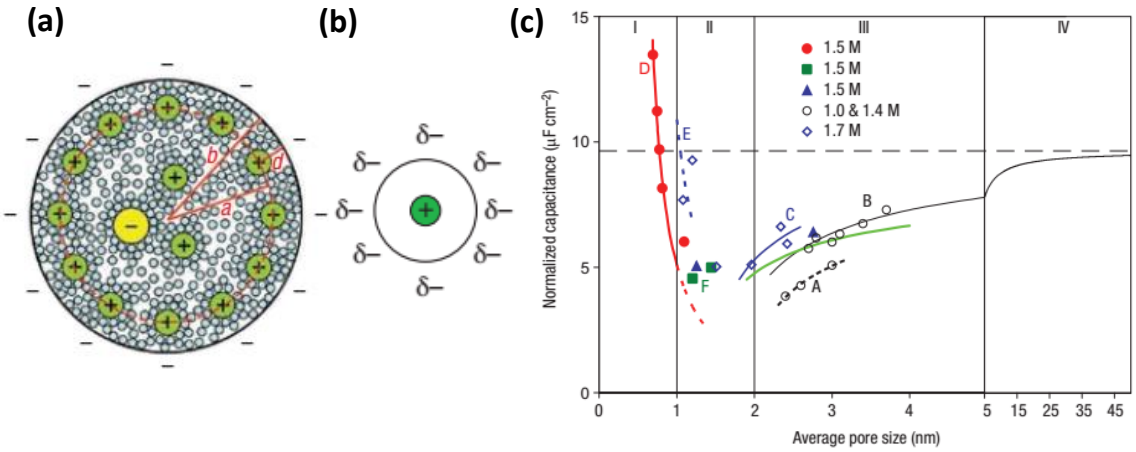

Figure 11. (a) Schematic illustrating mesopores allowing the formation of electric double-cylinder capacitors (EDCCs) whereas (b) shows confined spaces in micropores result in partial/full desolvation of ions resulting in an electric wire-in-cylinder type of capacitors (EWCCs).(*53*) (c) Effect of pore size on specific capacitance for different carbon samples (A, B-templated mesoporous carbons; C-activated mesoporous carbon; D, F-carbide-derived microporous carbon, and E-microporous activated carbon) in $NEt_4^+BF_4^-$-acetonitrile mixture. The unusual enhancement in the region I is attributed to the desolvation of ions in the micropores. *Adapted with permission from reference (49, 53, 54).*

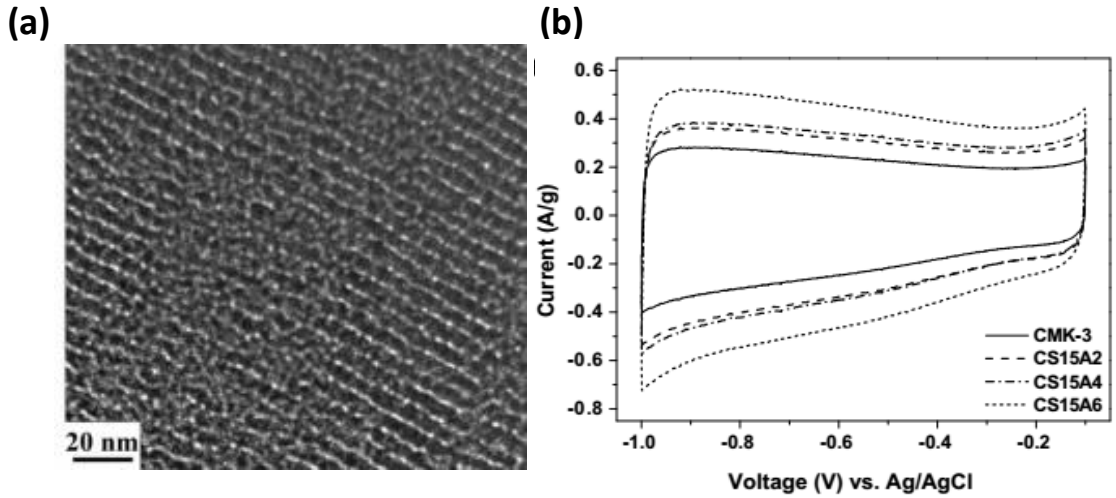

Figure 12. (a) TEM image and (b) CVs of hierarchical porous carbons obtained from CO_2 activation of CMK-3 respectively. Dotted curves are for derived carbons. *Adapted with permission from reference (56).*

CO_2 activation. The obtained material showed excellent capacity as well as capacity retention at different scan rates **(Figure 12)**.(*56*)

1.11 Pseudocapacitors:

Pseudocapacitance arises out of special thermodynamic condition wherein a finite derivative exists for dq/dV i.e. the amount of charge passed to the change in potential, unlike batteries.(*46*) Since pseudocapacitors involve actual electron transfer across the interface, they result in the change of the redox states of the electroactive material leading to higher storage capacity (~100 times) compared to EDLCs. Electronically conducting polymers (polypyrrole, polyaniline etc.), heteroatom (N, O etc.) doped carbons, carbons with electrosorbed H, RuO_2, Fe_3O_4, MnO_2 etc. are some of the well-studied pseudocapacitive systems.(*47*) RuO_2, a well-studied system on account of its good conductivity; high capacity (600 F g^{-1}), excellent electrochemical reversibility along with long cyclability has three redox states (II to IV) within 1.2 V under acidic conditions.(*46, 49*) Pseudocapacitive behavior involves simultaneous electron transfer and proton electro-adsorption on the surface RuO_2 particles.

$$RuO_2 + x\,H^+ + xe^- \rightleftharpoons RuO_{2-x}(OH)_x$$

Where $0 \leq x \leq 2$. The continuous variation of x during electrochemical cycling process results in capacitive type behavior with Frumkin-type isotherm for ion adsorption. The high cost and less abundance of the RuO_2 have given way to other metal oxides like MnO_2 but with lower capacities (300 F g^{-1}).(*47*) Often transition metal oxides and carbon based composites are used on account of their highly accessible porous structure, high specific surface area (SSA) resulting in enhanced volumetric capacity (305 F cm^{-3}).(*47*) Such systems involves contributions from EDLCs and as well as pseudocapacitance. Another important strategy to improve capacity involves the functionalization of high specific surface area (SSA) carbon with redox active moieties (quinone, catechol etc.).(*57*) Recently, redox active covalent organic frameworks (COFs) have shown to be excellent candidates for pseudocapacitive energy storage and have added advantage of well-developed porosity unlike conducting polymers.(*58*) Another technologically important strategy to enhance both energy density and power capability involves the fabrication of hybrid systems wherein EDLC (power electrode) type of electrode is combined with redox type electrode (energy electrode).(*47, 59*)

1.12 Carbon as a cathodic host for S in Li/Na-Sulfur batteries:

As the storage capacity of state-of-the-art Li-ion (intercalation based) batteries (420 Wh/kg) reaching theoretical limits and due to their limited capacity, the demand for alternative high energy density systems to be used in grid level storage, hybrid plug-in vehicles etc. becomes inevitable.(*60, 61*) Rechargeable Li-S systems is one such technology offering high energy density (2567 Wh/kg) along with low cost and lower CO_2 footprint compared to gasoline-driven vehicles today.(*62*) However, Li-S technology is yet to receive a major breakthrough as S based cathodes suffer from tremendous capacity fading upon cycling due to dissolution of higher order polysulfides (Li_2S_x; $8 \geq x \geq 4$) in the organic electrolytes causing insulating deposits of Li_2S_2 and Li_2S on either electrodes via shuttling effect, resulting in increased cell resistance and active mass loss. Besides, S is an insulator (1×10^{-28} S/m) and undergoes huge volume change (~80%) upon full lithiation (Li_2S).(*63*) Encapsulation of S in cathodic porous carbon hosts is an extensively implemented design-strategy to mitigate above issues. The versatility of carbon lies in its unique textural engineering along with its high conductivity, low cost and low density.(*64, 65*) The Li-S cell design principle and typical charge-discharge behavior along with the involved intermediates are shown in **Figure 13a-b.**(*62*)

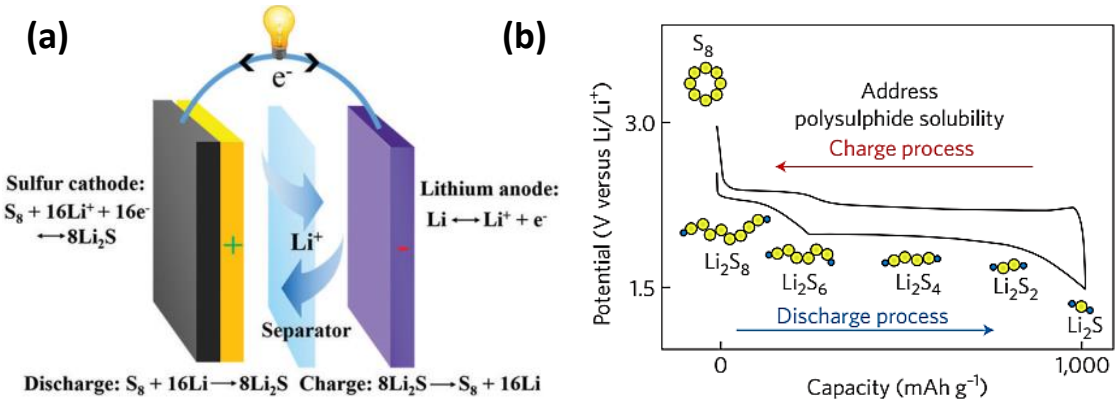

Figure 13. (a) Schematic of the electrochemical Li-S cell along with (b) galvanostatic charge-discharge profile showing two prominent plateaus with corresponding discharge intermediates. Adapted with permission from references (*62*) and *(66).*

Nazar et al.(*67*) were first to incorporate S into mesoporous conducting carbon (CMK-3) host thereby 'wiring' the sulfur with well-developed porosity and high sulfur loading (~70 wt.%). The nanostructured carbon-sulfur exhibited a high reversible capacity of 1320 mA h g^{-1} with excellent reversibility **(Figure 14).**

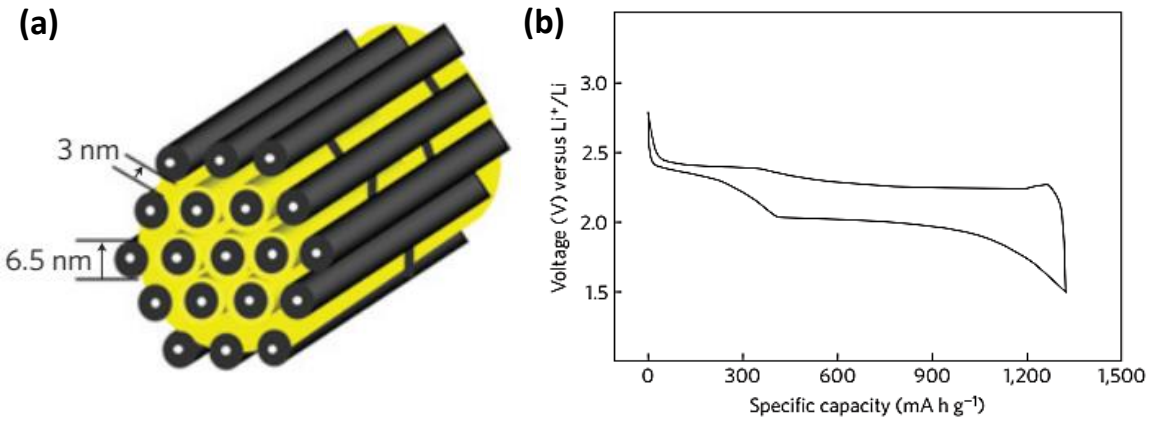

Figure 14. (a) Schematic indicating CMK-3/S composite with the former wiring the latter along with (b) galvanostatic charge-discharge profile. *Adapted with permission from reference (67).*

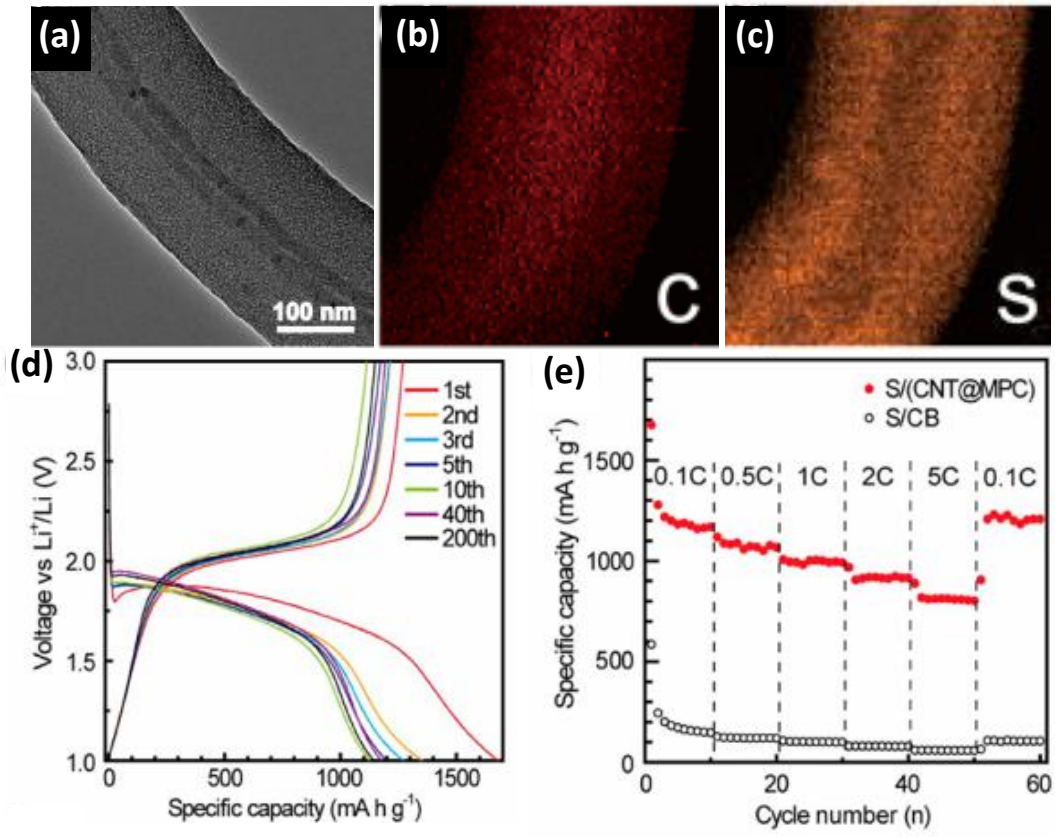

Figure 15. (a) TEM image of microporous carbon coaxially grown over CNT. (b) and (c) are EDS elemental mapping of C and S respectively. (d) Galvanostatic charge-discharge profiles and (e) rate capability performance of S/(CNT@MPC). *Adapted with permission from reference (68).*

Above work led to vigorous investigations in different types of carbon host materials with hierarchical textural properties(*69*) showing excellent mass transportability, including graphene/CNT based composites.(*68, 70, 71*) One notable work was reported from Wan et al. group, wherein, the metastable states corresponding to smaller S molecules (S_{2-4}) were entrapped into microporous carbon matrix grown coaxially over metallic CNTs (CNT@MPC).(*68*) Such design strategy mitigated unfavorable S_8 to S_4^{2-} transition leading to the elimination of shuttle effect **(Figure 15)**. The synthesized materials exhibited enhanced initial capacity (1667 mA h g^{-1}) with improved rate capability and good cycling stability (200 cycles) on account of low active mass loss.

The poor abundance of Li has stimulated the development of alternative energy systems based on Na-S couple due to similar chemistries and low cost.(*72, 73*) Although, carbon-based hosts have not been much explored for Na-S systems but the implications are much more severe for such batteries as the full sodiation of sulfur (Na_2S) involves a volume expansion of ~260 %.(*74, 75*) Flexible carbon framework with high SSA, interconnected hierarchical porous structure along with enhanced pore volume would be ideal for accommodating large volume changes associated with such battery systems. Recently, Shi et al.(*76*) reported interconnected mesoporous carbon hollow sphere (iMCHS) as S host against Na **(Figure 16)**.

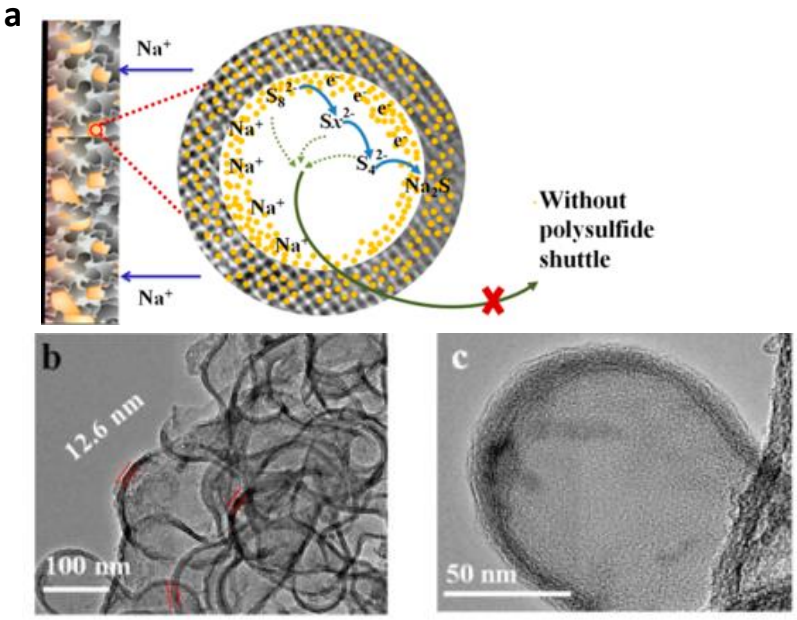

Figure 16. (a) Schematic indicating the trapping of the intermediate in iMCHS. (b) and (c) shows low and high magnification TEM images of S confined iMCHS respectively. Adapted with permission from reference (*76*).

1.13 Electrocatalysis and carbon based electrocatalysts (OER, HER and ORR):

Limited fossil fuel reserves and their adverse environmental impact have accelerated the research into sustainable and renewable(*77, 78*) energy technologies like fuel cells (FCs),(*79*) water splitting and metal-air ($M-O_2$)(*80, 81*) batteries. Since these domains are not limited by Carnot processes and hence promise to deliver much higher efficiencies compared to traditional energy sources (coal, gasoline etc.) along with the potential for scalability, higher energy density and benign end product viz. water.(*3*) Using renewable power (Sun, wind etc.) to store electrical energy into chemical form (H_2) via water splitting is an attractive alternative to overcome the problem of intermittency and unpredictability associated with such renewable resources.(*82*) Thus, we can harness energy even when the sun is not shining or when the wind is not blowing; theoretically leading towards carbon-neutral energy generation and consumption processes. Hydrogen, thus generated can be later used as an energy source (fuel) when oxidized in fuel cell leaving behind water as the end product. Similarly, oxygen can be used in a fuel cell or $M-O_2$ batteries as an oxidizer.

$$2H_2O\ (l) \rightarrow 2H_2(g) + O_2(g)$$

The bottleneck to the large-scale development of above technologies faces an uphill task to create effective, efficient, earth-abundant electrocatalysts which could catalyze oxygen evolution reaction (OER),(*83*) oxygen reduction reaction (ORR)(*84*) and hydrogen evolution reaction(*79*) near their thermodynamic potential (E_o). Particularly, kinetically sluggish $4e^-$ transfer processes involved in ORR/OER governs the overall efficiency of energy generation and conversion technologies. Most of the catalysts which are used today are based on precious metal (Pt/Ru) based systems and undergo time-dependent drift, CO poisoning, methanol crossover effects etc.(*85*) Renewable nature of such technologies must also have economical facets; therefore, it is imperative to look beyond traditional precious metal-based systems for large-scale commercial applications with activities similar to the state-of-the-art catalysts. Even though other earth-abundant d-block non-precious element (Fe, Co, Ni etc.) can be used as an electrocatalyst for carrying out above reactions but corrosion/instability impedes their applicability over a wider pH range.(*86*)

Carbon emerges as the natural choice to address above issues because of its rich chemistry, aiding us with the tool to tailor its properties at the molecular level. Various allotropes of carbon exhibit properties ranging from metallicity to excellent mechanical strength leave alone its superior resistance to extreme pH

solutions which would rarely be offered by any single element of the periodic table.(*18*) Doping with appropriate p block elements would open up exotic electronic properties and favorable catalytic sites. Our recent understanding in engineering porous carbons would greatly aid above properties resulting in superior mass transport ability at the electroactive interfaces. This synergistic effect would lead to the development of highly efficient earth-abundant catalysts which could reduce/replace precious metal based state-of-the-art catalysts.(*29*)

The prominent breakthrough in the development of heteroatom(N)-doped carbon for ORR was provided by the pioneering work of Liming Dai et al.,(*85*) wherein it was shown that N-doped vertically aligned carbon nanotubes (VA-NCNT) could efficiently catalyze the direct four-electron reduction of molecular O_2 to H_2O **(Figure 17)**. N-doping causes charge/spin redistribution on the adjacent carbon atom thereby generating favorable sites for catalyses wherein chemisorption mode of O_2 changes from end-on mode to side-on adsorption with effective weakening of O-O bond; facilitating ORR. Similarly, Yao Zheng et al.(*87*) developed synergistically coupled g-C_3N_4 and N-doped graphene (C_3N_4@NG) composite as an excellent electrocatalyst for HER. DFT calculations revealed that the free-energy $|\Delta G_{H^*}|$ for the intermediate adsorption (a major descriptor for HER activity) for C_3N_4@NG (0.19 eV) has an optimum value compared to both pristine g-C_3N_4 (-0.54 eV) and N-graphene (0.57 eV) leading to perfect adsorption-desorption interaction with surface resulting in enhanced performance **(Figure 18)**.

Later on it was shown that pore engineering (leading to excellent mass transport properties) and multi/mono-heteroatom-doping for tuning the electronic properties in carbons could be effectively utilized to create excellent bifunctional electrocatalysts; simultaneously catalyzing ORR/OER(*88*) and ORR/HER,(*89*) therefore it can be used in M-O_2 batteries and regenerative FCs respectively. Jintao Zhang et al. have shown that 3D N, P co-doped mesoporous carbon (NPMC) foam prepared by the carbonization of phytic acid containing polyaniline (PANi) aerogel could act as an excellent electrocatalyst for ORR and OER **(Figure 19)**.(*88*) Furthermore, NPMC foam was used as air electrode for the fabrication of primary as well as rechargeable Zn-air batteries with the former exhibiting an open-circuit potential of 1.48 V **(Figure 20)**.

The versatility of pore engineered, heteroatom doped-carbon in simultaneously catalyzing ORR, OER and HER under basic conditions was demonstrated by

the use of N and S co-doped carbon with stereoscopic holes in 2D graphitic structure (SHG) resulting in excellent mass transport ability. Additionally, the

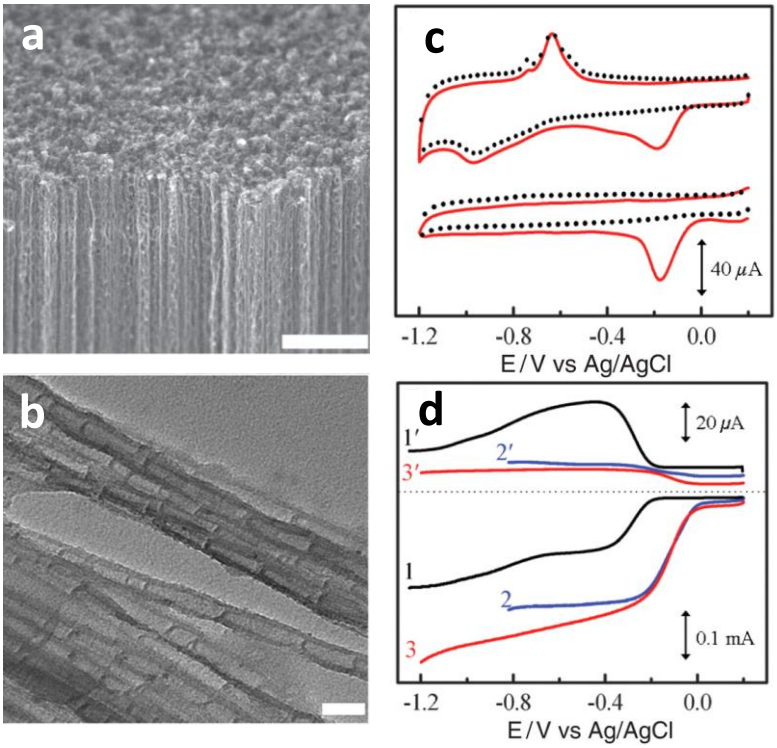

Figure 17. (a) and (b) are SEM and TEM images of vertically aligned nitrogen-doped carbon nanotubes (VA-NCNT) respectively. (c) CVs of VA-NCNT and Pt/C (dotted line and solid lines indicate measurements are performed under Ar and air saturated conditions respectively) whereas (d) depicts RRDE voltammograms. Scale bars: 2 μm (a); 50 nm (b). *Adapted from reference (85).*

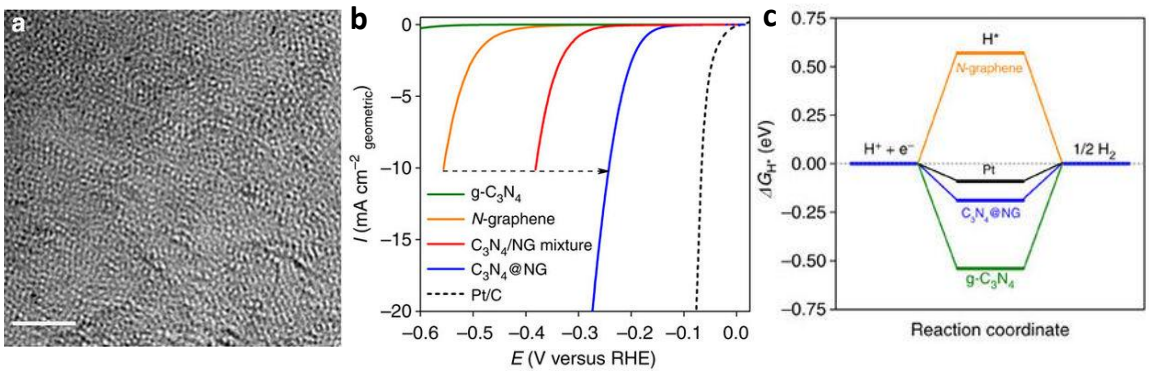

Figure 18. (a) TEM image of C_3N_4@NG hybrid. (b) LSV of C_3N_4@NG hybrid compared with pristine g-C_3N_4, N-graphene and Pt/C. (c) Calculated free-energy diagram of C_3N_4@NG, pristine g-C_3N_4, N-graphene and Pt/C. Adapted from reference (*87*).

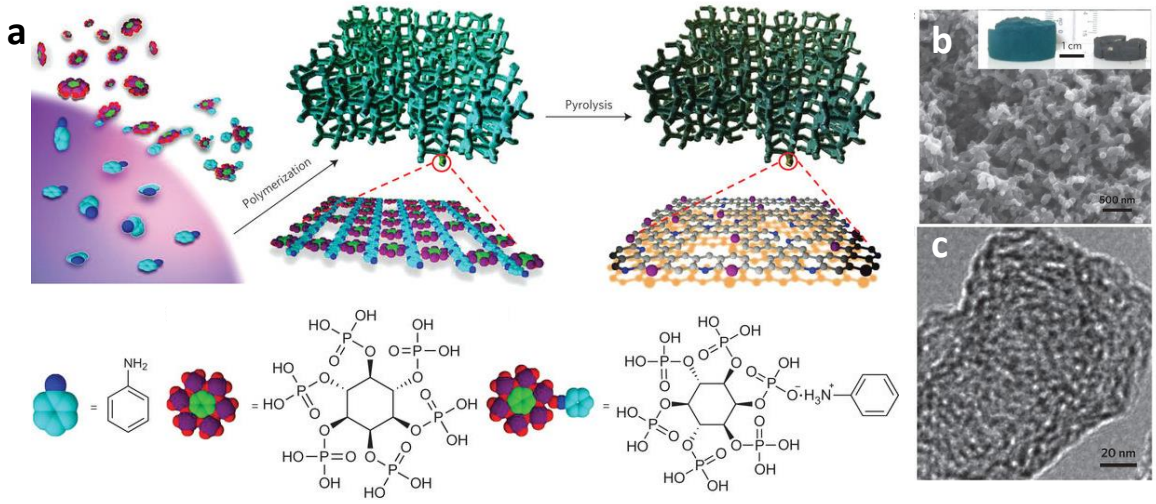

Figure 19. (a) Schematic illustrating the preparation of 3D N and P co-doped mesoporous carbon (NPMC) foam by pyrolysis of phytic acid containing polyaniline foam. (b) is SEM image of pyrolyzed carbon (NPMC). Inset of (b) shows optical images of polyaniline aerogel before (left) and after (right) pyrolysis. (c) HRTEM image of NPMC. *Adapted from reference (88).*

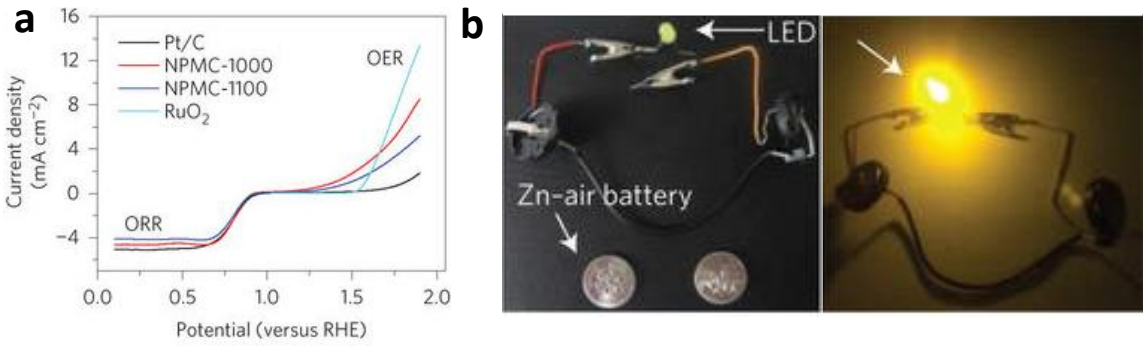

Figure 20. (a) Linear sweep voltammograms (LSV) of NMPC carbons along with that of state-of-the-art catalysts (Pt/C and RuO_2) in 0.1 M KOH (5 mV s^{-1}) at 1600 rpm, indicating bifunctional activity towards ORR and OER. (b) Digital images of an LED (~2.2 V), before and after being driven by two Zn-air batteries in series. *Adapted from reference (88).*

strategy demonstrated that by appropriately modulating bond polarities thereby charge tuning, interconnected pore structure with a balanced density of active sites and good conductivity leads to optimal overall activity similar to the state-of-the-art catalysts.(*90*)

Such dopants usually alter the electronic cloud around the neighboring carbon atoms thus activating carbon's π electron system by breaking their electroneutrality and hence provide favorable sites for such catalysis. Synergistic

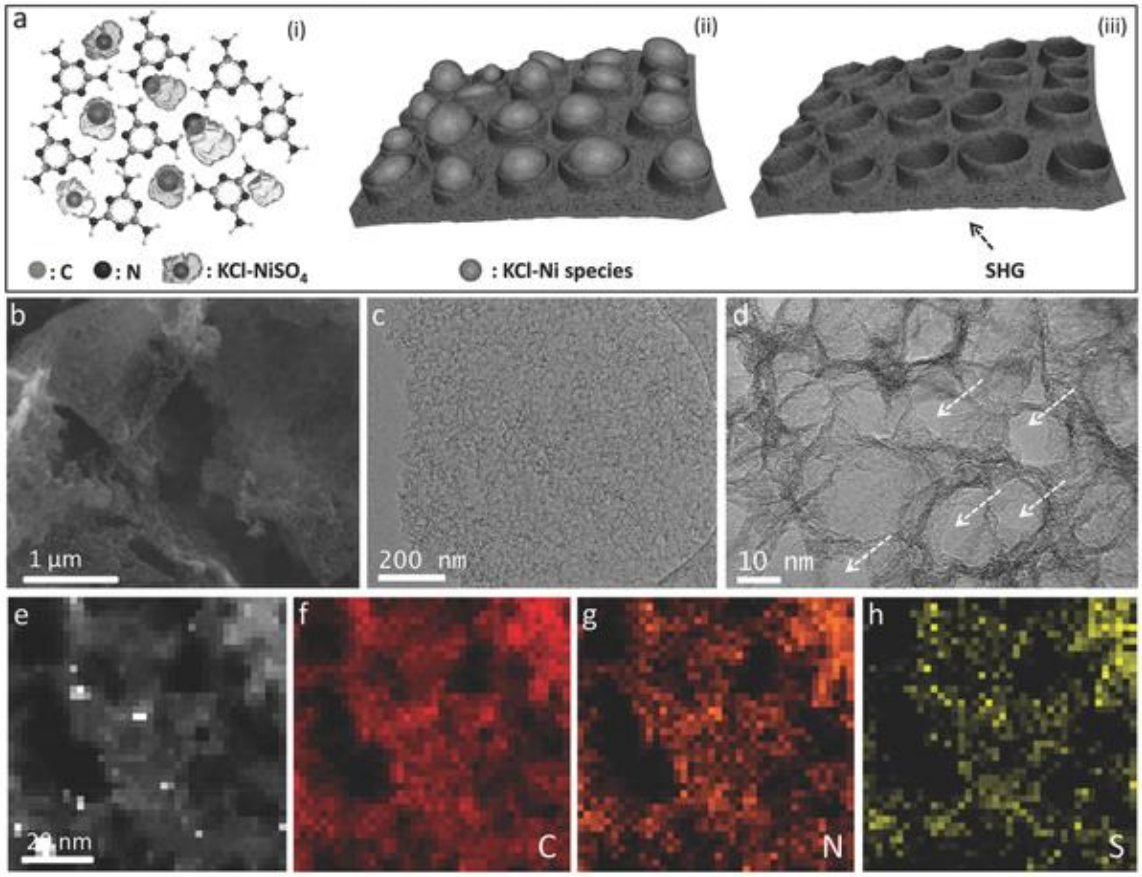

Figure 21. (a) Schematic illustration depicting the synthesis of stereoscopic holes containing graphitic carbon (SHG) prepared from melamine-$NiSO_4$-KCl precursor. (b) SEM whereas (c) and (d) are TEM images of SHG. (e) HAADF-STEM image of SHG along with corresponding energy dispersive X-ray spectroscopic elemental mapping (f-h) of C, N and S showing their uniform dispersion in the matrix. Adapted from reference (*90*).

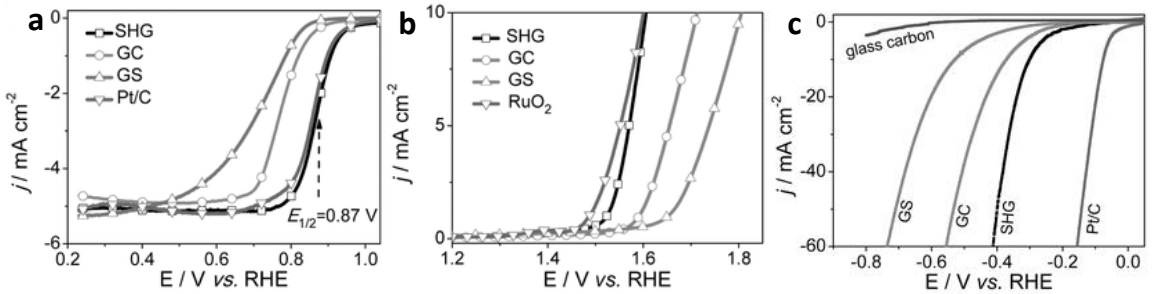

Figure 22. (a) ORR, (b) OER and (c) HER performance of SHG in 0.1 M KOH solution. Adapted with permission from reference (*90*).

effect of multiple heteroatoms (N, P, S etc.) doping was accounted for the observed bifunctional/trifunctional activities which otherwise is not possible in single heteroatom doped carbons **(Figure 21-22)**. Thus, highlighting multiple heteroatom doping is much more effective than single atom doping in tuning the electrocatalytic properties of the carbon materials.(*90, 91*) However, it is known that bifunctionality in catalyzing OER/ORR(*92*) or ORR/HER(*93*) can also be achieved either by mono-heteroatom doped (N) or intrinsic defect based carbon systems.(*94*)

It was shown that different nitrogen types (quaternary, pyridinic, pyrrolic etc.) create both p-type and n-type domains in the carbon frameworks thereby affecting the property of nearby carbons by either making them electrophilic or nucleophilic **(Figure 23)**.(*95*) Quaternary nitrogens present on the edge of the graphene are more active for ORR as it facilitates the formation of rate-determining OOH species. Besides topological defects,(*94*) certain theoretical results highlight the prospective positive effect of curvature(*37*) on the electrocatalytic performance of such carbon-based materials. This charge redistribution on the adjacent carbon atom controls the chemisorption mode of O_2 (side-on over end-on).

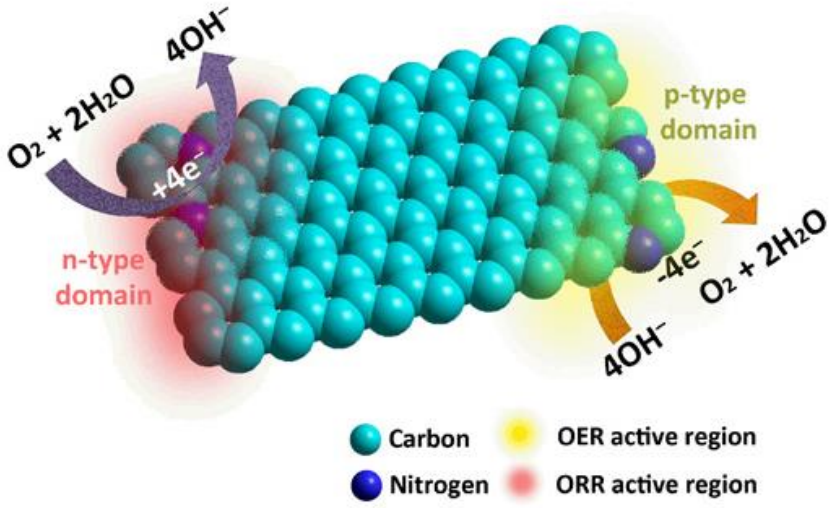

Figure 23. Schematic indicating different types of active sites in n- and p-type domains catalyzing ORR and OER in N-doped carbons. *Adapted from reference* (*95*).

1.13.1 Mechanisms of ORR and OER:

Molecular O_2 reduction can occur either through a direct efficient four-electron pathway resulting in of H_2O/HO^- formation or through a less efficient route

involving two-step, two-electron process with the intermediate H_2O_2 formation.(*88, 96*) Therefore, for ORR/OER under acidic conditions, we have:

$$O_2 + 4H_3O^+ + 4e^- \rightleftharpoons 6H_2O$$

The forward process leads to ORR whereas the reverse reaction would result in OER. The predominantly observed associative mechanism for ORR involves HOO* intermediate and the elementary steps include the following reaction:

$$* + O_2(g) \rightarrow O_2^*$$

$$O_2^* + H_3O^+ + e^- \rightarrow HOO^* + H_2O$$

$$HOO^* + H_3O^+ + e^- \rightarrow O^* + 2H_2O(l)$$

$$O^* + H_3O^+ + e^- \rightarrow HO^* + H_2O$$

$$HO^* + H_3O^+ + e^- \rightarrow 2H_2O(l) + *$$

Where O_2^* , HOO^*, $HO^*$and O^* are the adsorbed intermediates at the active site $*$ on the surface of the catalyst.

Since OER is a reverse process to that of ORR, above steps must be reversed to get elementary steps involved in the oxygen evolution reaction.

Similarly, for ORR/OER under basic conditions we have:

$$O_2 + 2H_2O + 4e^- \rightleftharpoons 4HO^-$$

As above, the forward and backward reaction leads to ORR and OER respectively. Associative pathway for ORR under basic conditions would include following elementary steps:

$$* + O_2(g) \rightarrow O_2^*$$

$$O_2^* + H_2O(l) + e^- \rightarrow HOO^* + HO^-$$

$$HOO^* + e^- \rightarrow O^* + HO^-$$

$$O^* + H_2O(l) + e^- \rightarrow HO^* + HO^-$$

$$HO^* + e^- \rightarrow HO^- + *$$

Needless to mention, elementary steps for OER can be deduced if the above ORR reactions are reversed.

1.13.2 Mechanisms of HER:

The cathodic H_2 evolution reaction is a 2 electron process with a single intermediate H* and under acidic conditions can be written as(*3, 4, 97*)

$$2H^+ + 2e^- \rightarrow H_2$$

The first step involves the adsorption of H^+ on an active site $*$ on the catalyst surface to yield an intermediate H*; this primary proton discharge step is known as the Volmer reaction (Tafel slope ~ 120 mV dec^{-1}).

$$* + H^+ \rightarrow H^* \qquad \text{(Volmer reaction)}$$

The amount of coverage of the intermediate H* on the surface dictates the subsequent mechanistic pathway. If the coverage is low, then the Heyrovsky pathway (Tafel slope ~ 40 mV dec^{-1}) predominates wherein adsorbed intermediate H* simultaneously combines with a proton and an electron to liberate molecular H_2.

$$H^* + H^+ + 2e^- \rightarrow H_2 \quad \text{(Heyrovsky reaction)}$$

In the case where the surface density of H* is high; usually, two adjacent intermediates combine to produce H_2 and is said to follow Tafel pathway (Tafel slope ~ 30 mV dec^{-1}).

$$H^* + H^* \rightarrow H_2 \quad \text{(Tafel reaction)}$$

Therefore, hydrogen evolution from any surface follows either Volmer-Heyrovsky or Volmer-Tafel mechanism. Sometimes, it has also been observed that the initially adsorbed species H* after Volmer step, migrates to different active sites on the electrode surface in what is referred to as "spill over process",(*98*) to form stabilized intermediate followed by H_2 liberation either by Heyrovsky or Tafel pathway.

1.14 Summary:

Therefore, it is clear that pore engineering plays a crucial role in electrochemical performance of a device as it significantly governs the mass transport at the electrodics. Carbon on account of its versatile properties viz. excellent electronic

conductivity, high abundance, easy maneuverability of textural parameters, tailored tuning of band-gap, low-density etc. emerges as a natural choice for advanced electrochemical applications.

1.15 References:

1. M. Winter, R. J. Brodd, What Are Batteries, Fuel Cells, and Supercapacitors? *Chem. Rev.* **104**, 4245 (2004).
2. A. J. Bard, L. R. Faulkner, *Electrochemical Methods: Fundamentals and Applications, 2nd Edition*. (John Wiley & Sons, 2000).
3. J. O. M. Bockris, A. K. N. Reddy, M. E. Gamboa-Aldeco, *Modern Electrochemistry 2A: Fundamentals of Electrodics*. (Springer US, 2001).
4. J. O. M. Bockris, A. K. N. Reddy, *Modern Electrochemistry 2B: Electrodics in Chemistry, Engineering, Biology and Environmental Science*. (Springer, 1998).
5. F. A. L. Dullien, *Porous Media: Fluid Transport and Pore Structure*. (Academic Press, 1979).
6. Z. Song, Z. Xu, Ultimate Osmosis Engineered by the Pore Geometry and Functionalization of Carbon Nanostructures. *Sci. Reports* **5**, 10597 (2015).
7. W. M. Deen, Hindered transport of large molecules in liquid-filled pores. *AlChE J.* **33**, 1409 (1987).
8. J. Rouquerol, F. Rouquerol, P. Llewellyn, G. Maurin, K. S. W. Sing, *Adsorption by Powders and Porous Solids: Principles, Methodology and Applications*. (Elsevier Science, 2013).
9. P. M. Adler, *Porous Media: Geometry and Transports*. (Butterworth-Heinemann Limited, 1992).
10. J. Bear, *Dynamics of Fluids in Porous Media*. (Dover, 1972).
11. M. I. Gariboldi, S. M. Best, Effect of Ceramic Scaffold Architectural Parameters on Biological Response. *Frontiers in Bioengineering and Biotechnology* **3**, (2015-October-09, 2015).
12. M. Majumder, N. Chopra, B. J. Hinds, Mass Transport through Carbon Nanotube Membranes in Three Different Regimes: Ionic Diffusion and Gas and Liquid Flow. *ACS Nano* **5**, 3867 (2011).
13. J. H. Bae, J.-H. Han, T. D. Chung, Electrochemistry at nanoporous interfaces: new opportunity for electrocatalysis. *Phys. Chem. Chem. Phys.* **14**, 448 (2012).
14. C. Chen *et al.*, Highly Crystalline Multimetallic Nanoframes with Three-Dimensional Electrocatalytic Surfaces. *Science* **343**, 1339 (2014).

15. W. Li, J. Liu, D. Zhao, Mesoporous materials for energy conversion and storage devices. *Nat. Rev. Mater.* **1**, 16023 (2016).
16. H. Chen *et al.*, Ultrafast all-climate aluminum-graphene battery with quarter-million cycle life. *Sci. Adv.* **3**, (2017).
17. H. Sun *et al.*, Three-dimensional holey-graphene/niobia composite architectures for ultrahigh-rate energy storage. *Science* **356**, 599 (2017).
18. R. L. McCreery, Advanced Carbon Electrode Materials for Molecular Electrochemistry. *Chem. Rev.* **108**, 2646 (2008).
19. W. Zhang *et al.*, Recent development of carbon electrode materials and their bioanalytical and environmental applications. *Chem. Soc. Rev.* **45**, 715 (2016).
20. W. Gu, G. Yushin, Review of nanostructured carbon materials for electrochemical capacitor applications: advantages and limitations of activated carbon, carbide-derived carbon, zeolite-templated carbon, carbon aerogels, carbon nanotubes, onion-like carbon, and graphene. *Wiley Interdisciplinary Reviews: Energy and Environment* **3**, 424 (2014).
21. H.-C. Wu, X. Chang, L. Liu, F. Zhao, Y. Zhao, Chemistry of carbon nanotubes in biomedical applications. *J. Mater. Chem.* **20**, 1036 (2010).
22. T. D. Burchell, *Carbon Materials for Advanced Technologies*. (Elsevier Science, 1999).
23. A. Tiwari, S. K. Shukla, *Advanced Carbon Materials and Technology*. (Wiley, 2014).
24. M. J. Allen, V. C. Tung, R. B. Kaner, Honeycomb Carbon: A Review of Graphene. *Chem. Rev.* **110**, 132 (2010).
25. E. H. L. Falcao, F. Wudl, Carbon allotropes: beyond graphite and diamond. *J. Chem. Tech. Biotech.* **82**, 524 (2007).
26. S. K. Tiwari *et al.*, Magical Allotropes of Carbon: Prospects and Applications. *Crit. Rev. Solid State Mater. Sci.* **41**, 257 (2016).
27. L. R. Radovic, *Chemistry & Physics of Carbon*. (Taylor & Francis, 2003).
28. H. O. Pierson, *Handbook of Carbon, Graphite, Diamonds and Fullerenes: Processing, Properties and Applications*. (Elsevier Science, 2012).
29. L. Dai, Y. Xue, L. Qu, H.-J. Choi, J.-B. Baek, Metal-Free Catalysts for Oxygen Reduction Reaction. *Chem. Rev.* **115**, 4823 (2015).
30. T. W. Ebbesen, *Carbon Nanotubes: Preparation and Properties*. (Taylor & Francis, 1996).
31. A. B. Yousaf *et al.*, Synergistic effect of graphene and multi-walled carbon nanotubes composite supported Pd nanocubes on enhancing

catalytic activity for electro-oxidation of formic acid. *Catalysis Science & Technology* **6**, 4794 (2016).

32. Y. Cheng, S. Lu, H. Zhang, C. V. Varanasi, J. Liu, Synergistic Effects from Graphene and Carbon Nanotubes Enable Flexible and Robust Electrodes for High-Performance Supercapacitors. *Nano Lett.* **12**, 4206 (2012).
33. O. Madelung, *Introduction to Solid-State Theory*. (Springer, 1996).
34. J. D. Wiggins-Camacho, K. J. Stevenson, Effect of Nitrogen Concentration on Capacitance, Density of States, Electronic Conductivity, and Morphology of N-Doped Carbon Nanotube Electrodes. *J. Phys. Chem. C* **113**, 19082 (2009).
35. M. Aliofkhazraei *et al.*, *Graphene Science Handbook: Nanostructure and Atomic Arrangement*. (CRC Press LLC, 2016).
36. I. Heller, J. Kong, K. A. Williams, C. Dekker, S. G. Lemay, Electrochemistry at Single-Walled Carbon Nanotubes: The Role of Band Structure and Quantum Capacitance. *J. Am. Chem. Soc.* **128**, 7353 (2006).
37. G.-L. Chai, Z. Hou, D.-J. Shu, T. Ikeda, K. Terakura, Active Sites and Mechanisms for Oxygen Reduction Reaction on Nitrogen-Doped Carbon Alloy Catalysts: Stone–Wales Defect and Curvature Effect. *J. Am. Chem. Soc.* **136**, 13629 (2014).
38. Y.-B. Tang *et al.*, Tunable Band Gaps and p-Type Transport Properties of Boron-Doped Graphenes by Controllable Ion Doping Using Reactive Microwave Plasma. *ACS Nano* **6**, 1970 (2012).
39. S. Sandoval *et al.*, Enhanced Thermal Oxidation Stability of Reduced Graphene Oxide by Nitrogen Doping. *Chem. Eur. J.* **20**, 11999 (2014).
40. C. Liang, Z. Li, S. Dai, Mesoporous Carbon Materials: Synthesis and Modification. *Angew. Chem. Int. Ed.* **47**, 3696 (2008).
41. M. Hartmann, Hierarchical Zeolites: A Proven Strategy to Combine Shape Selectivity with Efficient Mass Transport. *Angew. Chem. Int. Ed.* **43**, 5880 (2004).
42. C. Zhong *et al.*, A review of electrolyte materials and compositions for electrochemical supercapacitors. *Chem. Soc. Rev.* **44**, 7484 (2015).
43. A. Sayari, B.-H. Han, Y. Yang, Simple Synthesis Route to Monodispersed SBA-15 Silica Rods. *J. Am. Chem. Soc.* **126**, 14348 (2004).
44. S. Jun *et al.*, Synthesis of New, Nanoporous Carbon with Hexagonally Ordered Mesostructure. *J. Am. Chem. Soc.* **122**, 10712 (2000).

45. Y. Meng *et al.*, Ordered Mesoporous Polymers and Homologous Carbon Frameworks: Amphiphilic Surfactant Templating and Direct Transformation. *Angew. Chem. Int. Ed.* **44**, 7053 (2005).
46. B. E. Conway, *Electrochemical Supercapacitors: Scientific Fundamentals and Technological Applications*. (Springer US, 2013).
47. *Supercapacitors: Materials, Systems, and Applications*. (Wiley, 2013).
48. P. Simon, Y. Gogotsi, Capacitive energy storage in nanostructured carbon–electrolyte systems. *Acc. Chem. Res.* **46**, 1094 (2013).
49. P. Simon, Y. Gogotsi, Materials for electrochemical capacitors. *Nat. Mater.* **7**, 845 (2008).
50. L. L. Zhang, X. S. Zhao, Carbon-based materials as supercapacitor electrodes. *Chem. Soc. Rev.* **38**, 2520 (2009).
51. J.-G. Wang, F. Kang, B. Wei, Engineering of MnO_2-based nanocomposites for high-performance supercapacitors. *Prog. Mater Sci.* **74**, 51 (2015).
52. O. Barbieri, M. Hahn, A. Herzog, R. Kötz, Capacitance limits of high surface area activated carbons for double layer capacitors. *Carbon* **43**, 1303 (2005).
53. J. Huang, B. G. Sumpter, V. Meunier, Theoretical Model for Nanoporous Carbon Supercapacitors. *Angew. Chem. Int. Ed.* **47**, 520 (2008).
54. J. Huang, B. G. Sumpter, V. Meunier, A Universal Model for Nanoporous Carbon Supercapacitors Applicable to Diverse Pore Regimes, Carbon Materials, and Electrolytes. *Chem. Eur. J.* **14**, 6614 (2008).
55. J. Huang *et al.*, Curvature effects in carbon nanomaterials: Exohedral versus endohedral supercapacitors. *J. Mater. Res.* **25**, 1525 (2010).
56. K. Xia, Q. Gao, J. Jiang, J. Hu, Hierarchical porous carbons with controlled micropores and mesopores for supercapacitor electrode materials. *Carbon* **46**, 1718 (2008).
57. G. Pognon, T. Brousse, L. Demarconnay, D. Bélanger, Performance and stability of electrochemical capacitor based on anthraquinone modified activated carbon. *J. Power Sources* **196**, 4117 (2011).
58. C. R. DeBlase, K. E. Silberstein, T.-T. Truong, H. D. Abruña, W. R. Dichtel, β-Ketoenamine-Linked Covalent Organic Frameworks Capable of Pseudocapacitive Energy Storage. *J. Am. Chem. Soc.* **135**, 16821 (2013).
59. N. Choudhary *et al.*, Asymmetric Supercapacitor Electrodes and Devices. *Adv. Mater.* **29**, 1605336 (2017).

60. M. M. Thackeray, C. Wolverton, E. D. Isaacs, Electrical energy storage for transportation-approaching the limits of, and going beyond, lithium-ion batteries. *Energy Environ. Sci.* **5**, 7854 (2012).
61. J. B. Goodenough, Y. Kim, Challenges for Rechargeable Li Batteries. *Chem. Mater.* **22**, 587 (2010).
62. Z. W. Seh, Y. Sun, Q. Zhang, Y. Cui, Designing high-energy lithium-sulfur batteries. *Chem. Soc. Rev.* **45**, 5605 (2016).
63. C. Liang, N. J. Dudney, J. Y. Howe, Hierarchically Structured Sulfur/Carbon Nanocomposite Material for High-Energy Lithium Battery. *Chem. Mater.* **21**, 4724 (2009).
64. A. Manthiram, Y. Fu, Y.-S. Su, Challenges and Prospects of Lithium–Sulfur Batteries. *Acc. Chem. Res.* **46**, 1125 (2013).
65. D. Lv *et al.*, High Energy Density Lithium–Sulfur Batteries: Challenges of Thick Sulfur Cathodes. *Adv. Energy Mater.* **5**, 1402290 (2015).
66. P. G. Bruce, S. A. Freunberger, L. J. Hardwick, J. M. Tarascon, Li–O_2 and Li–S batteries with high energy storage. *Nat. Mater.* **11**, 19 (2012).
67. X. L. Ji, K. T. Lee, L. F. Nazar, A highly ordered nanostructured carbon–sulphur cathode for lithium–sulphur batteries. *Nat. Mater.* **8**, 500 (2009).
68. S. Xin *et al.*, Smaller Sulfur Molecules Promise Better Lithium–Sulfur Batteries. *J. Am. Chem. Soc.* **134**, 18510 (2012).
69. N. Jayaprakash, J. Shen, S. S. Moganty, A. Corona, L. A. Archer, Porous Hollow Carbon@Sulfur Composites for High-Power Lithium–Sulfur Batteries. *Angew. Chem.* **123**, 6026 (2011), *Angew. Chem. Int. Ed.* **50**, 5904 (2011).
70. L. Ji *et al.*, Graphene Oxide as a Sulfur Immobilizer in High Performance Lithium/Sulfur Cells. *J. Am. Chem. Soc.* **133**, 18522 (2011).
71. H.-J. Peng *et al.*, Nanoarchitectured Graphene/CNT@Porous Carbon with Extraordinary Electrical Conductivity and Interconnected Micro/Mesopores for Lithium-Sulfur Batteries. *Adv. Funct. Mater.* **24**, 2772 (2014).
72. S. Xin, Y.-X. Yin, Y.-G. Guo, L.-J. Wan, A High-Energy Room-Temperature Sodium-Sulfur Battery. *Adv. Mater.* **26**, 1261 (2014).
73. K. B. Hueso, M. Armand, T. Rojo, High temperature sodium batteries: status, challenges and future trends. *Energy Environ. Sci.* **6**, 734 (2013).

74. P. Adelhelm *et al.*, From lithium to sodium: cell chemistry of room temperature sodium–air and sodium–sulfur batteries. *Beilstein J. Nanotech.* **6**, 1016 (2015).
75. A. Manthiram, X. Yu, Ambient Temperature Sodium–Sulfur Batteries. *Small* **11**, 2108 (2015).
76. Y.-X. Wang *et al.*, Achieving High-Performance Room-Temperature Sodium–Sulfur Batteries With S@Interconnected Mesoporous Carbon Hollow Nanospheres. *J. Am. Chem. Soc.* **138**, 16576 (2016).
77. R. Chaubey, S. Sahu, O. O. James, S. Maity, A review on development of industrial processes and emerging techniques for production of hydrogen from renewable and sustainable sources. *Renew.Sustain. Energy Rev.* **23**, 443 (2013).
78. M. Momirlan, T. N. Veziroglu, The properties of hydrogen as fuel tomorrow in sustainable energy system for a cleaner planet. *Int. J. Hydrogen Energy* **30**, 795 (2005).
79. A. Lasia, in *Handbook of Fuel Cells*. (John Wiley & Sons, Ltd, 2010).
80. J. B. Goodenough, Evolution of Strategies for Modern Rechargeable Batteries. *Acc. Chem. Res.* **46**, 1053 (2013).
81. M. A. Rahman, X. Wang, C. Wen, High Energy Density Metal-Air Batteries: A Review. *J. Electrochem. Soc.* **160**, A1759 (January 1, 2013, 2013).
82. N. S. Lewis, D. G. Nocera, Powering the planet: Chemical challenges in solar energy utilization. *Proc. Natl. Acad. Sci.* **103**, 15729 (2006).
83. C. C. L. McCrory, S. Jung, J. C. Peters, T. F. Jaramillo, Benchmarking Heterogeneous Electrocatalysts for the Oxygen Evolution Reaction. *J. Am. Chem. Soc.* **135**, 16977 (2013).
84. J. Zhang, *PEM Fuel Cell Electrocatalysts and Catalyst Layers: Fundamentals and Applications*. (Springer London, 2008).
85. K. Gong, F. Du, Z. Xia, M. Durstock, L. Dai, Nitrogen-Doped Carbon Nanotube Arrays with High Electrocatalytic Activity for Oxygen Reduction. *Science* **323**, 760 (2009).
86. I. Roger, M. A. Shipman, M. D. Symes, Earth-abundant catalysts for electrochemical and photoelectrochemical water splitting. *Nat. Rev. Chem.* **1**, 0003 (2017).
87. Y. Zheng *et al.*, Hydrogen evolution by a metal-free electrocatalyst. *Nat. Commun.* **5**, 3783 (2014).

88. J. Zhang, Z. Zhao, Z. Xia, L. Dai, A metal-free bifunctional electrocatalyst for oxygen reduction and oxygen evolution reactions. *Nat. Nanotech.* **10**, 444 (2015).
89. J. Zhang *et al.*, N,P-Codoped Carbon Networks as Efficient Metal-free Bifunctional Catalysts for Oxygen Reduction and Hydrogen Evolution Reactions. *Angew. Chem. Int. Ed.* **55**, 2230 (2016).
90. C. Hu, L. Dai, Multifunctional Carbon-Based Metal-Free Electrocatalysts for Simultaneous Oxygen Reduction, Oxygen Evolution, and Hydrogen Evolution. *Adv. Mater.* **29**, 1604942 (2017).
91. Y. Zheng *et al.*, Toward Design of Synergistically Active Carbon-Based Catalysts for Electrocatalytic Hydrogen Evolution. *ACS Nano* **8**, 5290 (2014).
92. H. W. Park *et al.*, Bi-Functional N-Doped CNT/Graphene Composite as Highly Active and Durable Electrocatalyst for Metal Air Battery Applications. *J. Electrochem. Soc.* **160**, A2244 (January 1, 2013, 2013).
93. K. Sakaushi, K. Uosaki, Highly Efficient Oxygen and Hydrogen Electrocatalytic Activities of Self-Morphogenic Nanoporous Carbon, Nitrogen Architectures. *ChemNanoMat* **2**, 99 (2016).
94. H. Zhao *et al.*, Carbon for the oxygen reduction reaction: a defect mechanism. *J. Mater. Chem. A* **3**, 11736 (2015).
95. H. B. Yang *et al.*, Identification of catalytic sites for oxygen reduction and oxygen evolution in N-doped graphene materials: Development of highly efficient metal-free bifunctional electrocatalyst. *Sci. Adv.* **2**, (2016).
96. L. Zhang, Z. Xia, Mechanisms of Oxygen Reduction Reaction on Nitrogen-Doped Graphene for Fuel Cells. *J. Phys. Chem. C* **115**, 11170 (2011).
97. B. E. Conway, B. V. Tilak, Interfacial processes involving electrocatalytic evolution and oxidation of H2, and the role of chemisorbed H. *Electrochim. Acta* **47**, 3571 (2002).
98. V. Kiran, D. Mukherjee, R. N. Jenjeti, S. Sampath, Active guests in the $MoS_2/MoSe_2$ host lattice: efficient hydrogen evolution using few-layer alloys of $MoS_{2(1-x)}Se_{2x}$. *Nanoscale* **6**, 12856 (2014).

Chapter-2

No More HF: Teflon Assisted Ultrafast Removal of Silica to Generate High Surface Area Mesostructured Carbon for Enhanced CO_2 Capture and Supercapacitor Performance

Summary:

An innovative technique to obtain high surface area mesostructured carbon (2545 m^2g^{-1}) with significant microporosity uses Teflon (Polytetrafluoroethylene) as a silica template removal agent. This method not only shortens the synthesis time by combining silica removal and carbonization in a single step, but also assists in ultrafast removal of the template (in 10 min) with altogether elimination of toxic HF usage. The obtained carbon material (JNC-1) displays excellent CO_2 capture ability (ca. 26.2 wt.% at 0 ^oC under 0.88 bar CO_2 pressure), which is twice to that of CMK-3 obtained by HF etching method (13.0 wt.%). JNC-1 demonstrated higher H_2 adsorption capacity (2.8 wt.%) compared to CMK-3 (1.2 wt.%) at -196 ^oC under 1.0 bar H_2 pressure. The bimodal pore architecture of JNC-1 led to superior supercapacitor performance, with a specific capacitance of 292 F g^{-1} and 182 F g^{-1} at a drain rate of 1 A g^{-1} and 50 A g^{-1} respectively in 1 M H_2SO_4 compared to CMK-3 and activated carbon(AC).

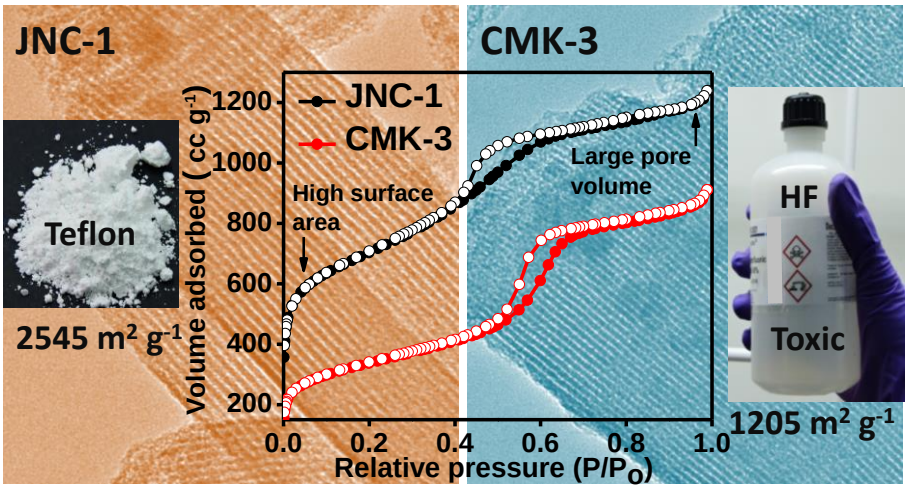

(A paper based on this work has appeared in *Angew. Chem. Int. Ed.* **55**, 2032, 2016).

2.1 Introduction:

Periodic mesoporous carbon(*1, 2*) materials have generated a great deal of technological interest by virtue of their ability to overcome the mass-transport limitations encountered in their disordered counterparts(*3*) and thus play a significant role in the area of catalysis (as a support),(*4*) Li-S batteries,(*5*) gas separation and storage,(*6, 7*) and electric double-layer capacitors (EDLC).(*8*) In contrast to disordered pore architectures, ordered nanoporous structures provide shorter diffusion pathways and minimal resistance to molecular motion, which improves transport properties.(*3*) The more versatile method to synthesize ordered mesoporous carbon materials relies on the inverse replica strategy using ordered mesoporous silica as a hard template and sucrose as the inexpensive carbon precursor.(*9*) However, removal of the hard silica template is a bottleneck to scale up the synthesis as it involves the use of HF or repeated treatment with NaOH solution at elevated temperatures.(*9*) HF is highly toxic(*10*) and its use is strongly discouraged in many countries, while NaOH treatment is time consuming, corrosive, and not-cost effective as it has to be operated at elevated temperatures.(*11*) Furthermore, the surface area of the ordered mesoporous carbon obtained through the hard-template method is very moderate in comparison to many high-surface-area disordered carbons.(*12, 13*) Though a silica-free strategy to prepare mesoporous carbon was reported as an alternate method, it involves usage of corrosive and expensive carbon precursors such as phenol and formaldehyde with a polymeric template such as F127.(*14*) Furthermore, it suffers from significant amount of structural shrinkage during the carbonization process, resulting in low surface areas, smaller pore sizes, and reduced pore volume.(*15*) Thus, a simple and less hazardous approach to remove silica without the direct use of HF is much needed to make the silica template strategy as a successful method to prepare high-surface-area mesostructured carbon.

2.2 Scope of the present investigation:

Herein, an innovative way of using Teflon powder instead of HF to etch out the silica is described in which the separate, carbonization, and silica removal are combined into one step (Scheme 1). The silica removal using Teflon is very straightforward, easy to handle (simply mixing the Teflon powder and the sample before carbonization), and extremely fast (silica removal is complete within 10 min). More importantly, the carbon thus obtained retains its mesoscale order and shows a very high surface area, which is more than two times higher than the carbon prepared by the HF etching method (Scheme 1).

The obtained ordered nanoporous carbon (JNC-1) shows remarkable performance for CO_2 capture, hydrogen storage, and dye adsorption in comparison to HF etched CMK-3 carbon. It also exhibits superior performance as a supercapacitor material.

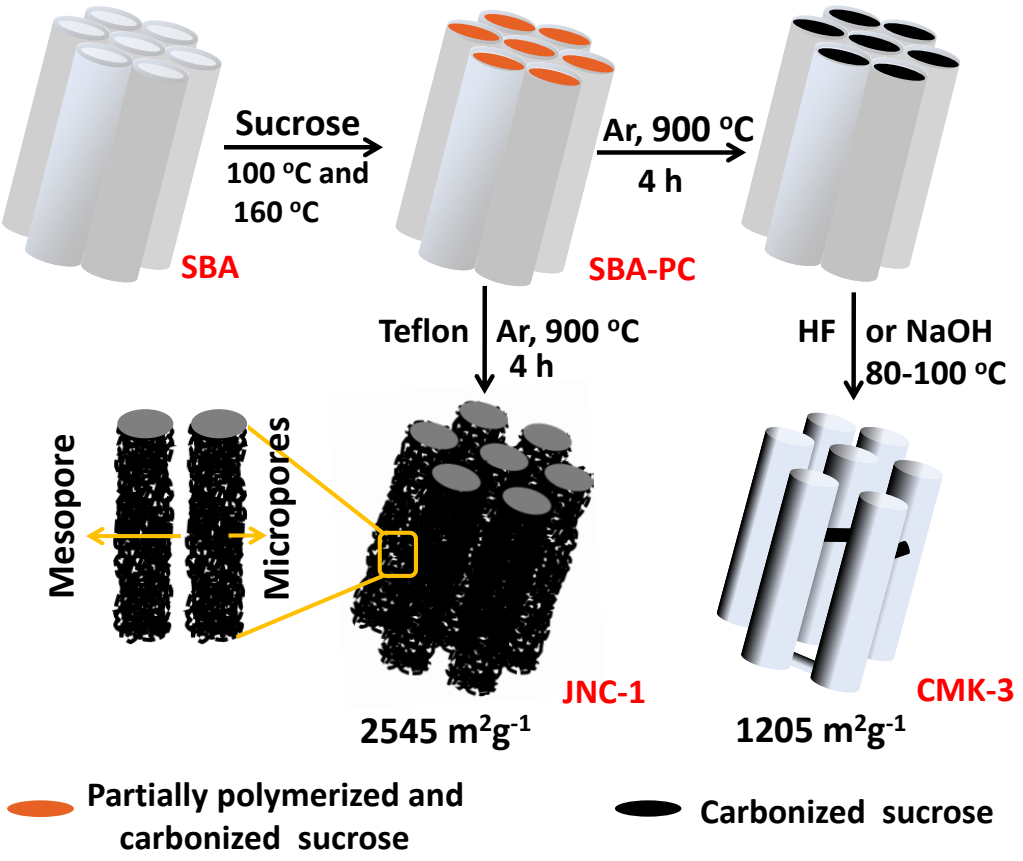

Scheme 1. Comparison of the conventional synthesis of CMK-3 with that of JNC-1.

2.3 Experimental procedures:

2.3.1 Materials used:

Pluronic P123, Tetraethylorthosilicate (TEOS), Sucrose, Nafion, Alizarin yellow and Congo red were purchased from Sigma-Aldrich. HCl (37%) and HF (48%) were procured from Merck. Polytetrafluoroethylene (Teflon) powder was obtained from Alfa Aesar. H_2SO_4 (98%) and Activated carbon (~ 1200 m^2 g^{-1}) was purchased from SD Fine Chemicals.

2.3.2 Instrumentation and characterization techniques:

All the gas sorption analyses were performed on Autosorb-iQ_2 (Quantachrome corp.). Prior to analyses the synthesized samples were degassed at 423 K under

vacuum for 24 h. Ultrahigh pure gases (99.9995%) were used in all the measurements. Bruker- D8 diffractometer having copper anode generating X-ray having wavelength of 1.54 Å (30 mA, 40 kV) was used for recording powder X-ray diffraction (PXRD) patterns of the samples. TEM (Transmission electron microscopy) images of the samples were obtained on JEOL JEM-3010 electron microscope. Nova-Nano SEM-600 (FEI, Netherlands) was used for acquiring FESEM (Field emission scanning electron microscopy) images of the samples. Raman spectra of the samples were obtained using Jobin Yvon LabRam HR spectrometer having 632 nm Ar laser. Thermogravimetric analyses (TGA) were performed using Mettler Toledo 850 under N_2/O_2 atmosphere with a ramp rate of 5/10 ^oC min^{-1}. Inductively coupled plasma optical emission spectroscopy (ICP-OES) was used for determining Si using Perkin-Elmer Optima 7000 DV instrument. Electrochemical measurements were carried out using electrochemical work station obtained from CH Instruments (660C, USA).

2.3.3 Electrochemical measurements:

Electrochemical studies were performed using conventional three-electrode assembly, with carbon sample (JNC-1/CMK-3/AC) coated glassy carbon (GC) (3 mm diameter) as a working electrode (WE), flag type Pt foil and saturated calomel electrode as a counter and reference electrode respectively. Fabrication of WE was achieved in the following way: 2 mg of the carbon sample was dispersed in water (0.8 mL)-ethanol (0.16 mL) mixture containing Nafion (0.04 mL) by sonication for 30 min. The obtained carbon dispersions were drop casted (5 μL) onto precleaned glassy carbon (GC) electrode and dried under open atmosphere.

2.3.4 Synthesis of SBA-15 (SBA): SBA was synthesized according to a reported procedure.(*16*)

2.3.5 Synthesis of CMK-3: CMK-3 was synthesized by the procedure reported by Jun et al.(*9*) Briefly, 1 g of SBA was dispersed in aqueous solution obtained by dissolving 1.25 g sucrose and 0.14 g H_2SO_4 in 5 g of water. It was then placed in oven at 100 ^oC for 6 h and further 6 h at 160 ^oC. Thereafter, obtained silica composite containing partially polymerized carbon was impregnated again with 5 mL of aqueous solution containing 0.8 g sucrose and 0.09 g H_2SO_4 and was subjected to same cyclic heat treatments as above to obtain SBA-polymeric carbon composite (SBA-PC). Carbonization was completed by heating the

obtained SBA-PC composite at 900 ^{o}C for 4 h under Ar atmosphere. The obtained carbon-silica composite was dispersed in HF solution at room temperature to dissolve silica template and obtain CMK-3 after washing several times with ethanol and drying in oven at 120 ^{o}C.

2.3.6 Synthesis of JNC-1: SBA-polymeric carbon composite (SBA-PC) and Teflon powder was intimately mixed (SBA-PC to Teflon = 2:9 weight ratio which corresponds to 0.09, SiO_2 to Teflon weight ratio, **Table 1**). Amount of SiO_2 in SBA-PC composite was determined to be around 42 wt.% using thermogravimetric analyses (TGA) performed under O_2 atmosphere, **Figure 1**) by grinding in a mortar and was subsequently transferred to an alumina boat. The boat was then placed inside alumina tube reactor and then heated to 900 ^{o}C at 5 ^{o}C min^{-1} for 4 h in an under Ar flow to obtain JNC-1. The textural parameters of mesostructured carbon with varying SiO_2 to Teflon weight ratio are listed in **Table 1**.

Materials	S_{BET} [a]	$S_{Micropore}$ [b]	V_{Total} [c]	$V_{Micropore}$ [d]	D_{Meso} [e]
SiO_2/Teflon* (wt./wt.)	(m^2 g^{-1})	(m^2 g^{-1})	(cm^3 g^{-1})	(cm^3 g^{-1})	(nm)
0.42	1919	441	1.401	0.195	4.5
0.15	1968	724	1.370	0.330	4.5
0.09 (JNC-1)	2545	1012	1.876	0.429	4.7

[a] BET (Brunauer-Emmett-Teller) specific surface area (SSA) calculated by taking criteria into account suggested by Rouquerol et al., [b] micropore surface area determined by t-plot method, [c] Total pore volume was calculated at P/P_o = 0.97, [d] micropore volume determined via t-plot analyses and [e] mesopore diameter calculated by QSDFT method.

Table 1. Effect of varying SiO_2 (in SBA-PC) to teflon weight ratios on the textural parameters of the obtained carbons (*amount of SiO_2 in SBA-PC composite was determined to be around 42 wt.% using thermogravimetric analyses (TGA) performed under O_2 atmosphere, **Figure 1**).

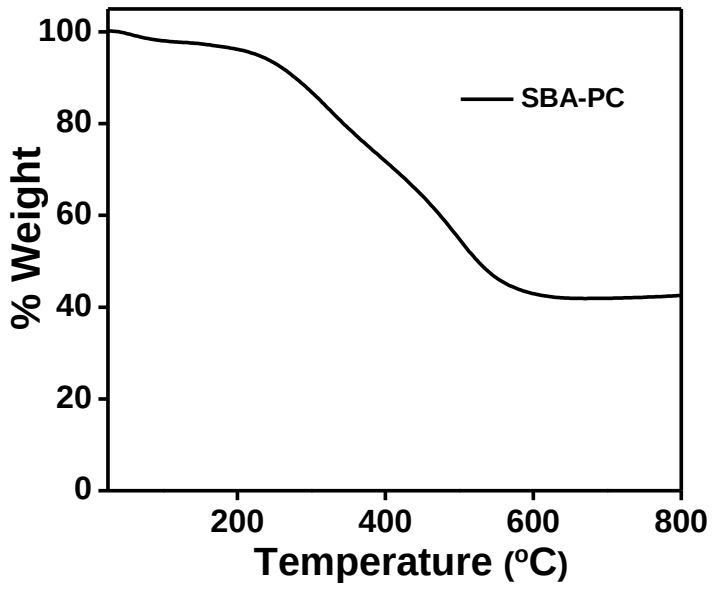

Figure 1. TGA curve of SBA-PC under O_2 atmosphere. Around 58 wt.% mass loss at 800 °C corresponds to burning of partially polymerized and carbonized sucrose leaving behind SiO_2 (SBA, 42 wt.%).

2.3.7 Synthesis of KIT-6 and CMK-8: Both KIT-6 and CMK-8 were synthesized according to a procedure reported in the literature.(*17*)

2.3.8 Synthesis of JNC-2: Synthesis of JNC-2 was similar to that of JNC-1, except for the fact that KIT-6 (having cubic *Ia3d* symmetry) was used as template instead of SBA-15.

2.3.9 Dye adsorption experiments were performed as follows: (a) Alizarin yellow: In the case of alizarin yellow, 2.5 mg of different adsorbents (JNC-1, CMK-3 and AC) were dispersed in 5 mL dye solutions of different concentrations ranging from 0.1 g L^{-1} to 3.5 L^{-1}. The resulting dispersions were vigorously shaken at 25 °C for 24 h in order to attain adsorption-desorption equilibrium. Thereafter, adsorbents were separated by centrifugation and the resulting supernatants were collected for UV-Vis analysis (at 353 nm) to determine the amount of alizarin yellow adsorbed by different materials after appropriate dilutions.

(b) Congo red: For Congo red adsorption studies, everything was same as above except for the fact that 3 mL of dye solutions having concentration from 0.1 g L^{-1} to 1.5 g L^{-1} were used instead. UV-Vis analyses were performed (at 498 nm) after appropriate dilutions to determine the amount of dye adsorbed by different carbons.

2.3.10 ICP-OES analyses: 5 mg of carbon (JNC-1/JNC-2/CMK-3) was dispersed in 10 ml of 5 wt.% HF solution and was stirred overnight. Afterwards the carbon was separated by centrifugation and supernatant liquid was collected for analyses.

2.4 Results and discussions:

Carbonization of SBA-PC at higher temperature followed by etching of silica with corrosive HF gives CMK-3 carbon **(Scheme 1; Figure 2)**, an inverse replica of SBA(*16, 18*) **(Figure 3)**. In a significant deviation from the conventional two-step process we simply mixed the SBA-PC with Teflon powder and heated to 900 °C for 4 h **(Scheme 1)** in Ar. The process combines the carbonization and silica removal in a single step with complete elimination of toxic HF usage. The carbon replica of SBA thus obtained is named JNC-1 **(Scheme 1, Figure 4a and Figure 5)**. Mesostructured carbon CMK-3 was also made from the same SBA-PC through the standard two-step process involving carbonization at high temperature (900 °C for 4 h) followed by HF etching (12 h at room temp) **(Figure 2)** of silica for comparison as reported by Jun et al.(*9*)

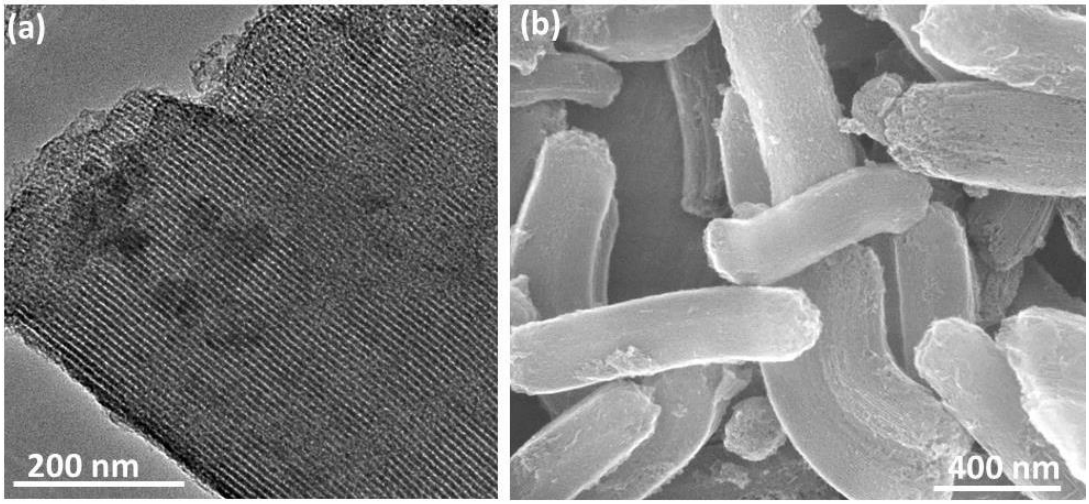

Figure 2. (a) TEM and (b) FESEM images of CMK-3.

The powder X-ray diffraction (PXRD) pattern of SBA **(Figure 4b)** shows characteristic low-angle peaks for mesostructured materials having a *p6mm* honeycomb lattice symmetry.(*16*) JNC-1 exhibits well-resolved low-angle peaks, as that of CMK-3 **(Figure 4b)**, which can be indexed as (100), (110), and (200) indicating faithful negative replication of mesostructural ordering of parent SBA.(*9*) Wide-angle PXRD pattern of JNC-1 **(Figure 6)**

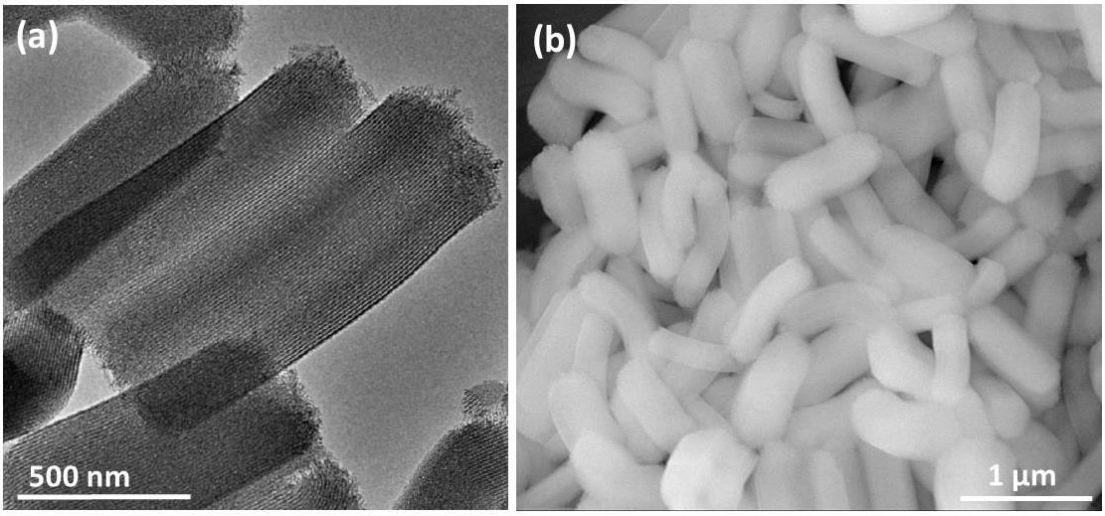

Figure 3. (a) TEM and (b) FESEM images of as synthesized SBA-15 (SBA) indicating rod shaped morphology.

showed broad diffraction peaks around 22° and 43° (2θ), indicating amorphous nature of the carbon walls,(*19*) similar to that of activated carbon (AC) and CMK-3, which was further confirmed by the observation of higher intensity D band (I_D) compared to the G band (I_G) in the Raman spectra **(Figure 7)**.(*20*) The absence of silicon (Si) peak in energy-dispersive X-ray spectroscopy (EDS) analyses of JNC-1 carbon shows the complete removal of silica template **(Figure 8a)**. A transmission electron microscope (TEM) image of JNC-1 **(Figure 4a)** indicates well-aligned mesochannels similar to that of CMK-3 **(Figure 2a-b)**, the exact negative replica of SBA-15 **(Figure 3a-b)**. N_2 adsorption–desorption isotherms of SBA **(Figure 4c)** exhibit type IV behavior characteristic of mesoporous materials(*21*) with a capillary condensation at around P/P_o of 0.75. The surface area of JNC-1 was found to be around 2545 $m^2 g^{-1}$, which is twice to that of CMK-3 (1205 $m^2 g^{-1}$; **Table 2**). It must be mentioned that the standard BET method for the calculation of surface area of micro-mesostructured materials is not applicable here and hence the criteria suggested by Rouquerol et al.(*22*) has been used for the calculation of surface areas **(Figure 9)**. Hysteresis loops of JNC-1 and CMK-3 **(Figure 4c)** exhibit H2 type characteristics with the effect being more pronounced for JNC-1, indicating the presence of significant amount of micropores.(*9*) Pore size distribution of SBA **(Figure 4d)** was calculated by NLDFT method whereas QSDFT method was implemented for the calculation of pore sizes for JNC-1 and CMK-3 **(Figure 4d)**, as it takes into account the nature of surface geometrical heterogeneity than merely treating the walls as a featureless plane surface as in NLDFT and

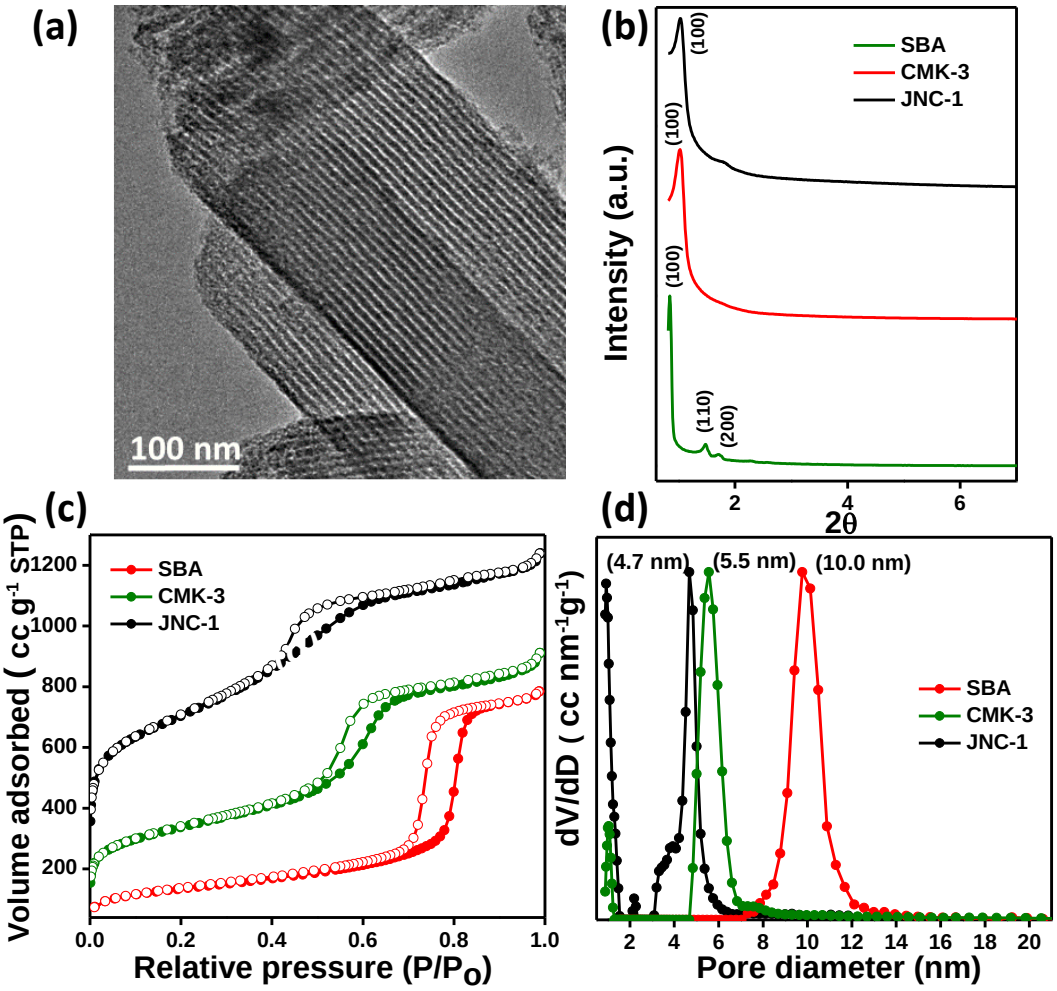

Figure 4. (a) TEM image of JNC-1. (b) PXRD patterns, (c) N_2 adsorption (closed symbols)–desorption isotherms (open symbols) and (d) corresponding pore size distributions (normalized, calculated using NLDFT/QSDFT method) of SBA, CMK-3 and JNC-1.

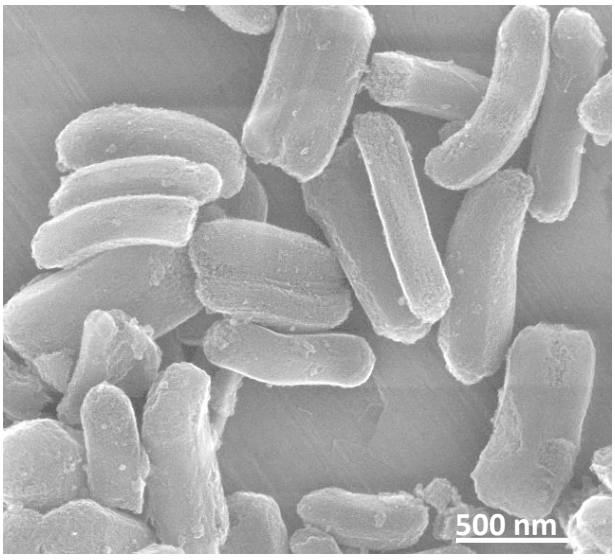

Figure 5. FESEM image of JNC-1 indicating morphological replication of SBA.

hence is more accurate.(*23*) In contrast to CMK-3, JNC-1 shows bimodal pore-size distribution **(Figure 4d)** having meso- and micropores with average pore diameters centered at 4.7 nm and 0.9 nm, respectively. As compared to CMK-3, JNC-1 shows significant amount of micropores indicated by very sharp N_2 uptake at very low pressure **(Figure 4c)** owing to the presence of abundant micropores of sizes about 0.9 nm **(Figure 4d)**. The t-plot analyses(*24, 25*) of JNC-1 indicate the presence of considerable fraction of microporous surface area (1012 $m^2 g^{-1}$; **Table 2**) and micropore volume (0.43 cc g^{-1}) as compared to CMK-3 (370 $m^2 g^{-1}$, 0.16 cc g^{-1}; **Table 2**). Furthermore, micropore analyses of JNC-1 and CMK-3 via CO_2 sorption at 0 °C indicate the presence of significant amount of micropores with a pore size of circa 0.8 nm in the former **(Figure 10)**.

2.4.1 Mechanism of silica removal:

Control experiments of silica (SBA) performed with Teflon and polyvinylidene fluoride (PVDF) suggests that silica removal occurs through the formation of SiF_4 by reaction of silica with in situ generated HF in the presence of partially polymerized sucrose carbon **(Figure 11–13)**. Silica is removed as SiF_4 on reaction with in situ generated HF during Teflon decomposition in the presence of partially polymerized and carbonized sucrose. It is well reported that Teflon

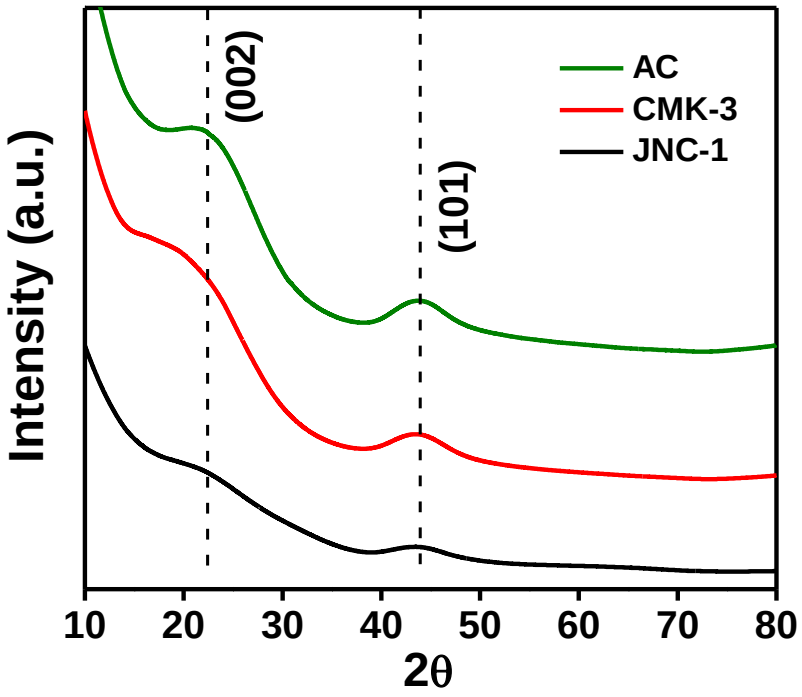

Figure 6. Wide-angle PXRD patterns of JNC-1, CMK-3 and AC.

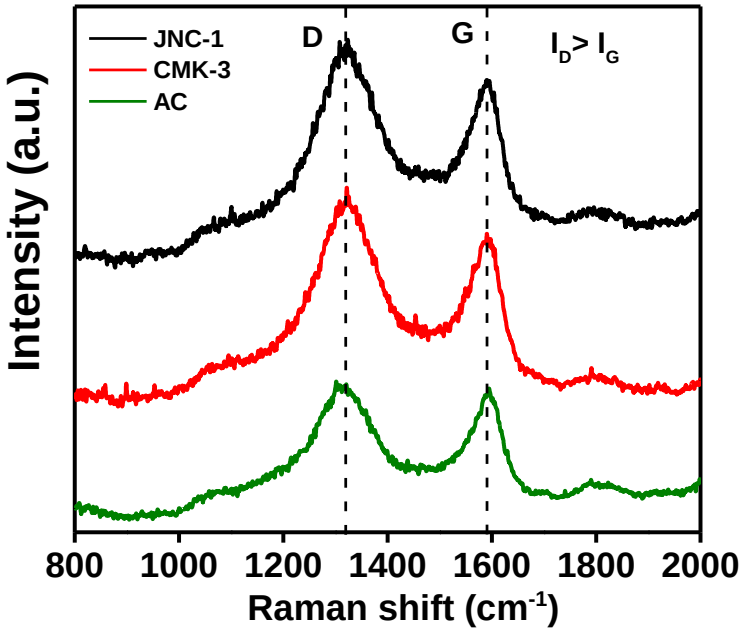

Figure 7. Raman spectra of JNC-1, CMK-3 and AC.

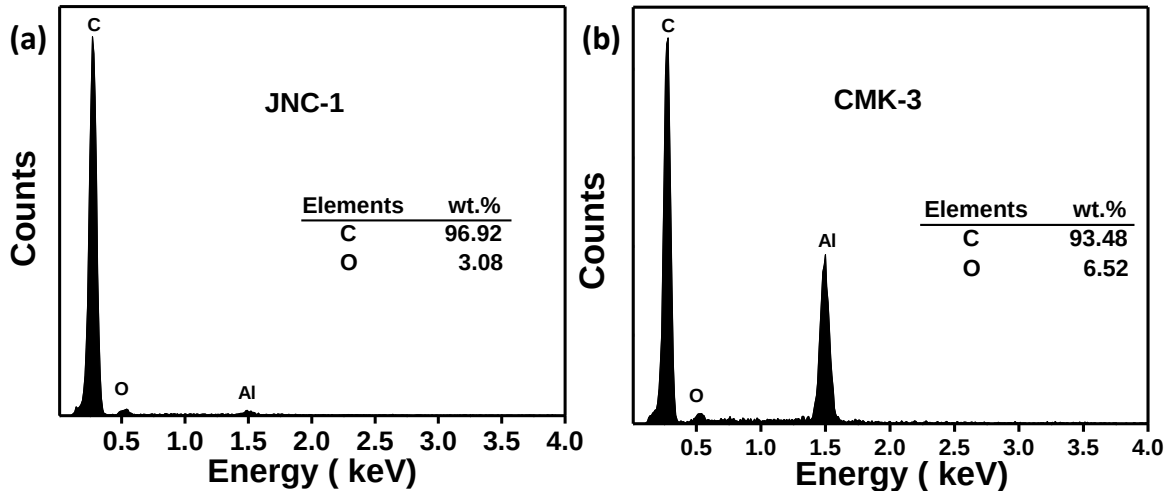

Figure 8. Energy dispersive X-ray spectroscopic (EDS) analyses of (a) JNC-1 and (b) CMK-3 indicate complete removal of Si (Al comes from sample holder); Tables inside (a) and (b) shows respective elemental content (wt.%).

decomposition in an inert atmosphere (N_2/Ar) would not generate HF and the major product (~97%) would be tetrafluoroethylene, the secondary reaction product, derived from the initially formed difluorocarbonradicals (RCF_2).(*26, 27*) On the other hand, hydrogen containing fluoropolymers like polyvinylidene fluoride (PVDF) are known to give HF as a major decomposition product on pyrolysis.(*27*) Control experiment showed no significant removal of silica on heating the silica (SBA-15)-Teflon mixture at 800 ^{o}C in N_2 atmosphere (**Figure**

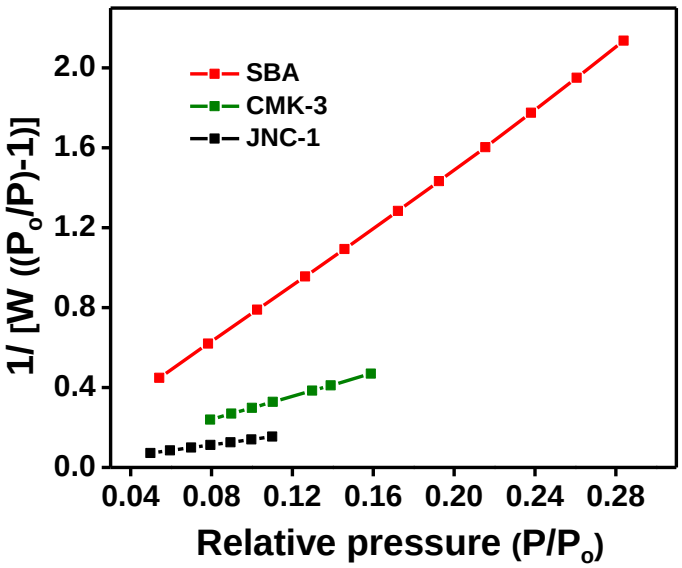

Figure 9. Relative pressure (P/P_o) range chosen for the calculation of surface areas taking into account criteria suggested by Rouquerol et al.

Materials	S_{BET} [a] ($m^2\ g^{-1}$)	$S_{Micropore}$ [b] ($m^2\ g^{-1}$)	V_{Total} [c] ($cm^3\ g^{-1}$)	$V_{Micropore}$ [d] ($cm^3\ g^{-1}$)	D_{Meso} [e] (nm)
SBA	477	83	1.192	0.036	9.8
CMK-3	1205	370	1.359	0.159	5.5
JNC-1	2545	1012	1.876	0.429	4.7

[a] BET (Brunauer-Emmett-Teller) specific surface area calculated by taking criteria into account suggested by Rouquerol et al., [b] micropore surface area determined by t-plot method, [c] Total pore volume was calculated at $P/P_o = 0.97$, [d] micropore volume determined via t-plot analyses and [e] mesopore diameter calculated by QSDFT method.

Table 2. Textural parameters of SBA, CMK-3 and JNC-1.

11a-b). TGA of Teflon under same condition leads to complete decomposition **(Figure 11b)**. Whereas, hydrogen containing fluoropolymer, PVDF, on heating with silica (SBA-15) under similar conditions nearly removed all the silica leaving behind only pyrolyzed carbon **(Figure 12a-b)**. This suggests that the difluorocarbonradicals (RCF_2)(*27*) formed at the initial decomposition of Teflon would react with the hydrogen containing, partially polymerized carbon present in the composite leading to hydrofluorocarbon formation which on subsequent decomposition gives rise to HF in the gas phase. This further reacts with silica

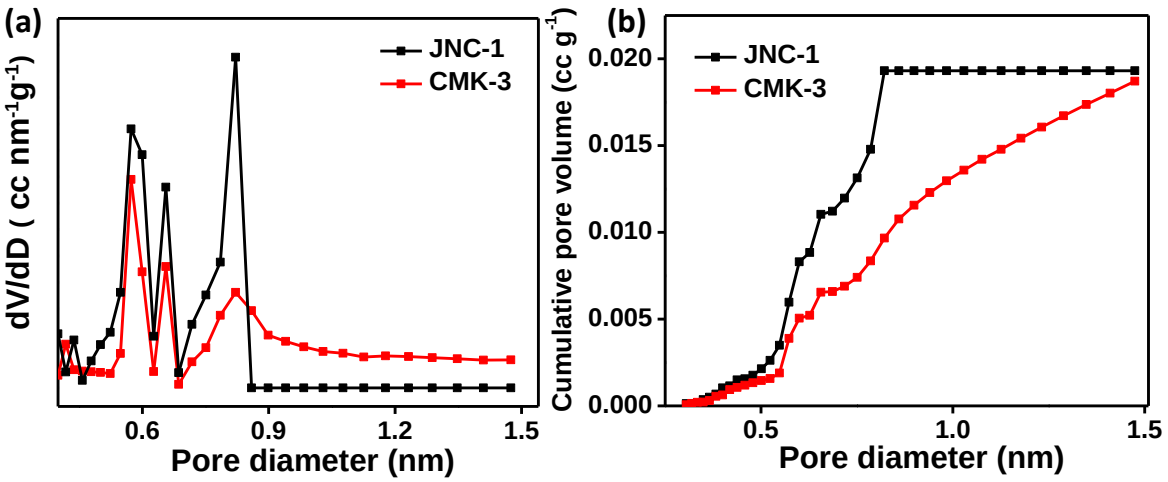

Figure 10. (a) Micropore size distributions of JNC-1 and CMK-3 calculated from CO_2 adsorptions at 0 °C and (b) corresponding cumulative pore volume plots calculated using NLDFT method.

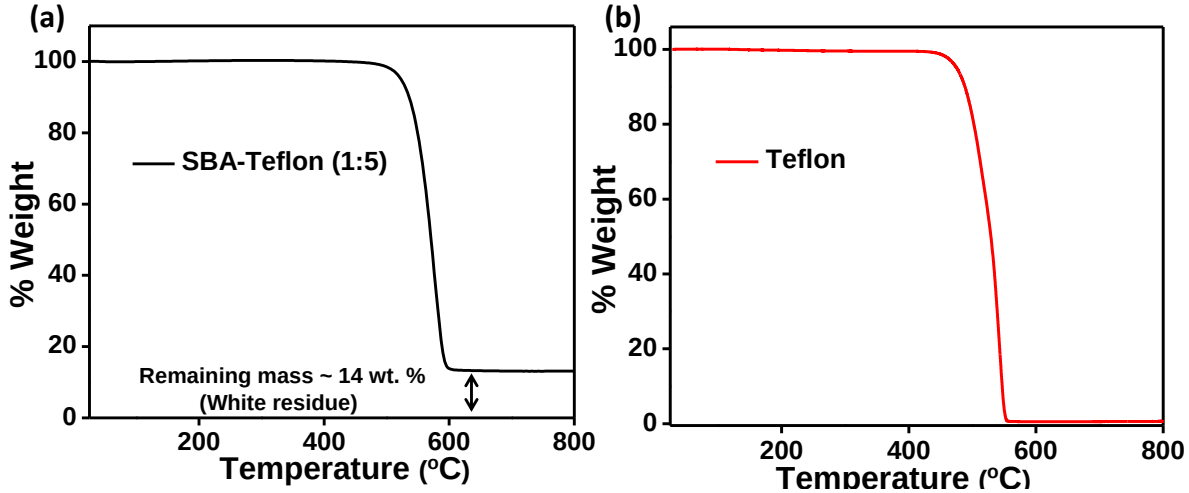

Figure 11. (a) TGA curve of SBA (silica)-Teflon mixture (containing 16 wt.% silica; SBA to Teflon = 1:5 wt. ratio) under N_2 atmosphere showing ~ 14 wt. % remaining mass. The white residue left over residue after 800 °C was found to be silica indicating inability of Teflon to remove silica. TGA curve of Teflon (b) under N_2 atmosphere indicating complete decomposition.

to give SiF_4 gas which will be carried away by argon stream and hydrolysed to hydrofluorosilicic acid by passing through water. ICP-OES analyses of the aqueous solution (through which outlet Ar stream was passed) indeed showed the presence of large amount of Si and in quantity corresponding to the amount of silica taken in the composite for pyrolysis. The resulting carbon JNC-1 is free of silica which was confirmed by EDS (**Figure 8a**) and ICP-OES analyses.

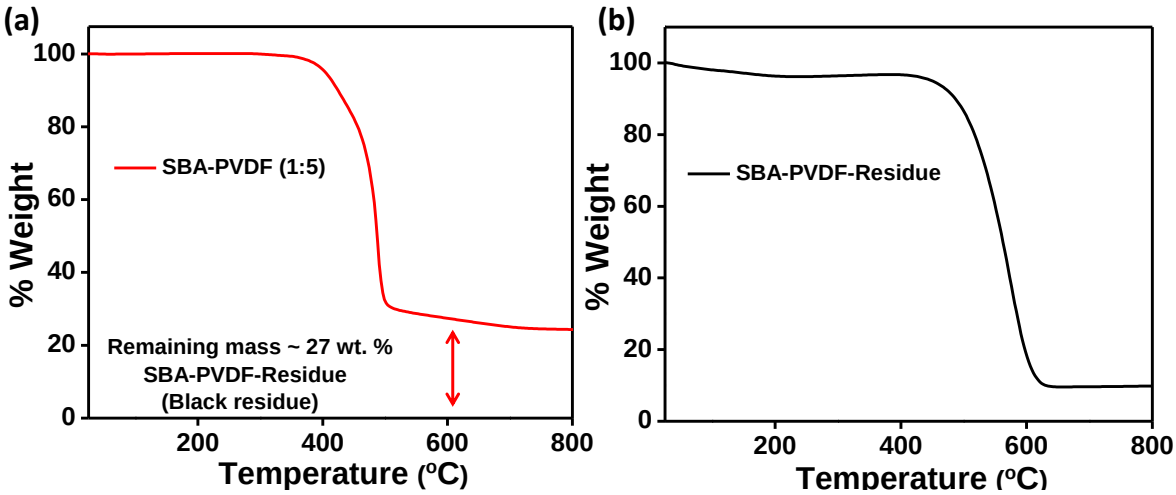

Figure 12. (a) TGA plot of SBA (silica)-polyvinylidene fluoride (PVDF) (containing 16 wt.% silica; SBA to PVDF = 1:5 wt. ratio) under N_2 atmosphere showing ~27 wt. % remaining black mass. Furthermore, TGA analyses (b) of above residue (SBA-PVDF-Residue) in O_2 indicate ~91 wt.% mass loss, which could possibly result from carbonization of PVDF. This indicates nearly all the silica is removed by PVDF which is further confirmed by near absence of silica in EDS analyses (Figure 13).

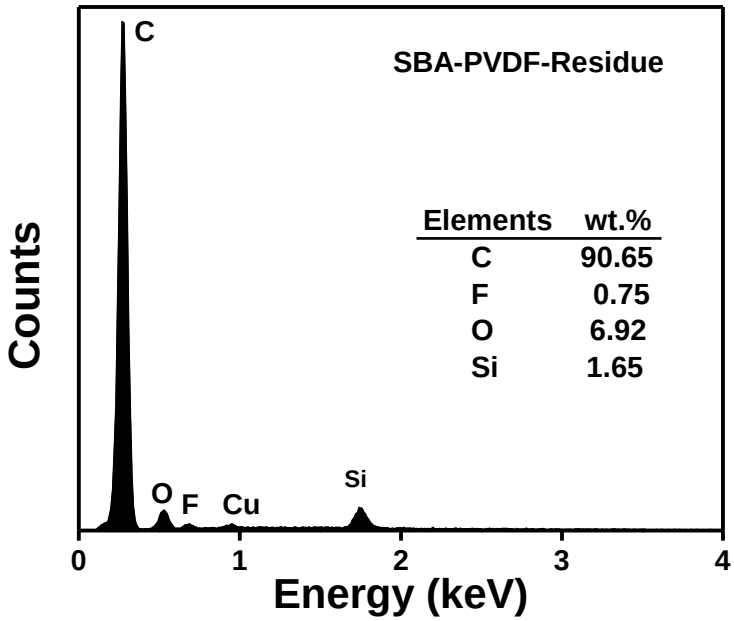

Figure 13. Energy dispersive X-ray spectroscopic (EDS) analyses of SBA-PVDF-Residue indicate that residue contains ~91 wt.% carbon by mass (Cu comes from sample holder).

Thermogravimetric analysis (TGA) shows that Teflon starts to decompose in an inert environment (N_2) at 450 ^{O}C and completes at 560 ^{O}C **(Figure 11b)**.(*26*) When SBA-PC was mixed with Teflon and heated at 650 ^{O}C (with a heating rate 5 ^{O}C min^{-1} from room temperature) in Ar for 10 min, entire silica was removed as evident from EDS analyses **(Figure 14a)**. Furthermore, the obtained material (JNC_{650}) shows 13 wt. % oxygen content **(Figure 14a)**, due to incomplete carbonization as compared to 3 wt. % oxygen obtained for JNC-1 **(Figure 8a)**. PXRD pattern of JNC_{650} **(Figure 15)** also exhibits the low angle peaks corresponding to the mesoscale ordering. This suggests that the mesostructure is preserved, notwithstanding the silica removal even before complete carbonization occurs **(Figures 17-18)**. The specific surface area is 1204 $m^2 g^{-1}$, which is equivalent to CMK-3 as well as the mesoporous carbon (1184 $m^2 g^{-1}$) obtained through similar carbonizing condition (650 ^{O}C–10 min) but with HF etching (CMK_{650}; **Table 3 and Figure 16**). Interestingly, subsequent heating of the silica free JNC_{650} and CMK_{650} in Ar at 900 ^{O}C for 4 h, referred to as JNC_{650}-900 and CMK_{650}-900 respectively, showed notable improvement in their surface areas (2459 $m^2 g^{-1}$ for JNC_{650}-900 and 2113 $m^2 g^{-1}$ for CMK_{650}-900) and total pore volume **(Table 3, Figures 17–20)**, which is possibly due to the creation of additional pores by the removal of volatile oxygen-containing moieties upon further pyrolysis.(*28, 29*) Mesoscale ordering of JNC_{650}-900 and CMK_{650}-900 was confirmed by low-angle PXRD peaks **(Figures 15, 16)**. This is in contrast to the relatively low surface area obtained for CMK-3 **(Table 2)**, where the silica was removed after the SBA-PC composite was carbonized at 900 ^{O}C for 4 h. The CMK-3 heated again in argon atmosphere at 900 °C for 4 h (CMK-3-900) gives a significant increase in surface area to 2548 $m^2 g^{-1}$ **(Table 4, Figures 21, 22)**. This clearly suggests that presence of silica impede the development of micropores by forming stable silica–carbon interface, thus inhibiting the thermal decomposition of surface carbon at 900 ^{O}C, which was facilitated when the silica free carbons (CMK-3, JNC_{650} and CMK_{650}) were heated at 900 ^{O}C in Ar for 4 h. When SBA-PC composite is mixed with Teflon and slowly heated in an argon environment, simultaneous carbonization and silica removal occurs within 650 ^{O}C, and further raise in temperature expedites the removal of volatile oxygen-containing moieties(*28, 29*) and hence the formation of micropores, leading to a high-surface-area ordered carbon structure in a single step. In the case of CMK-3, the presence of a silica–carbon interface

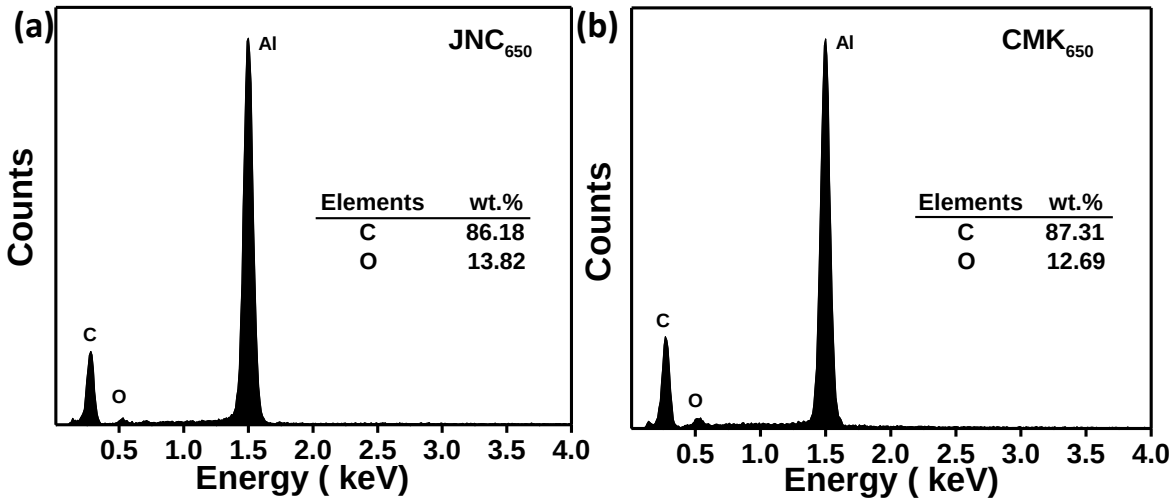

Figure 14. Energy dispersive X-ray spectroscopic (EDS) analyses of (a) JNC_{650} and (b) CMK_{650} indicating complete removal of Si (Al comes from sample holder); **Table**s inside (a) and (b) shows respective elemental content (wt.%).

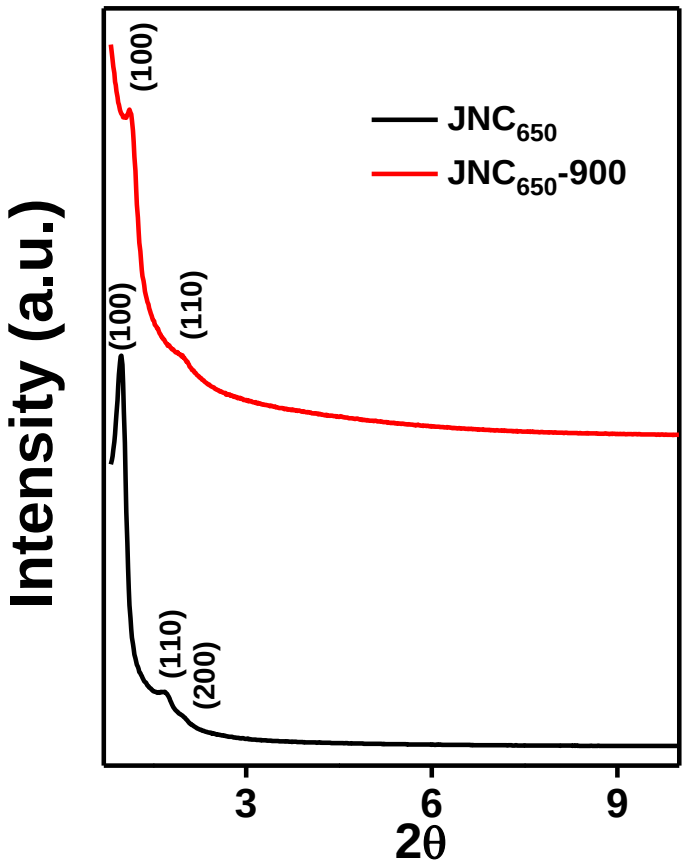

Figure 15. Low angle PXRD patterns of JNC_{650} and JNC_{650}-900.

during carbonization (at 900 ^{o}C) inhibits such a mechanism, resulting in a relatively low surface area. The carbon replica (JNC-2) obtained through the

analogous procedure using mesoporous silica KIT-6(*17*) template also shows high surface area when the silica was removed by Teflon **(Figures 23–27 and Table 5)**.

Materials	S_{BET} [a] ($m^2\ g^{-1}$)	$S_{Micropore}$ [b] ($m^2\ g^{-1}$)	V_{Total} [c] ($cm^3\ g^{-1}$)	$V_{Micropore}$ [d] ($cm^3\ g^{-1}$)	D_{Meso} [e] (nm)
JNC_{650}	1204	224	0.930	0.134	4.5
JNC_{650}-900	2459	803	1.831	0.354	4.5
CMK_{650}	1184	92	1.010	0.042	4.5
CMK_{650}-900	2113	460	1.660	0.173	4.5

[a] BET (Brunauer-Emmett-Teller) specific surface area calculated by taking criteria into account suggested by Rouquerol et al., [b] micropore surface area determined by t-plot method, [c] Total pore volume was calculated at P/P_o = 0.97, [d] micropore volume determined via t-plot analyses and [e] mesopore diameter calculated by QSDFT method.

Table 3. Textural parameters of JNC_{650}, JNC_{650}-900, CMK_{650} and CMK_{650}-900.

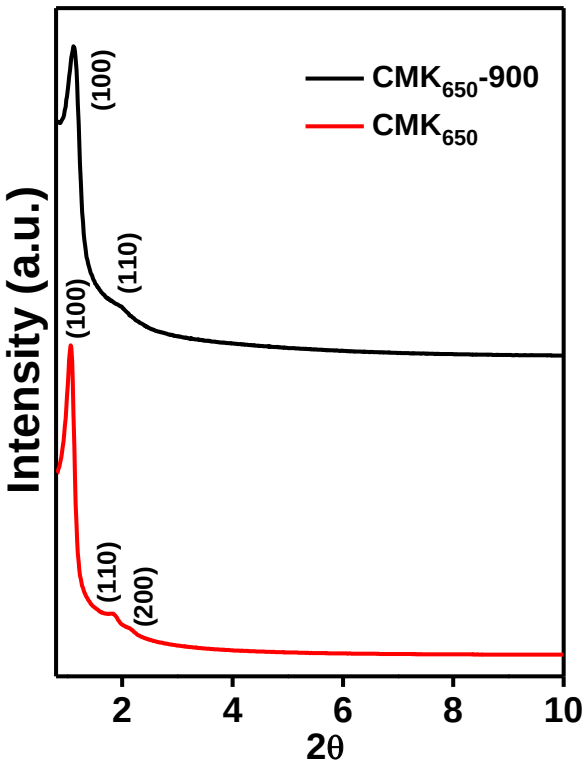

Figure 16. Low angle PXRD patterns of CMK_{650} and CMK_{650}-900.

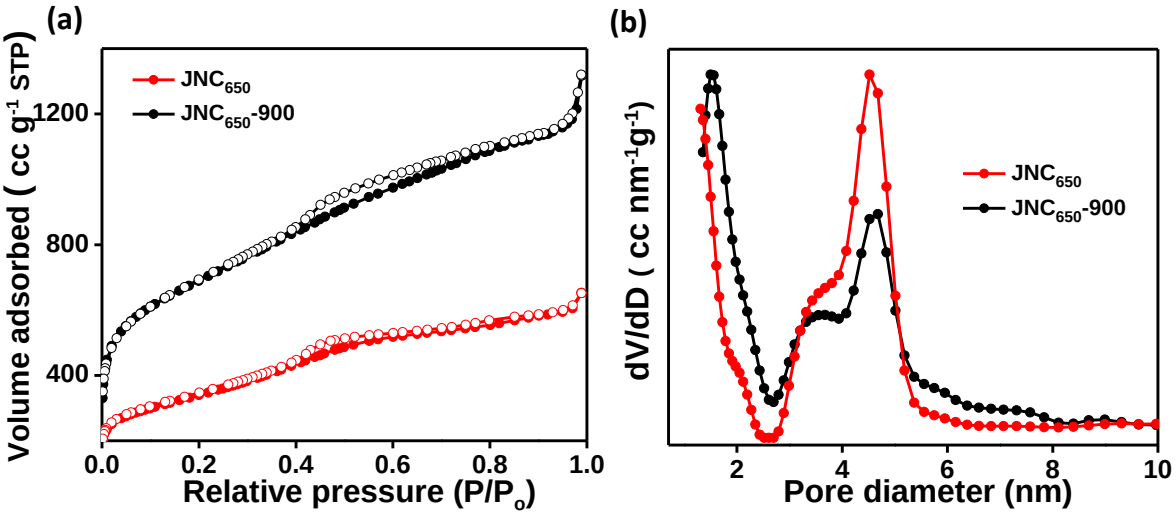

Figure 17. (a) N_2 adsorption-desorption isotherms of JNC_{650} and JNC_{650}-900 and (b) corresponding pore size distributions (normalized) calculated by QSDFT method.

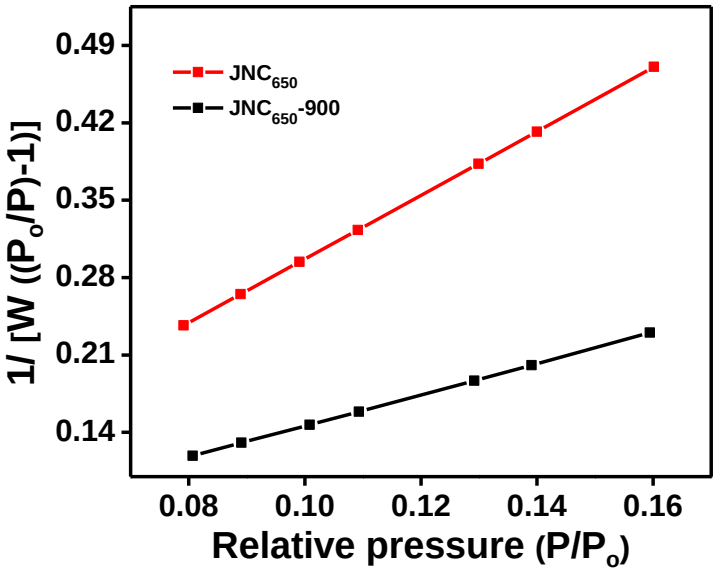

Figure 18. Relative pressure (P/P_o) range chosen for the calculation of surface areas of JNC_{650} and JNC_{650}-900 taking into account criteria suggested by Rouquerol et al. (*22*)

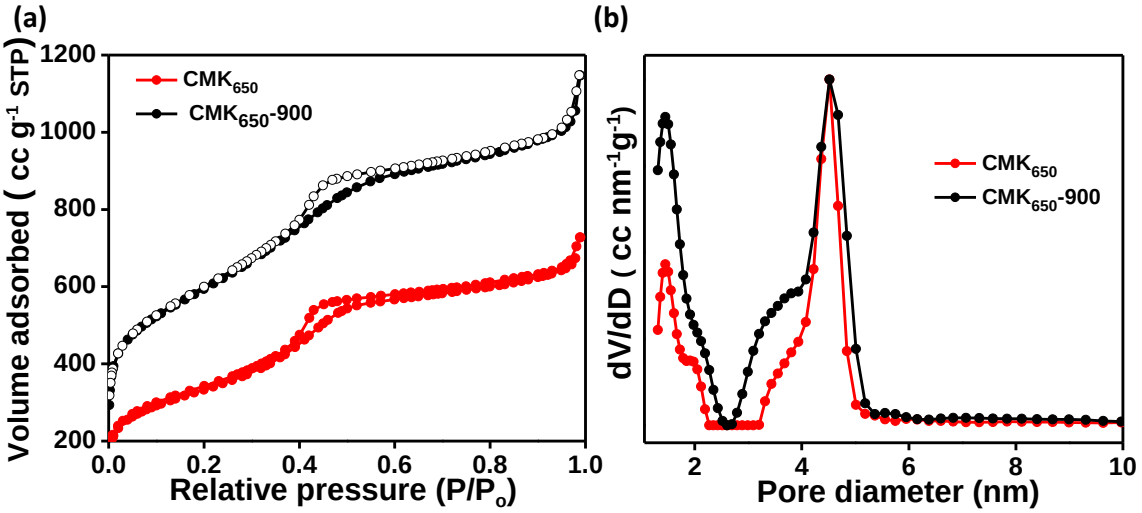

Figure 19. (a) N_2 adsorption-desorption isotherms and (b) corresponding pore size distributions of CMK_{650} and CMK_{650}-900 (normalized) calculated by QSDFT method.

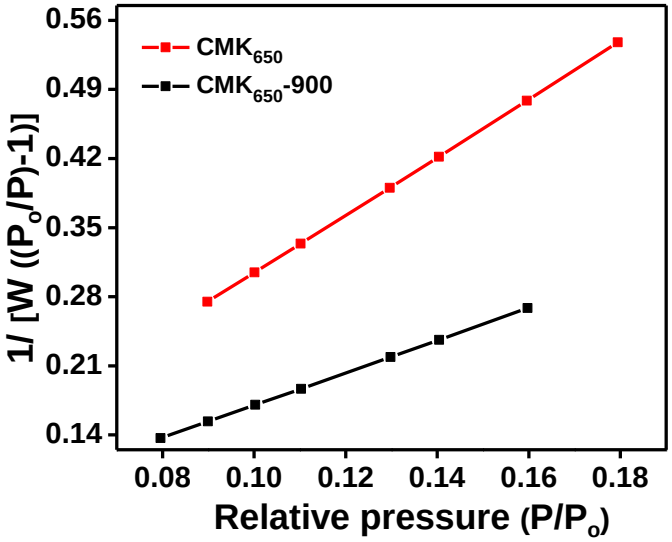

Figure 20. Relative pressure (P/P_o) range chosen for the calculation of surface areas of CMK_{650} and CMK_{650}-900 taking into account criteria suggested by Rouquerol et al.(*22*)

Materials	S_{BET} [a]	$S_{Micropore}$ [b]	V_{Total} [c]	$V_{Micropore}$ [d]	D_{Meso} [e]
	(m^2 g^{-1})	(m^2 g^{-1})	(cm^3 g^{-1})	(cm^3 g^{-1})	(nm)
CMK-3-900	2548	460	2.427	0.174	4.7

Table 4. Textural parameters of CMK-3-900 (superscripts stand for their usual meanings as explained in earlier **Tables**).

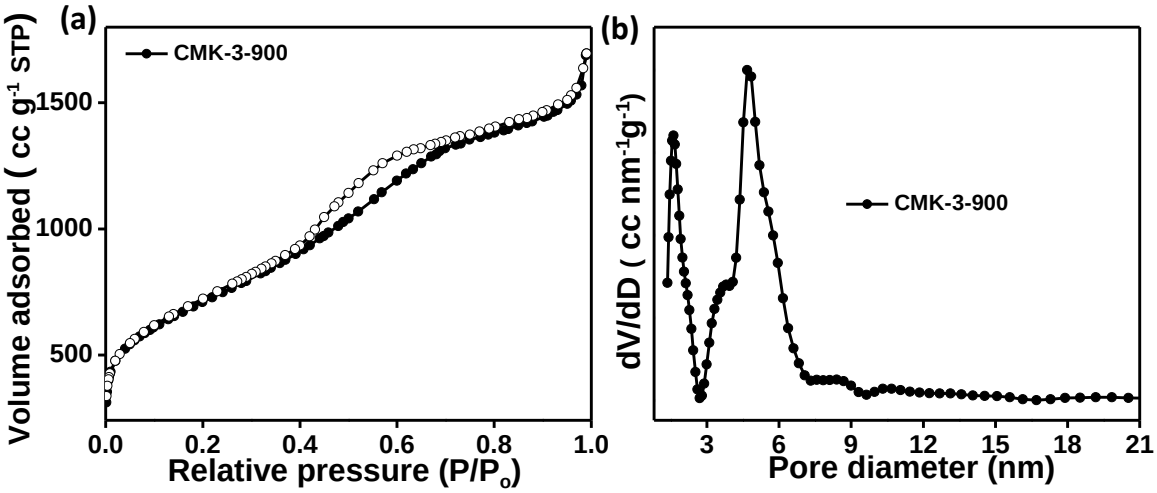

Figure 21. (a) N_2 adsorption-desorption isotherm and (b) corresponding pore size distribution of CMK-3-900 (normalized) calculated by QSDFT method.

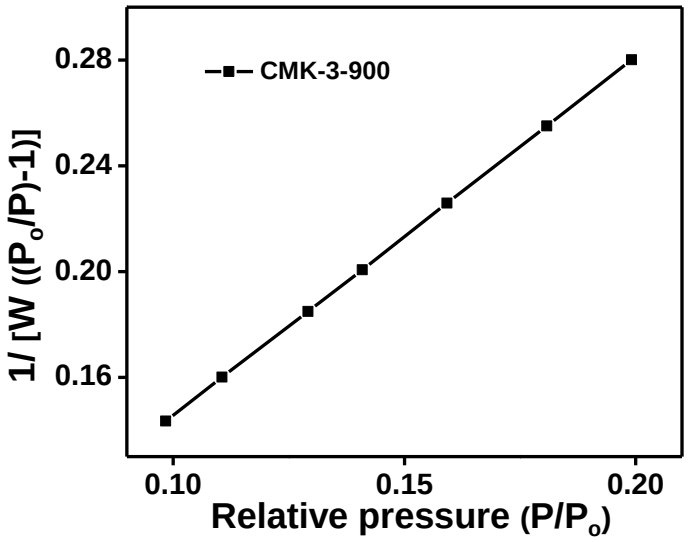

Figure 22. Relative pressure (P/P_o) range chosen for the calculation of surface areas of CMK-3-900 taking into account criteria suggested by Rouquerol et al.

The influence of bimodal (micro-meso) pore size distribution of JNC-1 on the sorption behavior of organic pollutants was investigated using two synthetic azo dyes of different sizes (Alizarin Yellow, size 1.3 nm and Congo Red, size ca. 2.6nm).(*30*) The sorption performance of JNC-1 was compared with the CMK-3 (mesopores) and activated carbon (AC). Liquid phase dye adsorption studies indicate very high uptake of Congo red and Alizarin yellow over JNC-1 in comparison to CMK-3 and AC **(Figure 28)**. Such superior dye uptake of JNC-1 can be explained by bimodal pore size distribution in JNC-1, avoiding mass transfer limitations encountered in narrow micropores and high surface area.

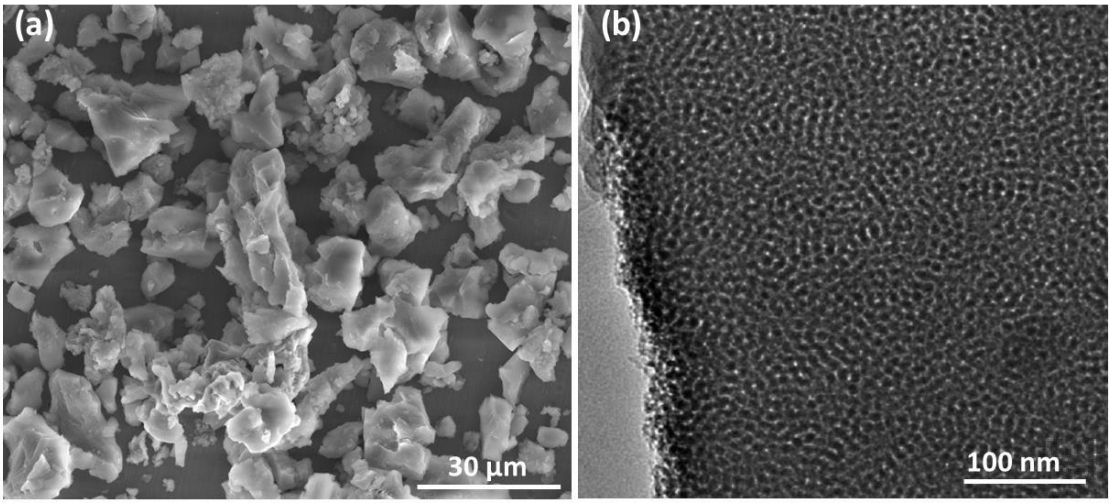

Figure 23. (a) FESEM and (b) TEM images of KIT-6.

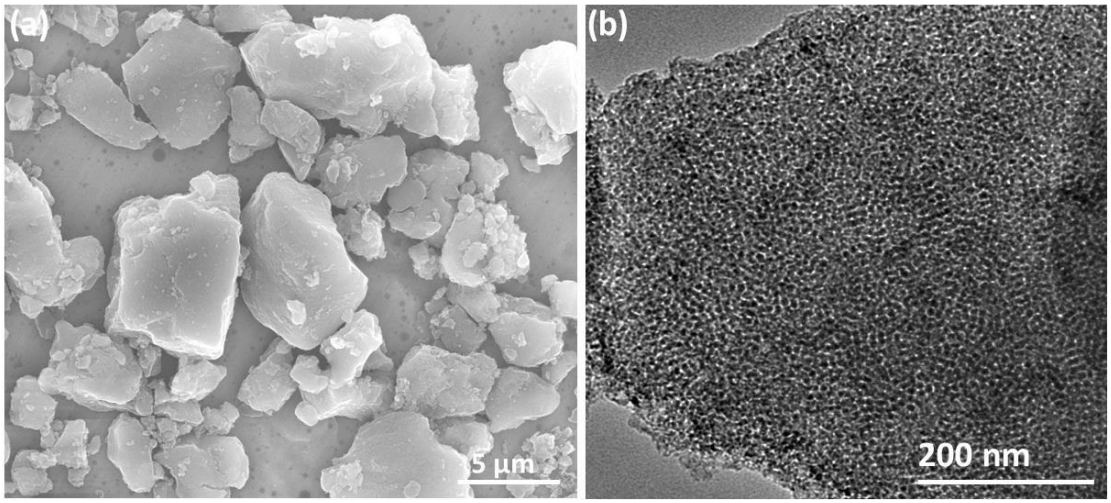

Figure 24. (a) FESEM and (b) TEM images of JNC-2.

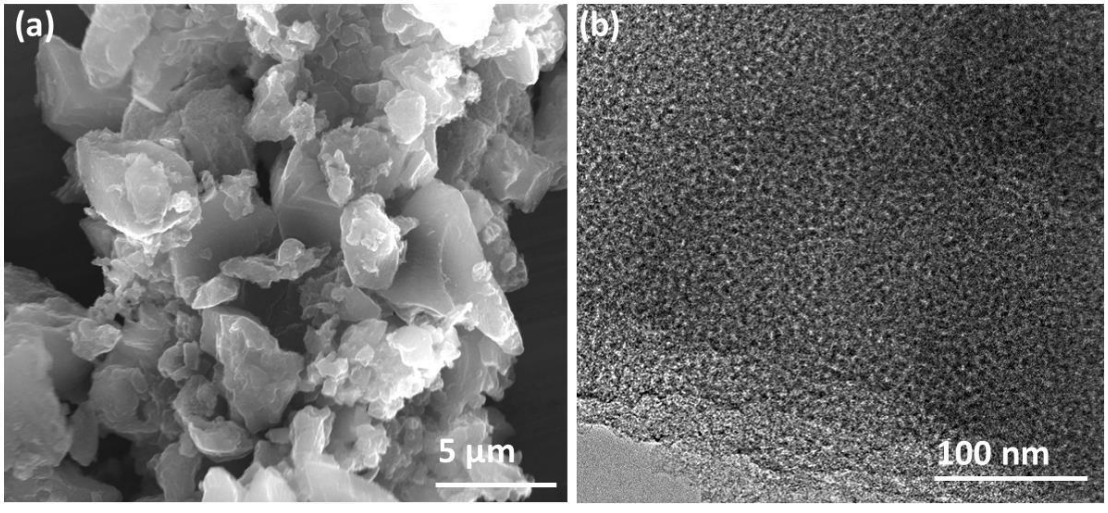

Figure 25. (a) FESEM and (b) TEM images of CMK-8.

Materials	S_{BET} [a] ($m^2\ g^{-1}$)	$S_{Micropore}$ [b] ($m^2\ g^{-1}$)	V_{Total} [c] ($cm^3\ g^{-1}$)	$V_{Micropore}$ [d] ($cm^3\ g^{-1}$)	D_{Meso} [e] (nm)
KIT-6	649	105	1.274	0.043	9.5
CMK-8	826	150	0.981	0.069	4.9
JNC-2	2264	886	1.558	0.381	4.5

[a] BET (Brunauer-Emmett-Teller) specific surface area calculated by taking criteria into account suggested by Rouquerol et al., [b] micropore surface area determined by t-plot method, [c] Total pore volume was calculated at $P/P_o = 0.97$, [d] micropore volume determined via t-plot analyses and [e] mesopore diameter calculated by QSDFT method.

Table 5. Textural parameters of KIT-6, CMK-8 and JNC-2.

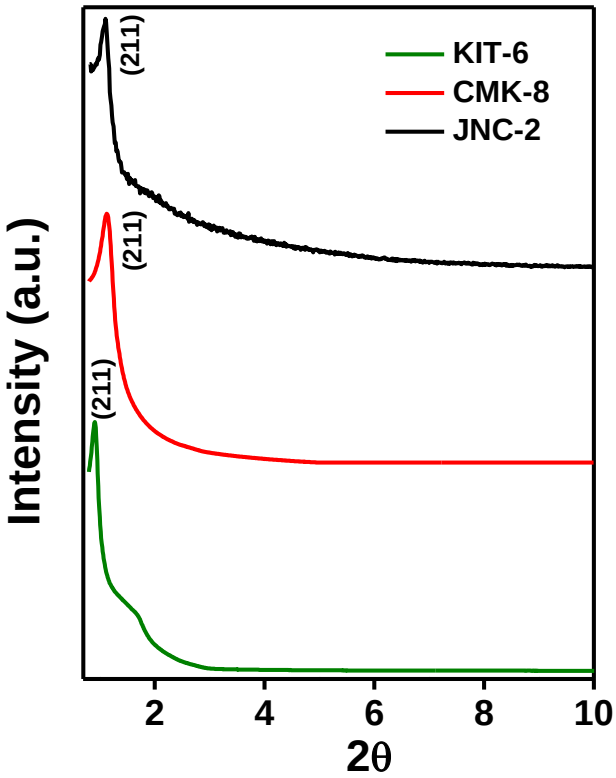

Figure 26. PXRD patterns of KIT-6, CMK-8 and JNC-2.

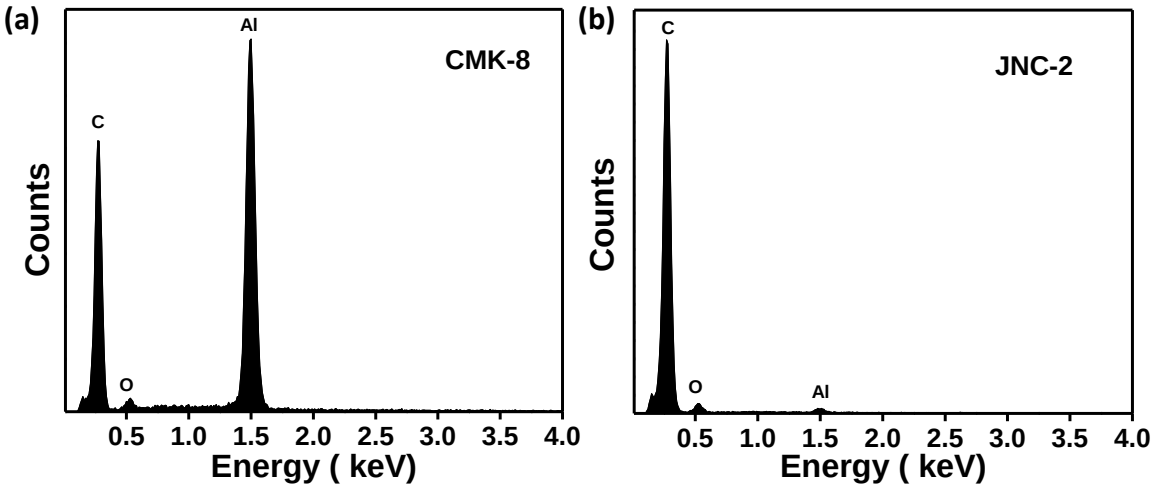

Figure 27. Energy dispersive X-ray spectroscopic (EDS) analyses of **(a)** CMK-8 and **(b)** JNC-2 indicating complete removal of Si (Al comes from sample holder).

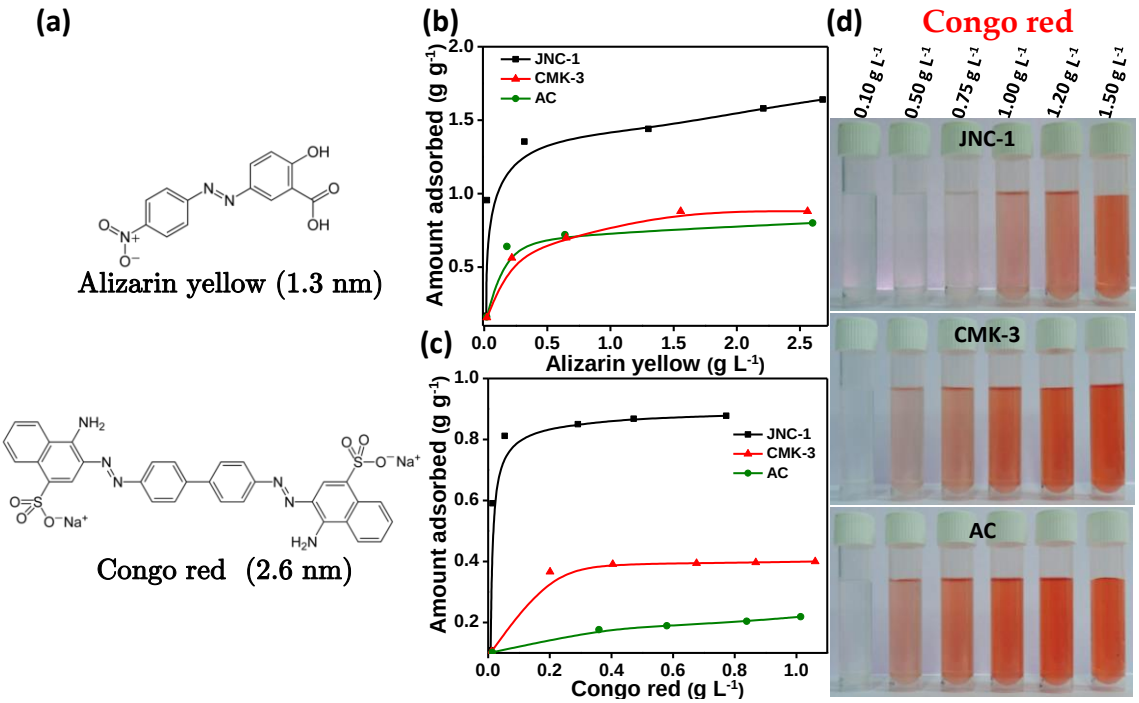

Figure 28. (a) Molecular structures of Alizarin yellow and Congo red. Adsorption isotherms of (b) Alizarin yellow and (c) Congo red over JNC-1, CMK-3 and AC. (d) Optical images of Congo red adsorption by different carbons (concentrations at the top of **Figure** d are initial concentrations with equal amount of different adsorbents added in each case).

Furthermore, carbon dioxide and hydrogen sorptions measurements were performed in order to evaluate the gas storage properties of JNC-1 on account of its bimodal pore size distribution. The uptake of CO_2 and H_2 in light weight, porous carbon materials is all the more important as the former (CO_2) being a greenhouse gas needs to be sequestered from the air or industry effluents and the latter (H_2) is an important source for clean energy but needs to be stored in a material for the safe and efficient usage. JNC-1 showed a very high uptake for CO_2 of around 154 wt.% at -78 °C (0.88 bar) as compared to 73 wt.% over CMK-3 under similar conditions **(Figure 29b)**. Even at 0 °C and 25 °C (under 0.88 bar of CO_2 pressure) the CO_2 sorption on JNC-1 was found to be around 26 wt.% and 15 wt.% respectively **(Figure 29c)** which are significantly higher

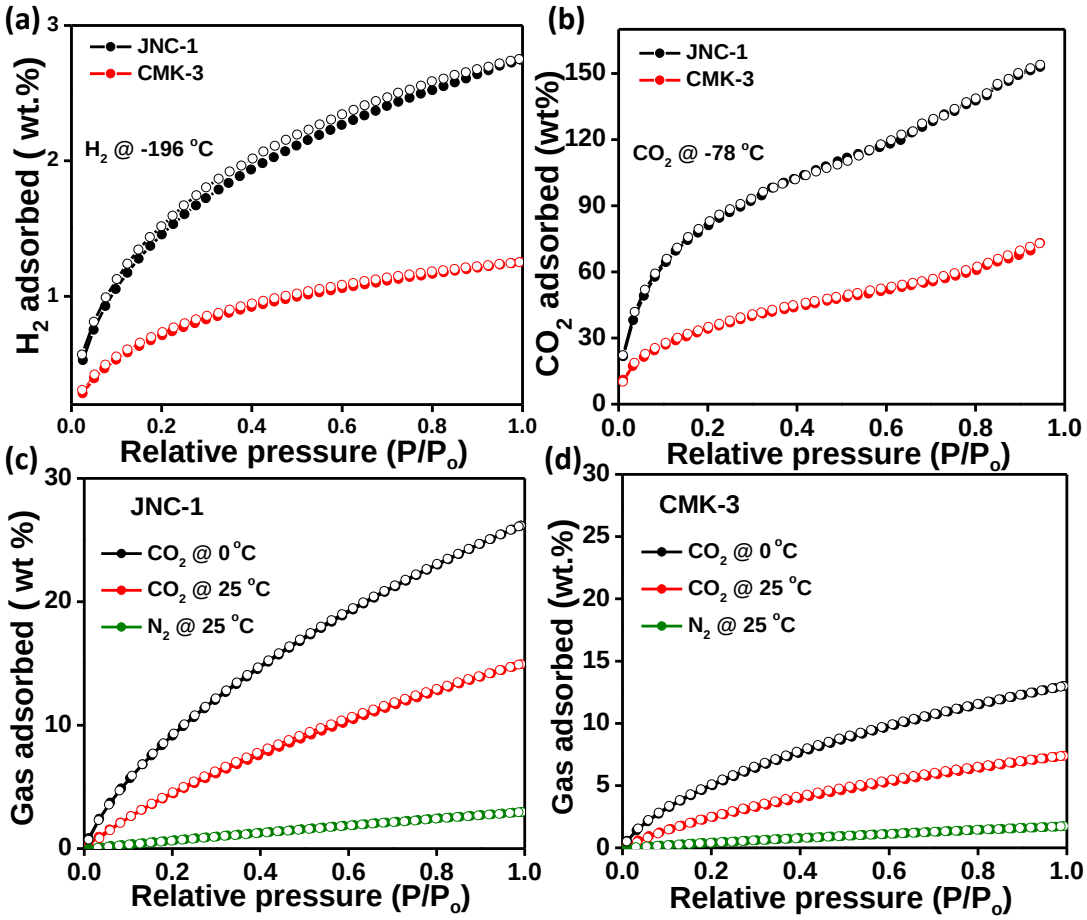

Figure 29. (a) H_2 and (b) CO_2 adsorption isotherms of JNC-1 and CMK-3 at -196 °C and -78 °C respectively. CO_2 adsorption isotherms (at 0 °C and 25 °C) along with N_2 adsorption isotherm (at 25 °C) of (c) JNC-1 and (d) CMK-3. (Note: closed and open circles represent adsorption and desorption points. P_o for N_2 and CO_2 isotherms is taken as 660 torr (0.88 bar) whereas for H_2 it is 760 torr (1.01 bar)).

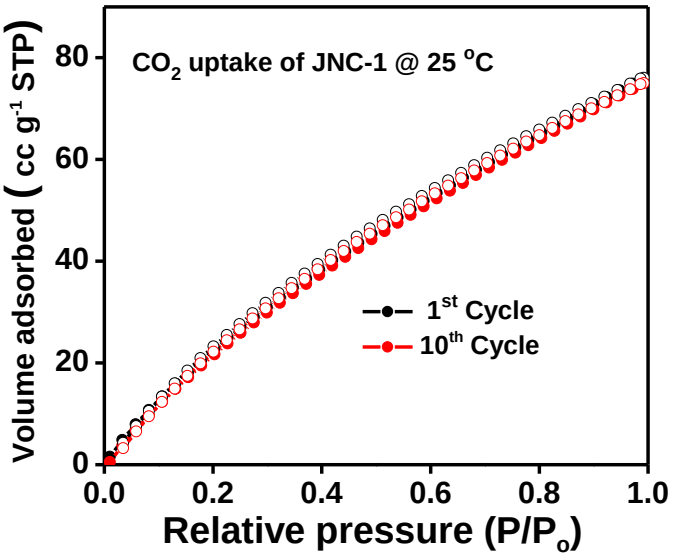

Figure 30. CO_2 uptake of JNC-1 under ambient conditions (1 bar) over different cycles.

CO_2 uptake of different porous materials @ 25 °C under 1 bar

Adsorbent	Surface area (m^2 g^{-1})	CO_2 uptake (mmol g^{-1})	Ref.
JNC-1	2545	3.5	Present work
Covalent organic frameworks	364-1054	0.7-1.7	(*31*)
Microporous organic polymers	653-4077	1.1-2.2	(*32*)
Different Carbon materials	310-2157	0.5-2.2	(*33*)
NH_2 modified mesoporous alumina and silica	812-1050	1.0-2.7	(*34*)
Nitrogen doped carbon	122-1588	1.0-4.3	(*35*)
Various MOFs	600-4034	0.6-8.4	(*36, 37*)

Table 6. Comparison of CO_2 uptake of JNC-1 under ambient conditions with literature values.

than those of CMK-3, whose sorption capacity were determined to be 13 wt.% and 7 wt.% at 0 °C and 25 °C respectively **(Figure 29d)**. Such exceptional CO_2 uptake **(Table 6)** can be attributed to unique textural parameters of JNC-1.(*38*) The uptake for CO_2 at 25 °C (1 bar) over JNC-1 remains the same even after 10 cycles. **(Figure 30)**. The selectivity for CO_2/N_2 separation (calculated from ratio of initial slopes) over JNC-1 at 25 °C was found to be ~7 compared to 6 of CMK-3 and can be attributed to the presence of abundant **(Figure 31)** micropores in the former.(*6, 39, 40*) Hydrogen uptake (2.8 wt.%) of JNC-1 at -196 °C (1.0 atm) **(Figure 29a)** was also found to be higher than that of CMK-3 (1.2 wt. %) **(Figure 29a and Table 7)** and is completely reversible throughout the pressure range studied. The presence of huge amount of micropores (40%) of size ~0.9 nm is within the accepted range of optimum micropore diameter for hydrogen storage (i.e. between 0.5-1.5 nm) and contributes as sites of high energy of adsorption thereby maximizing the uptake.(*41, 42*) On the other hand, CMK-3 obtained through HF etching shows negligible H_2 uptake due to lack of enhanced microporosity.(*43*)

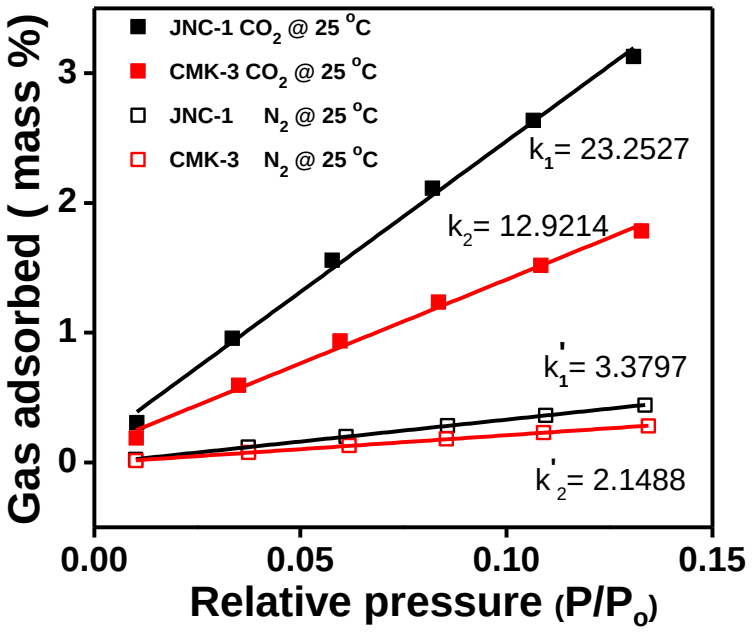

Figure 31. Initial slope calculations for N_2 and CO_2 adsorption on JNC-1 and CMK-3 at 25 °C.

Electrochemical performances of JNC-1, CMK-3 and AC were evaluated through cyclic voltammetry (CV), galvanostatic charge/discharge (CD) and electrochemical impedance spectroscopy (EIS) study using typical three electrode setup. CV curve of JNC-1 is pseudo rectangular in shape **(Figure 32a)** indicating capacitive type of behavior at the scan rate of 100 mV s^{-1}. As the

H_2 uptake of different carbon based porous materials @ -195 °C

Adsorbent	Surface area (m^2 g^{-1})	H_2 uptake (1 bar) (wt. %)	Ref.
JNC-1	2545	2.80	Present work
Mesoporous carbon	2314	1.78	(*44*)
Carbon nanotubes	1024	2.40	(*45*)
Microporous carbon templated from MOF	3405	2.77	(*46*)
Activated carbon	2500-3200	1.80-2.70	(*42*)

Table 7. Comparison of H_2 uptake of JNC-1 under at -195 °C (1 bar) with some relevant literature values.

scan rate is increased upto 2 V $s^{-1,}$ cyclic voltammograms, still retains rectangular shape **(Figure 33)** indicating fast charge-discharge and high power capability of the JNC-1.(*47*) Galvanostatic CD curve of JNC-1 is triangular in nature **(Figure 32b)**, which further confirms efficient ion transport without significant iR drop. The JNC-1 carbon exhibited specific capacitance of around 274 F g^{-1} at 1 A g^{-1} and value was retained till several cycles as compared to 132 F g^{-1} and 49 F g^{-1} for CMK-3 and AC respectively, at the same current density **(Figure 34)**. In fact, in one of the batches, a specific capacitance value of 292 F g^{-1} at 1 A g^{-1} **(Figure 32c)** was found and is one of the best reported values for pure carbon based materials **(Table 8)**.(*48, 49*) Additionally, JNC-1 exhibits excellent cyclic stability over studied 1200 cycles at 10 A g^{-1} retaining 98 % of the original capacity **(Figure 35)**. Rate capability performance of JNC-1 indicate a retention of specific capacitance around 213 F g^{-1} and 180 F g^{-1} at 10 A g^{-1} and 50 A g^{-1} respectively **(Figure 32c)**. To the best of our knowledge these values are one of the highest at such high drain rates for pure carbon based materials.[38,39] In comparison to CMK-3 and AC, Nyquist plot of JNC-1 is almost vertical to the imaginary axis **(Figure 32d)**, signifying the performance reaches to that of an ideal capacitor as the ion migrations are not hindered.(*50*)

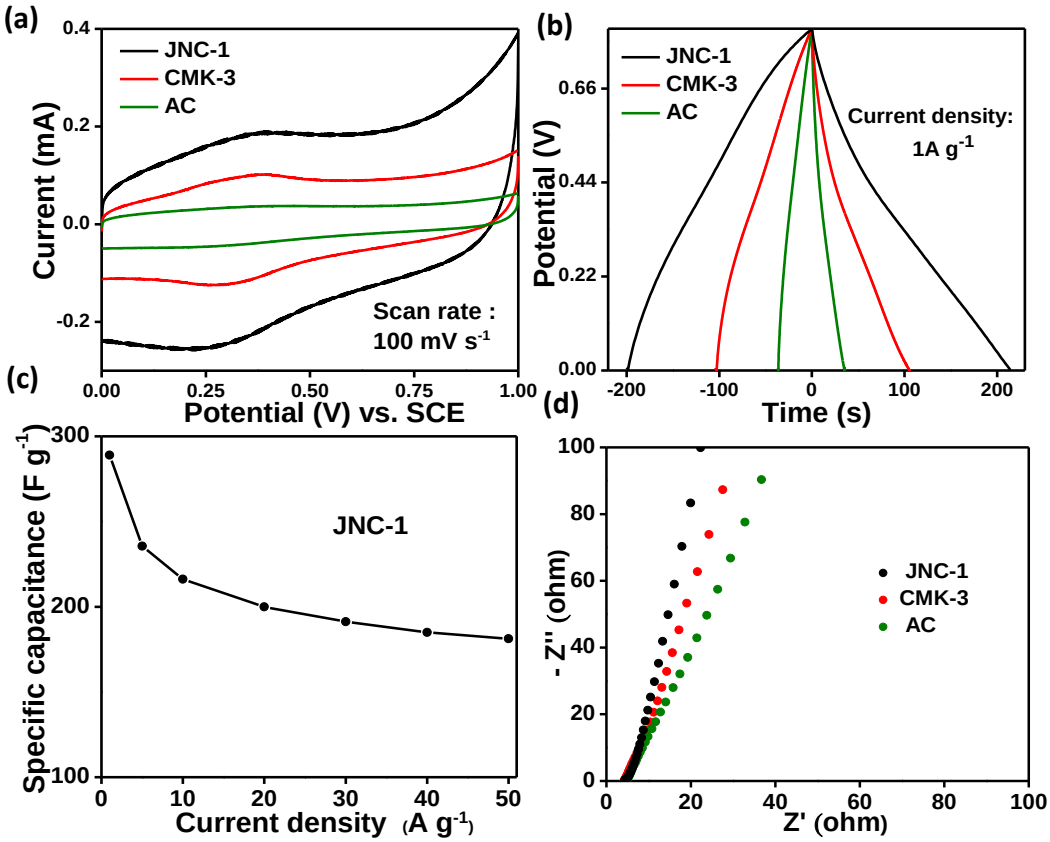

Figure 32. Comparison of electrochemical performances of JNC-1 with CMK-3 and AC. (a) Cyclic voltammetry (CV) curves (scan rate: 100 mV s^{-1}) and (b) galvanostatic charge/discharge (CD) profiles at a current density of 1 A g^{-1} of JNC-1, CMK-3 and AC in 1 M H_2SO_4. (c) Rate capability performance of JNC-1 and (d) shows Nyquist plot of different carbons studied, depicting ideal capacitor type of behavior for JNC-1.

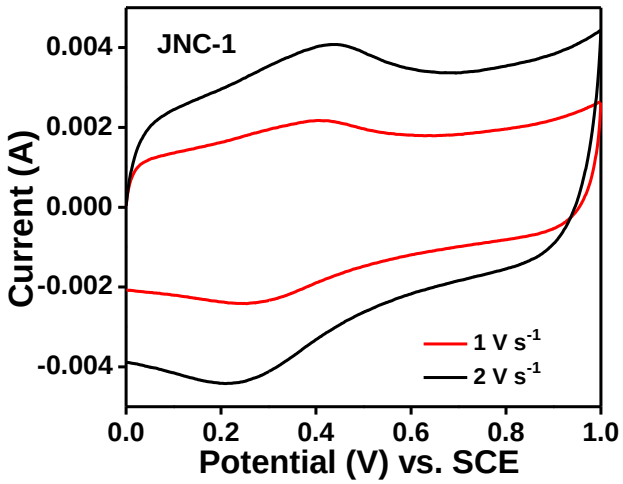

Figure 33. Cyclic voltammograms of JNC-1 at higher scan rates.

Mesopores helps in attaining high capacitance values at higher drain rate by rapid supply of ions to the active electrode interface which is not possible in purely microporous sample on account of limited space available for ion transport. Such performance metric can be traced back to highly connected bimodal pore size distribution of JNC-1, exhibiting synergistic effect of facilitating efficient charge transfer (mesopores) process and enhanced electric double layer formation (micropores).(*12, 47*) In other words, presence of huge amount micropores in JNC-1 contribute towards high energy density and equally large extent of mesopores aid towards enhanced power density.(*12, 47*)

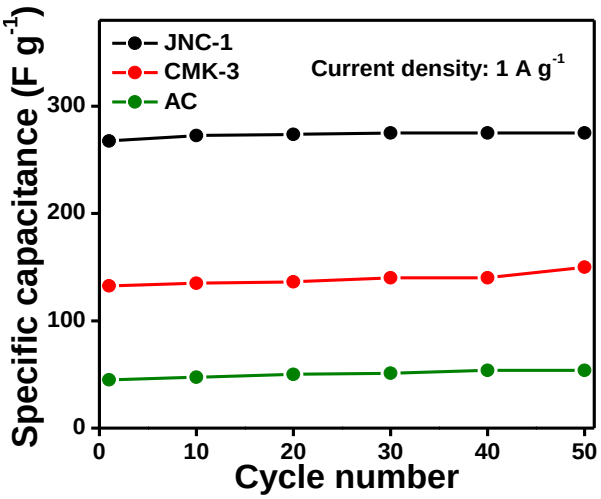

Figure 34. Comparison of specific capacitance of JNC-1, CMK-3 and AC with cycle number.

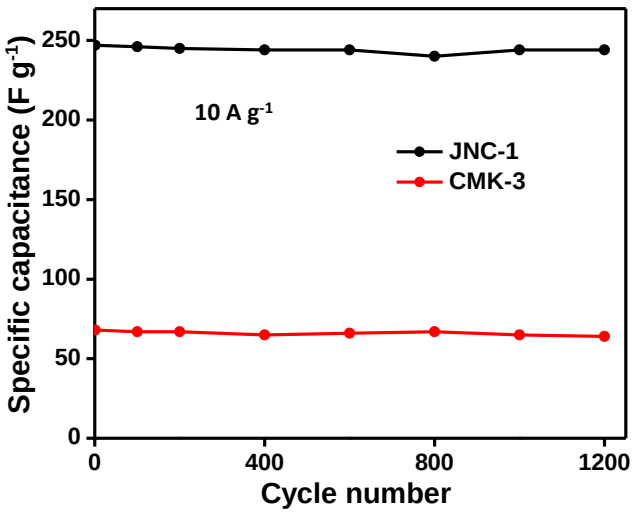

Figure 35. Comparison of cycling performance of JNC-1 with CMK-3 at 10 A g-1 indicating stable cycling behavior.

Electrode material	Surface area and pore size (m^2 g^{-1} and nm)	Capacitance (F g^{-1})/ Rate (A g^{-1})	Electrode Configuration	Electrolyte	Ref.
JNC-1	2545, bimodal 0.9 and 4.7 nm	292/1.0	Three electrode	1.0 M H_2SO_4	Present work
Resorcinol-pyrocatechol aerogel	519	175/0.1	Three electrode	1.0 M H_2SO_4	(*51*)
Resorcinol-formaldehyde aerogel	2119 and 4.8	250/0.5	Three electrode	6.0 M KOH	(*52*)
Graphene and SWNT	421	290/0.5	Two electrode	1.0 M KCl	(*53*)
Highly corrugated graphene	518	349/CV (2 mV s^{-1})	Three electrode	6.0 M KOH	(*54*)
Graphene aerogel (Supercritical drying)	830 and 4.0 nm	278/0.2	Three electrode	1.0 M H_2SO_4	(*55*)
Mesoporous carbon decorated graphene	927 and 6.3	213/0.5	Three electrode	6.0 M KOH	(*56*)
CNT-Carbon aerogel (CVD)	700	524/1 mA	Three electrode	5.0 M KOH	(*57*)

Table 8. Comparison of supercapacitor performance of JNC-1 at 1 A g^{-1} with different carbon based materials indicating good performance of JNC-1 at higher drain rate.

2.5 Conclusions: In conclusion, use of Teflon not only eliminates the handling of toxic HF or repeated NaOH wash but also drastically reduces the time required for mesopore carbon generation as it combines the carbonization and template removal step as a single step. Moreover, the obtained carbon material, JNC-1

exhibits superior supercapacitor performance and capacitance values are one of the highest reported for such ordered carbon material at such a higher drain rate. In addition JNC-1 exhibits excellent dye adsorption and exceptional gas storage properties (H_2 and CO_2) compared to CMK-3 which is comparable to most of the best reported MOF.

2.6 References:

1. R. Ryoo, S. H. Joo, M. Kruk, M. Jaroniec, Ordered Mesoporous Carbons. *Adv. Mater.* **13**, 677 (2001).
2. J. Lee, J. Kim, T. Hyeon, Recent progress in the synthesis of porous carbon materials. *Adv. Mater.* **18**, 2073 (2006).
3. A. Walcarius, Mesoporous materials and electrochemistry. *Chem. Soc. Rev.* **42**, 4098 (2013).
4. S. H. Joo *et al.*, Ordered nanoporous arrays of carbon supporting high dispersions of platinum nanoparticles. *Nature* **412**, 169 (2001).
5. X. L. Ji, K. T. Lee, L. F. Nazar, A highly ordered nanostructured carbon–sulphur cathode for lithium–sulphur batteries. *Nat. Mater.* **8**, 500 (2009).
6. J. Zhang *et al.*, Hypercrosslinked Phenolic Polymers with Well-Developed Mesoporous Frameworks. *Angew. Chem. Int. Ed.* **54**, 4582 (2015).
7. M. Choi, R. Ryoo, Mesoporous carbons with KOH activated framework and their hydrogen adsorption. *J. Mater. Chem.* **17**, 4204 (2007).
8. J. Wei *et al.*, A Controllable Synthesis of Rich Nitrogen-Doped Ordered Mesoporous Carbon for CO_2 Capture and Supercapacitors. *Adv. Funct. Mater.* **23**, 2322 (2013).
9. S. Jun *et al.*, Synthesis of New, Nanoporous Carbon with Hexagonally Ordered Mesostructure. *J. Am. Chem. Soc.* **122**, 10712 (2000).
10. J. C. Bertolini, Hydrofluoric acid: A review of toxicity. *J. Emer. Med.* **10**, 163 (1992).
11. J. Li *et al.*, Nanocasting synthesis of graphitized ordered mesoporous carbon using Fe-coated SBA-15 template. *Mater. Chem. Phys.* **138**, 484 (2013).
12. M. Karthik *et al.*, Effect of Mesopore Ordering in Otherwise Similar Micro/Mesoporous Carbons on the High-Rate Performance of Electric Double-Layer Capacitors. *J. Phys. Chem. C* **118**, 27715 (2014).

13. J. Pang *et al.*, Silica-Templated Continuous Mesoporous Carbon Films by a Spin-Coating Technique. *Adv. Mater.* **16**, 884 (2004).
14. Y. Meng *et al.*, Ordered Mesoporous Polymers and Homologous Carbon Frameworks: Amphiphilic Surfactant Templating and Direct Transformation. *Angew. Chem. Int. Ed.* **44**, 7053 (2005).
15. R. Liu *et al.*, Triconstituent Co-assembly to Ordered Mesostructured Polymer−Silica and Carbon−Silica Nanocomposites and Large-Pore Mesoporous Carbons with High Surface Areas. *J. Am. Chem. Soc.* **128**, 11652 (2006).
16. A. Sayari, B.-H. Han, Y. Yang, Simple Synthesis Route to Monodispersed SBA-15 Silica Rods. *J. Am. Chem. Soc.* **126**, 14348 (2004).
17. F. Kleitz, S. Hei Choi, R. Ryoo, Cubic Ia3d large mesoporous silica: synthesis and replication to platinum nanowires, carbon nanorods and carbon nanotubes. *Chem. Commun.*, 2136 (2003).
18. D. Zhao *et al.*, Triblock Copolymer Syntheses of Mesoporous Silica with Periodic 50 to 300 Angstrom Pores. *Science* **279**, 548 (1998).
19. Y. Xia, R. Mokaya, Synthesis of Ordered Mesoporous Carbon and Nitrogen-Doped Carbon Materials with Graphitic Pore Walls via a Simple Chemical Vapor Deposition Method. *Adv. Mater.* **16**, 1553 (2004).
20. T.-W. Kim, I.-S. Park, R. Ryoo, A Synthetic Route to Ordered Mesoporous Carbon Materials with Graphitic Pore Walls. *Angew. Chem.* **115**, 4511 (2003), *Angew. Chem. Int. Ed.* **42**, 4375 (2003).
21. K. S. W. Sing *et al.*, Reporting physisorption data for gas/solid systems with special reference to the determination of surface area and porosity (Recommendations 1984). *Pure Appl. Chem.* **57**, 603 (1985).
22. J. Rouquerol, P. Llewellyn, F. Rouquerol, in *Stud. Surf. Sci. Catal.,* F. R.-R. J. R. P.L. Llewellyn, N. Seaton, Eds. (Elsevier, 2007), vol. Volume **160**, pp. 49-56.
23. A. V. Neimark, Y. Lin, P. I. Ravikovitch, M. Thommes, Quenched solid density functional theory and pore size analysis of micro-mesoporous carbons. *Carbon* **47**, 1617 (2009).
24. B. C. Lippens, J. H. de Boer, Studies on pore systems in catalysts: V. The t method. *J. Catal.* **4**, 319 (1965).
25. S. Lowell, J. E. Shields, M. A. Thomas, M. Thommes, *Characterization of Porous Solids and Powders: Surface Area, Pore Size and Density*. (Springer Netherlands, 2012).

26. J. A. Conesa, R. Font, Polytetrafluoroethylene decomposition in air and nitrogen. *Poly. Eng. Sci.* **41**, 2137 (2001).
27. S. L. Madorsky, V. E. Hart, S. Straus, V. A. Sedlak, Thermal degradation of tetrafluoroethylene and hydrofluoroethylene polymers in a vacuum. *J. Res. Natl. Bur. Stand. (U. S.)* **51**, 327 (1953).
28. P. F. Nelson, I. W. Smith, R. J. Tyler, J. C. Mackie, Pyrolysis of coal at high temperatures. *Energy & Fuels* **2**, 391 (1988).
29. A.-H. Lu, D. Zhao, Y. Wan, *Nanocasting : a versatile strategy for creating nanostructured porous materials*. (Royal Society of Chemistry, Cambridge, 2010).
30. K. K. R. Datta *et al.*, Observation of Pore-Switching Behavior in Porous Layered Carbon through a Mesoscale Order–Disorder Transformation. *Angew. Chem. Int. Ed.* **50**, 3929 (2011).
31. N. Huang, X. Chen, R. Krishna, D. Jiang, Two-Dimensional Covalent Organic Frameworks for Carbon Dioxide Capture through Channel-Wall Functionalization. *Angew. Chem. Int. Ed.* **54**, 2986 (2015).
32. R. Dawson, E. Stockel, J. R. Holst, D. J. Adams, A. I. Cooper, Microporous organic polymers for carbon dioxide capture. *Energy Environ. Sci.* **4**, 4239 (2011).
33. V. Jiménez, A. Ramírez-Lucas, J. A. Díaz, P. Sánchez, A. Romero, CO_2 Capture in Different Carbon Materials. *Environ. Sci. Tech.* **46**, 7407 (2012).
34. C. Chen, W.-S. Ahn, CO_2 capture using mesoporous alumina prepared by a sol–gel process. *Chem. Eng. J.* **166**, 646 (2011).
35. V. Chandra *et al.*, Highly selective CO_2 capture on N-doped carbon produced by chemical activation of polypyrrole functionalized graphene sheets. *Chem. Commun.* **48**, 735 (2012).
36. J.-R. Li *et al.*, Carbon dioxide capture-related gas adsorption and separation in metal-organic frameworks. *Coord. Chem. Rev.* **255**, 1791 (2011).
37. S. Keskin, T. M. van Heest, D. S. Sholl, Can Metal–Organic Framework Materials Play a Useful Role in Large-Scale Carbon Dioxide Separations? *ChemSusChem* **3**, 879 (2010).
38. G. Srinivas, V. Krungleviciute, Z.-X. Guo, T. Yildirim, Exceptional CO_2 capture in a hierarchically porous carbon with simultaneous high surface area and pore volume. *Energy Environ. Sci.* **7**, 335 (2014).

39. L. K. C. de Souza *et al.*, Enhancement of CO_2 adsorption on phenolic resin-based mesoporous carbons by KOH activation. *Carbon* **65**, 334 (2013).
40. R. Banerjee *et al.*, Control of Pore Size and Functionality in Isoreticular Zeolitic Imidazolate Frameworks and their Carbon Dioxide Selective Capture Properties. *J. Am. Chem. Soc.* **131**, 3875 (2009).
41. B. Kuchta *et al.*, Open carbon frameworks - a search for optimal geometry for hydrogen storage. *J. Mol. Model.* **19**, 4079 (2013).
42. Y. Xia, Z. Yang, Y. Zhu, Porous carbon-based materials for hydrogen storage: advancement and challenges. *J. Mater. Chem. A* **1**, 9365 (2013).
43. M. Jordá-Beneyto, F. Suárez-García, D. Lozano-Castelló, D. Cazorla-Amorós, A. Linares-Solano, Hydrogen storage on chemically activated carbons and carbon nanomaterials at high pressures. *Carbon* **45**, 293 (2007).
44. J. Pang, J. E. Hampsey, Z. Wu, Q. Hu, Y. Lu, Hydrogen adsorption in mesoporous carbons. *Appl. Phys. Lett.* **85**, 4887 (2004).
45. B. Panella, M. Hirscher, S. Roth, Hydrogen adsorption in different carbon nanostructures. *Carbon* **43**, 2209 (2005).
46. H.-L. Jiang *et al.*, From Metal–Organic Framework to Nanoporous Carbon: Toward a Very High Surface Area and Hydrogen Uptake. *J. Am. Chem. Soc.* **133**, 11854 (2011).
47. K. Xia, Q. Gao, J. Jiang, J. Hu, Hierarchical porous carbons with controlled micropores and mesopores for supercapacitor electrode materials. *Carbon* **46**, 1718 (2008).
48. Y. B. Tan, J.-M. Lee, Graphene for supercapacitor applications. *J. Mater. Chem. A* **1**, 14814 (2013).
49. X.-L. Wu, A.-W. Xu, Carbonaceous hydrogels and aerogels for supercapacitors. *J. Mater. Chem. A* **2**, 4852 (2014).
50. C. Liu, Z. Yu, D. Neff, A. Zhamu, B. Z. Jang, Graphene-Based Supercapacitor with an Ultrahigh Energy Density. *Nano Lett.* **10**, 4863 (2010).
51. C. Moreno-Castilla, M. B. Dawidziuk, F. Carrasco-Marín, Z. Zapata-Benabithe, Surface characteristics and electrochemical capacitances of carbon aerogels obtained from resorcinol and pyrocatechol using boric and oxalic acids as polymerization catalysts. *Carbon* **49**, 3808 (2011).
52. D. Liu, J. Shen, N. Liu, H. Yang, A. Du, Preparation of activated carbon aerogels with hierarchically porous structures for electrical double layer capacitors. *Electrochim. Acta* **89**, 571 (2013).

53. Q. Cheng *et al.*, Graphene and carbon nanotube composite electrodes for supercapacitors with ultra-high energy density. *Phys. Chem. Chem. Phys.* **13**, 17615 (2011).
54. J. Yan, J. Liu, Z. Fan, T. Wei, L. Zhang, High-performance supercapacitor electrodes based on highly corrugated graphene sheets. *Carbon* **50**, 2179 (2012).
55. W. Si *et al.*, Reduced graphene oxide aerogel with high-rate supercapacitive performance in aqueous electrolytes. *Nanoscale Res. Lett.* **8**, 247 (2013).
56. M. Li, J. Ding, J. Xue, Mesoporous carbon decorated graphene as an efficient electrode material for supercapacitors. *J. Mater. Chem. A* **1**, 7469 (2013).
57. T. Bordjiba, M. Mohamedi, Molding versus dispersion: effect of the preparation procedure on the capacitive and cycle life of carbon nanotubes aerogel composites. *J. Solid State Electrochem.* **15**, 765 (2011).

Chapter-3

An Extremely High Surface Area Ordered Hierarchical Mesoporous-Microporous Networked Carbon for High Stability Li-S and Intermediate Temperature Na-S Rechargeable Batteries

Summary:

Hierarchically networked, ordered pore engineered carbon (JNC-1) with a high surface area (~2545 m^2g^{-1}) has been utilized as a cathodic host for sulphur in Li-S and Na-S rechargeable batteries. The unique interconnected mesoporous-microporous structure of the host provides facile pathways for Li-ion/electrolyte transport and potential landscapes for efficient and effective polysulfide traps thereby modulating S (polysulfide) flux across the cathode. Such textural engineering leads to superior mass transport properties coupled with intricate conducting C-S interfaces results in highly stable Li-S battery performance. The above-mentioned cathode material also leads to admirable Na-S performance at intermediate temperature (70 ^{O}C) which is contrary to the observed electrochemistry of such systems which are known to perform at elevated temperatures (100-300 ^{O}C).

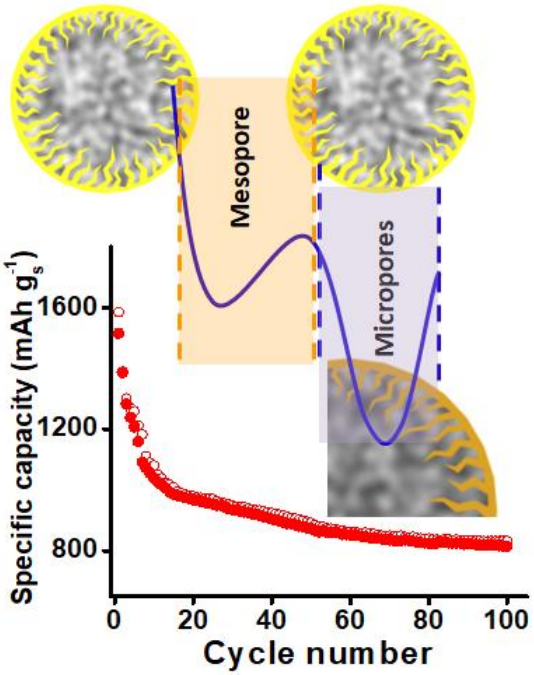

(A paper based on this work has appeared in *ChemistrySelect* **2**, 9249, 2017).

3.1 Introduction:

With the current state-of-art lithium-ion batteries (LiBs), based on intercalation chemistry attaining the apex of theoretical energy density limits, alternate higher specific energy storage systems with low cost is vigorously pursued to address technologies beyond portable devices viz. plug-in vehicles, grid energy storage etc.(*1-4*) Rechargeable Li-S batteries open up a new paradigm for future energy technologies with sulfur cathodes offering a specific energy density of 1675 mAh g^{-1} which is nearly an order higher than the conventional LiB cathodes ($LiCoO_2$, $LiFePO_4$ etc.).(*3, 5*) Besides, S is earth-abundant(*6-8*) and offers lower environmental impact along with cost competitiveness(*9*) compared to current high energy storage systems.(*5, 10, 11*) However, Li-S technology is yet to receive a breakthrough for widespread market entry as it suffers from tremendous capacity fading upon cycling indicating poor utilization of S.(*11, 12*) Dissolution of higher polysulfides (Li_2S_x; $8 \geq x \geq 4$, discharge intermediates) in the electrolytes and subsequent deposition of insulating Li_2S_2 and Li_2S on either electrode surfaces due to shuttling results in increased cell resistance (impeded ionic accessibility, lowering of electrode conductivity etc.), loss of active mass and lower Coulombic efficiency.(*13-17*) Such insulating deposits along with insulating nature of sulfur (5×10^{-28} S m^{-1}) can severely influence reaction kinetics at the interfaces and active mass utilization thereby influencing battery performance.(*18, 19*) Therefore several strategies have been implemented, aimed at enhancing the cyclability of Li-S batteries by trapping polysulfides intermediates and maximizing sulfur utilization using conductive matrices (such as carbons),(*20*) which form enhanced carbon-sulfur interfaces thereby increasing overall conductivity of the cathode. Although composites incorporating Al_2O_3, SiO_2, SnO_2 etc. have been used to trap polysulfides using ionic interactions but the gain is offset by their lower energy density and low electronic conductivity.(*21, 22*) Therefore, major work has focused upon plethora of carbon based framework, invoking different architectures to address above issues.(*21*) Except for a few reports, it was invariably observed that systems with high specific energy and enhanced cyclability is usually associated with low sulfur loadings(*23*) which again would penalize volumetric as well as gravimetric energy density of the overall cathode. Another important hurdle to the development of effective hosts for Li-S system is associated with the huge volumetric expansion (~80 %) due to the conversion of S_8 to Li_2S.(*24*) Henceforth, any cathode design must accommodate above mentioned volumetric changes. Additionally, the cathode material should have high sulfur loading and

the textural properties of the host must synergistically allow for maximum S utilization thereby enhancing capacity even after prolonged cycle life. Most of the carbon based cathode designs indicate towards the beneficial roles of balanced pore architectures (micro/mesoporous).(*21, 25, 26*)

Additionally, the poor abundance of Li(*27*) has stimulated the development of alternative energy systems based on Na-S couple due to similar chemistries compared to Li-S based systems. Na is earth abundant and combination with sulfur (S) is going to make Na-S batteries even cheaper compared to Li-S battery.(*28*) Na-S systems operating at elevated temperatures (~300 ^{O}C) have been commercialized nearly a decade ago and recently published reports also discuss about the reversible redox Na-S batteries at high temperatures (~150 ^{O}C) using conventional liquid electrolytes.(*29, 30*) These reports employ porous/hollow carbon as the sulfur confining host and also use specific cell configurations for achieving optimal electrochemical performance. Thus, the challenge now is to develop a high specific energy Na-S battery functioning at room temperature and at intermediate temperatures (~100 ^{O}C).(*30, 31*) To the best of our knowledge, there are very few reports so far which solely focuses upon room temperature operation of Na-S batteries very similar to that of Li-S batteries.(*32*) The problems associated with room temperature Na-S battery are anticipated to be very similar to that of Li-S battery. Here too, the design of structured porous hosts, which can efficiently trap sulfur and the sodium-polysulfides during successive discharge-charge processes needs to be devised. The host should be so designed that it can accommodate severe volume expansion without affecting the integrity of its structure. Although carbon-based hosts have not been much explored for Na-S systems, the implications are much more severe for such batteries as the full sodiation of sulfur (Na_2S) involves a much higher volume expansion.(*33, 34*) Flexible carbon framework with high SSA, interconnected hierarchical porous structure along with enhanced pore volume would be ideal for accommodating large volume changes associated with such battery systems. Advance designs pertaining to microscopic as well as mesoscopic textural engineering is crucial to the development of new carbon-based cathodes with stable performance.

3.2 Scope of the present investigation:

Hierarchical pore architecture of the nanostructured carbon (mesopores) would ensure easy electrolyte access at active interfaces allowing faster Li/Na-ion/electrolyte transport assisting in rapid redox reactions.(*35, 36*) The presence

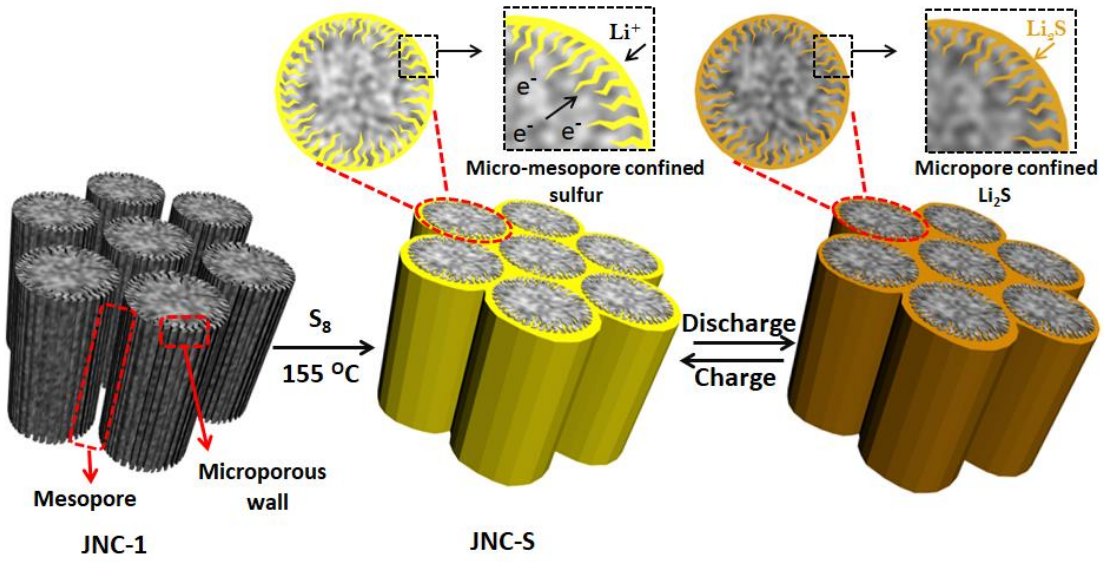

Scheme 1. Schematic illustrating the incorporation of S inside JNC-1 to form JNC-S composite via melt-diffusion strategy. Hierarchical ordered micro-mesoporous architecture of the host (JNC-1) aid in facile Li^+ ion/electrolyte transport across the interface leading to efficient reversible electrochemistry of Li-S systems whereas, micropores modulate S/polysulfide flux via advantageous entrapment of the lithiated sulfide intermediates.

of abundant micropores (situated inside mesoporous walls where active interface actually exists) would complement mesopores in trapping polysulfides formed at the genesis site thus ensuring minimal polysulfide transport once it is formed. Such sorption property of micropores could be attributed to the stronger overlap of the adsorbent-adsorbate interaction potentials of the opposite walls in the confined spaces (<2 nm) thereby increasing the energy barrier for polysulfide dissolution in the electrolyte and hence mitigate sulfur dissolution.(*23, 25, 37*) It may be noted that existence of micropores alone would impede ion transport (Li^+/Na^+) resulting in poor mass utilization which in turn affects the rate capability performance.(*38-40*) Furthermore, it must be noted that the previous carbon-based cathodes are purely microporous or mesoporous carbons (or both), usually resulted in lower sulfur loading except in few cases which would severely lower energy density and volumetric capacity.(*23, 41*) Wider mesopores would lack enhanced intimate S interfaces compared to micropores therefore, the reaction would only take place at the periphery leading to poor mass utilization.(*42*) Therefore it is highly desirable to engineer such carbons which could address all the pertinent issues related mass utilization and volume expansion with intricately balanced textural properties.

Herein, we report a high surface area (2545 m^2 g^{-1}) hierarchical (micro-mesopore) carbon (JNC-1)-sulfur based composite (JNC-S) as active cathode material for Li-S/Na-S battery application.(*43*) **Scheme 1** illustrates the synthetic strategy implemented to synthesize JNC-S composite based cathode, wherein melt induced diffusion strategy was implemented to incorporate S into JNC-1.(*44*) As shown in the scheme, such hierarchical structures by virtue of their high pore volume (~1.9 cc g^{-1}) ensures higher sulfur loading (~70 wt. %) while high surface area with abundant micropores (~40 %; 0.9 nm) warrants enhanced electrically conducting intimate C-S interface formation assisting in higher mass utilization. It is to be noted that the sulfur loading is being equally complemented by large interfaces existing in JNC-1(2545 m^2g^{-1}) leading the diffusional arrest of polysulfides at the microporous sites. The hierarchical framework is expected to provide facile charge transport pathways across active boundaries through carbon rods (**Scheme 1**) leading to superior utilization of active material which again is being aided by the unhindered Li^+/Na^+ ion transport (mesopores) at the electrodics resulting in superior kinetics.

The presence of pores of varying length scales is expected to generate potential energy landscapes with varying well depths, acting as efficient polysulfide traps.(*37*) Thus, uniquely designed framework, formed by template inversion method is beneficial in coping up with the volumetric changes associated with the conversion of S_8 to Li_2S or Na_xS (formation of Na_2S depends on the lower cut-off of the discharge voltage). Additionally, carbon matrix can well accommodate for volume expansion during the discharging process due to its flexible framework/structures. All these benefits make the host JNC-1 highly promising material for application as S-cathode in Li-S and Na-S rechargeable batteries.

3.3 Experimental procedures:

3.3.1 Materials used:

Sulfur (assay ≥ 99.5%) was procured from Sigma-Aldrich and was purified by sublimation twice before use. Lithium bis(trifluoromethanesulfone)imide (LiTFSI, ~99%), 1,3-dioxolane (DOL, ~99%), cyclopentanone (99%) and 1,2-dimethoxyethane (DME, ~99%) were obtained from Sigma-Aldrich and was used as received. The conductive carbon paint was obtained from Bare Conductive Ltd. Sulphuric acid and sucrose was acquired from Merck and sucrose was purchased from Sigma-Aldrich.

3.3.2 Instrumentation and characterization techniques:

The powder X-ray diffraction (PXRD) patterns were collected on PANalytical diffractometer using Cu Kα radiation, (λ = 1.542 Å). Transmission electron microscopic (TEM) and the energy filtered TEM (EFTEM) images were acquired using the FEI Titan3^{TM} 80−300 microscope (300 kV) equipped with an image aberration corrector. Field emission scanning electron microscopic (FESEM) images of the samples were obtained on Nova-Nano SEM-600 (FEI, Netherlands). The Raman spectra were recorded on a Renishaw Micro-Raman 2000 Spectrometer via Horiba LabRAM HR implementing diode pumped solid state laser excitation (wavelength = 532 nm) with a beam spot size of about 2 μm. Gas sorption analyses were performed using ultrahigh pure N_2 (99.9995%) on Autosorb-iQ_2 (Quantachrome corp.). Prior to analyses, the samples were degassed at 150 ^{O}C under vacuum for 24 h. BET (Brunauer-Emmett-Teller) specific surface area was calculated by taking into account certain criteria suggested by Rouqureal et al. Micropore surface area was determined by the t-plot method. Pore size distributions were obtained using QSDFT/NLDFT method. The thermogravimetric analysis (TGA) was performed on Perkin Elmer Pyris 6000 by heating the samples from room temperature to 700 ^{O}C at 5 ^{O}C/min under N_2 atmosphere. X-ray photoelectron spectroscopic (XPS) data were recorded on an AXIS-Ultra instrument from Kratos using monochromatic Al Kα radiation (225 W, 15 mA, 15 kV). Conducting carbon painting on one side of the aluminum foil current collector was accomplished by using Elcometer Doctor Blade Film Applicator 4340. The galvanostatic charge/discharge (CC) cycling were performed on an Arbin Instrument (Model BT 2000) Corp., USA at different C-rates in the voltage range of 1.3–3.0 V (versus Li^+/Li) for S. Temperature dependent cell cycling was done by inserting the Swagelok^{TM} cell in an environmental chamber (Kaleidoscope Climatic Solutions, Bengaluru) for the temperature control, while cell cycling was done using Arbin Instrument.

3.3.3 Synthesis of JNC-1:

JNC-1 has been synthesized according to the procedure reported in the previous chapter.(*43*)

3.3.4 Synthesis of S encapsulated JNC-1(JNC-S):

Sulfur encapsulation in JNC-1 was carried out by pressure induced melt diffusion strategy. Doubly sublimed sulfur was thoroughly grounded with previously degassed JNC-1 in the weight ratio of 10:1. Thereafter, the mixture

was loaded onto a glass boat (volume = 1.62 cm^3) and was placed inside a quartz tube and subsequently evacuated using a suction pump (min. pressure: 1 × 10^{-3} mbar, Hind High Vacuum (P) Ltd.) for at least 30 min. Afterwards, the tube containing the mixture was slowly put inside the tube furnace preheated to 155 ^{O}C where sulfur melts and diffuses into the pores of JNC-1. After about 30 min, the vacuum is released by passing N_2 into the tube and the process is continued for 3 more times followed by cooling. This step ensures thorough filling of liquid sulfur into the micro-mesopores of JNC-1, which upon cooling is entrapped in the various stable as well as metastable sulfur phases causing efficient confinement. The composite thus obtained was thoroughly washed with toluene in order to remove the excess sulfur deposited over the particles to obtain JNC-S. For comparison, a physical mixture of JNC-1 with sublimed sulfur was also prepared by grinding them intimately and was abbreviated as JNC-S-PM.

3.3.5 Electrochemical cell assembly:

Electrochemical stability and lithium/sodium battery performance were tested using Swagelok^{TM} half-cells with lithium foil (Aldrich)/sodium coin (Aldrich) as a counter and reference electrode respectively. Whatman glass fiber was used as a separator and 1 M Lithium bis(trifluoromethanesulfonyl)imide (LiTFSI) in DOL:DME (1:1 v/v) and 1 M $NaPF_6$ in DOL:DME (1:1 v/v) was used as an electrolyte for evaluating Li-S and Na-S battery performance respectively. The electrochemical measurements were carried out by preparing a slurry of the active materials (e.g. JNC-S and JNC-S-PM) with acetylene carbon black (Alfa Aesar) and polyvinylidene fluoride (PVDF, Kynar Flex) in a weight ratio of 80:10:10 in cyclopentanone and casting it on a carbon-coated Al foil. The carbon coated aluminum foil was prepared by putting conductive carbon paint (Bare Conductive Ltd.) and dried in open air for 24 h. The areal loading of S in the Swagelok^{TM} cell is ~5 mg cm^{-2}. All cell assembly was done at 25 ^{O}C in a glove box (MBraun) under Ar (H_2O < 0.5 ppm, O_2 < 0.5 ppm). About 120 µL of 1 M LiTFSI in DOL:DME (1:1 by volume) and 70 µL of 1 M $NaPF_6$ in DOL:DME (1:1 by volume) was used in the Li-S and Na-S cell assembly respectively, for similar electrode loading. A thinner Whatman separator (0.5 mm) was used in the fabrication of Na-S cell assembly. For the temperature dependent study, the Na-S cell was exposed to step-by-step temperature variation from room temperature to 70 ^{O}C in a humidity-temperature controllable chamber. Humidity was fixed at 75% throughout the measurement.

3.4 Results and discussions:

The presence of low-angle peaks in the powder X-ray diffraction (PXRD) pattern **(Figure 1a)** indicates mesostructural ordering in JNC-1 with *p6mm* honeycomb lattice symmetry. Wide-angle PXRD pattern of the host shows two broad humps centered at 23^{O} and 44^{O} (2θ) **(Figure 1b)** reflecting its amorphous nature. Encapsulation of S inside JNC-1 does not change the crystallinity of the former and the peaks in PXRD pattern in JNC-S match with that of S and can be attributed to alpha-octa sulphur (JCPDS No. 00-024-0733) phase **(Figure 1b)**. Furthermore, the presence of the crystalline state of the sulfur inside the porous host was additionally confirmed by Raman spectroscopy. The characteristic stretching (473 cm^{-1}) and bending (212 cm^{-1}) vibrations modes **(Figure 2a)** observed for crystalline S are however highly diminished in JNC-S. The appearance of new stretching (457 cm^{-1}) and bending bands (a doublet at 248 cm^{-1} and 267 cm^{-1}) strongly suggests that sulfur resides in an alternative form inside the micropores of JNC-1. The generation of newer bands can be attributed to the existence of diradical polymeric sulfur chains which are formed during S incorporation inside the host and are trapped by the micropores.(*45*) However, S remains in its native crystalline state in the mesopores.(*46*) Raman spectra of JNC-1 **(Figure 2b)** shows typical G and D band characteristic of carbon materials with the intensity of D band greater than that of the former further confirming the disordered nature of the pore walls and matches well with the PXRD data **(Figure 1b)**. It is highly probable that inside the mesoporous of JNC-1, the metastable linear diradical polymeric chain slowly

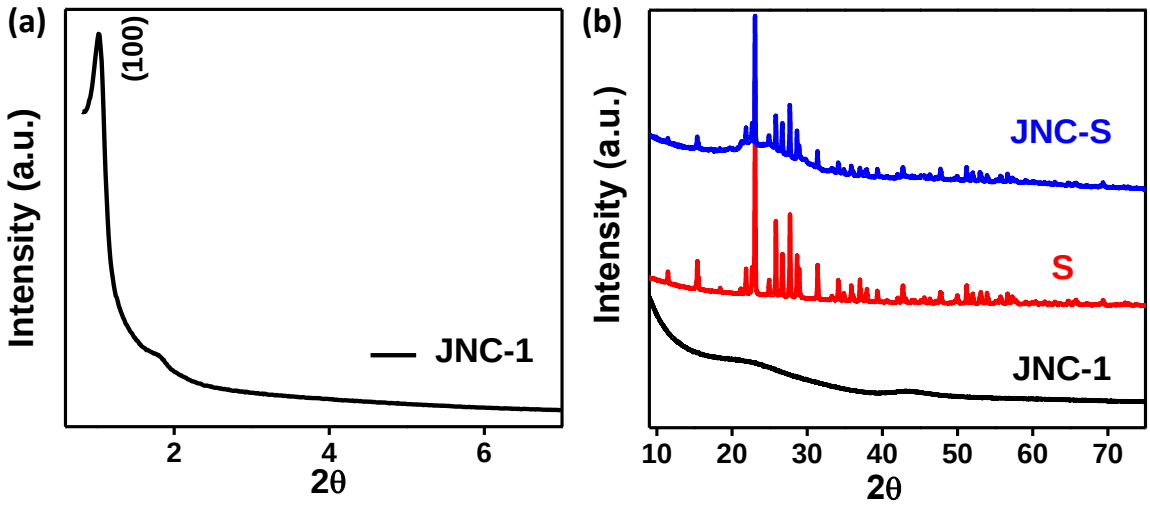

Figure 1. (a) Low-angle PXRD pattern of JNC-1 whereas (b) shows wide-angle PXRD patterns of JNC-1, S and sulfur encapsulated JNC-1 (JNC-S).

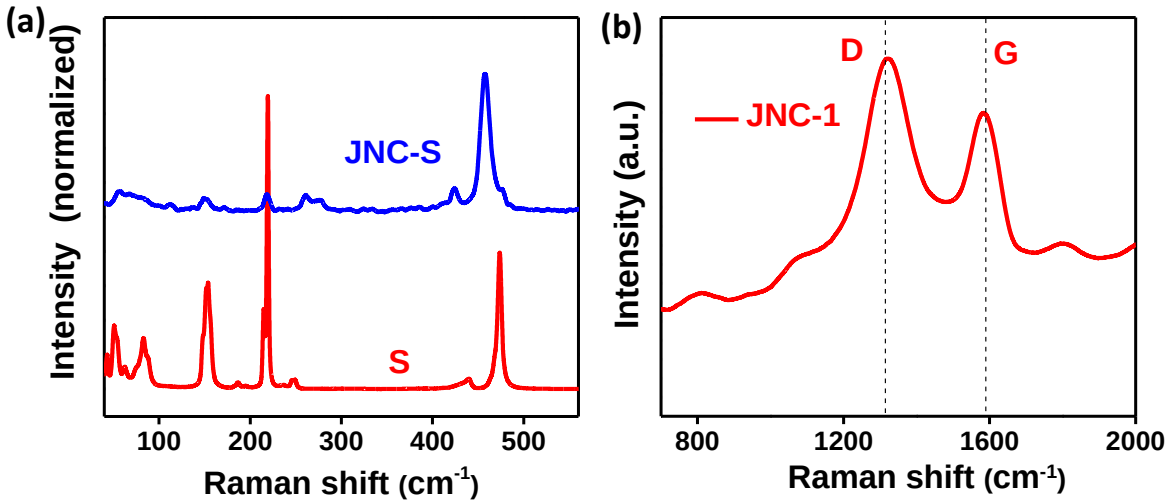

Figure 2. (a) Raman Spectra of S, JNC-S and (b) JNC-1.

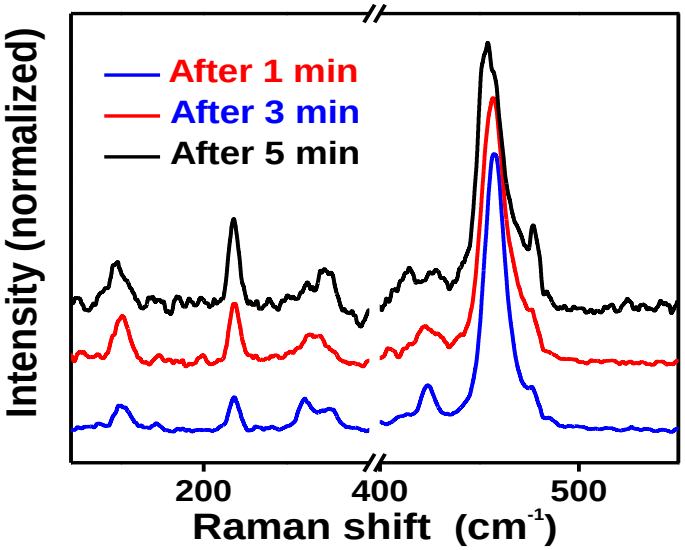

Figure 3. Raman spectra of JNC-S showing the gradual conversion of polymeric chains to stable S_8 forms with time.

converts to stable S_8 form, especially when exposed to the laser beam during Raman measurements.(*47, 48*) **Figure 3** clearly shows the gradual decrease in the intensity of the principle band of JNC-S at 457 cm^{-1} with time while the intensities of the Raman bands corresponding to S_8 slowly increases. This indicates that the unique structure of the host provides ample space for S to undergo a wide range of configurational changes. This is also beneficial to accommodate the volume expansion of sulfur upon complete reduction to Li_2S/Na_2S during battery cycling.

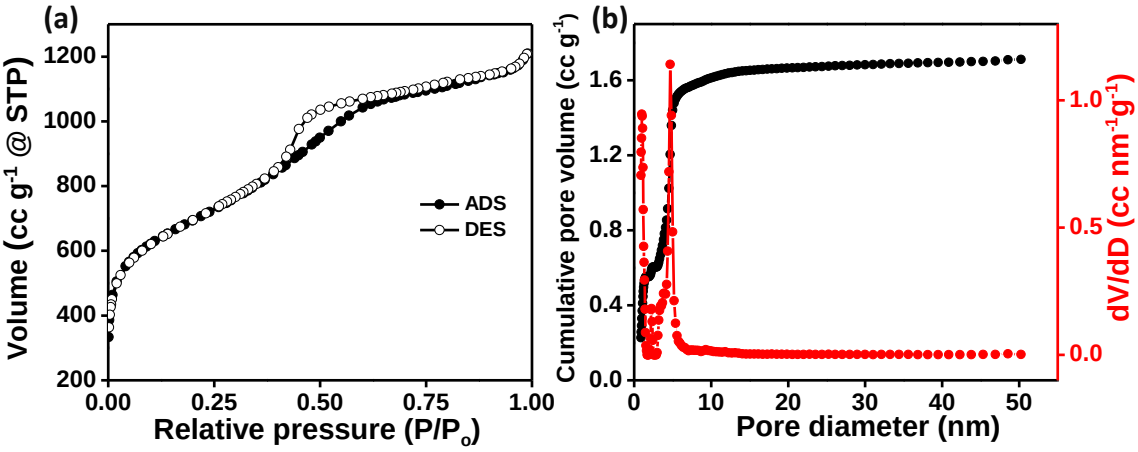

Figure 4. (a) N_2 adsorption-desorption isotherms of JNC-1. (b) Pores size distribution of JNC-1 along with cumulative uptake (calculated using QSDFT method).

N_2 sorption experiments carried out at 77 K in order to evaluate the textural parameters of JNC-1, exhibited type IV behavior with H2 type hysteresis **(Figure 4)**. Surface area calculated by the method as suggested by Rouquerol et al. was found to be around 2545 m^2 g^{-1} and t-plot analyses reveal the microporous surface area ~1012 m^2 g^{-1}. QSDFT indicate a bimodal pore size distribution for JNC-1 centered at 4.7 nm (mesopores) and 0.9 nm (micropores) **(Figure 4)**. The pore volume of JNC-1 was found to be around 1.84 cc g^{-1}.

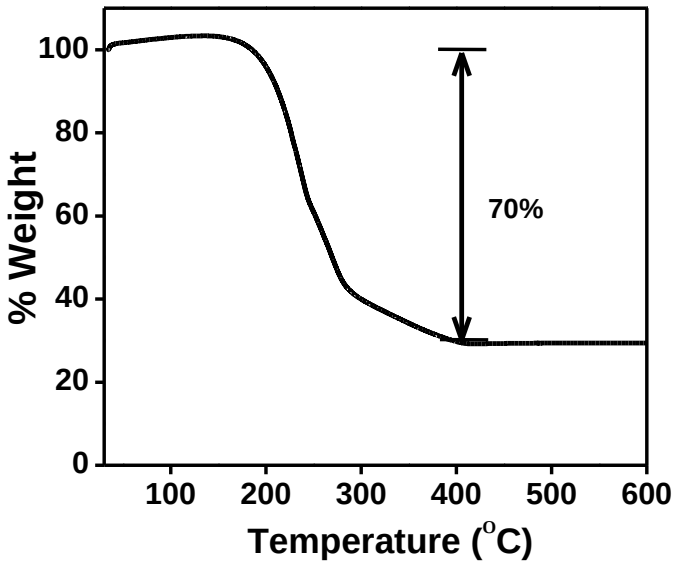

Figure 5. TGA of JNC-S.

Thermogravimetric analyses (TGA) shows a high loading of S (~71%) inside JNC-1 **(Figure 5)** reflecting the effectiveness of systematic pressure-regulated melt diffusion strategy to encapsulate sulfur. Assuming the density of sulphur to

be ~2.0 g cc^{-1}; therefore theoretically JNC-S can accommodate about 3.68 g of sulfur which corresponds to about 79 % of the total mass of sulphur which corroborates well with the TGA data. Step-wise weight loss in TGA **(Figure 5)** indicates the existence of various stable as well as metastable states of S in the hierarchical porous host (JNC-1). Furthermore, X-ray photoelectron spectroscopic data shows a doublet at 163.8 eV and 164.8 eV corresponding to that of S in JNC-S indicating that encapsulation does not change the oxidation state of the sulfur **(Figure 6)**.

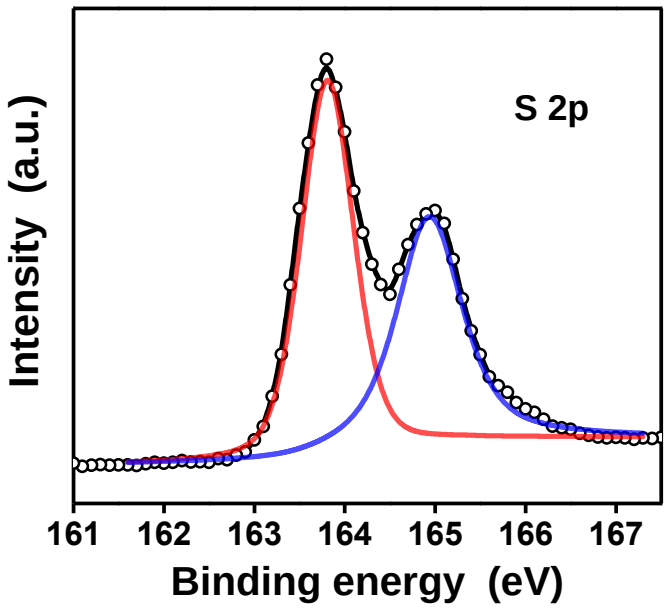

Figure 6. XPS spectrum of S 2p in JNC-S.

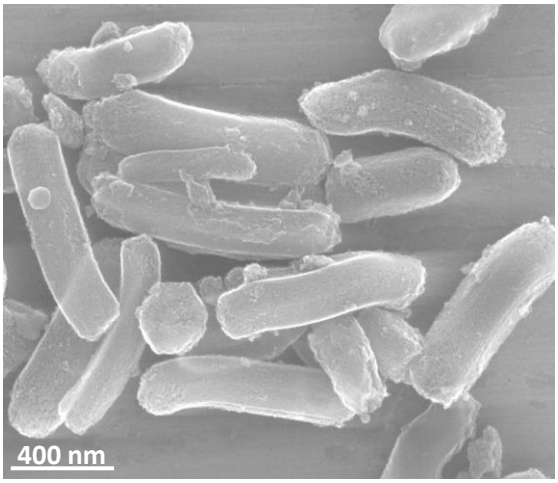

Figure 7. FESEM image of JNC-1 indicating faithful morphological replication of parent SBA-15.

The Field emission scanning electron microscopic (FESEM) image **(Figure 7)** of JNC-1 indicates rod-shaped morphology which is similar to that of parent SBA-15 indicating faithful morphological replication of the template. The

spectroscopic findings of the JNC-S were further confirmed by the transmission electron microscopic (TEM) analyses as discussed below **(Figure 8)**. Transmission electron microscopy (TEM) image of JNC-1 **(Figure 8a)** indicates typical rod-shaped morphology similar to that of parent SBA-15 whereas HRTEM image **(inset of Figure 8a)** of the same shows intact parallel mesopore channels of diameter ~4.7 nm which matches well with N_2 sorption data. Also, it reveals that the walls of the SBA-15 have become pores for JNC-1; a consequence of inverse replication strategy **(inset of Figure 9a)**. Although well-aligned mesochannels can be easily seen in the above **(Figure 8a)** it is difficult to visualize the micropores in TEM. However, the presence of micropores is proved by N_2 sorption measurements **(Figure 4)**. Micropores exists inside the

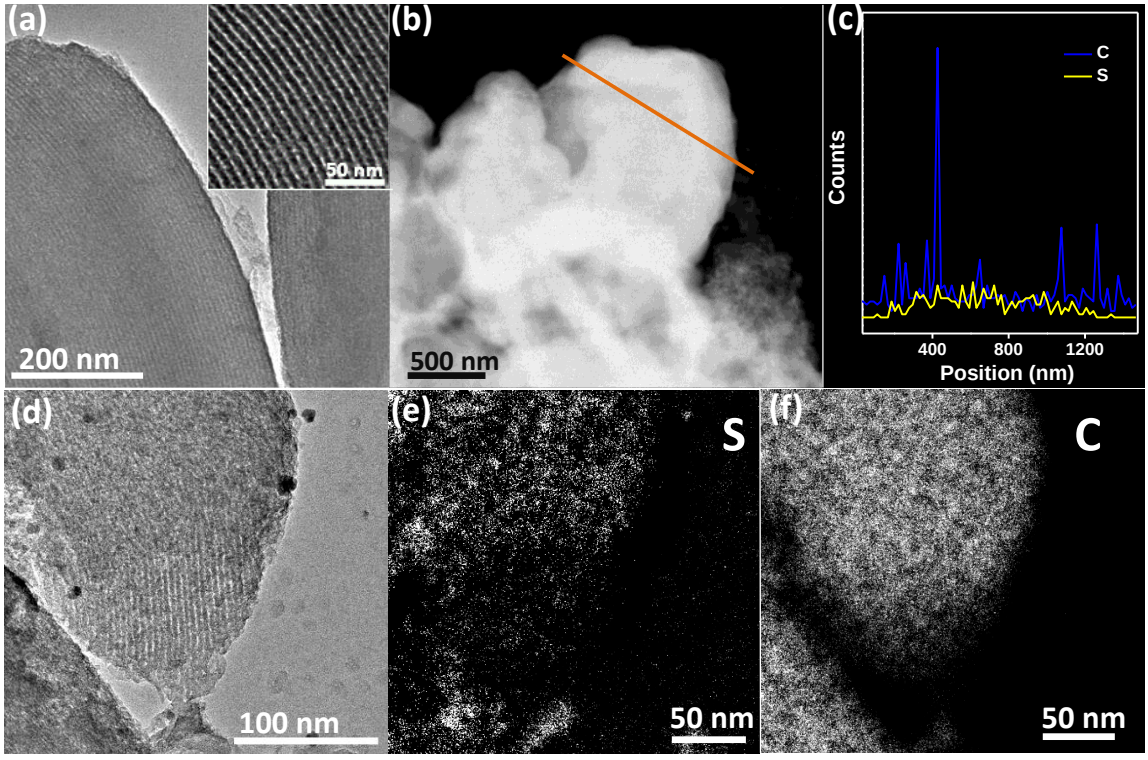

Figure 8. (a) TEM image of JNC-1 (inset shows HRTEM image of JNC-1 indicating well-aligned mesochannels). (b) Scanning transmission electron microscopic (STEM) image of JNC-S and corresponding (c) EDS intensity profiles of C and S along the line shown in (b). (d) Bright-field (zero loss) TEM image of JNC-S and corresponding energy filtered TEM (EFTEM) images showing the uniform dispersion of sulfur (e) in carbon (f).

carbon walls which form the aligned mesopores in JNC-1. This unique hierarchical architecture helps in easy access to the micropores via mesopores and has been utilized to capture polysulfides while maintaining an optimum

electrolyte transport throughout the system. Further, to prove the encapsulation of sulfur inside the hierarchical pores rather than S existing as independent particles, a detailed TEM analysis was carried out on JNC-S. Low contrast difference between S and C forbids the speculation of S in bright field TEM images. Therefore, scanning transmission electron microscopy (STEM) image **(Figure 8b)** of JNC-S was obtained and corresponding energy dispersive X-ray spectroscopic (EDS) intensity profiles of C and S along the line shown in (b) is depicted in **Figure 8c**. Clearly, **Figure 8c** shows uniform dispersion of S in JNC-1 and the intensity profile reveals the precise confinement of sulphur. Above results were further corroborated by the bright field (zero loss) image **(Figure 8d)** of JNC-S and corresponding energy filtered TEM (EFTEM) images **(Figure 8e-f)**. **Figure 8e-f** reveal the unique dispersing ability of the carbon (JNC-1) towards S and precise entrapment of the latter in the former and matches well with EDS data **(Figure 8c)**.

Cyclic voltammograms (CVs) of JNC-S shows double cathodic (reduction) peaks at 1.90 V and 2.25 V and a single broad anodic (oxidation) peak at 2.60 V **(Figure 9a)**. The repeated occurrence of these peaks at the same position with almost similar current responses is indicative of excellent reversibility of JNC-S cathode. The anodic and cathodic peaks in the CV match well with the galvanostatic charge and discharge curves. The plateaus at 2.35 V and 2.00 V in the discharge curve **(Figure 9b)** indicates a two-step sequential conversion mechanism wherein sulfur (S_8) first converts to long chain soluble polysulfides (S_8-S_4^{2-}) followed by the formation of lower order insoluble polysulfides/sulfides such as Li_2S_2 to Li_2S (2.00 V). The latter step is kinetically slow and involves maximum lithiation per S atom thereby contributing maximum toward specific capacity. However, the reverse process of conversion of Li_2S to S_8 occurs in a single step at a voltage plateau of 2.6 V. The galvanostatic discharge-charge profile **(Figure 9c)** for JNC-S shows a very stable battery cycling performance with capacity retention of 830 mAh g^{-1} at the end of 100 cycles at a current rate of 0.2 C. From the first cycle discharge capacity of 1514 mA h g^{-1}, the capacity drops to 986 mA h g^{-1} at the 15^{th} cycle followed by further decrease in capacity at a slower rate to 830 mA h g^{-1} at the end of 100 cycles. The capacity retention is 68% till the 10^{th} cycle followed by an increase to 84% at the 50^{th} cycle finally reaching 95% at the end of 100 cycles (at a high current rate of 0.2 C). The battery cycling at a lower current rate of 0.1 C is also tested which shows a similar trend with higher capacity retention at the end of the 100^{th} cycle retaining a stable capacity of 950 mA h g^{-1}. The gradual capacity drop can be

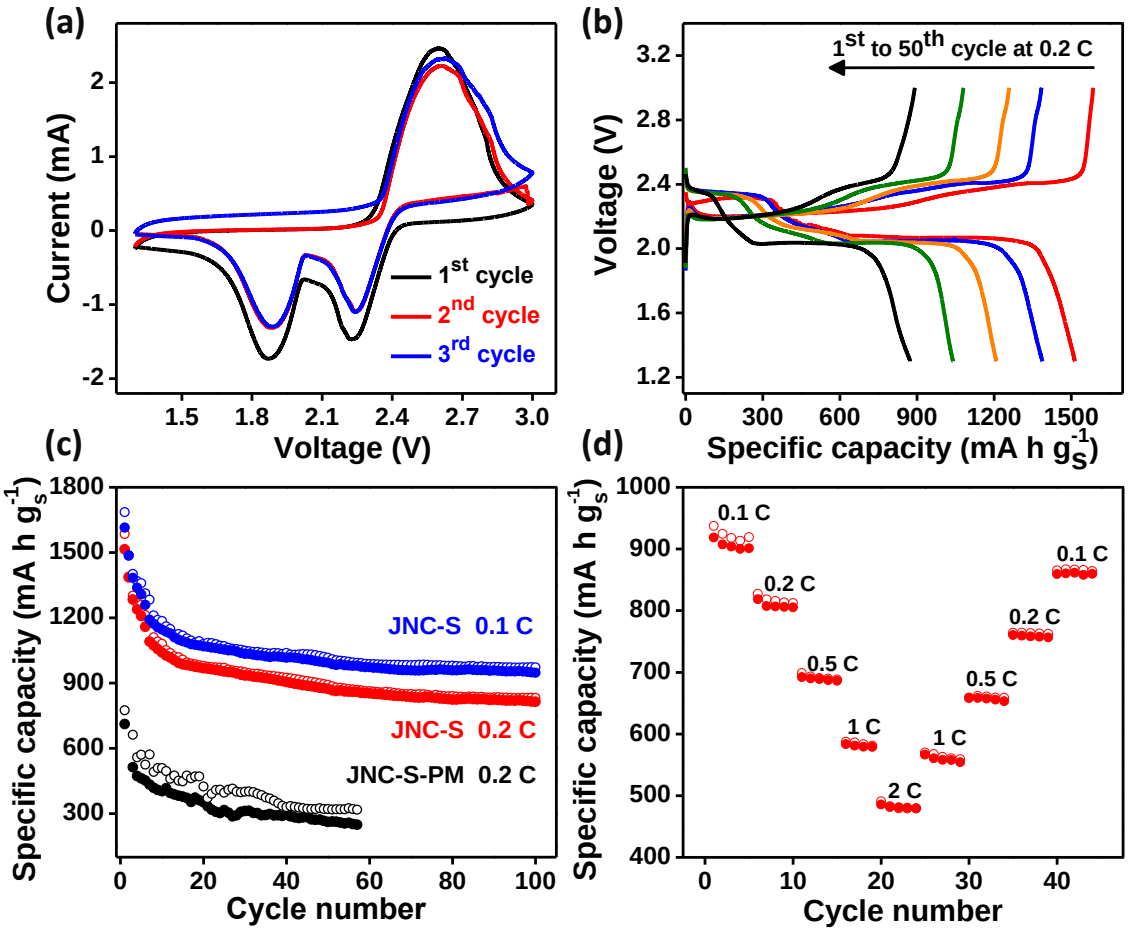

Figure 9. (a) Cyclic voltammograms and (b) voltage vs. specific capacity plot (at 0.2 C) of JNC-S. (c) Galvanostatic discharge-charge profiles for JNC-S and JNC-S-PM at different drain rates. (d) Shows rate capability performance of JNC-S. (Note: specific capacities are calculated based on mass of S only).

primarily attributed to some loss of (excess) polysulfide from JNC-1. The polysulfides are formed both inside the micro and mesoporous channels which possesses energy landscapes with potential wells of varying depths. As the polysulfides attempt to escape from the mesopores, where it is predominant, the unique architecture of the host compels the leaching out polysulfides to move into micropores assisted by the electrolyte. The entry of polysulfides in the micropores results in trapping of the polysulfides in even deeper wells leading to complete entrapment.(*49*) The polysulfide flux from mesopore into micropores may expel the excess sulfur which mostly gets trapped into the micropores during the S-cathode synthesis. The micropore confined polysulfide, which is more exposed to the electrolyte, gets liberated into the electrolyte thus leading to the initial loss of capacity. A state of saturation is reached when all excess polysulfide has been liberated. Following the release of the excess polysulfide (in

the 1st 10 cycles), the capacity of JNC-S gradually stabilizes leading to a stable capacity over 100 cycles. In this work, the sorption properties of the pure carbonaceous micro and mesoporous host have been utilized extensively to trap the polysulfide. The absence of heteroatoms completely rules out the possibility of polysulfide anchoring by bonding interactions with the heteroatoms. It is important to note that JNC-S exhibits excellent cycling at a higher extent of sulfur content (~70%) and high mass loading on the electrode (~5 mg cm^{-2}) compared to some of the work discussed in the literature.(*50-52*) To further ascertain the beneficial role of hierarchical pores in polysulfide trapping, the electrochemical performance of the physical mixture of JNC-1 with sulfur, denoted as JNC-S-PM, was also evaluated. Needless to mention the Li-S performance of JNC-S-PM is much inferior compared to JNC-S as shown in **Figure 9c**. The cell with JNC-S-PM shows a very low capacity of approximately 200 mA h g^{-1} at the end of the 60th cycle at a current rate of 0.1 C. **Figure 9d** shows excellent rate capability performance of JNC-S. The discharge capacities are found to be 910 mA h g^{-1}, 805 mA h g^{-1}, 686 mA h g^{-1}, 580 mA h g^{-1} and 470 mA h g^{-1} at the current rates of 0.1 C, 0.2 C, 0.5 C, 1 C and 2 C respectively. By decreasing the current back to 0.1 C, the cell exhibits a capacity of 860 mA h g^{-1} which is in close to that of the capacity obtained at similar drain rate (0.1 C) prior to ramping up of the current.

Owing to the superior performance of JNC-S versus Li, we explored the possibility of employing the JNC-S as cathode against Na. Our main aim here was to explore and demonstrate a Na-S rechargeable battery operating at room and intermediate temperatures (<100 ^{O}C). **Figure 10a** shows the electrochemical performance of JNC-S against Na. The redox peaks for both cathodic and anodic reactions in case of Na-S battery are well reported in the literature.(*34*) The cathodic reaction of Na with S is similar to that of Li i.e. S_8 converts to Na_2S_x at a voltage of 2.2 V followed by Na_2S_x to Na_2S_2 at a voltage of 1.7 V **(Figure 10a)**. Unlike Li-S, the anodic process in Na-S systems occurs in two steps viz. from Na_2S_2 to Na_2S_x at a potential of 1.8 V followed by, Na_2S_x to S_8 at a potential of 2.2 V.(*34*) The complete conversion from Na_2S_2 to Na_2S was not observed as the process occurs at a much lower voltage (0.8 V). Additionally, this may have a detrimental effect on the reversibility and stability of such systems.(*53*) The cathodic and anodic processes of Na-S battery **(Figure 10a)** correspond well with the galvanostatic charge-discharge profiles; as shown in **Figure 10b**. In spite of the modest capacities of JNC-S versus Na, it is quite remarkable to observe the stable cyclability of Na-S battery over 100 cycles

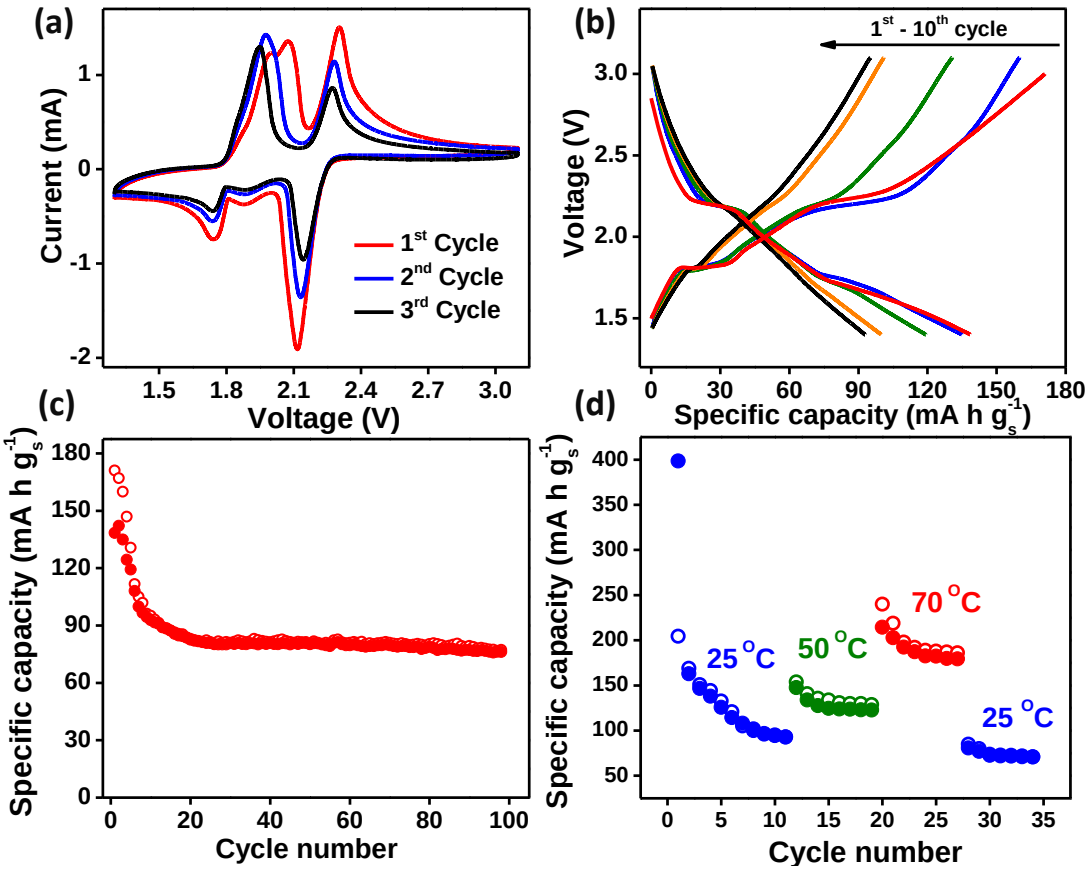

Figure 10. (a) Cyclic voltammograms and (b) voltage vs. specific capacity plot (at 0.05 C) of JNC-S vs. Na. (c) Galvanostatic discharge-charge (CC) profiles at room temperatures and (d) temperature dependent CC performance for JNC-S. Shows rate capability performance of JNC-S. (Note: specific capacities are calculated based on the mass of S only).

(Figure 10c). To the best of our knowledge, this is probably the first time an attempt towards the demonstration of a rechargeable Na-S battery at room temperature has been undertaken. The charge-discharge profiles exhibit two plateaus appearing at 1.7 V and 2.1 V during discharge along with the two charging plateaus at 1.85 V and 2.2 V which correspond well with the CV results **(Figure 10a)**. However, the first discharge capacity is an order lower than the theoretical value **(Figure 10b)**. This is attributed to the fact that the cell is cycled to only 1.25 V which prevents the complete conversion of S_8 to Na_2S. Na-S cell can be actually discharged to the maximum extent where Na_2S forms at a much lower voltage of 0.8 V. However, this has been intentionally avoided due to massive volume expansion of 260% during the formation of Na_2S.(*34, 53*) We strongly feel that the simple battery configuration employed here, which is similar to that of the Li-S battery, is insufficient for operation at such low voltages and also at elevated temperatures. Special cell configurations

reported in the literature, especially those employed for operation at elevated temperatures may be a possibility for the completion of the reversible reaction $S_8 \rightleftharpoons Na_2S$ and eventually achieving higher capacities.(*29, 54-58*) Several works exhibit complicated electrolyte designs to capture and restrict polysulfides in Na-S batteries.(*59*) However, as this is not the focus of the present work, so no strategy towards optimization of the cell configuration was attempted here. The specific capacity versus cycle number curve shows nearly stable cycling behavior with a specific capacity of 80 mA h g^{-1} over 100 cycles. The low specific capacity of JNC-S against Na can also be partially attributed to the low ionic mobility of Na and massive volume expansion (~170%) associated with the Na_2S_x formation. The intermediate Na_2S_x and polysulfide tend to form a solid precipitate at room temperature and hence may further reduce the capacity. The battery cycling data for the physical mixture of JNC-1 with sulfur (abbreviated as JNC-S-PM), exhibits inferior cycling behavior as shown **Figure 11**.

To study the effect of operating temperature on the cyclability, the assembled cell Na/1 M $NaPF_6$ DOL-DME (1:1 v/v)/JNC-S was subjected to a temperature variation from room temperature to 70 ^{O}C. At approximately 10 successive charge-discharge cycles at a constant temperature, the specific capacities stabilize **(Figure 10d)**. At cycles >10, the specific capacities was observed to increase with an increase in temperature **(Figure 10d and 12)**. The charge-discharge curves, as shown in **Figure 12,** exhibit redox plateaus at nearly similar potentials and are highly reproducible. However, the capacity values gradually decrease from the 1st to the 10th cycle due to the usual sulfur/polysulfide dissolution. The assembled Swagelok^{TM} cell was subjected to a stepwise temperature rise and stabilized at each temperature for 3 h before recording the cycling data **(Figure 13)**. At room temperature, the first discharge capacity was observed to be 400 mA h g^{-1}, followed by a sudden decrease to 163 mA h g^{-1} and finally stabilizing at 93 mA h g^{-1} after 10 cycles (100th cycle capacity = 80 mAh g^{-1}). After stabilizing at 50 ^{O}C, the first discharge capacity increases to about 150 mA h g^{-1} and gradually decreased to 122 mA h g^{-1} after 5 cycles. Finally, as the temperature was raised to 70 ^{O}C, the capacity reaches to 214 mA h g^{-1} indicating that JNC-S has a great possibility to be used as intermediate temperature Na-S battery. After running 8 cycles at a temperature of 70 ^{O}C, the capacity stabilizes at 180 mA h g^{-1}. When the cell was cooled to room temperature, the capacity drops back to 80 mA h g^{-1}, which indicates an

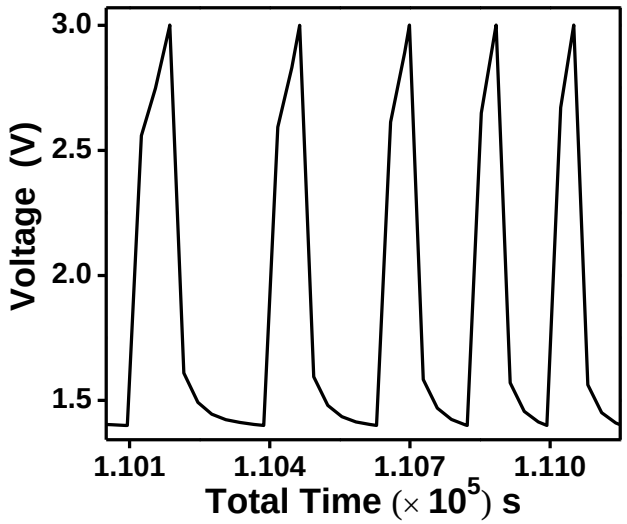

Figure 11. Galvanostatic cycling performance of physical mixture of JNC-S-PM against Na.

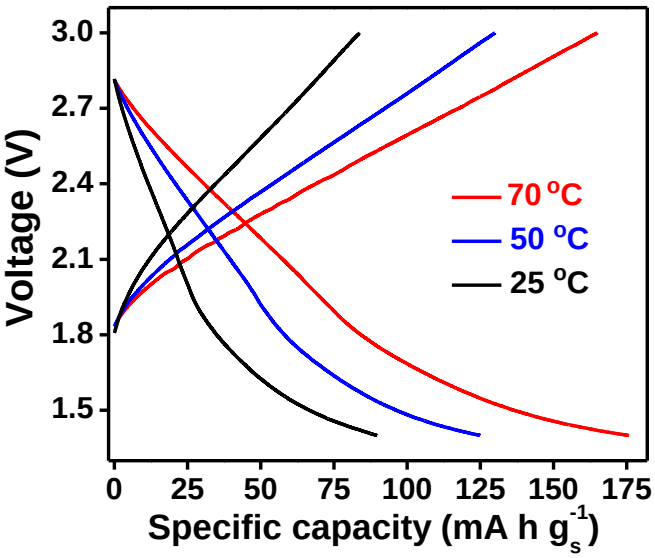

Figure 12. Voltage vs. specific capacity plot of JNC-S against Na at various temperatures (data is shown for the final cycle for each set of temperatures).

influence of temperature on the battery performance. The upper limit of temperature was kept at 70 ^{O}C, as beyond this temperature the cell performance is observed to degrade drastically in this simple cell configuration. As discussed earlier, no strategies towards optimization of the cell configuration, which includes special S-cathode:current collector assemblies and electrolyte compositions, for operation at lower voltages and higher temperatures was attempted here. What is absolutely clear here is that the JNC-S has the potential as S-cathode for operation in the room as well intermediate temperature Na-S batteries.

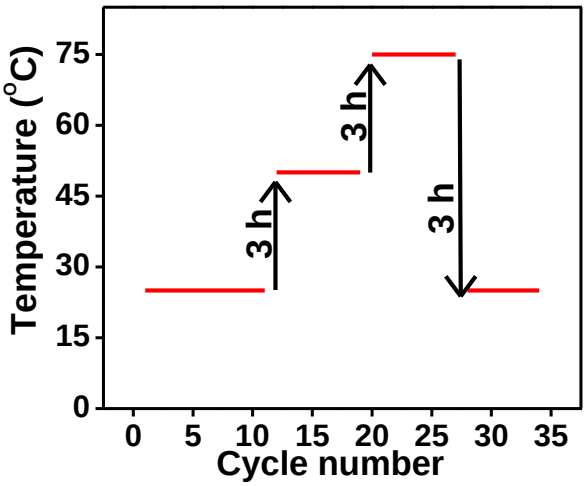

Figure 13. Temperature programme implemented for Na-S measurements.

3.5 Conclusions:

We have shown that JNC-1 carbon, having hierarchical porous architecture coupled with high surface area, performed as cathodic hosts for S leading to superior Li-S battery performance with excellent rate capability and cyclability. The unique interconnected mesoporous-microporous structure of the host provides facile Li-ion/electrolyte transport pathways and simultaneously acts as the high-energetic potential landscape for efficient and effective polysulfide traps thereby modulating S (polysulfide) flux across the cathode. Above cathode material also leads to reasonable intermediate temperature Na-S performance which is contrary to the observed electrochemistry of such systems which are known to perform at elevated temperatures (100-300 ^{O}C). Such strategy opens up newer design principles to develop carbon-based materials for the development of practical S based battery systems.

3.6 References:

1. C. P. Grey, J. M. Tarascon, Sustainability and in situ monitoring in battery development. *Nat. Mater.* **16**, 45 (2017).
2. M. M. Thackeray, C. Wolverton, E. D. Isaacs, Electrical energy storage for transportation-approaching the limits of, and going beyond, lithium-ion batteries. *Energy Environ. Sci.* **5**, 7854 (2012).
3. J. B. Goodenough, K.-S. Park, The Li-Ion Rechargeable Battery: A Perspective. *J. Am. Chem. Soc.* **135**, 1167 (2013).

4. J. B. Goodenough, Y. Kim, Challenges for Rechargeable Li Batteries. *Chem. Mater.* **22**, 587 (2010).
5. P. G. Bruce, S. A. Freunberger, L. J. Hardwick, J. M. Tarascon, Li–O_2 and Li–S batteries with high energy storage. *Nat. Mater.* **11**, 19 (2012).
6. S.-H. Chung, A. Manthiram, Carbonized Eggshell Membrane as a Natural Polysulfide Reservoir for Highly Reversible Li-S Batteries. *Adv. Mater.* **26**, 1360 (2014).
7. G. Kutney, *Sulfur: history, technology, applications & industry*. (ChemTec Publishing, 2007).
8. T. Rauchfuss, Under sulfur's spell. *Nat. Chem.* **3**, 648 (2011).
9. W. J. Chung *et al.*, The use of elemental sulfur as an alternative feedstock for polymeric materials. *Nat. Chem.* **5**, 518 (2013).
10. J. M. Tarascon, M. Armand, Issues and challenges facing rechargeable lithium batteries. *Nature* **414**, 359 (2001).
11. S. Evers, L. F. Nazar, New approaches for high energy density lithium–sulfur battery cathodes. *Acc. Chem. Res.* **46**, 1135 (2013).
12. M. A. Pope, I. A. Aksay, Structural Design of Cathodes for Li-S Batteries. *Adv. Energy Mater.* **5**, 1500124 (2015).
13. K. Kumaresan, Y. Mikhaylik, R. E. White, A Mathematical Model for a Lithium–Sulfur Cell. *J. Electrochem. Soc.* **155**, A576 (August 1, 2008, 2008).
14. Y. Yang, G. Zheng, Y. Cui, Nanostructured sulfur cathodes. *Chem. Soc. Rev.* **42**, 3018 (2013).
15. S. S. Zhang, New insight into liquid electrolyte of rechargeable lithium/sulfur battery. *Electrochim. Acta* **97**, 226 (2013).
16. S. S. Zhang, Liquid electrolyte lithium/sulfur battery: Fundamental chemistry, problems, and solutions. *J. Power Sources* **231**, 153 (2013).
17. Z. Deng *et al.*, Electrochemical Impedance Spectroscopy Study of a Lithium/Sulfur Battery: Modeling and Analysis of Capacity Fading. *J. Electrochem. Soc.* **160**, A553 (January 1, 2013, 2013).
18. Q. Pang, X. Liang, C. Y. Kwok, L. F. Nazar, Advances in lithium–sulfur batteries based on multifunctional cathodes and electrolytes. *Nat. Energy* **1**, 16132 (2016).
19. C. Liang, N. J. Dudney, J. Y. Howe, Hierarchically Structured Sulfur/Carbon Nanocomposite Material for High-Energy Lithium Battery. *Chem. Mater.* **21**, 4724 (2009).
20. X. Ji, K. T. Lee, L. F. Nazar, A highly ordered nanostructured carbon-sulphur cathode for lithium-sulphur batteries. *Nat. Mater.* **8**, 500 (2009).

21. D.-W. Wang *et al.*, Carbon-sulfur composites for Li-S batteries: status and prospects. *J. Mater. Chem. A* **1**, 9382 (2013).
22. N. Jayaprakash, J. Shen, S. S. Moganty, A. Corona, L. A. Archer, Porous Hollow Carbon@Sulfur Composites for High-Power Lithium–Sulfur Batteries. *Angew. Chem. Int. Ed.* **50**, 5904 (2011).
23. Z. Zhang *et al.*, 3D Interconnected Porous Carbon Aerogels as Sulfur Immobilizers for Sulfur Impregnation for Lithium-Sulfur Batteries with High Rate Capability and Cycling Stability. *Adv. Funct. Mater.* **24**, 2500 (2014).
24. Z. W. Seh, Y. Sun, Q. Zhang, Y. Cui, Designing high-energy lithium-sulfur batteries. *Chem. Soc. Rev.* **45**, 5605 (2016).
25. Z. Li *et al.*, A Highly Ordered Meso@Microporous Carbon-Supported Sulfur@Smaller Sulfur Core–Shell Structured Cathode for Li–S Batteries. *ACS Nano* **8**, 9295 (2014).
26. X. L. Ji, K. T. Lee, L. F. Nazar, A highly ordered nanostructured carbon–sulphur cathode for lithium–sulphur batteries. *Nat. Mater.* **8**, 500 (2009).
27. J.-M. Tarascon, Is lithium the new gold? *Nat Chem* **2**, 510 (2010).
28. S. Xin, Y. X. Yin, Y. G. Guo, L. J. Wan, A High-Energy Room-Temperature Sodium-Sulfur Battery. *Adv. Mater.* **26**, 1261 (2014).
29. K. B. Hueso, M. Armand, T. Rojo, High temperature sodium batteries: status, challenges and future trends. *Energy Environ. Sci.* **6**, 734 (2013).
30. T. H. Hwang, D. S. Jung, J.-S. Kim, B. G. Kim, J. W. Choi, One-Dimensional Carbon–Sulfur Composite Fibers for Na–S Rechargeable Batteries Operating at Room Temperature. *Nano Lett.* **13**, 4532 (2013).
31. Y.-X. Wang *et al.*, Achieving High-Performance Room-Temperature Sodium–Sulfur Batteries With S@ Interconnected Mesoporous Carbon Hollow Nanospheres. *J. Am. Chem. Soc.* **138**, 16576 (2016).
32. S. Wei *et al.*, A stable room-temperature sodium–sulfur battery. *Nat. Commun.* **7**, 11722 (2016).
33. P. Adelhelm *et al.*, From lithium to sodium: cell chemistry of room temperature sodium–air and sodium–sulfur batteries. *Beilstein J. Nanotech.* **6**, 1016 (2015).
34. A. Manthiram, X. Yu, Ambient Temperature Sodium–Sulfur Batteries. *Small* **11**, 2108 (2015).
35. H. Sun *et al.*, Three-dimensional holey-graphene/niobia composite architectures for ultrahigh-rate energy storage. *Science* **356**, 599 (2017).

36. C. Hoffmann *et al.*, Nanocasting Hierarchical Carbide-Derived Carbons in Nanostructured Opal Assemblies for High-Performance Cathodes in Lithium–Sulfur Batteries. *ACS Nano* **8**, 12130 (2014).
37. S. Lowell, J. E. Shields, M. A. Thomas, M. Thommes, *Characterization of Porous Solids and Powders: Surface Area, Pore Size and Density*. (Springer Netherlands, 2012).
38. W. Gu, G. Yushin, Review of nanostructured carbon materials for electrochemical capacitor applications: advantages and limitations of activated carbon, carbide-derived carbon, zeolite-templated carbon, carbon aerogels, carbon nanotubes, onion-like carbon, and graphene. *Wiley Interdisciplinary Reviews: Energy and Environment* **3**, 424 (2014).
39. M. Hartmann, Hierarchical Zeolites: A Proven Strategy to Combine Shape Selectivity with Efficient Mass Transport. *Angew. Chem. Int. Ed.* **43**, 5880 (2004).
40. K. Xia, Q. Gao, J. Jiang, J. Hu, Hierarchical porous carbons with controlled micropores and mesopores for supercapacitor electrode materials. *Carbon* **46**, 1718 (2008).
41. F. Sun *et al.*, High Efficiency Immobilization of Sulfur on Nitrogen-Enriched Mesoporous Carbons for Li–S Batteries. *ACS Appl. Mater. Interfaces* **5**, 5630 (2013).
42. S. Xin *et al.*, Smaller Sulfur Molecules Promise Better Lithium–Sulfur Batteries. *J. Am. Chem. Soc.* **134**, 18510 (2012).
43. D. K. Singh, K. S. Krishna, S. Harish, S. Sampath, M. Eswaramoorthy, No More HF: Teflon-Assisted Ultrafast Removal of Silica to Generate High-Surface-Area Mesostructured Carbon for Enhanced CO_2 Capture and Supercapacitor Performance. *Angew. Chem. Int. Ed.* **55**, 2032 (2016).
44. D. Dutta *et al.*, Pressure-Induced Capillary Encapsulation Protocol for Ultrahigh Loading of Sulfur and Selenium Inside Carbon Nanotubes: Application as High Performance Cathode in Li–S/Se Rechargeable Batteries. *J. Phys. Chem. C* **120**, 29011 (2016).
45. K. S. Andrikopoulos, A. G. Kalampounias, O. Falagara, S. N. Yannopoulos, The glassy and supercooled state of elemental sulfur: Vibrational modes, structure metastability, and polymer content. *The J. Chem. Phys.* **139**, 124501 (2013).
46. D. W. Scott, J. P. McCullough, Vibrational assignment and force constants of S8 from a normal-coordinate treatment. *J. Mol. Spectrosc.* **6**, 372 (1961).

47. P. D. Dapkus, C. H. Henry, Degradation of bulk luminescence in GaP : Zn,O induced by laser excitation. *J. Appl. Phys.* **47**, 4061 (1976).
48. J. D. Dow, R. E. Allen, Role of dangling bonds and antisite defects in rapid and gradual III-V laser degradation. *Appl. Phys. Lett.* **41**, 672 (1982).
49. J. Wang, H. Zhou, J. Zhuang, Q. Liu, Influence of spatial configurations on electromagnetic interference shielding of ordered mesoporous carbon/ordered mesoporous silica/silica composites. *Sci. Reports* **3**, 3252 (2013).
50. W. Li *et al.*, High-performance hollow sulfur nanostructured battery cathode through a scalable, room temperature, one-step, bottom-up approach. *Proc. Natl. Acad. Sci.* **110**, 7148 (2013).
51. Z. Wei Seh *et al.*, Sulphur–TiO_2 yolk–shell nanoarchitecture with internal void space for long-cycle lithium–sulphur batteries. *Nat. Commun.* **4**, 1331 (2013).
52. D. S. Jung *et al.*, Hierarchical Porous Carbon by Ultrasonic Spray Pyrolysis Yields Stable Cycling in Lithium–Sulfur Battery. *Nano Lett.* **14**, 4418 (2014).
53. S. Wenzel *et al.*, Thermodynamics and cell chemistry of room temperature sodium/sulfur cells with liquid and liquid/solid electrolyte. *J. Power Sources* **243**, 758 (2013).
54. Y.-X. Wang *et al.*, Achieving High-Performance Room-Temperature Sodium–Sulfur Batteries With S@Interconnected Mesoporous Carbon Hollow Nanospheres. *J. Am. Chem. Soc.* **138**, 16576 (2016).
55. X. Yu, A. Manthiram, Room-Temperature Sodium–Sulfur Batteries with Liquid-Phase Sodium Polysulfide Catholytes and Binder-Free Multiwall Carbon Nanotube Fabric Electrodes. *J. Phys. Chem. C* **118**, 22952 (2014).
56. X. Yu, A. Manthiram, Performance Enhancement and Mechanistic Studies of Room-Temperature Sodium–Sulfur Batteries with a Carbon-Coated Functional Nafion Separator and a Na_2S/Activated Carbon Nanofiber Cathode. *Chem. Mater.* **28**, 896 (2016).
57. X. Yu, A. Manthiram, Capacity Enhancement and Discharge Mechanisms of Room-Temperature Sodium–Sulfur Batteries. *ChemElectroChem* **1**, 1275 (2014).

58. D. Kumar, M. Suleman, S. A. Hashmi, Studies on poly(vinylidene fluoride-co-hexafluoropropylene) based gel electrolyte nanocomposite for sodium–sulfur batteries. *Solid State Ionics* **202**, 45 (2011).

59. M. Kohl, F. Borrmann, H. Althues, S. Kaskel, Hard Carbon Anodes and Novel Electrolytes for Long-Cycle-Life Room Temperature Sodium-Sulfur Full Cell Batteries. *Adv. Energy Mater.* **6**, 1502185 (2016).

Chapter-4

Two in One: N-doped Tubular Carbon Nanostructure as an Efficient Metal-free Dual Electrocatalyst for Hydrogen Evolution and Oxygen Reduction Reactions

Summary:

An efficient, N-doped, pore engineered carbon as a dual electrocatalyst for hydrogen evolution reaction (HER) and oxygen reduction reaction (ORR) is developed with a potential to replace traditional precious metal (Pt) based catalysts. Rationally designed, N-doped carbons (NDCs) with wider mesopores (15-27 nm) for better mass transfer properties were obtained by pyrolysis and demineralization of polydopamine coated halloysite clay nanotubes. NDCs thus obtained exhibit promising electrocatalytic activity for hydrogen evolution reaction (HER) with lower onset potential (117 mV), smaller Tafel slope (94 mV dec^{-1}) and high exchange current density (j_o =1.5 x 10^{-2} mA cm^{-2}); which is comparable and even higher to other multiple heteroatom doped carbons and transition metal chalcogenide/oxide based systems reported previously. Furthermore, NDC participate in efficient, direct four-electron pathway for the reduction of molecular oxygen to water. The observed bifunctional electrocatalytic activity of NDC can be attributed to synergistic effect of enhanced mass and efficient charge transfer processes at the electrodics and hence deems fit to be a promising candidate for future renewable energy blueprints viz. metal-air batteries and regenerative fuel cell technology.

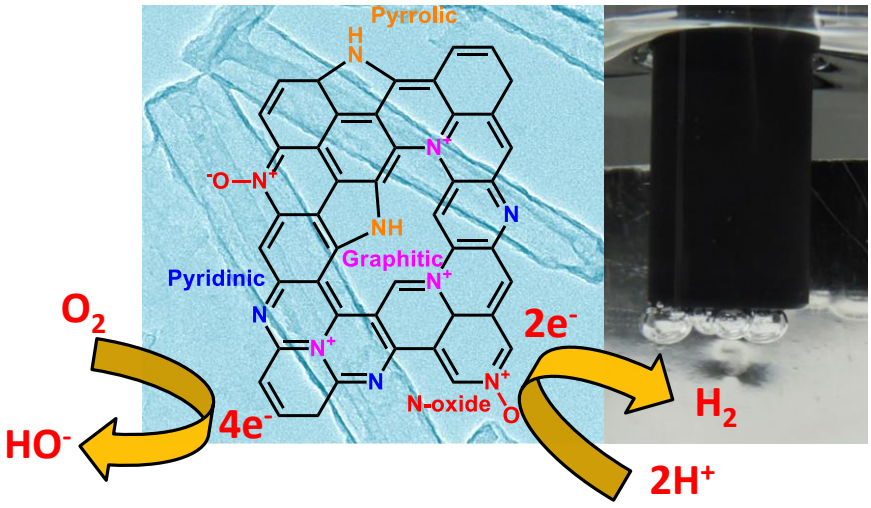

(A paper based on this work has appeared in *Journal of Materials Chemistry A* **5**, 6025, 2017).

4.1 Introduction:

The emergence of metal free, heteroatom-doped carbons as effective electrocatalysts(*1-3*) for oxygen reduction (ORR),(*1, 4*) oxygen evolution (OER)(*2, 5*) and hydrogen evolution reactions (HER)(*6-9*) has given a new thrust to the future renewable and sustainable energy(*10-12*) blueprints like fuel cells (FCs),(*7, 12*) metal-air (M-O_2) batteries(*13, 14*) and water splitting.(*5, 8*) The heteroatom dopants (like N, P, S etc.) alter the electronic cloud around the neighboring carbon atoms (thus activate carbon's π electron) by breaking their electroneutrality thus providing favorable sites for such catalyses.(*15-17*) Nevertheless, these heteroatom doped carbons (single/multiple heteroatom doped carbons) often perform as monofunctional catalysts and are efficient only for one type of reaction either ORR or HER or OER.(*18-24*) Recent reports on the ability of multiple-heteroatoms (N, P, S etc.) doped carbons to simultaneously drive ORR and OER,(*2*) or ORR and HER(*25*) reactions generated a great deal of interest in search of new carbons having bifunctional activity with immense potential in rechargeable M-O_2 batteries(*2, 26*) and regenerative fuel cells (r-FCs) technology.(*27, 28*) Unitized r-FC technologies developed from carbon based architectures with superior energy density compared to batteries are expected to boost solar powered spacecrafts, satellites, hybrid propulsion systems and as well could serve as complementary off-grid power generation source utilizing solar cells, wind turbines etc. for load leveling.

It is believed that the synergistic effect of multiple heteroatoms (N, P, S etc.) doping favors bifunctional activities which is otherwise difficult to achieve in single heteroatom doped carbons.(*17*) For example ionic liquid derived C, N based architectures shows good ORR activity (n = 3.87) but failed to show good HER performance (onset potential ~200 mV vs. RHE, η = 490 mV @ 10 mA cm^{-2} and a Tafel slope of 120 mV dec^{-1})(*29*) compared to multi heteroatom doped carbons. It is believed that certain topological defects(*30*) and charge transfer kinetics (intrinsic conductivity) would significantly influence the electrocatalytic performance of carbon-based materials. Besides, theoretical studies highlight the prospective positive effect of local curvature(*31*) (induced by heteroatom doping) on the electrocatalytic performance. Furthermore, the pore size plays a significant role in efficient mass and charge transfer across electrode-electrolyte interface resulting in superior electrochemical activity. Wider mesopores are expected to facilitate the gas detachment (in HER and other gas evolution reactions) at the active interfaces thereby continuously

regenerating the sites resulting in unhindered kinetics while maintaining the electrode integrity.(*32, 33*) Although graphene among other carbons having high electronic conductivity, a favorable parameter for electron transport, it is difficult to obtain graphene-based materials with larger mesopores (>15 nm) as they tend to aggregate due to strong π-π interactions.(*34*) Various template based strategies (SBA-15, MCM-41, clays etc.) have been implemented to synthesize carbons with high surface areas (>1200 m^2 g^{-1}) with moderate pore volume (~1.1 cc g^{-1}) but usually results in lower pore diameter (~4 nm for CMK-3).(*35, 36*) Only few reports exists where wider mesopores are reported but are not ordered architectures.(*37*) In our present investigation we have strategically chosen halloysite based clay as template to obtain carbon having micropores and wider cylindrical mesopores (>15 nm) favorable for efficient mass transport with the aim to minimize the confinement effects associated with micropores; therefore a balanced pore architecture combining the best of both.(*38, 39*)

4.2 Scope of the present investigation:

Herein, we report for the first time, nitrogen-doped, partially graphitic carbon nanotubes having wide mesopores (>15 nm) acting as a bifunctional

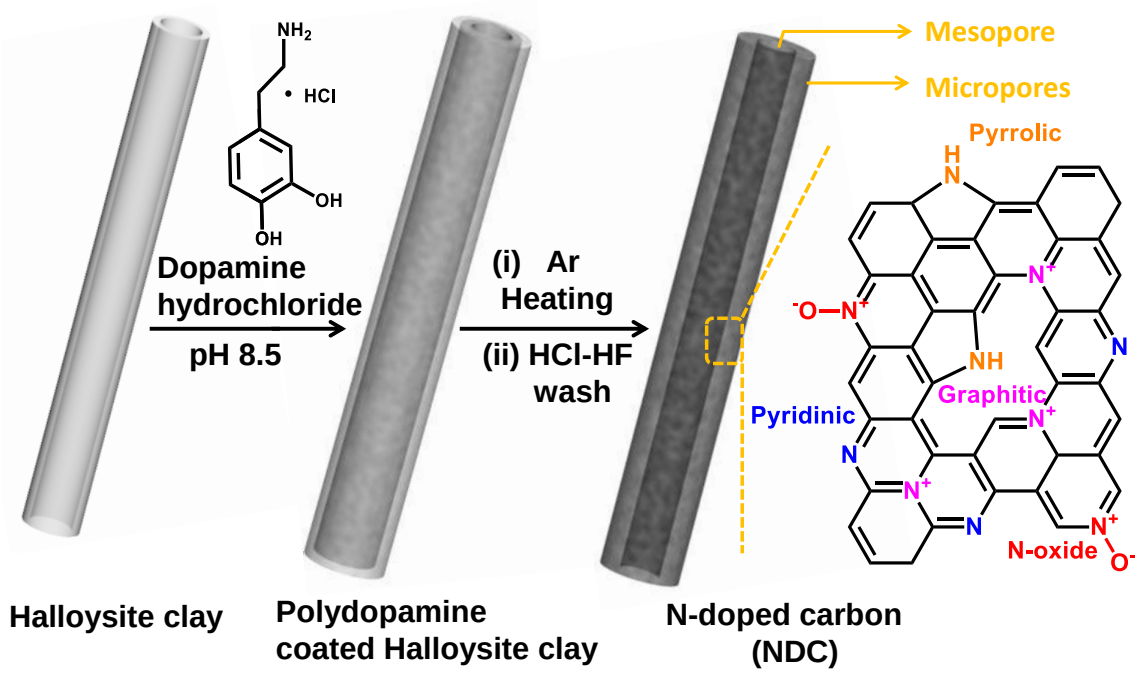

Scheme 1. Illustration depicting halloysite nanoclay templated synthesis of N-doped carbon (NDC) having tubular structure.

electrocatalyst; participating in efficient direct four-electron reduction of O_2 to H_2O (ORR) and simultaneously acting as HER catalyst with lower onset potential (which is superior compared to other multi-heteroatom doped carbons and certain metal chalcogenides), lower Tafel slope and higher stability thus making it a viable electrocatalyst for r-FCs.

N-doped carbon nanotubes were synthesized using tubular halloysite clay **(Figure 3a)** of diameter in the range of 15 nm to 27 nm and wall thickness ~28 nm as the template **(Scheme 1)**. Self-polymerization of dopamine hydrochloride (the carbon source) under basic conditions (pH ~8.5) resulted in polydopamine coated nanoclay **(Scheme 1)**. Further pyrolysis at elevated temperatures (700-900 ^{O}C) and subsequent demineralization (using HCl-HF solution) resulted in N-doped carbon, abbreviated as NDCs **(Scheme 1)**.

4.3 Experimental procedures:

4.3.1 Materials used:

Halloysite nanoclay and Nafion® perfluorinated resin solution were procured from Sigma-Aldrich. HCl (37%), HF (48%) and KOH were obtained from Merck. Dopamine hydrochloride was purchased from Alfa Aesar. H_2SO_4 (98 %) was obtained from SD Fine Chemicals. All the chemicals were used as received without any further purification.

4.3.2 Instrumentation and characterization techniques:

Transmission electron microscopy (TEM) images of the samples were obtained using Technai F30 UHR electron microscope operating at an accelerating voltage of 200 kV. Gas sorption measurements were performed on Autosorb-iQ_2 (Quantachrome corp.) at 77 K and prior to analyses, the synthesized samples were degassed under high vacuum for 12 h at 423 K. Ultrahigh pure N_2 (99.9995%) was used in all the measurements. Field emission scanning electron microscopic (FESEM) images of the samples were acquired on Nova-Nano SEM-600 (FEI, Netherlands). X-ray photoelectron spectroscopic analyses were performed using Omicron photoelectron spectrometer equipped with Al Kα ($h\nu$ = 1486.6 eV) as the X-ray source. Jobin Yvon LabRam HR spectrometer having 632 nm Ar laser was used for acquiring Raman spectra of the samples. Electrochemical measurements were carried out using electrochemical work station obtained from CH instruments (660C, USA) for evaluating the electrochemical activities of the synthesized materials towards hydrogen

evolution reaction (HER) and oxygen reduction reaction (ORR). Inductively coupled plasma optical emission spectroscopy (ICP-OES) analyses were performed on Perkin-Elmer Optima 7000DV instrument.

4.3.3 Synthesis of NDCs:

In a typical synthesis, 235 mg of halloysite clay was dispersed in 250 mL of 10 mM TRIS buffer (pH 8.5) and was sonicated for 30 min. Thereafter, 155 mg of dopamine hydrochloride was added to the above dispersion and was further sonicated for 5 min and then left to stir for 22 h at room temperature. Polydopamine coated halloysite clay was obtained after centrifugation and repeated wash with water and ethanol. Further pyrolysis at elevated temperature under Ar for 4 h and subsequent sequential demineralization with 15 mL HCl (6 M) and 15 mL HF (12 M) for 12 h each and thorough washing with water-ethanol resulted in different NDCs (viz. NDC-700, NDC-800 and NDC-900; where the numbers denote the temperatures of pyrolysis in ^{O}C). The final yield of NDCs was about 30 mg (20 wt.% in terms of carbon precursor, dopamine hydrochloride).

4.3.4 Electrode preparation and electrochemical measurements:

The electroactive material (2 mg) was ultrasonically dispersed in water (0.70 mL) and isopropanol (0.30 mL) mixture containing 10 µL of 5 wt.% Nafion® solution until a homogeneous catalyst ink was obtained. Thereafter, 10 µL of above dispersion was drop-casted onto a pre-cleaned glassy carbon electrode (GCE) with 3 mm diameter resulting in a catalyst loading of ~0.28 mg cm^{-2}. The catalyst modified GCE was dried under ambient conditions which served as a working electrode (WE).

Electrochemical measurements were carried out in a standard three-electrode cell using large area Pt foil as a counter electrode and saturated calomel electrode (SCE) as a reference electrode for studying HER activity in acidic medium (1 M H_2SO_4) and whereas mercury-mercuric oxide reference electrode was used for evaluating ORR activity in basic medium (0.1 M KOH). For HER, separate measurements were performed in an H-type cell wherein working and reference electrodes were kept in one compartment while Pt counter electrode was kept in the other in order to avoid any artifact arising from the dissolution of Pt and deposition of the same on the working electrode. All the polarization curves were corrected for *iR* losses arising due to ohmic resistance of the cell and the measured potentials vs. SCE or Hg/HgO were calibrated with respect

to reversible hydrogen electrode (RHE). The obtained current densities were normalized to geometrical area of the GCE. Linear sweep voltammograms were recorded in 1 M H_2SO_4/ 0.1 M KOH at a scan rate of 5 mV s^{-1} in O_2/N_2 saturated aqueous electrolytes. Cyclic voltammograms (CV) were recorded under similar conditions and at different scan rates (20-200 mV s^{-1}) between -0.10 V and 0.40 V (vs. RHE) in order to evaluate electrochemical double layer capacitance (C_{dl}), representing electrochemically active surface area (ESCA).

4.3.5 Calculation of electron transfer number from Koutecky-Levich equation for oxygen reduction reaction (ORR):

Rotating disk electrode data was used to determine the number of electrons transferred per O_2 molecule using the Koutecky-Levich equation:

$$\frac{1}{j} = \frac{1}{j_k} + \frac{1}{j_l} = \frac{1}{j_k} + \frac{1}{B\omega^{1/2}} \qquad (1)$$

Where j is the measured current density, j_k and j_l are the kinetic and diffusion limited current densities respectively and ω is the electrode rotation speed. B is Levich slope and is determined from Koutecky-Levich plots using equation below (2):

$$B = 0.62nFC_{O_2}(D_{O_2})^{\frac{2}{3}}v^{-\frac{1}{6}} \qquad (2)$$

Where n is the number of electrons transferred per O_2 molecule, F is the Faraday constant (96485 $Cmol^{-1}$), C_{O_2} is the bulk concentration of O_2 in the electrolyte, D_{O_2} is the diffusion coefficient of O_2 and v is the kinematic viscosity of the electrolyte.

4.3.6 Calibration of reference electrodes:

The reference electrodes (SCE and Hg/HgO), used in different media were calibrated with respect to reversible hydrogen electrode using large area Pt foil (1.0 x 1.2 cm^2) as a working and counter electrodes. High purity hydrogen gas was purged in the respective solutions for at least 45 min before the experiments and thereafter a constant overhead purge was maintained during the measurements **(Figure 1-2)**.

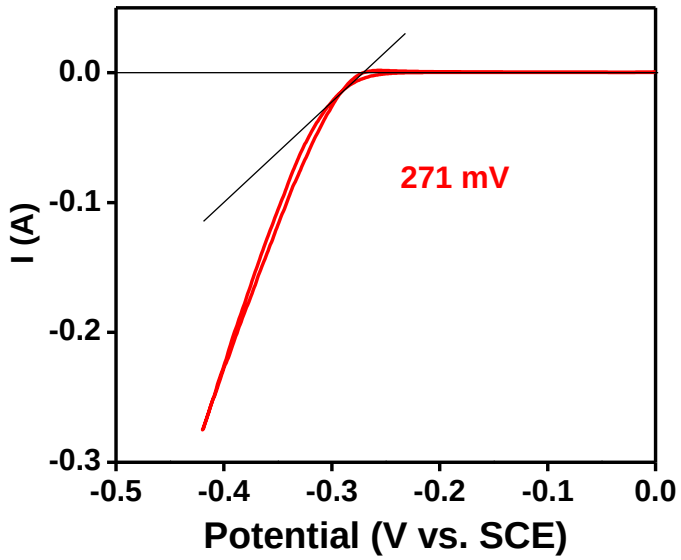

Figure 1. Calibration of saturated calomel electrode (SCE) with respect to reversible hydrogen electrode (RHE) in 1.0 M H_2SO_4 at 1 mV s^{-1}.

Therefore, we have for 1.0 M H_2SO_4:

$$\mathbf{E_{RHE} = E_{SCE} + 0.271\ V}$$

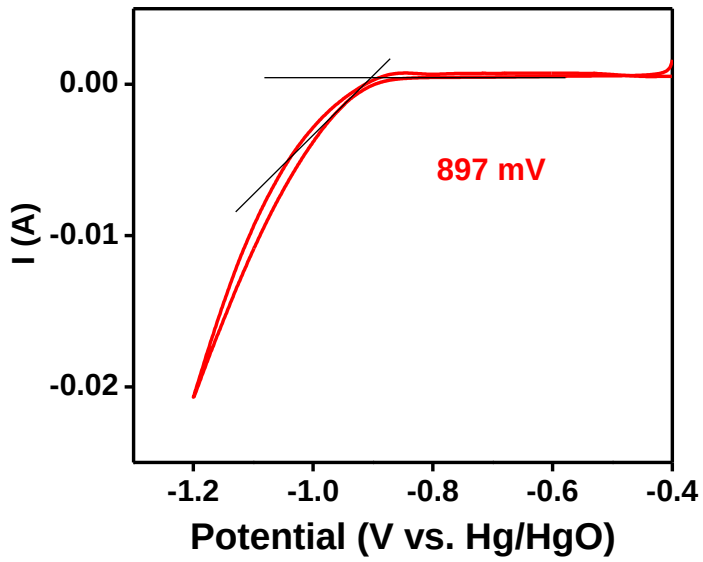

Figure 2. Calibration of mercury/mercury oxide (Hg/HgO) electrode with respect to reversible hydrogen electrode (RHE) in 0.1 M KOH at 1 mV s^{-1}.

Therefore, we have for 0.1 M KOH:

$$\mathbf{E_{RHE} = E_{Hg/HgO} + 0.897\ V}$$

4.3.7 Faradaic efficiency measurements:

Faradaic efficiency for the hydrogen evolution reaction was monitored by quantifying the amount of gas evolved as a function of time. Chronoamperometric measurements were performed at -0.369 V vs. RHE using a typical H-shaped electrochemical cell in order to eliminate any contribution from oxygen reduction. Working electrode (modified by catalyst coating, NDC-800) and reference electrode (SCE) were kept in one compartment of H-cell while a large area Pt counter electrode was placed in the other. The quantity of gas evolved was measured using inverse burette method. It was observed that NDC-800 can produce around 7 mL of H_2 gas within 1.5 h. The amount of gas evolved during the reaction is in close agreement with the theoretical value, suggesting nearly 100% faradaic efficiency. Theoretically, the amount of H_2 gas evolved can be calculated from the equation based on Faraday's law (Equation 3) where I is the applied current, t is the time and F is Faraday constant, 96485.34 C. Therefore, we have

$$Moles\ of\ H_2 = \frac{1}{2F}\int_0^t Idt \qquad (3)$$

4.4 Results and discussions:

Pyrolysis of polydopamine coated halloysite clay at 800 ^{O}C (Ar) resulted in NDC-800. Field emission scanning electron microscopic (FESEM) and transmission electron microscopic (TEM) images of the obtained NDC-800 **(Figure 3b-c)** exhibit negative morphological replication of halloysite nanoclay tubular morphology **(Figure 3a)** with a variable pore diameter (15-25 nm). We have also observed the formation of incomplete tubular morphologies due to variation in the coating level of dopamine over halloysite template. High-resolution TEM (HRTEM) images **(Figure 3d)** of the tubular walls show regions of graphitic nature which is conducive to good electronic conductivity. N_2 adsorption-desorption isotherms of halloysite clay display type II behavior(*40*) **(Figure 4)**. On the other hand, NDC-800 a relatively sharp increase in the N_2 uptake at low P/P_o **(inset of Figure 4)**, associated with micropores present in tubular walls followed by a type II behavior with a sharp N_2 condensation step at higher P/P_o (0.95), similar to halloysite **(Figure 4)**, indicating the presence of wider mesopores. The pore size distributions further confirm the presence of wider mesopores (15-27 nm) **(Figure 5a-b)**. As the nature of nitrogen and degree of graphitization is expected to have a direct

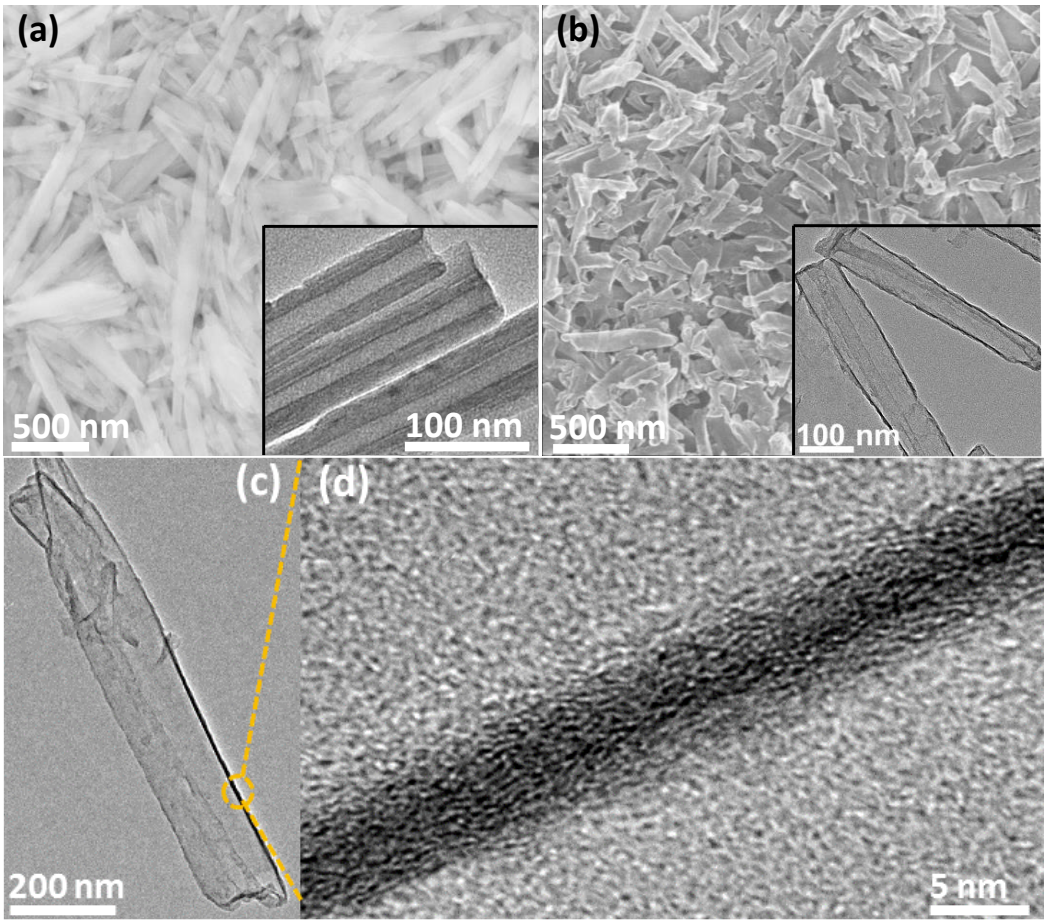

Figure 3. (a) FESEM and TEM (inset) images of halloysite clay. (b) FESEM and TEM (inset) images of NDC-800 indicating tubular morphology. (d) Shows HRTEM image of the region circled in dotted lines in (c) indicating graphitic nature of the carbon walls.

bearing on the HER and ORR performances, N-doped carbons having tubular morphology with different nitrogen contents were also prepared through similar method but pyrolyzed at 700 ^{o}C (NDC-700) and 900 ^{o}C (NDC-900) **(Figure 6-9 and Table 1)**. The observed low specific surface area of NDC-900 (368 m^2 g^{-1}) compared to NDC-800 (570 m^2 g^{-1}) is attributed to the enhanced degree of graphitization in the former **(Table 1)**. Furthermore, inductively coupled plasma optical emission spectroscopy (ICP-OES) analyses confirmed the absence of any trace amount of metal (Fe, Co etc.) impurities in NDCs.

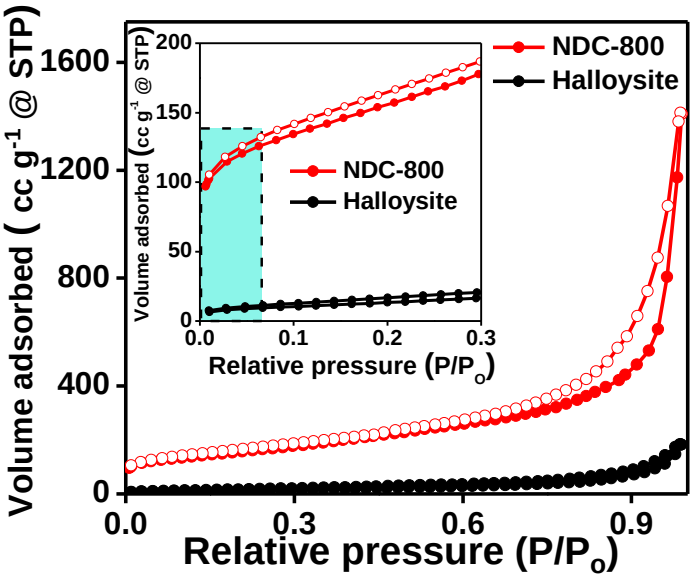

Figure 4. N_2 adsorption-desorption isotherms of halloysite clay and NDC-800; inset indicates microporous nature of the latter. (Note: closed and open symbols indicate adsorption and desorption isotherms respectively.)

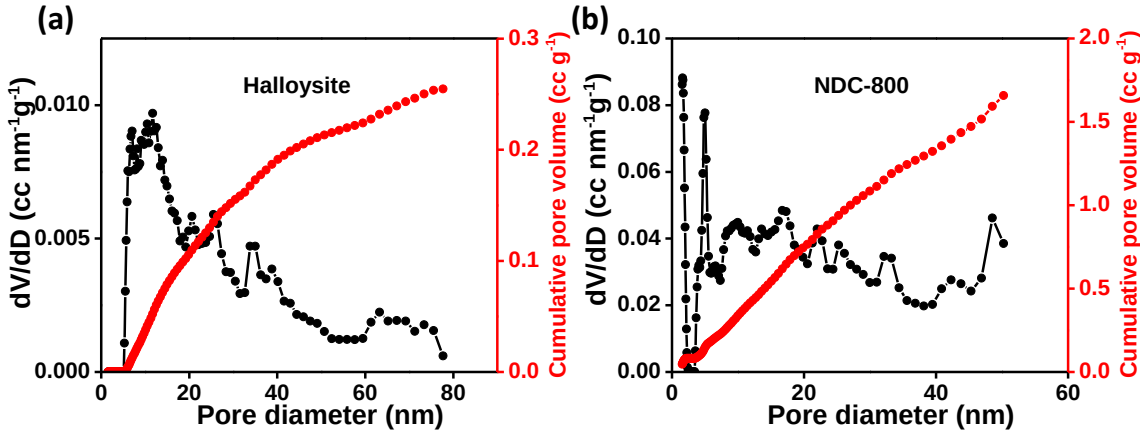

Figure 5. Pore size distribution of (a) halloysite clay and (b) NDC-800 along with corresponding cumulative pore uptakes; calculated by NLDFT/QSDFT (Non-local/Quenched solid density function theory) method.

XPS survey spectrum of NDC-800 **(Figure 10)** indicates the presence of carbon (C 1s), nitrogen (N 1s) and oxygen (O 1s) without any trace of impurities. Deconvolutions of high-resolution N 1s peak indicate the presence of pyridinic (N-1: 398.5 eV), pyrrolic (N-2: 400.0 eV), graphitic (N-3: 401.0 eV) and pyridinic-oxide (N-4: 403.8 eV) type of nitrogen atoms **(Figure 11)**.(*41*) Similar analyses were performed for NDC-700 **(Figure 12a and 13a)** and NDC-900 **(Figure 12b and 13b)** and the percentage of total nitrogen content shows

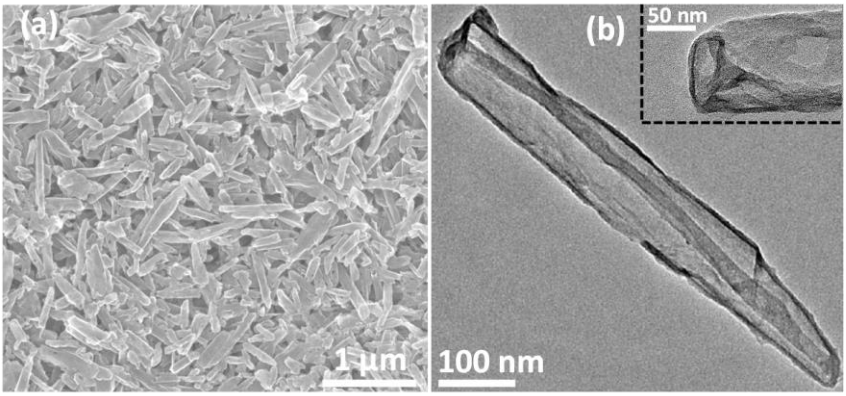

Figure 6. (a) FESEM images of NDC-700 indicating faithful morphological replication of parent halloysite clay and (b) TEM image of NDC-700 indicating tubular structure (inset shows tubular opening).

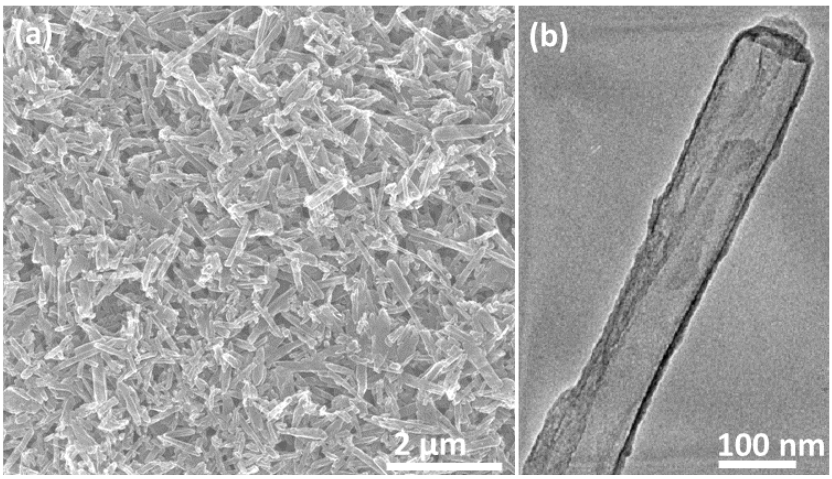

Figure 7. (a) FESEM and (b) TEM images of NDC-900 indicating tubular morphology.

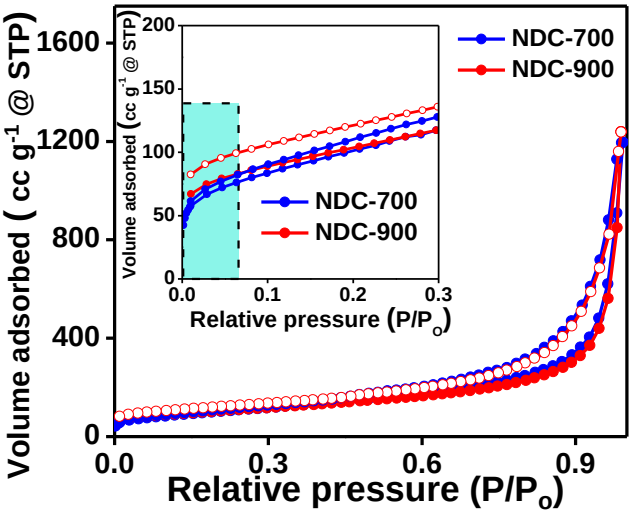

Figure 8. N_2 adsorption-desorption isotherms of NDC-700 and NDC-900; inset indicate microporous nature of the NDCs.

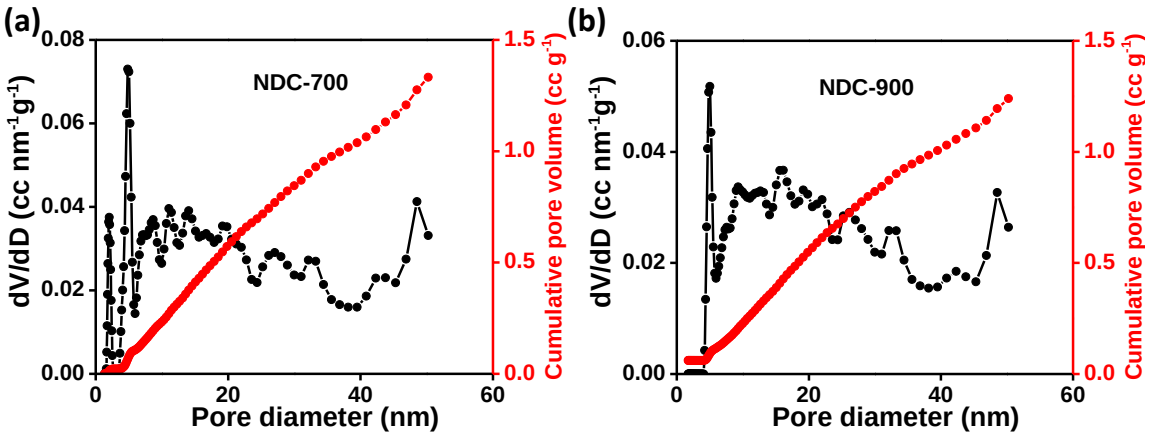

Figure 9. Pore size distributions along with corresponding cumulative pore uptakes of (a) NDC-700 and (b) NDC-900 calculated by QSDFT method.

Materials	S_{BET} [a] ($m^2 g^{-1}$)	V_T [b] ($cm^3 g^{-1}$)	D_{meso} [c] (nm)
Halloysite	52	0.228	>15
NDC-700	373	1.406	>15
NDC-800	570	1.879	>15
NDC-900	368	1.313	>15

Table 1. Textural parameters of halloysite nanoclay and NDCs.

[a] BET (Brunauer-Emmett-Teller) specific surface area calculated in the relative pressure (P/P_o) range of 0.5 to 0.27, [b] Total pore volume was calculated at P/P_o = 0.97 and [c] mesopore diameter calculated by QSDFT/NLDFT method.

decreasing trend starting from NDC-700 to NDC-900 which are summarized in **Table 2** as a a function of pyrolysis temperature.

HER performance of NDC-800 was investigated in 1.0 M H_2SO_4 using a typical three-electrode setup with a mass loading of 0.28 mg cm^{-2} on a glassy carbon electrode (GCE) and was compared with state-of-the-art 40 wt.% Pt/C as a reference. HER polarization curve **(Figure 14a)** shows NDC-800 with much lower onset potential of ~117 mV (measured at 0.3 mA cm^{-2}) compared to many carbon-based materials and non-noble metal chalcogenide based catalysts reported in literature **(Table 3)**.(*17, 23, 42, 43*) Furthermore, NDC-800 exhibits an overpotential of 276 mV to achieve a cathodic current density of 10 mA cm^{-2}

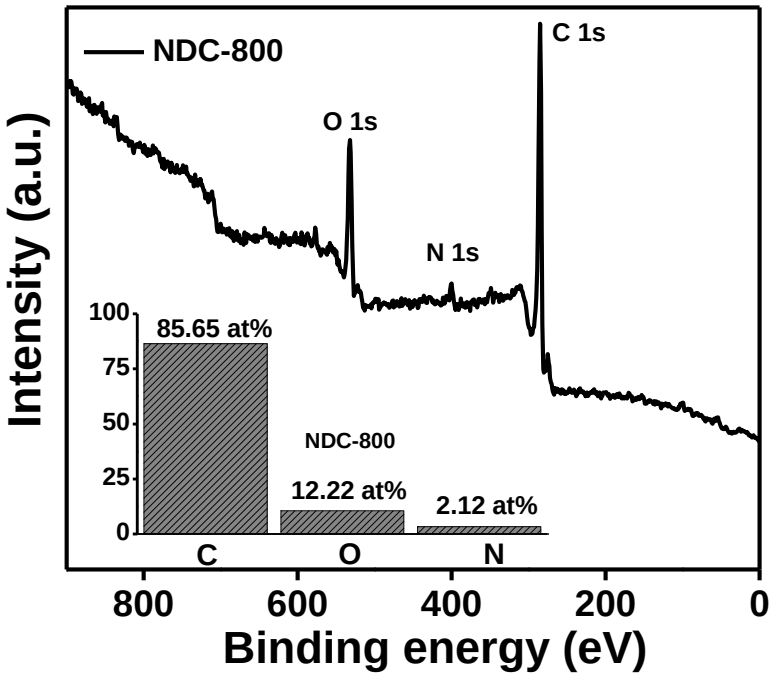

Figure 10. XPS survey spectrum of NDC-800; inset shows corresponding elemental content in atomic percentages.

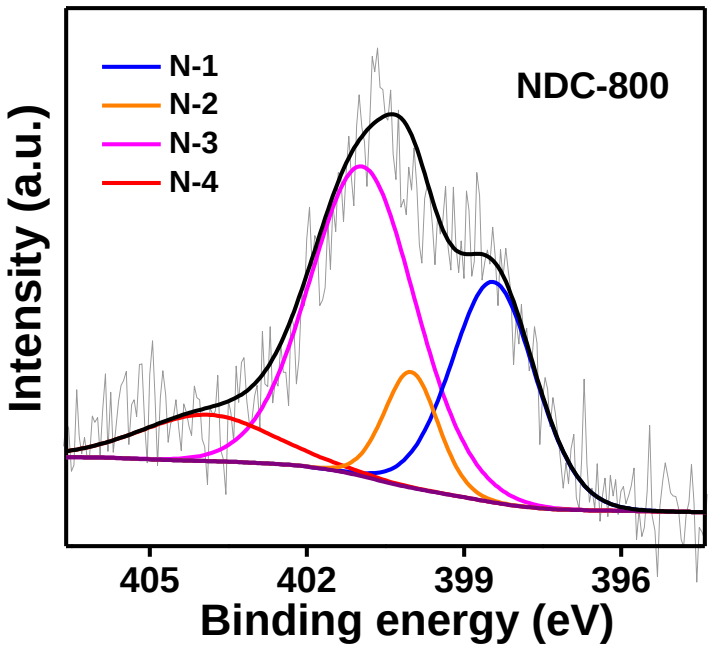

Figure 11. Deconvolution of high-resolution N 1s XPS spectrum of NDC-800 indicating the presence of different types of N.

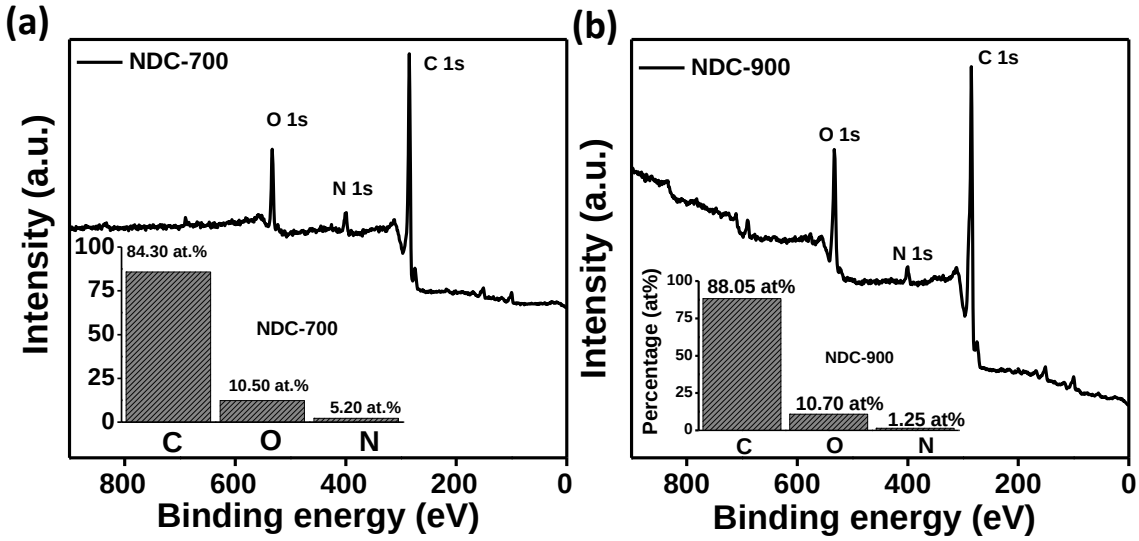

Figure 12. XPS survey spectra of (a) NDC-700 and (b) NDC-900; inset shows corresponding elemental contents in atomic percentages.

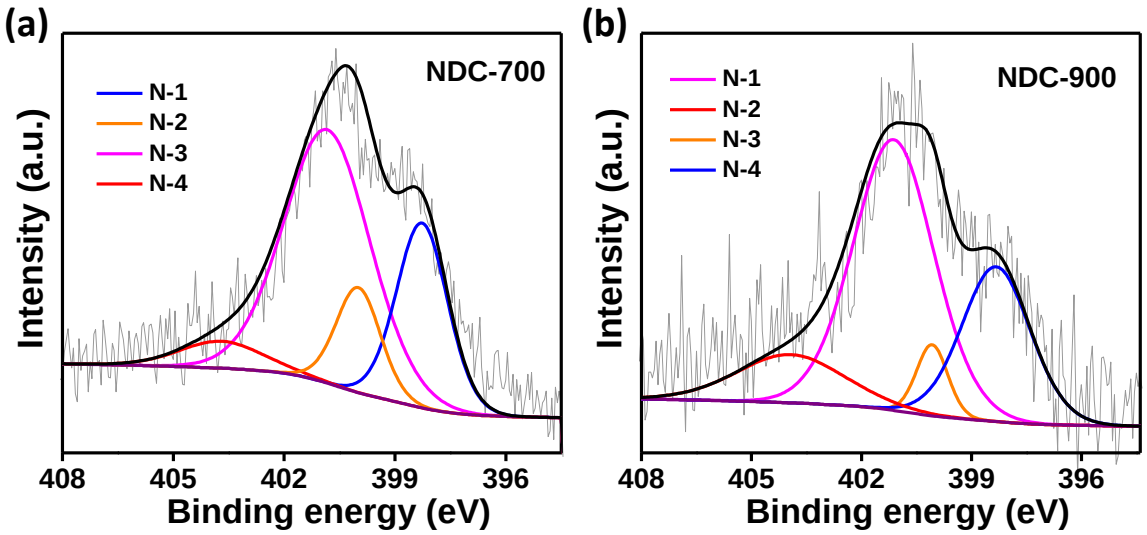

Figure 13. Deconvolution of high-resolution N 1s XPS spectrum of (a) NDC-700 and (b) NDC-900 indicating the presence of different types of N.

which is significant compared to NDC-900 (η = 489 mV) and NDC-700 (η = 529 mV) **(Figure 14a)**. Additionally, NDC-800 exhibits lowest Tafel slope of 94 mV dec^{-1} **(Figure 14b)** indicating Volmer-Heyrovsky as principle HER mechanism with primary proton adsorption step being rate limiting.(*9, 33, 44, 45*) Faradaic efficiency measurements indicating nearly 100% efficiency further confirmed that cathodic current purely stems from proton reduction rather than oxygen reduction. The exchange current density (j_o) calculated by extrapolation

Electocatalysts	N content (at. %)	Pyridinic-N (%)	Pyrrolic-N (%)	Graphitic-N (%)	Pyridinic N-oxide (%)
NDC-700	5.20	33.27	16.43	42.41	7.89
NDC-800	2.12	29.04	9.75	51.48	9.72
NDC-900	1.25	26.66	5.57	54.81	12.96

Table 2. % N content and relative percentages of different types of nitrogen in NDCs calculated from deconvolution of high-resolution N 1s XPS spectra.

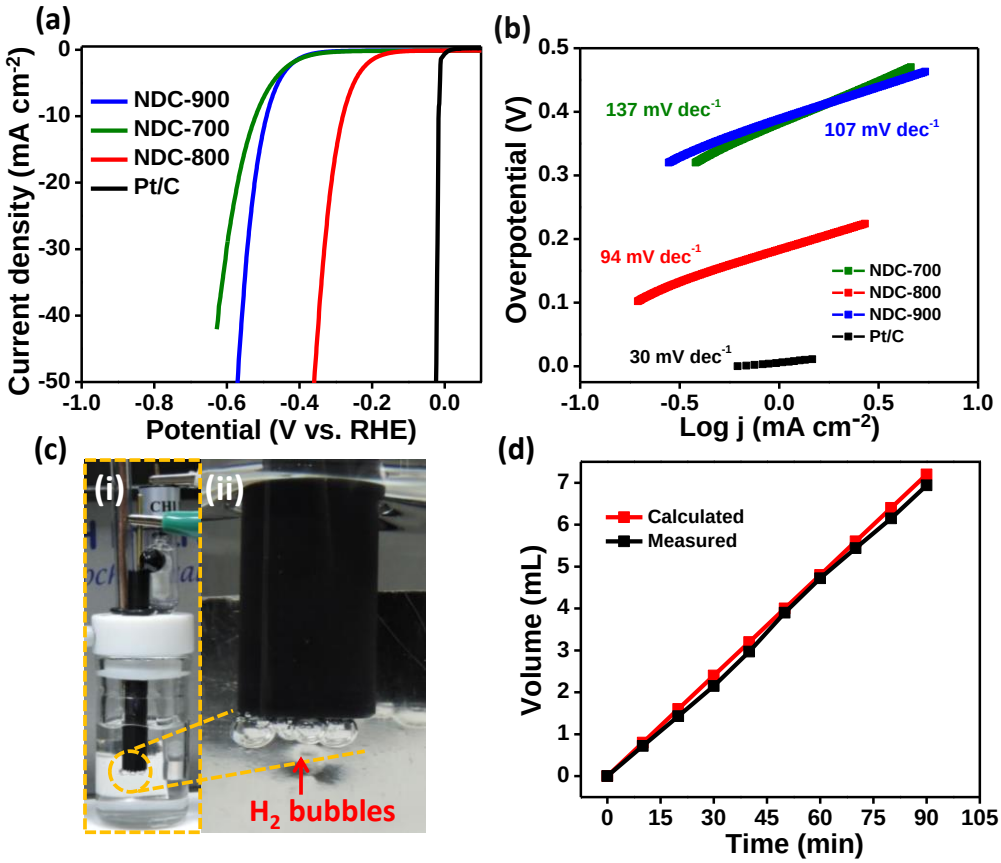

Figure 14. (a) The HER polarization curves after *iR* compensation of different NDCs in 1 M H_2SO_4 at a scan rate of 5 mV s^{-1}. (b) Tafel slopes of various NDCs and Pt/C. (c) Digital photographs showing the evolution of H_2 at NDC-800 coated GC electrode; (ii) is the expanded view at GC electrode in (i). (d) Faradaic efficiency plots indicating the amount of H_2 evolved as a function of time along with the expected values.

Catalysts	η @ 10 mA cm^{-2} (mV)	Tafel Slope (mV dec^{-1})	Onset Potential (mV)	j_o ($mAcm^{-2}$)	Ref.
NDC-800	276	94	117	1.50×10^{-2}	This work
N-doped graphene	490	116	330	7.01×10^{-5}	(*6*)
P-doped graphene	553	133	370	9.00×10^{-6}	(*6*)
N, P co-doped graphene	420	91	289	2.44×10^{-4}	(*6*)
C, N architectures	490	120	~200	1.45×10^{-2}	(*29*)
S-doped graphene	391	130	240	9.90×10^{-3}	(*23*)
N, S co-doped graphene	276	81	130	8.40×10^{-3}	(*23*)
Core-shell MoO_3-MoS_2 nanowires	250	55	150-200	0.08×10^{-3}	(*42*)
Mesoporous double gyroid MoS_2	250-300	50	150-200	0.69×10^{-3}	(*43*)

Table 3. Comparison of HER parameters of some of the heteroatom-doped carbon materials and non-precious transition metal chalcogenides with NDC-800.

method indicates a very high value for NDC-800 (1.5 x 10^{-2} mA cm^{-2}) which is higher by two orders of magnitude compared to other NDCs and is even larger compared to many heteroatom-doped carbon materials and certain transition metal chalcogenides **(Table 3)**, signifying its high intrinsic ability to drive such reactions.

The observed difference among NDCs in the electrocatalytic performance indicates that the right balance between the nature of dopant (pyridinic and graphitic nitrogen) and the degree of graphitization of carbon is an essential parameter for the good performance of N-doped carbons in HER reactions. Pyridinic and graphitic nitrogen are known to induce asymmetry in charge

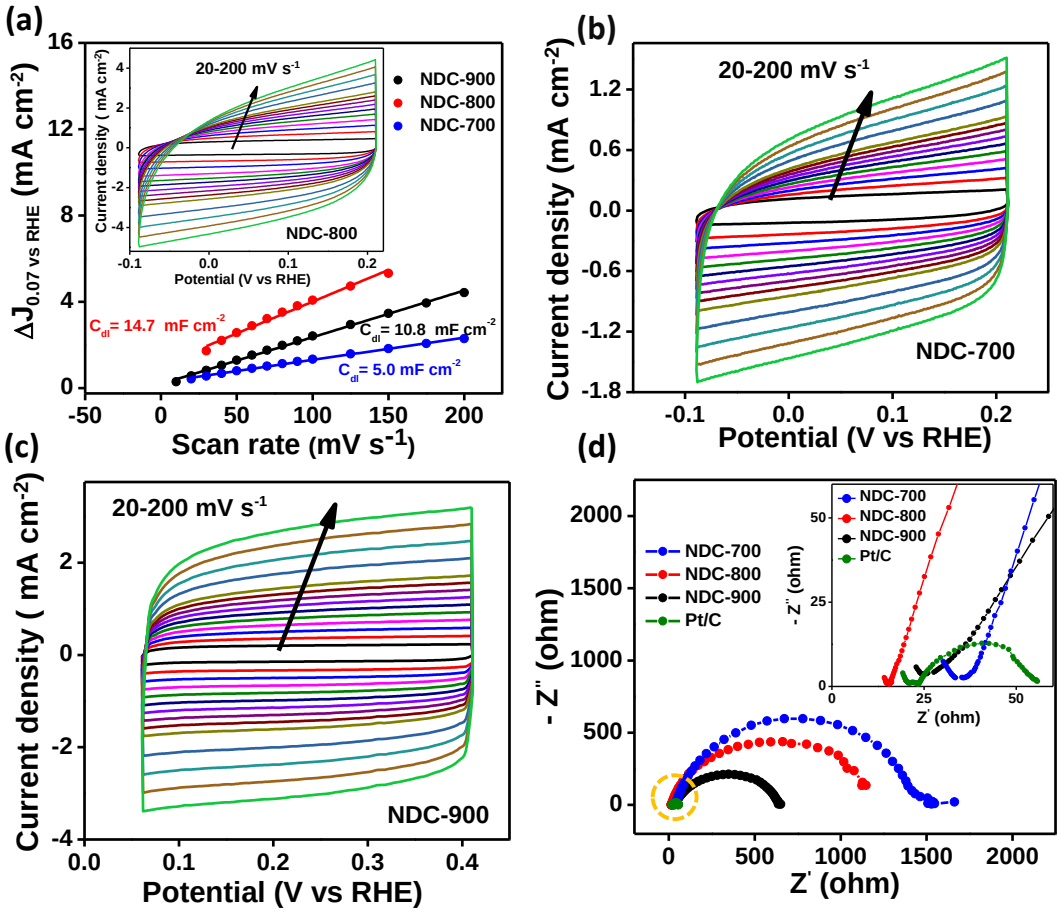

Figure 15. (a) Evaluation of double layer capacitance of different NDCs at 0.07 V (vs. RHE); inset shows CVs of NDC-800 at different scan rates (20-200 mV s^{-1}) in the potential range of -0.10 V to 0.20 V. (b) And (c) indicate CVs of NDC-700 and NDC-900 respectively at different scan rates in the above mentioned non-faradaic region. (d) Nyquist plots of various NDCs obtained at their corresponding onset potentials; inset is the expanded view of the region marked in dotted circle.

distribution around their adjacent carbon atoms which in turn enhances the HER activity by attaining an optimum value of |ΔGH*| (Gibbs free-energy for hydrogen adsorption).(*17*) On the other hand, highly graphitized carbon facilitates the electron transfer process. Though high-temperature pyrolysis is expected to enhance the HER performance (due to high degree of graphitization thus lowering the charge-transfer resistance as can be seen in the Nyquist plot, **Figure 15d**) the gain will be offset by the loss of pyridinic and graphitic nitrogen as thermodynamic equilibrium favors the removal of nitrogen molecule at higher temperatures. Understandably, NDC-700 with high amount of pyridinic nitrogen (but less graphitic carbon) and NDC-900 with more graphitized carbon (but less pyridinic/graphitic nitrogen) **(Table 2)** show two orders of magnitude lower exchange current density than NDC-800 (1.5 x 10^{-2} mA cm^{-2}) where there was an optimum balance between the amount/nature of dopant and the degree of graphitization. Furthermore, the high Cdl (double layer capacitance)**(Figure 15a-c)** representing electrochemically active surface area (ESCA) available for NDC-800 greatly contributes to its large j_o and HER activity as compared to that of NDC-700 and NDC-900. Operational stability for HER performance of NDC-800 (at constant η of 240 mV) using chronoamperometry indicate stable performance over 36400 s **(Figure 16)**, without any deterioration in activity which was found to be superior compared to Pt/C (at η = 20 mV). Such a performance can be rationalized in terms of pore properties, as wider mesopores tend to facilitate gas detachment process while maintaining electrode integrity with unhindered kinetics.

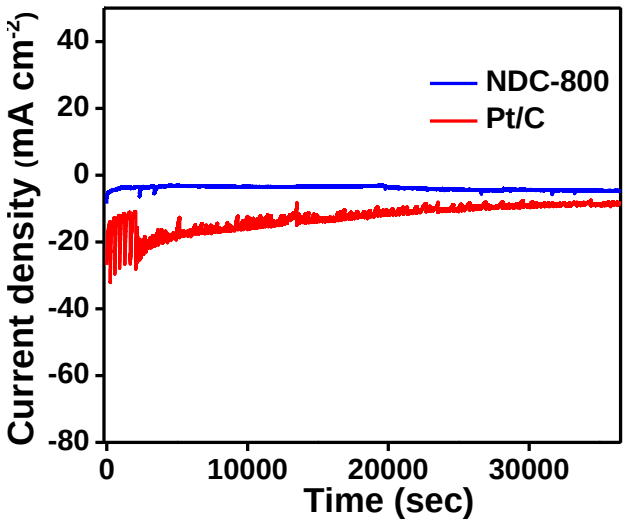

Figure 16. Comparison of HER stability performance of NDC-800 (at η = 240 mV) with Pt/C (at η = 20 mV).

The performance of NDC-800 as an ORR catalyst was also established from cyclic voltammograms (CVs) which shows well-defined O_2 reduction peak in oxygen saturated 0.1 M KOH solution and no such peaks in Ar saturated conditions **(Figure 17a)**. As the performance of ORR catalyst primarily depends upon the efficiency of electron transfer which in turn depends on the degree of graphitization, NDC pyrolyzed at 900 ^{o}C was also studied for comparison. As expected a concurrent positive shift in the peak potentials for oxygen reduction **(Figure 17a-18)** was observed for NDCs with increase in pyrolysis temperature

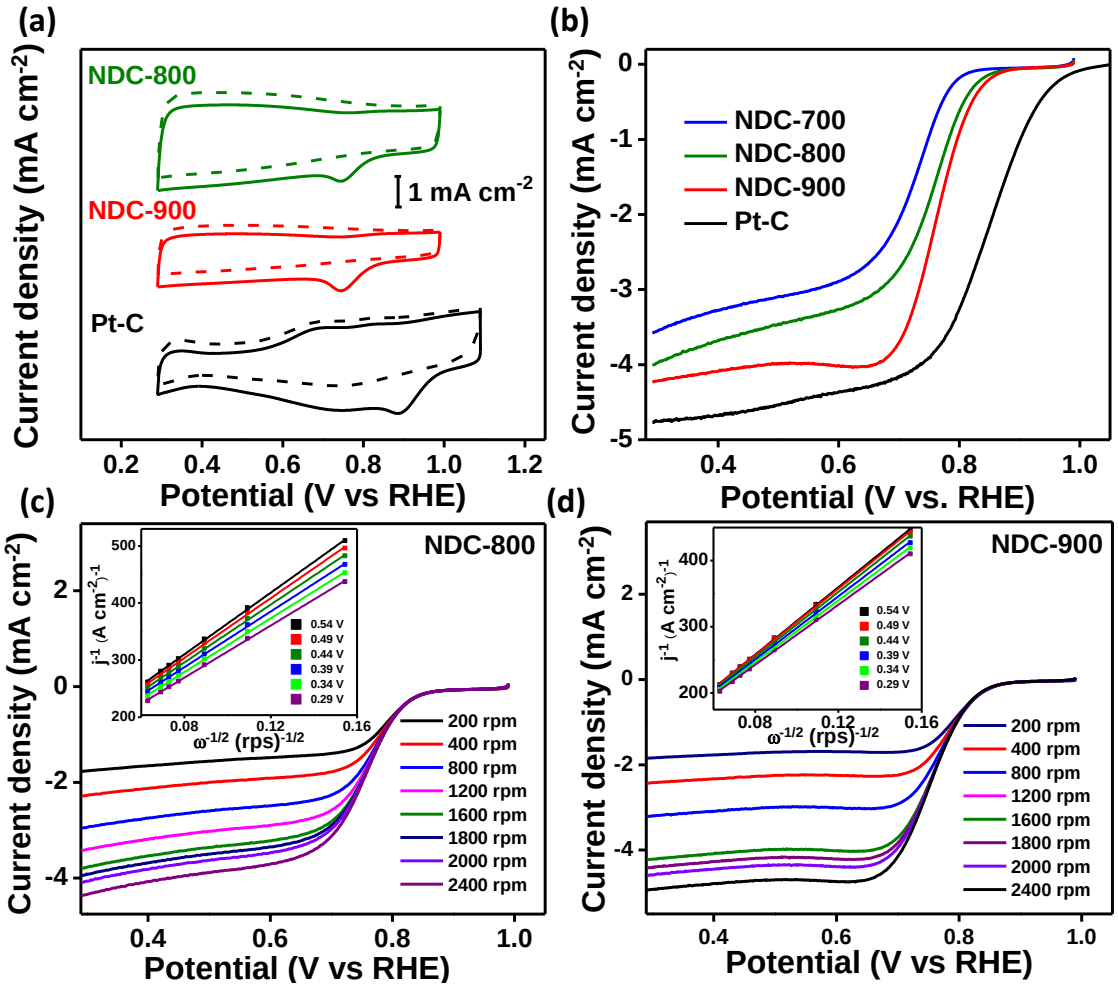

Figure 17. (a) CV curves of NDC-800, NDC-900 and Pt/C in O_2-saturated (solid line) and Ar-saturated (dashed line) 0.1 M KOH at 50 mV s^{-1}. (b) Comparison of linear sweep voltammetry (LSV) polarization curves of NDCs with Pt/C in oxygen saturated 0.1 M KOH at 1600 rpm with a sweep rate of 5 mV s^{-1}. (c) and (d) are the rotating disk electrode (RDE) voltammograms of NDC-800 and NDC-900 respectively at different rotation rates in 0.1 M KOH rates at 5 mV s^{-1}. Inset shows the respective Koutecky-Levich plots extracted from RDE voltammograms.

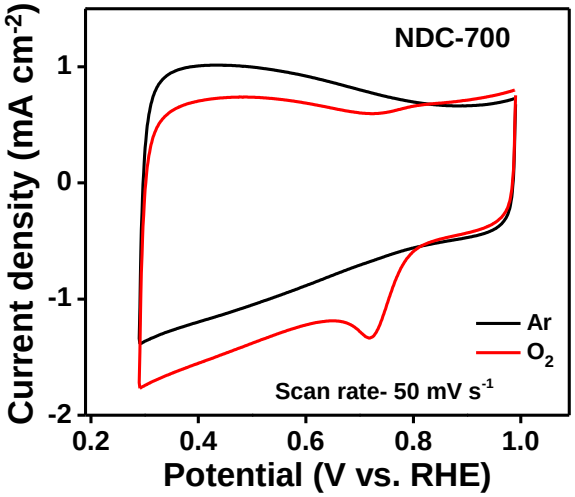

Figure 18. Cyclic voltammograms (CVs) of NDC-700 in O_2-saturated and Ar-saturated 0.1 M KOH at 50 mV s^{-1}.

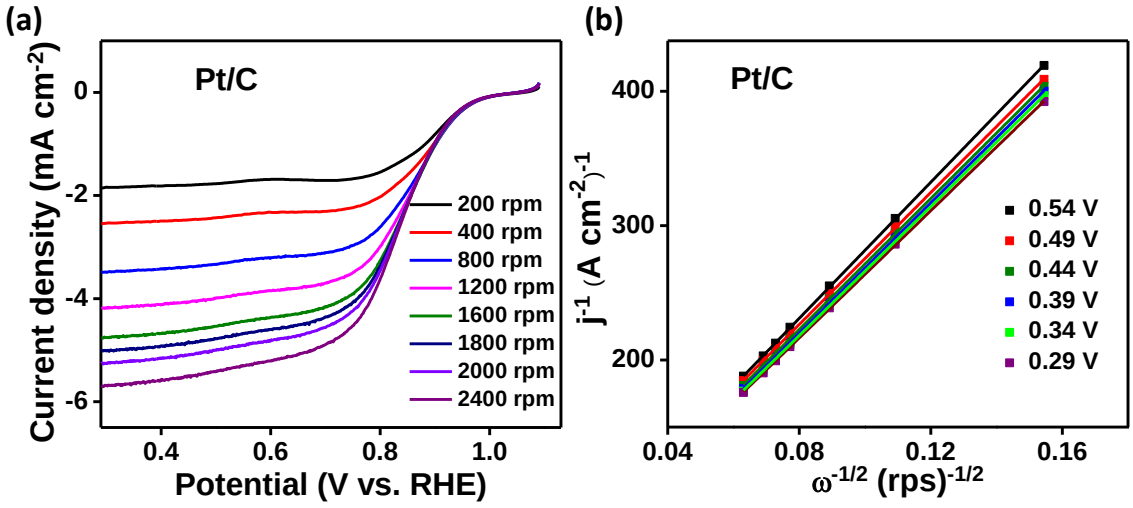

Figure 19. (a) Rotating disk electrode (RDE) voltammograms of Pt/C at different rotation rates in O_2 saturated 0.1 M KOH at 5 mV s^{-1}. (b) Shows corresponding Koutecky-Levich plots extracted from polarized LSV curves in (a).

from 700 to 900 ^{o}C. Polarized linear sweep voltammograms (LSVs) at rotating disk electrode (RDE) shows **(Figure 17b)** little variation in the onset potentials for NDC-800 (0.851 V) and NDC-900 (0.862 V) for molecular O_2 reduction. On the other hand, NDC-700 shows very high onset potential **(Figure 17b and Figure 18)** of 0.813 V as compared to NDC-800 and NDC-900. The limiting current densities of NDC-800 and NDC-900 at 0.29 V are more or less same under identical conditions reflecting similar diffusion limited current densities in both the cases. To gain further insight into ORR kinetics and mechanisms, LSV polarization curves were recorded at different rotation rates **(Figure 17 c-d,**

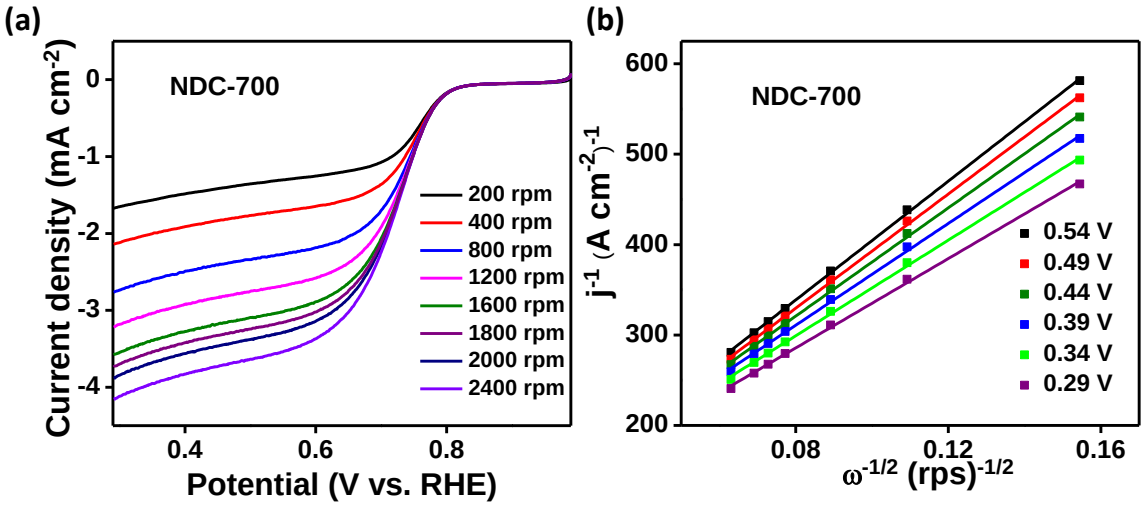

Figure 20. (a) Rotating disk electrode (RDE) voltammograms of NDC-700 at different rotation rates in O_2 saturated 0.1 M KOH at 5 mV s^{-1}. (b) Shows corresponding Koutecky-Levich plots extracted from polarized LSV curves in (a).

Figure 19a and Figure 20a) which shows increase in limiting current densities with increase in rotation rates.

Koutecky-Levich (K-L) plots(*46, 47*) extracted from above steady state voltammograms (between 0.54 V to 0.29 V) **(inset of Figure 17c and 17d, Figure 19b and Figure 20b)** exhibit linear relationship between J^{-1} and $\omega^{-1/2}$ and near parallelism of the slopes for all the catalysts indicating first-order reaction kinetics with respect to dissolved O_2. The kinetic current density(J_k), an inherent measure of the intrinsic activity of the catalyst indicate the highest activity for NDC-900 with j_k of 17 mA cm^{-2} at 0.39 V **(Figure 21a)** as compared to NDC-800. Nevertheless the number of electrons transferred (n) per oxygen molecule (at 0.39 V) derived from slopes of K-L plots indicate both NDC-800 (n = 3.9) and NDC-900 (n = 4.0) participate in efficient 4 electron pathway resulting in the direct reduction of O_2 to HO^- which is similar to state-of-the-art catalyst, 40 wt.% Pt/C, **(Figure 21a)** signifying the direct utility of such catalysts in metal-air batteries and fuel cells. Furthermore, ORR activity of NDC-800 remained unchanged even after 1000 cycles **(Figure 22)**, indicating its superior stability over long-term performance. The excellent ability of NDC-800 and NDC-900 to efficiently catalyze ORR can be rationalized in terms of enhanced degree of graphitization (**Figure 15d**, Nyquist plot) leading to efficient charge transfer at the interfaces along with predominant amount of graphitic (N-3) and pyridinic (N-1) nitrogen atoms which can effectively tailor spin density and charge density distribution on neighboring carbon atoms much

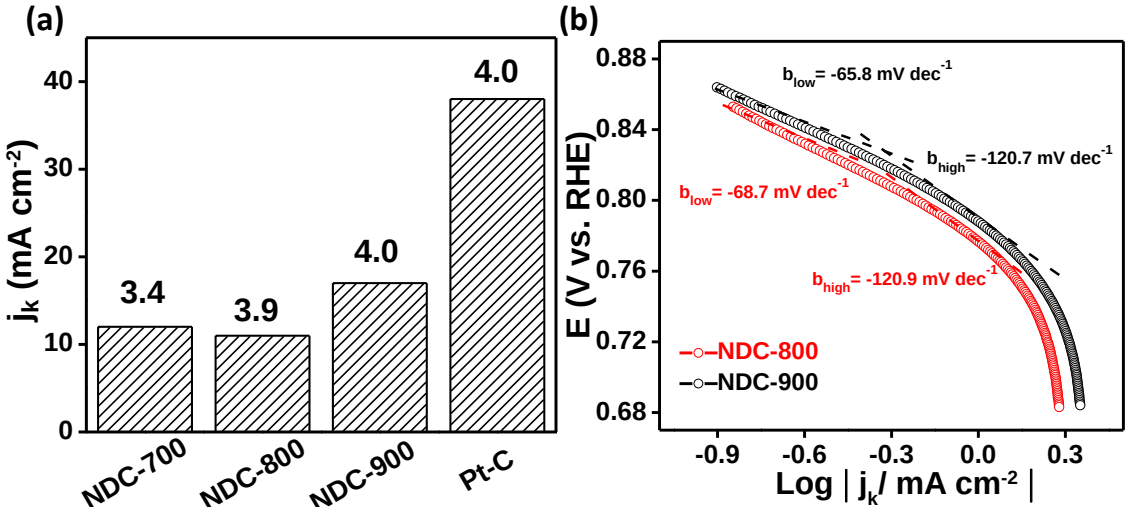

Figure 21. (a) The kinetic current density (j_k) along with the number of electrons transferred per oxygen molecule (on the top of the bars) of various NDCs and Pt/C at 0.39 V. (b) Mass transport corrected Tafel plots of NDC-800 and NDC-900.

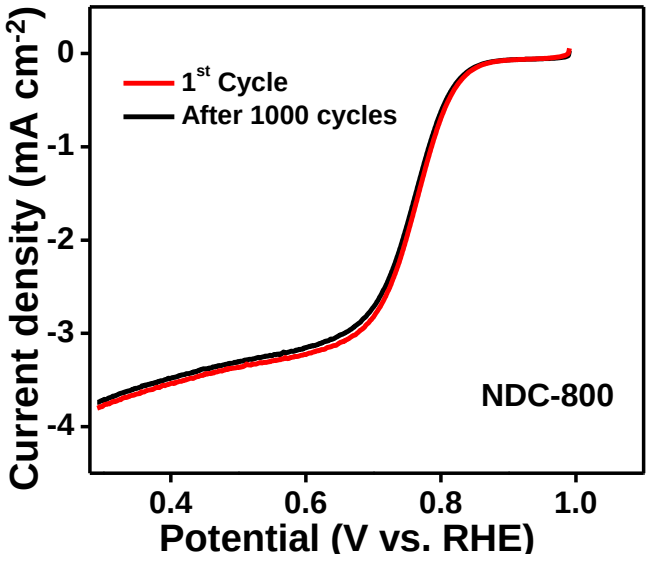

Figure 22. Comparison of linear sweep voltammograms (LSV) of NDC-800 at 1st cycle and after 1000 cycles.

more than other forms (viz. N-2 and N-4), thereby observed enhanced ORR performance.(*48*)

Adsorption mechanisms of O_2 over NDCs were studied using mass-transport corrected Tafel plots **(Figure 21b)** to eliminate diffusion effects on the former. **Figure 21b** indicates the presence of two slopes in the low and high current density regions of NDC-800 (-68.7 mV dec^{-1} and -120.9 mV dec^{-1}) and NDC-900

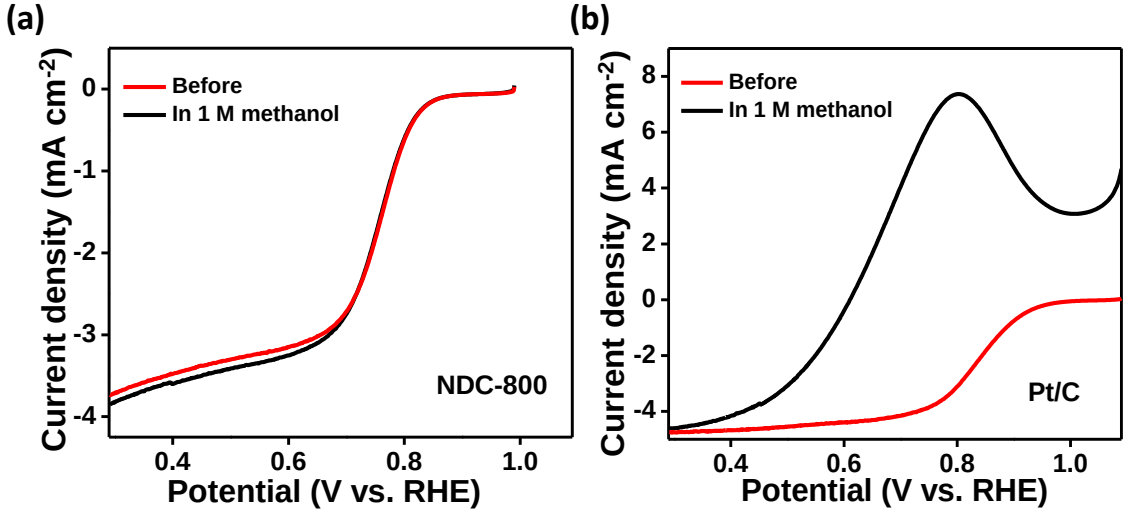

Figure 23. Linear sweep voltammograms (LSV) of NDC-800 (a) and Pt/C (b), before and after addition of methanol to oxygen saturated 0.1 M KOH at 1600 rpm (5 mV s^{-1}).

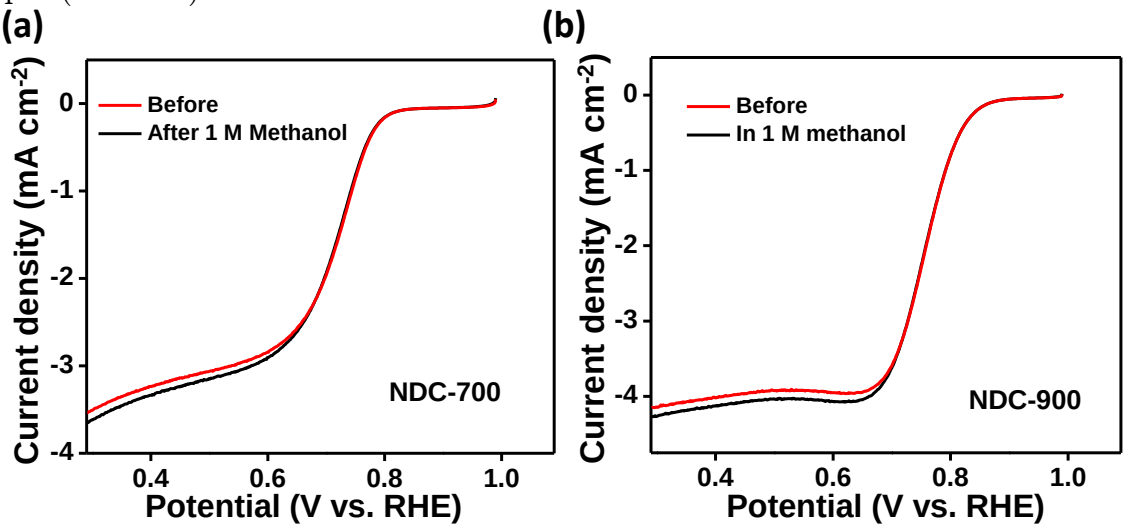

Figure 24. Linear sweep voltammograms (LSV) of NDC-700 (a) and NDC-900 (b), before and after addition of methanol to O_2 saturated 0.1 M KOH at 1600 rpm (5 mV s^{-1}).

(-65.8 mV dec^{-1} and -120.7 mV dec^{-1}) indicating a change of adsorption mechanisms from Temkin to Langmuir(*49, 50*) which are similar to those observed in 40 wt.% Pt/C (-60.0 mV dec^{-1} and -109.0 mV dec^{-1}). This suggests that O_2 adsorption mechanism for NDCs are similar to that of Pt and the observed facile kinetics of the former akin to latter. Fuel crossover is an important challenge in fuel cell applications and the performances of NDCs were investigated in the presence and absence of methanol. Linear sweep voltammograms exhibited stable performance for NDCs both in the presence and absence of 1 M methanol as shown in **Figure 23a** and **Figure 24a-b**,

indicating superior tolerance to methanol crossover effect of the NDCs compared to Pt/C catalyst **(Figure 23b)**. In the case of Pt/C, a huge anodic current(*51*) resulting from oxidation of fuel molecule (methanol) was observed **(Figure 23b)** under similar conditions indicating the importance of NDCs as a stable and durable catalyst in practical applications.

4.5 Conclusions:

In conclusion, we have developed sustainable and efficient mono, heteroatom (N)-doped pore engineered carbon nanostructures (NDCs) with balanced pore architecture, using clay templated strategy as a metal-free efficient bifunctional electrocatalyst for hydrogen production and oxygen reduction that could potentially reduce/replace Pt-based catalysts in future renewable energy sources like r-FCs, FCs and M-O_2 battery. The observed high performances of NDCs can be attributed to unique textural parameters leading to enhanced mass transfer property along with the balanced tuning of electronic properties by heteroatom doping and graphitization aiding in adsorption of species and subsequent electron transfer.

4.6 References:

1. L. Dai, Y. Xue, L. Qu, H.-J. Choi, J.-B. Baek, Metal-Free Catalysts for Oxygen Reduction Reaction. *Chem. Rev.* **115**, 4823 (2015).
2. J. Zhang, Z. Zhao, Z. Xia, L. Dai, A metal-free bifunctional electrocatalyst for oxygen reduction and oxygen evolution reactions. *Nat. Nanotech.* **10**, 444 (2015).
3. Z. Zhao, M. Li, L. Zhang, L. Dai, Z. Xia, Design Principles for Heteroatom-Doped Carbon Nanomaterials as Highly Efficient Catalysts for Fuel Cells and Metal–Air Batteries. *Adv. Mater.* **27**, 6834 (2015).
4. Y. Nie, L. Li, Z. Wei, Recent advancements in Pt and Pt-free catalysts for oxygen reduction reaction. *Chem. Soc. Rev.* **44**, 2168 (2015).
5. S. Park, Y. Shao, J. Liu, Y. Wang, Oxygen electrocatalysts for water electrolyzers and reversible fuel cells: status and perspective. *Energy Environ. Sci.* **5**, 9331 (2012).
6. Y. Zheng, Y. Jiao, M. Jaroniec, S. Z. Qiao, Advancing the Electrochemistry of the Hydrogen-Evolution Reaction through Combining Experiment and Theory. *Angew. Chem. Int. Ed.* **54**, 52 (2015).
7. A. Lasia, in *Handbook of Fuel Cells*. (John Wiley & Sons, Ltd, 2010).

8. M. Wang, Z. Wang, X. Gong, Z. Guo, The intensification technologies to water electrolysis for hydrogen production – A review. *Renewable Sustainable Energy Rev.* **29**, 573 (2014).
9. B. E. Conway, B. V. Tilak, Interfacial processes involving electrocatalytic evolution and oxidation of H_2, and the role of chemisorbed H. *Electrochim. Acta* **47**, 3571 (2002).
10. R. Chaubey, S. Sahu, O. O. James, S. Maity, A review on development of industrial processes and emerging techniques for production of hydrogen from renewable and sustainable sources. *Renewable Sustainable Energy Rev.* **23**, 443 (2013).
11. M. Momirlan, T. N. Veziroglu, The properties of hydrogen as fuel tomorrow in sustainable energy system for a cleaner planet. *Int. J. Hydrogen Energy* **30**, 795 (2005).
12. P. P. Edwards, V. L. Kuznetsov, W. I. F. David, N. P. Brandon, Hydrogen and fuel cells: Towards a sustainable energy future. *Energy Policy* **36**, 4356 (2008).
13. Z. Peng, S. A. Freunberger, Y. Chen, P. G. Bruce, A reversible and higher-rate Li–O_2 battery. *Science* **337**, 563 (2012).
14. J. B. Goodenough, Evolution of Strategies for Modern Rechargeable Batteries. *Acc. Chem. Res.* **46**, 1053 (2013).
15. Y. Zhao *et al.*, Can Boron and Nitrogen Co-doping Improve Oxygen Reduction Reaction Activity of Carbon Nanotubes? *J. Am. Chem. Soc.* **135**, 1201 (2013).
16. K. N. Wood, R. O'Hayre, S. Pylypenko, Recent progress on nitrogen/carbon structures designed for use in energy and sustainability applications. *Energy Environ. Sci.* **7**, 1212 (2014).
17. Y. Zheng *et al.*, Toward Design of Synergistically Active Carbon-Based Catalysts for Electrocatalytic Hydrogen Evolution. *ACS Nano* **8**, 5290 (2014).
18. R. Liu, D. Wu, X. Feng, K. Müllen, Nitrogen-doped ordered mesoporous graphitic arrays with high electrocatalytic activity for oxygen reduction. *Angew. Chem. Int. Ed.* **49**, 2565 (2010).
19. Z.-W. Liu *et al.*, Phosphorus-Doped Graphite Layers with High Electrocatalytic Activity for the O_2 Reduction in an Alkaline Medium. *Angew. Chem. Int. Ed.* **50**, 3257 (2011).
20. A. Aijaz, N. Fujiwara, Q. Xu, From Metal–Organic Framework to Nitrogen-Decorated Nanoporous Carbons: High CO_2 Uptake and Efficient Catalytic Oxygen Reduction. *J. Am. Chem. Soc.* **136**, 6790 (2014).

21. Y. Zheng *et al.*, Hydrogen evolution by a metal-free electrocatalyst. *Nat. Commun.* **5**, 3783 (2014).
22. L. Wei *et al.*, A high-performance metal-free hydrogen-evolution reaction electrocatalyst from bacterium derived carbon. *J. Mater. Chem. A* **3**, 7210 (2015).
23. Y. Ito, W. Cong, T. Fujita, Z. Tang, M. Chen, High Catalytic Activity of Nitrogen and Sulfur Co-Doped Nanoporous Graphene in the Hydrogen Evolution Reaction. *Angew. Chem. Int. Ed.* **54**, 2131 (2015).
24. Y. Zhao, R. Nakamura, K. Kamiya, S. Nakanishi, K. Hashimoto, Nitrogen-doped carbon nanomaterials as non-metal electrocatalysts for water oxidation. *Nat. Commun.* **4**, 2390 (2013).
25. J. Zhang *et al.*, N,P-Codoped Carbon Networks as Efficient Metal-free Bifunctional Catalysts for Oxygen Reduction and Hydrogen Evolution Reactions. *Angew. Chem. Int. Ed.* **55**, 2230 (2016).
26. H. W. Park *et al.*, Bi-Functional N-Doped CNT/Graphene Composite as Highly Active and Durable Electrocatalyst for Metal Air Battery Applications. *J. Electrochem. Soc.* **160**, A2244 (2013).
27. F. Barbir, T. Molter, L. Dalton, Efficiency and weight trade-off analysis of regenerative fuel cells as energy storage for aerospace applications. *Int. J. Hydrogen Energy* **30**, 351 (2005).
28. G. Chen, S. R. Bare, T. E. Mallouk, Development of Supported Bifunctional Electrocatalysts for Unitized Regenerative Fuel Cells. *J. Electrochem. Soc.* **149**, A1092 (2002).
29. K. Sakaushi, K. Uosaki, Highly Efficient Oxygen and Hydrogen Electrocatalytic Activities of Self-Morphogenic Nanoporous Carbon, Nitrogen Architectures. *ChemNanoMat* **2**, 99 (2016).
30. H. Zhao *et al.*, Carbon for the oxygen reduction reaction: a defect mechanism. *J. Mater. Chem. A* **3**, 11736 (2015).
31. G.-L. Chai, Z. Hou, D.-J. Shu, T. Ikeda, K. Terakura, Active Sites and Mechanisms for Oxygen Reduction Reaction on Nitrogen-Doped Carbon Alloy Catalysts: Stone–Wales Defect and Curvature Effect. *J. Am. Chem. Soc.* **136**, 13629 (2014).
32. K. Xia, Q. Gao, J. Jiang, J. Hu, Hierarchical porous carbons with controlled micropores and mesopores for supercapacitor electrode materials. *Carbon* **46**, 1718 (2008).
33. X. Huang, Y. Zhao, Z. Ao, G. Wang, Micelle-Template Synthesis of Nitrogen-Doped Mesoporous Graphene as an Efficient Metal-Free Electrocatalyst for Hydrogen Production. *Sci. Rep.* **4**, 7557 (2014).

34. A. Achari, K. K. R. Datta, M. De, V. P. Dravid, M. Eswaramoorthy, Amphiphilic aminoclay-RGO hybrids: a simple strategy to disperse a high concentration of RGO in water. *Nanoscale* **5**, 5316 (2013).
35. S. Jun *et al.*, Synthesis of New, Nanoporous Carbon with Hexagonally Ordered Mesostructure. *J. Am. Chem. Soc.* **122**, 10712 (2000).
36. B. Tian *et al.*, Novel approaches to synthesize self-supported ultrathin carbon nanowire arrays templated by MCM-41. *Chem. Commun.*, 2726 (2003).
37. X. Huang *et al.*, Functional Nanoporous Graphene Foams with Controlled Pore Sizes. *Adv. Mater.* **24**, 4419 (2012).
38. A. Walcarius, Mesoporous materials and electrochemistry. *Chem. Soc. Rev.* **42**, 4098 (2013).
39. Z. Wang *et al.*, Realizing ordered arrays of nanostructures: A versatile platform for converting and storing energy efficiently. *Nano Energy* **19**, 328 (2016).
40. K. S. W. Sing *et al.*, Reporting physisorption data for gas/solid systems with special reference to the determination of surface area and porosity (Recommendations 1984). *Pure Appl. Chem.* **57**, 603 (1985).
41. W. Wei *et al.*, Nitrogen-Doped Carbon Nanosheets with Size-Defined Mesopores as Highly Efficient Metal-Free Catalyst for the Oxygen Reduction Reaction. *Angew. Chem. Int. Ed.* **53**, 1570 (2014).
42. Z. Chen *et al.*, Core–shell MoO_3–MoS_2 Nanowires for Hydrogen Evolution: A Functional Design for Electrocatalytic Materials. *Nano Lett.* **11**, 4168 (2011).
43. J. Kibsgaard, Z. Chen, B. N. Reinecke, T. F. Jaramillo, Engineering the surface structure of MoS2 to preferentially expose active edge sites for electrocatalysis. *Nat. Mater.* **11**, 963 (2012).
44. J. O. M. Bockris, E. C. Potter, The Mechanism of the Cathodic Hydrogen Evolution Reaction. *J. Electrochem. Soc.* **99**, 169 (April 1, 1952, 1952).
45. J. G. N. Thomas, Kinetics of electrolytic hydrogen evolution and the adsorption of hydrogen by metals. *Trans. Faraday Soc.* **57**, 1603 (1961).
46. A. J. Bard, L. R. Faulkner, *Electrochemical Methods: Fundamentals and Applications, 2nd Edition*. (John Wiley & Sons, 2000).
47. S. Treimer, A. Tang, D. C. Johnson, A Consideration of the Application of Koutecký-Levich Plots in the Diagnoses of Charge-Transfer Mechanisms at Rotated Disk Electrodes. *Electroanalysis* **14**, 165 (2002).

48. G. Panomsuwan, N. Saito, T. Ishizaki, Nitrogen-doped carbon nanoparticles derived from acrylonitrile plasma for electrochemical oxygen reduction. *Phys. Chem. Chem. Phys.* **17**, 6227 (2015).
49. N. Wakabayashi, M. Takeichi, M. Itagaki, H. Uchida, M. Watanabe, Temperature-dependence of oxygen reduction activity at a platinum electrode in an acidic electrolyte solution investigated with a channel flow double electrode. *J. Electroanal. Chem.* **574**, 339 (2005).
50. G. Ma *et al.*, Nitrogen-Doped Hollow Carbon Nanoparticles with Excellent Oxygen Reduction Performances and Their Electrocatalytic Kinetics. *J. Phys. Chem. C* **115**, 25148 (2011).
51. Y.-Z. Chen *et al.*, From Bimetallic Metal-Organic Framework to Porous Carbon: High Surface Area and Multicomponent Active Dopants for Excellent Electrocatalysis. *Adv. Mater.* **27**, 5010 (2015).

Chapter-5

Ultrafast Synthesis of Uniformly Dispersed Co_3O_4 in Highly Interconnected 3D Meso-macroporous Carbon with Enhanced Oxygen Evolution Kinetics

Summary:

Mass transport and charge transfer at an interface plays a detrimental role in governing the electrochemical performance of a material. Wider meso-macropores are expected to enhance the reaction kinetics by facilitating the ion-transport rapidly to and fro from an active interface rapidly thereby continuously regenerating it at accelerated rates. Herein, we report a generic technique to obtain an ultrafast (less than a minute) and easy synthesis of pore engineered 3D carbons prepared from organic precursors with excellent mass transport ability, containing uniformly dispersed low amount of (~1 wt.%) Co in highly graphitized carbon matrix. The obtained catalyst (Co_3O_4@CS) exhibits similar onset potential and superior oxygen evolution kinetics at higher current densities compared to the state-of-the-art catalyst, RuO_2. Moreover, the synthesized material exhibits excellent cycling performance over 2000 cycles. Such performance metric can be attributed to the uniform dispersion of active sites (Co_3O_4) over low density highly interconnected conducting carbon matrix leading to facile mass transport and charge transfer respectively.

(Manuscript submitted.)

5.1 Introduction:

Water electrolyzers(*1, 2*) and fuel cells (FCs)(*3, 4*) are two key players to address future problems pertinent to energy and environmental issues posed by fossil fuels. Generation of H_2/O_2 (water splitting) via renewable resources solves the problem of intermittency in tapping the solar as well as wind energies even in their absences.(*5, 6*) Electrochemical energy generation and storage processes inherit several advantages over conventional fossil fuels: (1) since these technologies are not limited by Carnot cycles, their efficiencies are closer to their theoretical values and (2) energy generation and consumption processes involve near-zero carbon footprint and (3) scope for extending to grid-level storage, fuel cell cars etc.(*7, 8*) Most of the industrial hindrance to the development of the practical prototypes stems from sluggish oxygen evolution kinetics at the anode during water electrolysis (and conversely oxygen reduction reaction, ORR in FCs).(*9-14*) Even the generation of H_2 at the cathode in water electrolyzers is affected by sluggish multi-electron (4e-) kinetics involved in oxygen evolution reaction (OER).(*15, 16*) A large amount of overpotential (η) is required to drive such processes and often elevated temperatures (80 ^{O}C) are employed in the electrolytic cells to lower η when coupled with efficient catalysts to obtain appreciable current densities.(*17, 18*) Therefore, it is clear that O_2 generation has two-fold issues viz. firstly, the evolution of oxygen itself and secondly its interference with hydrogen generation. Consequently, efficient and effective catalysts are required to drive such reactions near their thermodynamic potentials at current densities close to practical applications.(*19*)

Traditionally, Ru based catalysts are used for OER(*15, 20-22*) but the development of practical energy devices is deeply plagued by their prohibitively high cost along with their toxic nature. Alternative earth-abundant elements (Ni, Fe, Co etc.) based systems are explored to carry out above reactions but are hindered by their stabilities under extreme pH conditions.(*6, 17, 23-25*) Metal in the form of oxides are typically non-conducting in nature.(*26-28*) Usually, higher loadings of such oxides are required to obtain significant activity due to the low density of active sites which is further aggravated by poor textural parameters. Even when used in phosphide forms (to enhance conductivity),(*27*) oxide formation at the interface is inevitable (due to the participation of lattice oxygen)(*29*) leading to the loss of the electrode integrity thereby affecting long-term performance.(*27, 30, 31*) Therefore, it is imperative to select low-density carbon supports which will not only be conducting but also

porous in nature for easy access of the electrolytes.(*32-35*) Furthermore, the catalytic oxides should be in intimate contact with the conducting carbon phase which ensures minimum loading with maximum dispersion resulting in higher activity at much lower loadings due to greater number of exposed sites.(*36, 37*) Also, the rate of accessibility of active sites will be synergistically boosted by the rapid flux of electrolytes aided by the favorable textural parameters of the composites.(*38, 39*) The incorporation of oxides on the preformed carbon supports (carbon nanotubes, graphene etc.)(*40-42*) often lead to poor interfacial contact leading to high internal polarization and leaching of oxides thus compromising its stability. Utilizing the conductive property of carbon by in situ phase engineering with non-conducting metal oxides and implementing beneficial textural parameters of carbon (high dispersion of active sites along with its excellent accessibility) would lead to the development of synergistic catalyst system with superior activity.(*38, 43*) Additionally, lower loading of the metal-oxide along with its embedded nature in carbon would mitigate leaching issues.

5.2 Scope of the present investigation:

Herein we report an innovative, ultrafast (less than a minute) one-step strategy to synthesize Co_3O_4 embedded carbon composites whose OER activity is excellent compared to state-of-the-art catalyst (RuO_2). The strategy adopted here is a scalable combustion technique involving simple carbon precursor piperidine mixed with Co(II) acetate as a fuel. Addition of cobalt(II) acetate to excess piperidine results in the formation of Co(II)-piperidine complex indicated by an instantaneous color change from pink (Co(II) acetate) to a violet solution which was further confirmed by UV-Vis spectroscopy **(Figure 1)**. The Co containing piperidine solution thus obtained was allowed to combust in a controlled way using capillarity action **(Figure 1)** of a cotton wick to produce Co_3O_4 containing carbon soot (Co_3O_4@CS) over a glass slide as shown in **Figure 2**. For control experiments, blank piperidine without Co(II) precursor was used as a fuel to obtain CS.

5.3 Experimental procedures:

5.3.1 Materials used:

Co(II) acetate tetrahydrate and Nafion® perfluorinated resin solution were procured from Sigma-Aldrich. KOH pellets and HNO_3 (69%) were obtained from Merck. H_2O_2 (30%) was purchased from SD Fine Chemicals. Piperidine was acquired from Spectrochem.

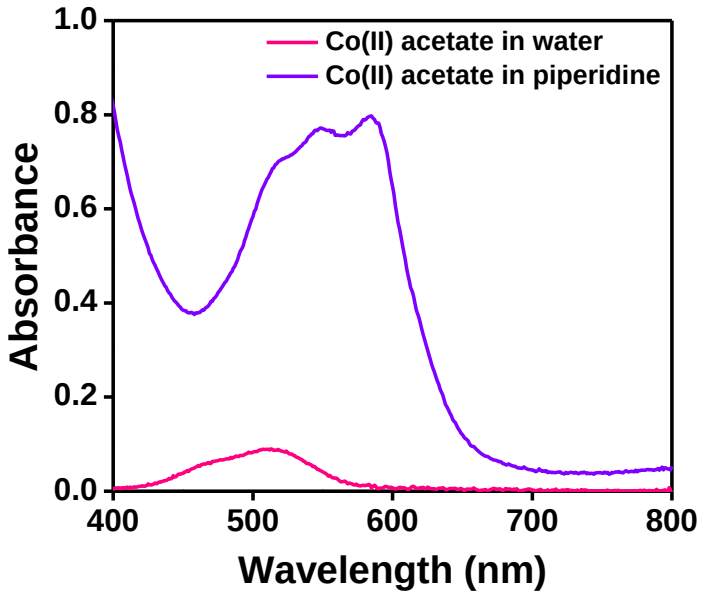

Figure 1. UV-Vis spectra of 15.0 mM Co(II) acetate in piperidine and 3.2 mM Co(II) acetate in water. A distinct shift in the absorbance bands of Co(II) acetate in piperidine compared to that in water along with the concurrent emergence of new bands indicates the complex formation between Co(II) and piperidine. Also, to be noted that the concentration difference of the salts in two different media and their respective absorbances.

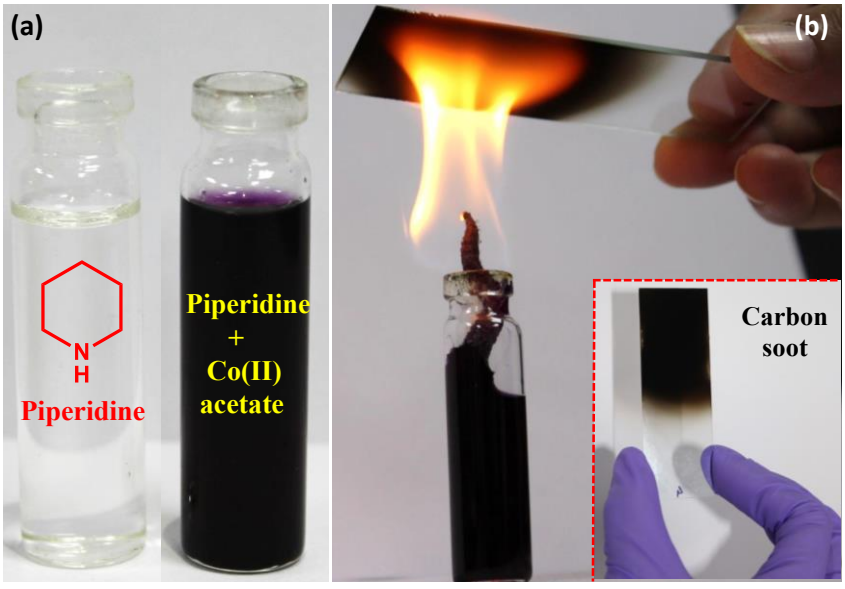

Figure 2. (a) Digital photographs indicating the distinct color change (violet) upon complexation of Co(II) acetate (pink; not shown here) with piperidine. (b) Images showing the utilization of piperidine and cobalt acetate complex as a fuel for the synthesis of carbon soot. The inset shows the collected soot over a glass slide.

5.3.2 Instrumentation and characterization techniques:

Technai F30 UHR electron microscope operating at an accelerating voltage of 200 kV was used for acquiring transmission electron microscopic (TEM) images of the samples. Field emission scanning electron microscopic (FESEM) images of the samples were obtained via. Nova-Nano SEM-600 (FEI, Netherlands). All the gas sorption measurements were performed on Autosorb-iQ_2 (Quantachrome corp.) at 77 K using ultrahigh pure N_2 (99.9995%) and prior to analyses the synthesized samples were degassed under high vacuum for 12 h at 423 K. X-ray photoelectron spectroscopic (XPS) analyses were performed using Omicron EA 125 spectrometer using Al-K_α (1486.6 eV) as the X-ray source. Jobin Yvon LabRam HR spectrometer equipped with frequency-doubled Nd:YAG solid-state laser (532 nm) was used for acquiring Raman spectra of the samples. Electrochemical measurements for evaluating oxygen evolution activities of the synthesized samples were performed on the electrochemical workstation (760E, USA) obtained from CH Instruments, Inc. Inductively coupled plasma optical emission spectroscopic (ICP-OES) analyses were performed on Perkin-Elmer Optima 7000DV instrument to ascertain Co composition in the samples.

5.3.3 Synthesis of Co_3O_4@CS/CS:

30mg of Co(II) acetate tetrahydrate was added to excess piperidine (3 mL) taken in a 15 mL glass vial resulting in the formation of Co(II)-piperidine complex indicated by instantaneous colour change from pink (Co(II) acetate) to violet colored solution **(Figure 1)** which was further confirmed by UV-Vis spectroscopy. The Co containing piperidine solution thus obtained was allowed to combust in a controlled way using the capillary action of a cotton wick to produce Co_3O_4 containing carbon soot (Co_3O_4@CS) over a glass slide as shown in **Figure 2**. The glass slide was held just above the middle of the flame (~1200-1330 ^{O}C, nearly 70% height from the base of the flame, **Figure 2**). Keeping the glass slide too low or too high didn't result in substantial soot formation which can be easily rationalized in terms of types of species present, oxygen concentration and temperature profiling of the candle flame.(*44, 45*) It is to be noted that there is continuous variation of temperature along the flame length with distinct colour zones reflecting the different types of species present. (*44, 45*) For control experiments, blank piperidine without Co(II) precursor was used as a fuel to obtain CS. The resultant electrocatalysts (Co_3O_4@CS/CS) was obtained by simple scratching of the glass surface and was used for further measurements and analyses.

5.3.4 Electrode preparation and electrochemical measurements:

Catalyst ink was prepared in the following way: 2 mg of Co_3O_4@CS was ultrasonically dispersed in water (0.7 mL)-isopropanol (0.3 mL) mixture containing 5 µL Nafion® (5 wt.%) solution for 6 h until a homogeneous suspension was obtained. Thereafter, 5 µL of the above catalyst ink was drop casted onto a pre-clean glassy carbon (GC) electrode (3 mm diameter) and allowed to dry in open atmosphere. The catalyst (Co_3O_4@CS/CS) modified GC electrode was used as a working electrode.

Electrochemical measurements were carried out in a standard three-electrode set-up with Hg/HgO (1.0 M NaOH) and large surface area Pt coil as a reference and counter electrode respectively.

5.3.5 Sample preparation for ICP-OES analyses:

10.7 mg of Co_3O_4@CS was dispersed with 3 mL of 30% H_2O_2 taken in a 15 mL glass vial and kept at 80 °C overnight. Afterwards, 3 mL of HNO_3 (69%) was added to the above residue and was further heated at 120 °C with continuous stirring for 12 h. Thereafter, 10 mL of water was added to the above vial and the obtained solution was used for ICP analysis.

5.4 Results and discussions:

Field emission scanning electron microscopic (FESEM) images of Co_3O_4@CS **(Figure 3a)** and CS **(Figure 4a)** show interconnected foamy network of carbon with ample porosity. Transmission electron microscopic (TEM) investigations **(Figure 3b and Figure 4b-c)** further support FESEM data indicating prominent interconnected porous structure with hierarchical distribution of pores at meso-macro length scales (>30 nm). High-resolution transmission electron microscopic (HRTEM) investigations of Co_3O_4@CS reveal intimate and uniform dispersion of Co_3O_4 particles in highly graphitic carbon which is conducive for good electronic conductivity **(Figure 3c)**. Most of the particles were found to be smaller than 2 nm while at very few places bigger particles (5-10 nm) were also observed. Lattice spacings analyzed for a number of regions suggests that the dispersed nanoparticles predominantly exist as Co_3O_4 species **(Figure 3d-e)**. The (220) planes (0.286 nm) and (311) planes (0.244 nm) of Co_3O_4 were observed in most of the regions **(Figure 3d-e)**.(*46*) In addition at fewer places, (400) planes (0.202 nm) of Co_3O_4 were also present.(*46*) Selected area electron diffraction (SAED) pattern of Co_3O_4@CS shows **(Figure 3f)** the presence of (220), (311),

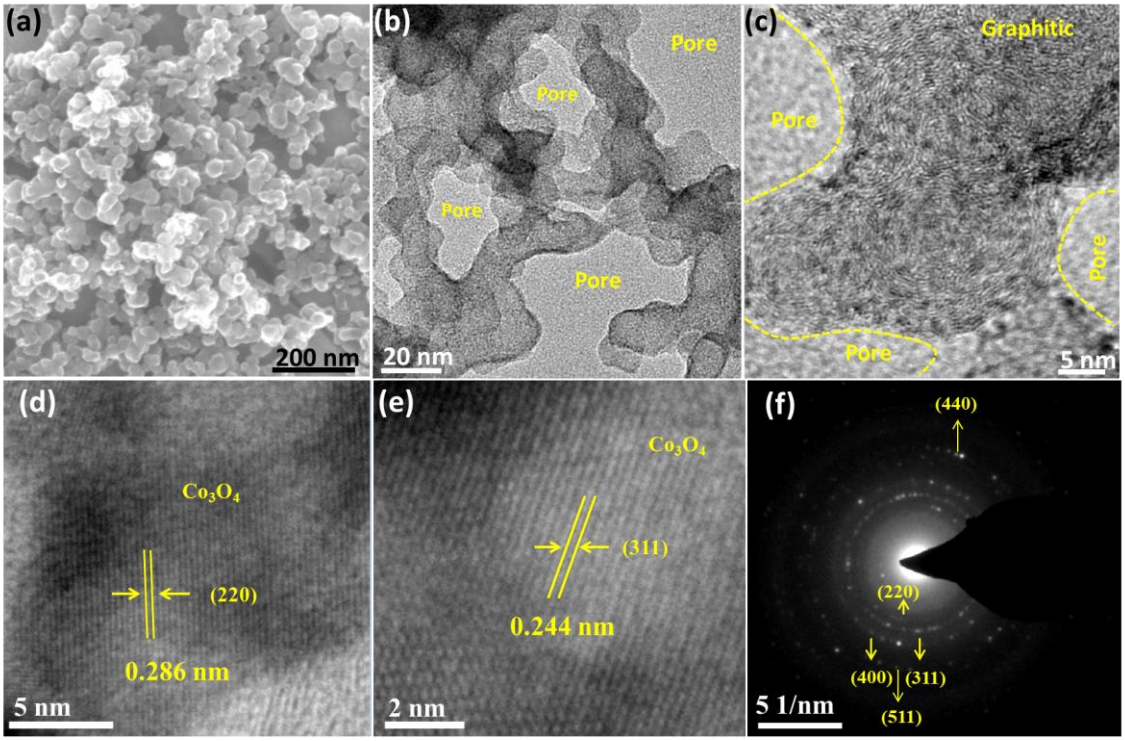

Figure 3. (a) FESEM and (b) TEM images of Co_3O_4@CS showing 3D mesh network with highly interconnected macro-mesoporous structure. (c) HRTEM image of Co_3O_4@CS showing graphitic nature of the carbon walls along with highly dispersed Co_3O_4 nanoparticles. (d-e) HRTEM images of Co_3O_4@CS indicating lattice fringes corresponding to (220) and (311) planes of Co_3O_4. (e) Selected area electron diffraction (SAED) pattern of Co_3O_4@CS with indexed bright spots corresponding to the (220), (311), (400), (511) and (440) planes of Co_3O_4 superimposed over polycrystalline graphitic carbon rings.

(400), (511) and (440) planes associated with polycrystalline Co_3O_4.(*47*) The Co_3O_4 phase was further confirmed by the presence of very weak peaks (a corollary to low loading of Co ~1.wt.%) at 36.9° and 31.3 ° (2θ) in powder X-ray diffraction pattern **(Figure 5a-b)** corresponding to (311) and (220) planes respectively which corroborates well with SAED pattern **(Figure 3f)**. TEM analyses reveals high degree of graphitization in Co_3O_4@CS **(Figure 3c)** as compared to CS **(Figure 4c)** probably due to metal oxide nanoparticle induced catalytic graphitization.(*48*) N_2 sorption measurements performed at 77 K in order to evaluate textural properties of the synthesized electrocatalysts (Co_3O_4@CS and CS) indicate a typical type II behavior(*49*) **(Figure 6a)** indicating interconnected meso-macroporous structure. Furthermore, the interconnected hierarchical structure is well supported by the quenched solid density functional theory (QSDFT) calculated pore size distributions.(*50*)

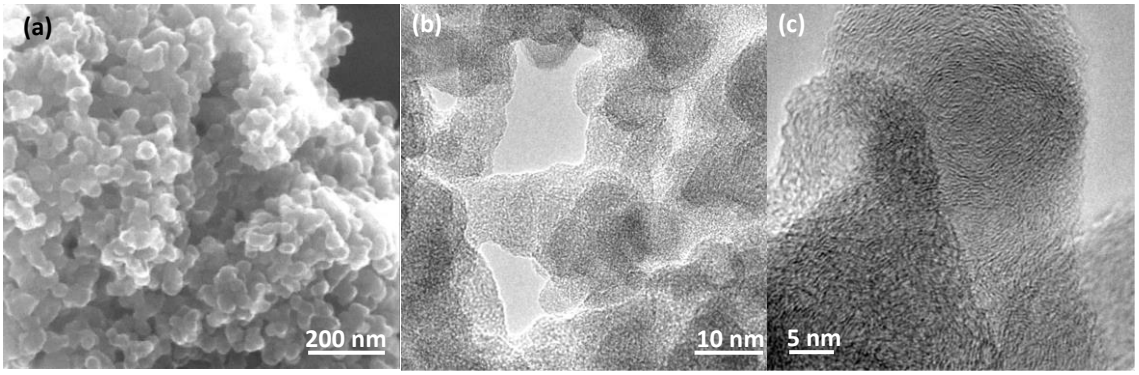

Figure 4. (a) FESEM image of CS whereas (b-c) are TEM images of CS.

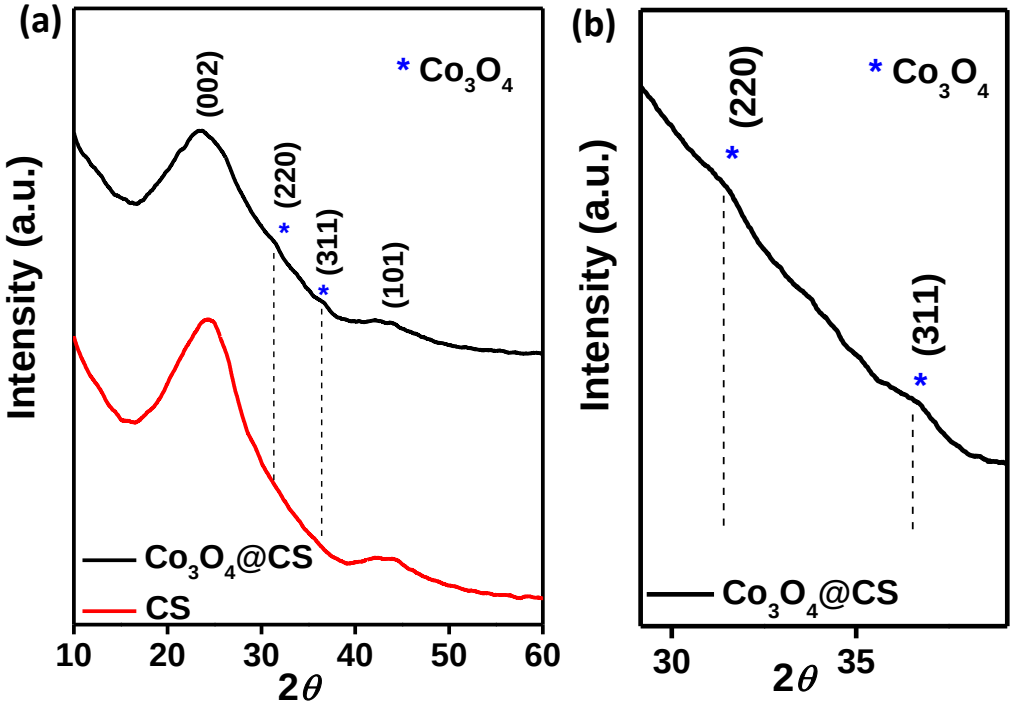

Figure 5. (a) PXRD patterns of CS and Co_3O_4@CS. The peak marked in asterisk corresponds to (220) and (311) plane of Co_3O_4. (b) Shows expanded view of a region in (a), indicating (220) and (311) plane of the Co_3O_4. Also, to be noted that (311) reflection has higher intensity compared to (220) peaks.

Both CS and Co_3O_4@CS shows a wide range of pore size distribution **(Figure 6a-b)** in the entire mesopore regime which further supports the observed foamy texture of the materials and results from the inter-particle induced porosity with aggregation density dictating the non-vanishing distribution. BET analyses shows higher specific surface area (SSA) for CS (165 $m^2 g^{-1}$) compared to that of Co_3O_4@CS (124 $m^2 g^{-1}$).

Since, both the materials are synthesized in an analogous way the observed difference in SSA can be attributed to the higher degree of the graphitization

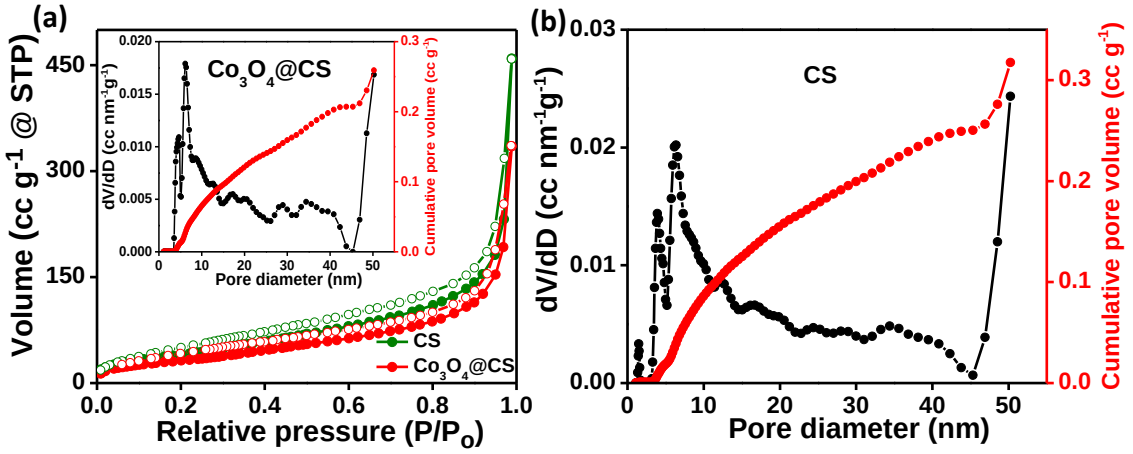

Figure 6. (a) N_2 adsorption (closed symbols)-desorption (open symbols) isotherms of Co_3O_4@CS and CS. The inset shows pore size distribution of Co_3O_4@CS along with corresponding cumulative uptake calculated via QSDFT method. (b) Pore size distribution along with cumulative uptake for CS.

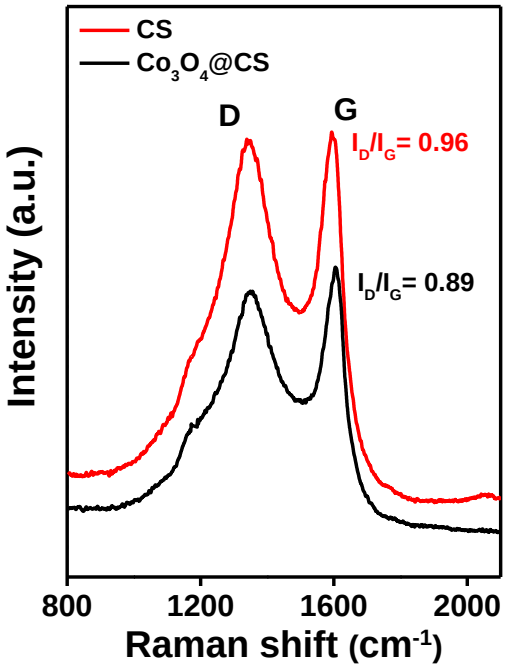

Figure 7. Raman spectra of CS and Co_3O_4@CS.

(as evident from TEM images; **Figure 3c** and **Figure 4c** and is further confirmed by impedance measurements; *vide infra*) in Co_3O_4@CS induced by the presence of Co.(*48, 51, 52*) The observation of higher intensity of G band (compared to D band) in the Raman spectra for Co_3O_4@CS ($I_D/I_G = 0.89$) as compared to CS ($I_D/I_G = 0.96$) **(Figure 7)** further supports the positive role of metal/metal-oxide nanoparticles in inducing higher degree of graphitization in the former.(*48, 53*) Inductively coupled optical emission spectroscopic (ICP-OES) analysis of

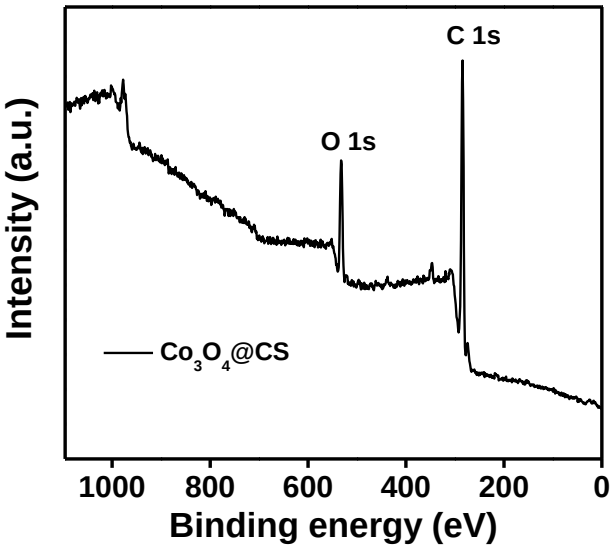

Figure 8. XPS survey spectrum of Co_3O_4@CS.

Co_3O_4@CS indicates that the Co content of the sample is around 1.0 wt.%. However, X-ray photoelectron spectroscopic investigations did not show any Co signal **(Figure 8)** which can be attributed to the combined effect of low cobalt loading along with the fact that the analyses is surface sensitive with a small penetration depth of the photons (1-10 nm).(*54*) Prominent C 1s (284.5 eV) and O 1s (532.5 eV) were present in the survey scan along with concomitant absent of N 1s which can be attributed to the implemented combustion technique for carbon synthesis as the thermodynamic equilibrium favors the formation of N_2 or nitrogen oxides rather than doping.

OER activity of the Co_3O_4@CS was evaluated in 1.0 M KOH and was compared with CS and state-of-the-art catalyst RuO_2 (Sigma-Aldrich). Polarized linear sweep voltammograms (LSVs) at rotating disk electrode (RDE) indicates **(Figure 9a)** that the activity of Co_3O_4@CS is similar to that of RuO_2 in terms of the onset potential. However, the activity of Co_3O_4@CS showed significant improvement at higher overpotentials (η). For instance, RuO_2 (1.54 V) requires 20 mV higher overpotential compared to Co_3O_4@CS @CS (1.52 V) to achieve an anodic current density of 10 mA cm^{-2}. While for the current densities of 20 mA cm^{-2} and 30 mA cm^{-2} the differences being 40 mV and 70 mV respectively. Since an electrochemical current is a measure of the kinetics of a reaction, the observed improved current density (j) for Co_3O_4@CS results from better oxygen evolution kinetics. Such kinetics stems from the accelerated gas detachment at the active interfaces or electrodics (highly dispersed Co_3O_4 in low density conducting carbon matrix) synergistically aided by superior mass transport properties resulting from highly interconnected meso-macroporous network

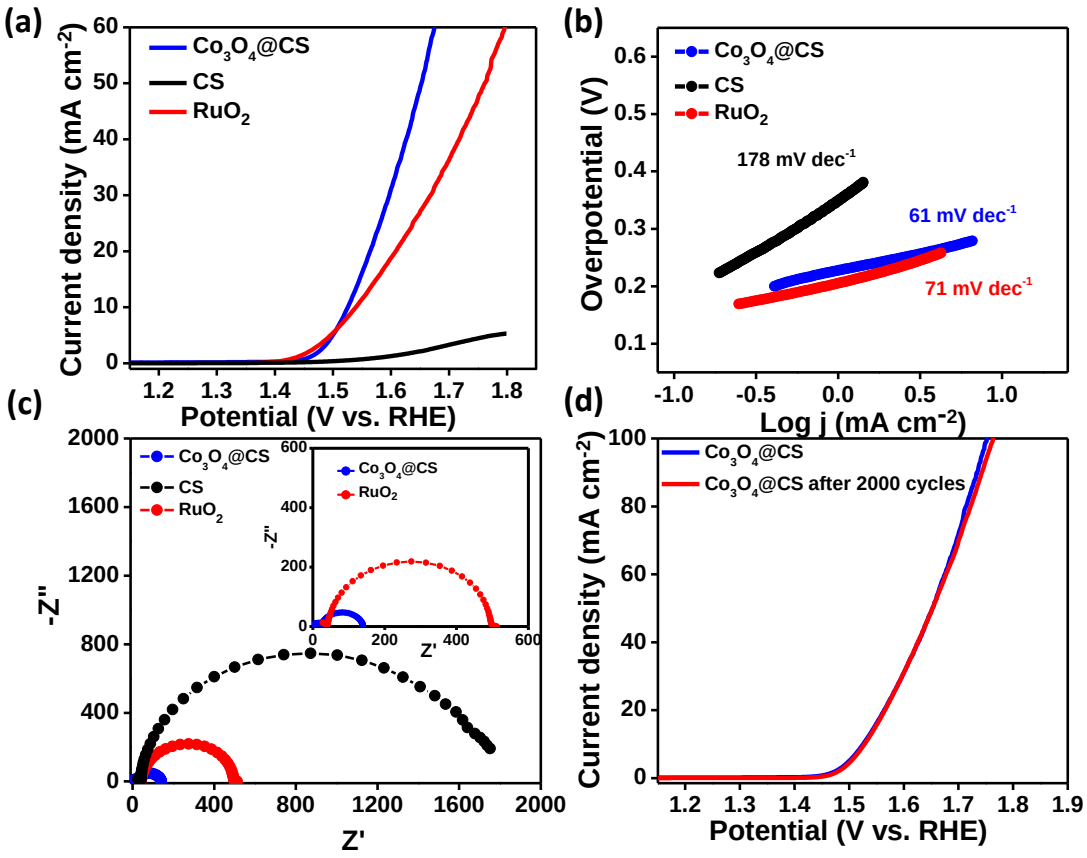

Figure 9. (a) Polarized LSVs at RDE for Co_3O_4@CS, CS, and RuO_2 with corresponding Tafel analyses (b) in their respective kinetic regions. (c) EIS data indicating least charge transfer resistance for Co_3O_4@CS; inset shows the expanded view of the higher frequency region. (d) Stability performance of Co_3O_4@CS before and after 2000 cycles.

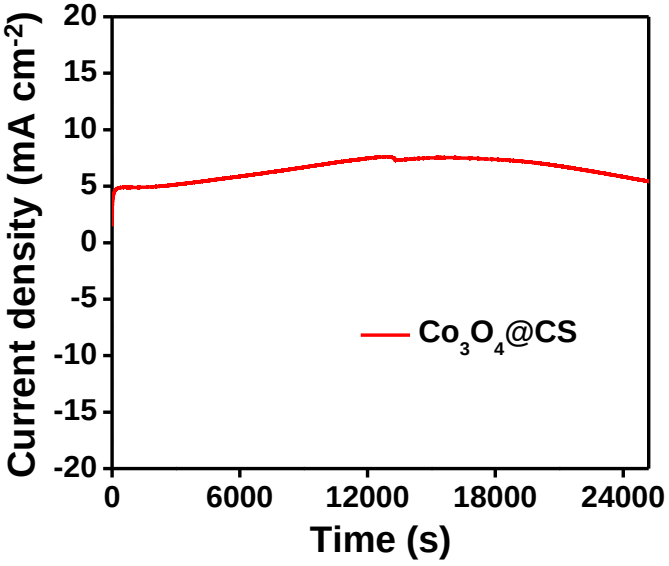

Figure 10. i-t curve of Co_3O_4@CS.

Material	η_{10} (mV)	Tafel slope (mV dec^{-1})	Co loading	Ref.
Co_3O_4@CS	290	61	1 wt.%	Present Work
Co embedded N-doped Carbon nanotubes	200	50	1.71 wt.%	(*55*)
N-doped graphene supported Co@CoO nanoparticles	350	68	45.9 wt.%	(*56*)
Co embedded N-doped graphene	430	-	0.5 at.% (from XPS)	(*57*)
Co_3O_4 nanoparticles on N-doped Carbon	300	83	-	(*58*)
Cobalt phosphide doped N-doped C nanostructures	320	49	-	(*59*)
$Co_3(PO4)_2$ nanoparticles embedded in N-doped Carbon	290	82	13.4 wt.%	(*60*)
In situ CoO-Co/ N-doped Carbon	260	-	29.6 wt.%	(*61*)
Co_3O_4 nanocrystals on reduced graphene oxide	310	67	20 at.% (from XPS)	(*62*)
Co nanoparticles embedded in N-doped Carbon	371	61	60.8 wt.%	(*63*)
ZIF-67-derived Co-NC@CoP-NC nanopolyhedra	330	79	CoP 45 wt.% and Co is 55 wt.%	(*64*)

Table 1. Comparison of OER parameters of some of the heteroatom doped carbon-Co composites with Co_3O_4@CS.

leading to the rapid generation of electrocatalytically active sites per unit time. Whereas, the activity of CS was found to be inferior compared to both RuO_2 and Co_3O_4@CS **(Figure 9a)**. Tafel analyses in the kinetically dominant region reveal smaller value for Co_3O_4@CS (61 mV dec^{-1}) compared to RuO_2 (71 mV dec^{-1}) and as well as CS (178 mV dec^{-1}) indicating improved OER kinetics of the former **(Figure 9b)**. To gain insights into the observed OER performance

electrochemical impedance spectroscopic (EIS) measurements were performed at their respective onset potentials. Clearly, Co_3O_4@CS shows least charge transfer resistance (R_{ct}) **(Figure 9c)** exhibiting a value of (142 **Ω**) which is much smaller compared to RuO_2 (497 **Ω**) and CS (1770 **Ω**) indicating excellent electronic conductivity of the former. Since oxygen evolution is a multi-electron ($4e^-$) process the efficiency of such faradaic process is governed by the effectiveness with which the electrons are transferred to the adsorbed intermediates which in turn is governed by the conductivity of the adsorbent. Clearly, the observed activity of the Co_3O_4@CS at least partially can be attributed to the excellent conducting nature of the carbon matrix. Practical implications of such catalysts in industrial water electrolyzers are governed by their cyclic stability performance. Accelerated degradation test reveal superior stability of Co_3O_4@CS even after 2000 cycles **(Figure 9d)**. The observed performance of Co_3O_4@CS is much better compared to other heteroatom-doped carbon systems with higher Co loading reported previously in terms of overpotential at a current density of 10 mA cm^{-2} as shown in **Table 1.**

Furthermore, chronoamperometric performance at 5 mA cm^{-2} indicates stable performance over 7 h. The increase in current after sometime can be attributed to the better wettability of the electrode during the run leading to better exposure of active sites.

5.5 Conclusions:

In conclusion, we have shown that metal salt complexed organic solvents (Co(II) and piperidine in our case) can be directly used as fuel to synthesize metal/metal-oxide containing carbon composites. The synthesized material on account of its unique pore architecture and highly accessible active sites shows excellent OER activity in terms of kinetics compared to the state-of-the-art catalyst at higher overpotentials.

5.6 References:

1. M. Carmo, D. L. Fritz, J. Mergel, D. Stolten, A comprehensive review on PEM water electrolysis. *Int. J. Hydrogen Energy* **38**, 4901 (2013).
2. S. Park, Y. Shao, J. Liu, Y. Wang, Oxygen electrocatalysts for water electrolyzers and reversible fuel cells: status and perspective. *Energy Environ. Sci.* **5**, 9331 (2012).
3. A. Lasia, in *Handbook of Fuel Cells*. (John Wiley & Sons, Ltd, 2010).

4. P. P. Edwards, V. L. Kuznetsov, W. I. F. David, N. P. Brandon, Hydrogen and fuel cells: Towards a sustainable energy future. *Energy Policy* **36**, 4356 (2008).
5. N. S. Lewis, D. G. Nocera, Powering the planet: Chemical challenges in solar energy utilization. *Proc. Natl. Acad. Sci.* **103**, 15729 (2006).
6. I. Roger, M. A. Shipman, M. D. Symes, Earth-abundant catalysts for electrochemical and photoelectrochemical water splitting. *Nat. Rev. Chem.* **1**, 0003 (2017).
7. J. O. M. Bockris, A. K. N. Reddy, M. E. Gamboa-Aldeco, *Modern Electrochemistry 2A: Fundamentals of Electrodics*. (Springer US, 2001).
8. J. O. M. Bockris, A. K. N. Reddy, *Modern Electrochemistry 2B: Electrodics in Chemistry, Engineering, Biology and Environmental Science*. (Springer, 1998).
9. I. Katsounaros, S. Cherevko, A. R. Zeradjanin, K. J. J. Mayrhofer, Oxygen Electrochemistry as a Cornerstone for Sustainable Energy Conversion. *Angew. Chem. Int. Ed.* **53**, 102 (2014).
10. W. T. Hong *et al.*, Toward the rational design of non-precious transition metal oxides for oxygen electrocatalysis. *Energy Environ. Sci.* **8**, 1404 (2015).
11. M. S. Burke, L. J. Enman, A. S. Batchellor, S. Zou, S. W. Boettcher, Oxygen Evolution Reaction Electrocatalysis on Transition Metal Oxides and (Oxy)hydroxides: Activity Trends and Design Principles. *Chem. Mater.* **27**, 7549 (2015).
12. A. A. Gewirth, M. S. Thorum, Electroreduction of Dioxygen for Fuel-Cell Applications: Materials and Challenges. *Inorg. Chem.* **49**, 3557 (2010).
13. L. Dai, Y. Xue, L. Qu, H.-J. Choi, J.-B. Baek, Metal-Free Catalysts for Oxygen Reduction Reaction. *Chem. Rev.* **115**, 4823 (2015).
14. J. Zhang, Z. Zhao, Z. Xia, L. Dai, A metal-free bifunctional electrocatalyst for oxygen reduction and oxygen evolution reactions. *Nat Nanotech.* **10**, 444 (2015).
15. M. G. Walter *et al.*, Solar Water Splitting Cells. *Chem. Rev.* **110**, 6446 (2010/11/10, 2010).
16. A. Dutta, A. K. Samantara, S. K. Dutta, B. K. Jena, N. Pradhan, Surface-Oxidized Dicobalt Phosphide Nanoneedles as a Nonprecious, Durable, and Efficient OER Catalyst. *ACS Energy Lett.* **1**, 169 (2016).
17. P. Atkins, J. de Paula, *Atkins' Physical Chemistry*. (OUP Oxford, 2010).

18. C. C. L. McCrory *et al.*, Benchmarking Hydrogen Evolving Reaction and Oxygen Evolving Reaction Electrocatalysts for Solar Water Splitting Devices. *J. Am. Chem. Soc.* **137**, 4347 (2015).
19. M. Kuang, G. Zheng, Nanostructured Bifunctional Redox Electrocatalysts. *Small* **12**, 5656 (2016).
20. M. Wohlfahrt-Mehrens, J. Heitbaum, Oxygen evolution on Ru and RuO_2 electrodes studied using isotope labelling and on-line mass spectrometry. *J. Electroanal. Chem.* **237**, 251 (1987).
21. M. E. G. Lyons, S. Floquet, Mechanism of oxygen reactions at porous oxide electrodes. Part 2-Oxygen evolution at RuO_2, IrO_2 and $Ir_xRu_{1-x}O_2$ electrodes in aqueous acid and alkaline solution. *Phys. Chem. Chem. Phys.* **13**, 5314 (2011).
22. Y. Lee, J. Suntivich, K. J. May, E. E. Perry, Y. Shao-Horn, Synthesis and Activities of Rutile IrO_2 and RuO_2 Nanoparticles for Oxygen Evolution in Acid and Alkaline Solutions. *J. Phys. Chem. Lett.* **3**, 399 (2012).
23. X. Liu, B. You, Y. Sun, Facile Surface Modification of Ubiquitous Stainless Steel Led to Competent Electrocatalysts for Overall Water Splitting. *ACS Sustainable Chem. Eng.* **5**, 4778 (2017).
24. F. Moureaux, P. Stevens, G. Toussaint, M. Chatenet, Development of an oxygen-evolution electrode from 316L stainless steel: Application to the oxygen evolution reaction in aqueous lithium–air batteries. *J. Power Sources* **229**, 123 (2013).
25. F. Yu, F. Li, L. Sun, Stainless steel as an efficient electrocatalyst for water oxidation in alkaline solution. *Int. J. Hydrogen Energy* **41**, 5230 (2016).
26. C. C. L. McCrory, S. Jung, J. C. Peters, T. F. Jaramillo, Benchmarking Heterogeneous Electrocatalysts for the Oxygen Evolution Reaction. *J. Am. Chem. Soc.* **135**, 16977 (2013).
27. A. Dutta, N. Pradhan, Developments of Metal Phosphides as Efficient OER Precatalysts. *J. Phys. Chem. Lett.* **8**, 144 (2017).
28. J. Suntivich, K. J. May, H. A. Gasteiger, J. B. Goodenough, Y. Shao-Horn, A Perovskite Oxide Optimized for Oxygen Evolution Catalysis from Molecular Orbital Principles. *Science* **334**, 1383 (2011).
29. X. Rong, J. Parolin, A. M. Kolpak, A Fundamental Relationship between Reaction Mechanism and Stability in Metal Oxide Catalysts for Oxygen Evolution. *ACS Catalysis* **6**, 1153 (2016).

30. A. Grimaud *et al.*, Activating lattice oxygen redox reactions in metal oxides to catalyse oxygen evolution. *Nat. Chem.* **9**, 457 (2017).
31. J. O. Bockris, T. Otagawa, Mechanism of oxygen evolution on perovskites. *J. Phys. Chem.* **87**, 2960 (11983).
32. F. Rodríguez-reinoso, The role of carbon materials in heterogeneous catalysis. *Carbon* **36**, 159 (1998).
33. Y. Yang, K. Chiang, N. Burke, Porous carbon-supported catalysts for energy and environmental applications: A short review. *Catal. Today* **178**, 197 (2011).
34. I. Matos, M. Bernardo, I. Fonseca, Porous carbon: A versatile material for catalysis. *Catal. Today* **285**, 194 (2017).
35. Y.-C. Park, H. Tokiwa, K. Kakinuma, M. Watanabe, M. Uchida, Effects of carbon supports on Pt distribution, ionomer coverage and cathode performance for polymer electrolyte fuel cells. *J. Power Sources* **315**, 179 (2016).
36. X. Liu, I. S. Amiinu, S. Liu, K. Cheng, S. Mu, Transition metal/nitrogen dual-doped mesoporous graphene-like carbon nanosheets for the oxygen reduction and evolution reactions. *Nanoscale* **8**, 13311 (2016).
37. L. Shang *et al.*, Well-Dispersed ZIF-Derived Co,N-Co-doped Carbon Nanoframes through Mesoporous-Silica-Protected Calcination as Efficient Oxygen Reduction Electrocatalysts. *Adv. Mater.* **28**, 1668 (2016).
38. H. Sun *et al.*, Three-dimensional holey-graphene/niobia composite architectures for ultrahigh-rate energy storage. *Science* **356**, 599 (2017).
39. H. Chen *et al.*, Ultrafast all-climate aluminum-graphene battery with quarter-million cycle life. *Science Adv.* **3**, (2017).
40. Y.-M. Zhao *et al.*, Cobalt and Iron Oxides Co-supported on Carbon Nanotubes as an Efficient Bifunctional Catalyst for Enhanced Electrocatalytic Activity in Oxygen Reduction and Oxygen Evolution Reactions. *ChemistrySelect* **3**, 207 (2018).
41. D. Zhou *et al.*, NiCoFe-Layered Double Hydroxides/N-Doped Graphene Oxide Array Colloid Composite as an Efficient Bifunctional Catalyst for Oxygen Electrocatalytic Reactions. *Adv. Energy Mater.*, 1701905.
42. D. H. Youn *et al.*, One-pot synthesis of NiFe layered double hydroxide/reduced graphene oxide composite as an efficient electrocatalyst for electrochemical and photoelectrochemical water oxidation. *J. Power Sources* **294**, 437 (2015).
43. W. Li, J. Liu, D. Zhao, Mesoporous materials for energy conversion and storage devices. *Nat. Rev. Mater.* **1**, 16023 (2016).

44. M. Faraday, *The Chemical History of a Candle*. (Dover Publications, 1885).
45. Z. Su, W. Zhou, Y. Zhang, New insight into the soot nanoparticles in a candle flame. *Chem. Commun.* **47**, 4700 (2011).
46. K. Liu *et al.*, N-Doped carbon supported Co_3O_4 nanoparticles as an advanced electrocatalyst for the oxygen reduction reaction in Al-air batteries. *RSC Advances* **6**, 55552 (2016).
47. S. Kalasina, N. Phattharasupakun, M. Sawangphruk, A new energy conversion and storage device of cobalt oxide nanosheets. *J. Mater. Chem. A* **6**, 36 (2018).
48. J. Hoekstra *et al.*, Base Metal Catalyzed Graphitization of Cellulose: A Combined Raman Spectroscopy, Temperature-Dependent X-ray Diffraction and High-Resolution Transmission Electron Microscopy Study. *J. Phys. Chem. C* **119**, 10653 (2015).
49. K. S. W. Sing *et al.*, Reporting physisorption data for gas/solid systems with special reference to the determination of surface area and porosity (Recommendations 1984). *Pure Appl. Chem.* **57**, 603 (1985).
50. A. V. Neimark, Y. Lin, P. I. Ravikovitch, M. Thommes, Quenched solid density functional theory and pore size analysis of micro-mesoporous carbons. *Carbon* **47**, 1617 (2009).
51. L. Yu, L. Sui, Y. Qin, F. Du, Z. Cui, Catalytic synthesis of carbon nanofibers and nanotubes by the pyrolysis of acetylene with iron nanoparticles prepared using a hydrogen-arc plasma method. *Mater. Lett.* **63**, 1677 (2009).
52. F. J. Derbyshire, A. E. B. Presland, D. L. Trimm, Graphite formation by the dissolution—precipitation of carbon in cobalt, nickel and iron. *Carbon* **13**, 111 (1975).
53. Y. Zhang, K. Fugane, T. Mori, L. Niu, J. Ye, Wet chemical synthesis of nitrogen-doped graphene towards oxygen reduction electrocatalysts without high-temperature pyrolysis. *J. Mater. Chem.* **22**, 6575 (2012).
54. E. Marie, W. Torbjörn, in *Handbook for Cleaning/Decontamination of Surfaces,* P. Somasundaran, Ed. (Elsevier Science B.V., Amsterdam, 2007), pp. 747-789.
55. Z. Wang *et al.*, Cobalt-Embedded Nitrogen Doped Carbon Nanotubes: A Bifunctional Catalyst for Oxygen Electrode Reactions in a Wide pH Range. *ACS Appl. Mater. Interfaces* **7**, 4048 (2015).

56. S. Zhang *et al.*, N-Doped graphene-supported Co@CoO core-shell nanoparticles as high-performance bifunctional electrocatalysts for overall water splitting. *J. Mater. Chem. A* **4**, 12046 (2016).
57. Y. Hou *et al.*, An Advanced Nitrogen-Doped Graphene/Cobalt-Embedded Porous Carbon Polyhedron Hybrid for Efficient Catalysis of Oxygen Reduction and Water Splitting. *Adv. Funct. Mater.* **25**, 872 (2015).
58. X. Yang *et al.*, Novel Co_3O4 Nanoparticles/Nitrogen-Doped Carbon Composites with Extraordinary Catalytic Activity for Oxygen Evolution Reaction (OER). *Nano-Micro Lett.* **10**, 15 (November 14, 2017).
59. C. Zhu *et al.*, Sugar Blowing-Induced Porous Cobalt Phosphide/Nitrogen-Doped Carbon Nanostructures with Enhanced Electrochemical Oxidation Performance toward Water and Other Small Molecules. *Small* **13**, 1700796 (2017).
60. P. Feng, X. Cheng, J. Li, X. Luo, $Co_3(PO4)_2$ Nanoparticles Embedded in Nitrogen-Doped Carbon as an Advanced Electrocatalyst for OER in Alkaline Solution. *Catal. Lett.* **148**, 214 (January 01, 2018).
61. H. Jin *et al.*, In situ Cobalt–Cobalt Oxide/N-Doped Carbon Hybrids As Superior Bifunctional Electrocatalysts for Hydrogen and Oxygen Evolution. *J. Am. Chem. Soc.* **137**, 2688 (2015).
62. Y. Liang *et al.*, Co_3O_4 nanocrystals on graphene as a synergistic catalyst for oxygen reduction reaction. *Nature Materials* **10**, 780 (2011).
63. Y. Su *et al.*, Cobalt nanoparticles embedded in N-doped carbon as an efficient bifunctional electrocatalyst for oxygen reduction and evolution reactions. *Nanoscale* **6**, 15080 (2014).
64. X. Li *et al.*, ZIF-67-derived Co-NC@CoP-NC nanopolyhedra as an efficient bifunctional oxygen electrocatalyst. *J. Mater. Chem. A* **4**, 15836 (2016).

Chapter-6

Harnessing Pseudocapacitive Energy of Redox Active Covalent Organic Polymer via Graphene Interface Engineering

Summary:

Herein we report the synthesis of a new class of viologen based redox active covalent organic polymer (COP) phase engineered with graphene for pseudocapacitive energy storage. It is the first report on charged COP showing pseudocapacitive energy storage behavior of redox active functionalities. Viologen moieties endow charge storage as well as easy wetting of electrode due to their charged nature. The non-conducting COP grown over conducting graphene enhances its performance by extensive interface formation. All the redox states can be reversibly attained over entire potential regime without significant polarization which is not possible in simple COPs (without graphene) as they tend towards irreversible/pseudo-reversible behavior due to lack of electron conducting pathways. The intimate and dense conducting pathways in graphene-COP composites facilitates the charge transfer across interface leading to effective and reversible participation of redox moieties across the entire range over 1000 cycles. Also, we show that the strategy being universal in nature and aid in electron transfer in dense 3D networks which lacks traditional π-π stacking of 2D crystalline networks(COF).

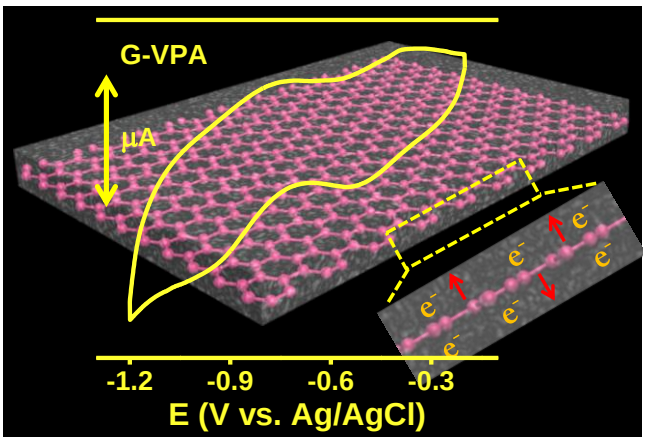

(Manuscript is under preparation.)

6.1 Introduction:

Pseudocapacitive electrodes based on quicker faradaic reactions,(*1, 2*) tremendously enhances the charge storage capacity of materials as compared to electrical double layer capacitors (EDLCs);(*3*) wherein limited capacity is achieved due to electrosorption of ions at the electrode-electrolyte interface.(*3, 4*) The fast electron transfer across the electrolytic interface significantly enhances the charge storage capacity of the pseudocapacitors such as IrO_2, RuO_2 etc.(*5*) (10-100 times larger than carbon-based EDLCs)(*1*) however; their high cost limits their large-scale applications. Another class of pseudocapacitors, electronically conducting polymers, suffers from irreversible electrode degradation on repeated insertion/deinsertion of ions/electrons leading to swelling, loss of mechanical strength, loss of conductivity etc.(*3, 6-10*) Thus, it is imperative to develop a new, low cost and low density carbon based materials with high gravimetric as well as volumetric energy density beyond the traditional oxide based systems (IrO_2, RuO_2 etc.).(*11, 12*) One approach to improve the charge storage capacity of carbon is to introduce redox moieties which could enhance its performance through quick faradic reactions.(*11-13*) Nevertheless, the participation of all redox active components (in the faradic reactions) at the electrode interface is a big challenge and is governed by several factors viz. inherent conductivity of such moieties, thickness as well as the morphology of the particles at the interface.(*2, 14-20*) A three-dimensional control over particle morphology is expected to improve the performance of the material over long cycle life.(*17, 21-23*) Materials capturing the essence of carbon-based systems along with pseudocapacitive properties are desirable because of their high gravimetric capacity. (*11, 12*) Covalent organic polymers (COPs) are emerging as a new class of materials offering diverse functionality thus catering need specific demands by rational design of molecule of our choice as the starting materials.(*13, 24-34*) However, the non-conducting nature of most of the COPs(*34*) leads to rapid decay of reversibility after few cycles. Addition of large amount (~60 wt. %) of conducting carbon (like Vulcan carbon) as an additive to improve the conductivity often results in huge weight penalty to the electrode system with low active mass.(*13*) Additionally, the presence of such conducting phase doesn't necessarily promise intimate electron transport pathways due to their ill-defined morphology arising purely on geometrical considerations.(*17, 21, 35*) The packing and hence the contact between two phases is highly statistical in nature leading to low volume fraction utilization and diminished electron conducting pathways. Interface engineering with graphene with atomically thick, high lateral dimensions and conducting

nature would significantly overcome such issues if the contact between the conducting (graphene) and non-conducting phases (COPs) be conformal.(*36, 37*) Moreover owing to the greater mechanical strength of graphene, repeated electron transfers would not lead to the degradation of electrodes unlike electronically conducting polymers.(*38*)

6.2 Scope of the present investigation:

We have strategically grown viologen(*39*) based 3D COP over graphene to overcome the above-mentioned issues. Taking viologen-based system as an example; we have shown that interface engineering of COP with graphene retains electrochemical activity even after prolonged cycling whereas the native systems lack or show rapid degradation in activity after few cycles. Furthermore, it is shown that even in 3D system which lacks traditional π-π stacking (an additional factor for the facile through plane electron transfer) of 2D (COP) system; such manipulation leads to better charge transfer kinetics at the interfaces indicating the much-improved activity compared to traditional 2D systems.

There are significant changes in the polarity of the different redox states of the viologen leading to difficulty of electron transfer during oxidation. Since the viologen undergoes stepwise two-electron reduction with successive reduction becoming more difficult; therefore attaining oxidative reversibility becomes strained.(*39-41*) Therefore, intimate contact between viologen containing redox polymer laterally grown over graphene would be expected to circumvent above issues leading to improved reversibility over prolonged cycles.

Herein, we report the synthesis of a new class of 3D covalent organic polymeric network namely VPA, by Schiff base condensation of 1,1'-bis(4-formylbenzyl)-[4,4'-bipyridine]-1,1'-diium bromide (VD), a viologen dialdehyde moiety, and a non-planar (pararosaniline, PA) tri-amine precursor to obtain VPA. The incorporation of redox active viologen moieties in VPA act as faradaically active component contributing towards pseudocapacitive energy storage. Such frameworks by virtue of their high-density redox-active centers are expected to enhance the energy storage capacity as compared to carbons containing redox active components. It must, however, be noted that mere construction of redox active covalent networks need not necessarily guarantee the effective utilization of active centers; especially in the case of 3D networks.(*42, 43*) The redox centers embedded deep inside the particle would not be able to participate in such reactions due to poor electronic conducting pathways.(*44*) Such active sites

must find good electrically conducting conduits in order to participate in charge-transfer reactions efficiently. Due to intrinsic non-conducting nature of such materials, we have strategically grown such networked architectures over graphene in order to study the effect of electron transfer kinetics as well as reversibility of the system. Such intimate interfacial contact between COP and graphene is expected to overcome the conductivity problems associated and also would reduce the amount of conductive additives added to enhance cyclability.

6.3 Experimental procedures:

6.3.1 Materials used:

Pararosaniline (>97%) was purchased from TCI. Mesitylene (97%) was purchased from kemphasol. Graphite powder (<20 μm) and sodium borohydride were purchased from Sigma-Aldrich. H_2SO_4 was procured from SD Fine Chemicals. All the other solvents were acquired from Spectrochem and were used after appropriate purifications. Terephthalaldehyde and 4,4'-Bipyridine was obtained from Alfa Aesar.

6.3.2 Instrumentation and characterization techniques:

N_2 sorption analyses were performed using Autosorb-iQ_2 (Quantachrome corp.) at 77 K using ultrahigh pure gas (99.9995%) and prior to the measurement the sample was degassed at 423 K under high vacuum for 12 h. Transmission electron microscopy (TEM) images of the samples were obtained on JEOL JEM-3010 model operating at an accelerating voltage of 300 kV. Nova-Nano SEM-600 (FEI, Netherlands) was used for acquiring field emission scanning electron microscopy (FESEM) images of the samples. Powder X-ray diffraction (PXRD) pattern of the sample was recorded using Bruker-D8 diffractometer fixed with copper anode generating X-ray having a wavelength of 1.54 Å (30 mA, 40 kV). Fourier transform infrared spectroscopy (FTIR) spectra of the samples were recorded using Bruker IFS 66v/S spectrometer. All the electrochemical measurements were performed on CHI 760E (USA). ^{1}H NMR spectrum was recorded on Bruker AVANCE 400 (400 MHz) Fourier transform spectrometer with chemical shifts reported in parts per million (ppm) using tetramethylsilane (TMS) as an internal reference.

6.3.3 Electrode preparation and electrochemical measurements:

VPA (2 mg) was ultrasonically dispersed in isopropanol (0.4 mL)-water (0.6 mL) mixture. Thereafter, 5 μL of 5 wt.% Nafion® solution was added to the

above dispersion and was further sonicated until a uniform dispersion was obtained. Subsequently, the working electrode was prepared by coating 10 µL of above electroactive dispersion onto a pre-cleaned glassy carbon electrode (3 mm diameter) and was left to dry at room temperature for 12 h.

A standard three electrode set-up was used for all the electrochemical measurements wherein Pt coil and Ag/AgCl (1 M KCl) was used as counter and reference electrodes respectively.

6.3.4 Synthesis of 1,1'-bis(4-formylbenzyl)-[4,4'-bipyridine]-1,1'-diium bromide (VD):

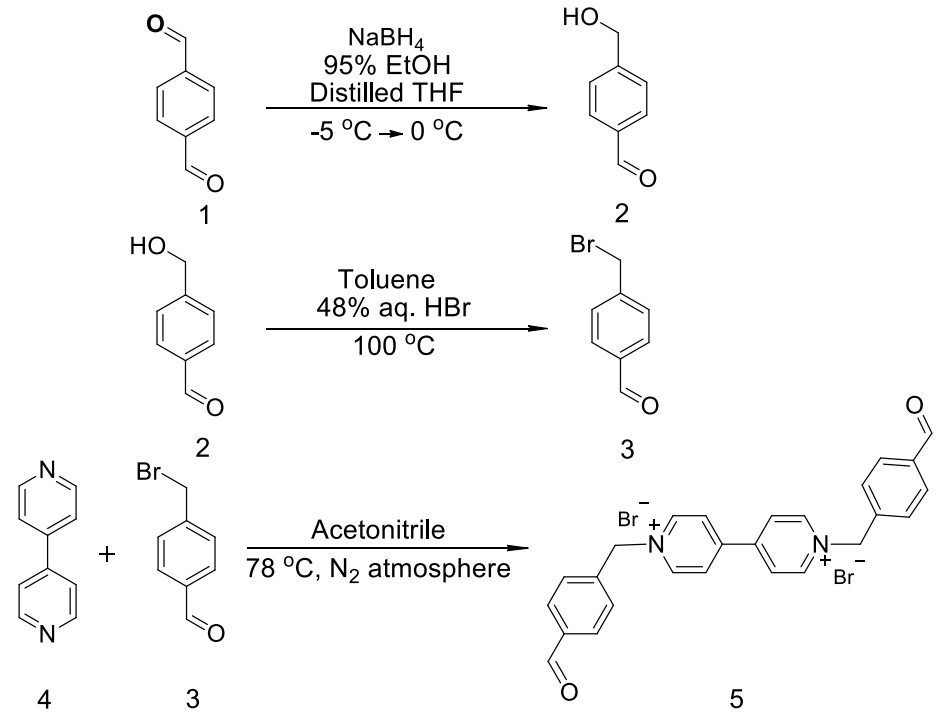

Figure 1. Synthetic strategy for VD.

Molecule **1** and **2** were synthesized using the reported procedure.(*45*)

A solution of **4** (98mg, 0.63 mmol) in dry acetonitrile (10 mL) was stirred for 10 minutes under nitrogen atmosphere. To it, a solution of **3** in dry acetonitrile (10 mL) was added and the reaction mixture was stirred at 78 °C for 7 hours. **5** was a pale yellow precipitate which was filtered and washed with chloroform to obtain pure product in 90% yield (310 mg). ^{1}H NMR (400 MHz, D_2O, TMS): δ (ppm) 10.03 (s, 2H), 9.25 (d, J = 7.2, 4H), 8.63 (d, J = 6.8, 4H), 8.09 (d, J = 8.0, 4H), 7.74 (d, J = 8.4, 4H), 6.11 (s, 4H).

6.3.5 Synthesis of VPA:

Viologen dialdehyde (40 mg, 0.072 mmol) and pararosaniline (14.7, 0.048) were ultrasonically dispersed in a glass tube containing mixture of 0.65 mL dioxane, 0.65 mesitylene and 0.20 mL of 3 M acetic acid. Thereafter, it was subjected to three freeze-pump-thaw cycles using liquid N_2 (77 K) as freezing agent and was subsequently sealed under vacuum and heated at 120 °C for 72 h. The final product was obtained by repeatedly washing it with ethanol until clear supernatant was obtained and was left to dry overnight at 60 °C.

6.3.6 Synthesis of G-VPA:

Synthesis of G-VPA was same as above except 10 mg of graphene was added additionally to the above mixture.

6.3.7 Synthesis of graphite oxide: Graphite oxide was synthesized according to modified Hummers method.(*46*) Briefly, 1.5 g of $NaNO_3$ was dissolved in 75 mL of concentrated H_2SO4 in a 1000 mL beaker at room temperature and stirred well for 10 min. Thereafter, 1.5 g of graphite powder (<20 μm) was added to the above mixture and was further stirred for 10 min. To the above mixture 10 g of $KMnO_4$ was added slowly with precaution so as not to exceed the suspension temperature beyond the room temperature. The temperature of the suspension was raised to 40 ^{O}C and was further mixed thoroughly for ~45 min until effervescence had minimized resulting in pasty mixture. Thereafter, 75 mL of distilled water was added to the above mixture with constant stirring and the temperature of the bath was raised to 70 ^{O}C and was maintained there for further 15-20 min resulting in brown color suspension. The temperature of the bath was then raised to 80 ^{O}C with further addition of 150 mL of warm water along with 15 mL of H_2O_2 in order to reduce the unreacted $KMnO_4$ and MnO_2 to colorless manganese sulfate, resulting in yellow colored suspension. The stirring was stopped and it was allowed to cool down to room temperature allowing suspension to settle down. Thereafter, the supernatant liquid was decanted leaving behind yellow colored pasty mixture. The resultant paste was dialyzed until a near neutral dialysate was obtained. The resultant paste was lyophilized to obtain fluffy graphite oxide powder.

6.3.8 Synthesis of exfoliated graphene:

Graphene was prepared by thermal shock induced exfoliation of previously prepared graphite oxide.(*47, 48*) Briefly, 150 mg of graphite oxide was

introduced into the hot zone of a tube furnace previously maintained at 300 ^{O}C resulting in sudden burst along with the formation of exfoliated graphene.

6.4 Results and discussions:

Scheme 1 shows the synthetic strategy to construct redox active, VPA, incorporating viologen moieties as faradaically active components.(*39*) Additionally, graphene composites of VPA was also synthesized (G-VPA; **Scheme 1**) in order to study the effect of intimate conducting pathways on the reversibility of redox active moieties. The powder X-ray diffraction (PXRD) pattern of VPA/G-VPA reflects a lack of 2D ordering of traditional crystalline frameworks (COFs)(*25, 49, 50*) and instead forms a 3D network as confirmed by absence of low angle peaks in PXRD pattern **(Figure 2)**. The higher angle peak at ~21^{O} (2θ) in **Figure 2** corresponds to the disordered π stacking of the carbon frameworks. It is to be noted that 2D COPs (either crystalline or non-crystalline) often displays a high degree of aggregation due to strong π-π interaction and structural charge neutrality (due to choice of functionally neutral precursors) and hence develops wettability issues with the electrode when measurements are performed in aqueous medium.(*51, 52*) In contrast, both VPA/G-VPA synthesized via charged viologen dialdehyde moiety is positively charged would lead to better wettability (of the electrode) and enhanced electrochemical activity in aqueous medium. Furthermore, Fourier-transformed infrared (FTIR) spectrum of VPA shows characteristic C=N stretching band at 1634 cm^{-1} indicating the formation of imine network **(Figure 3)**.(*53*) Furthermore, the disappearance of N-H bending (1619 cm^{-1}) and stretching modes (3347 and 3192 cm^{-1}) of PA and the carbonyl stretching mode (1690 cm^{-1}) of VD in VPA spectrum supports the imine linkage formation. Additionally, C-H stretching modes of H-C=O (at 3034 cm^{-1} and 2973 cm^{-1}) in VD were also absent for VPA **(Figure 3)**.

N_2 sorption analyses shows low specific surface area (SSA) of 43 m^2 g^{-1} for VPA **(Figure 4)**. The observed low specific surface area is often associated with intercalated bromide anions in the structure.(*52*) Field emission scanning electron microscopic (FESEM) image **(Figure 5a)** of VPA indicates the presence of dense structure which is consistent with the observed low SSA of VPA. Transmission electron microscopic (TEM) investigations of VPA **(Figure 5b)** further supports FESEM findings. Energy dispersive X-ray spectroscopic (EDS) elemental analyses shows a uniform distribution of elements (C, N, Br and O) thus revealing that the network is entirely built by condensation of redox active viologen centers and PA **(Figure 5c-f)**. FESEM image **(Figure 6b)** of G-VPA

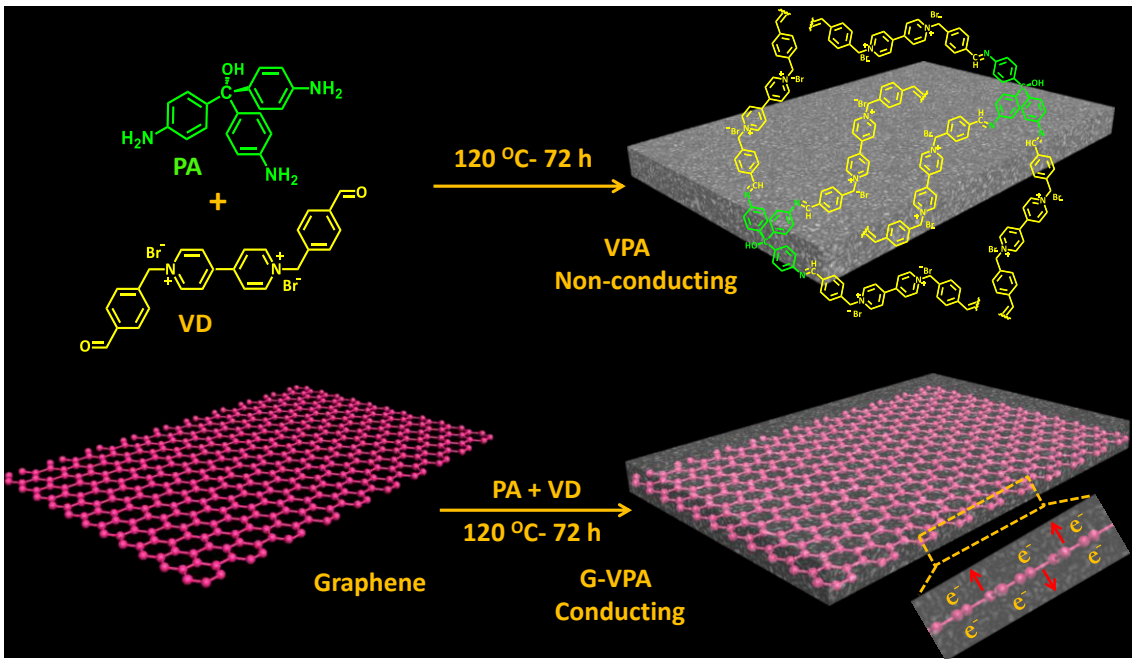

Scheme 1. Illustration depicting synthetic strategy implemented to construct viologen containing redox active polymer; VPA and conducting composite of the same with graphene (G-VPA).

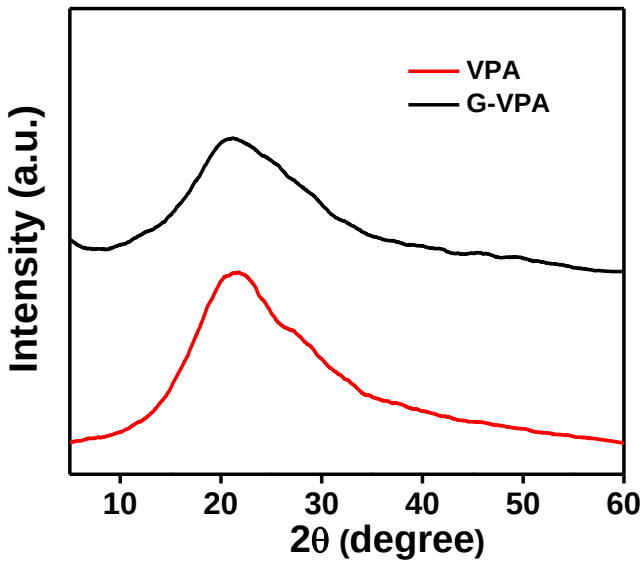

Figure 2. PXRD patterns of VPA and G-VPA.

indicates flaky morphology (a consequence of graphene incorporation, **Figure 6a**) due to the growth of VPA over graphene. Furthermore, TEM images of G-VPA shows conformal growth of VPA **(Figure 7a-b)** over graphene backbone illustrating intimate contact.

Pseudocapacitive energy storage behavior of VPA was investigated in 1 M KCl using cyclic voltammetry (CV) **(Figure 8)**. The cyclic voltammogram of VPA shows **(Figure 8b)** a pair of well resolved cathodic peaks (-0.51 V and -1.04 V)

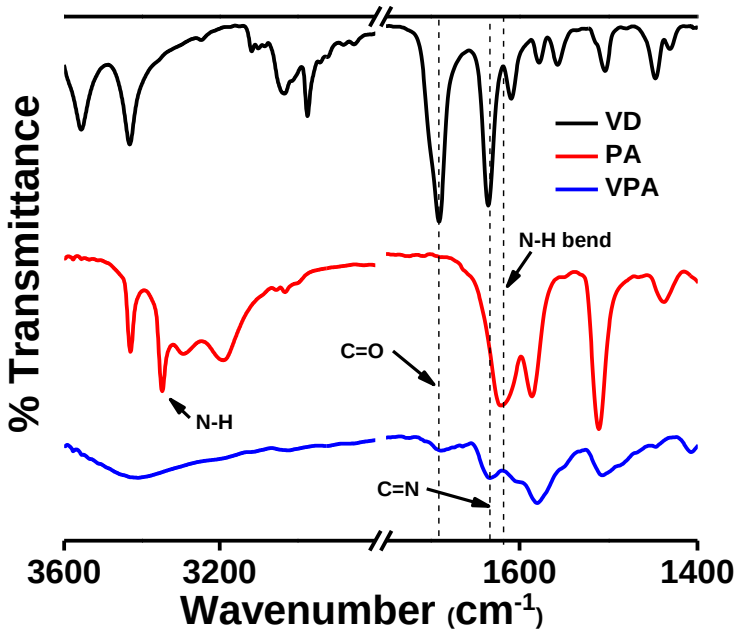

Figure 3. FTIR spectra of PA, VD, and VPA indicating the formation of imine linkages in VPA.

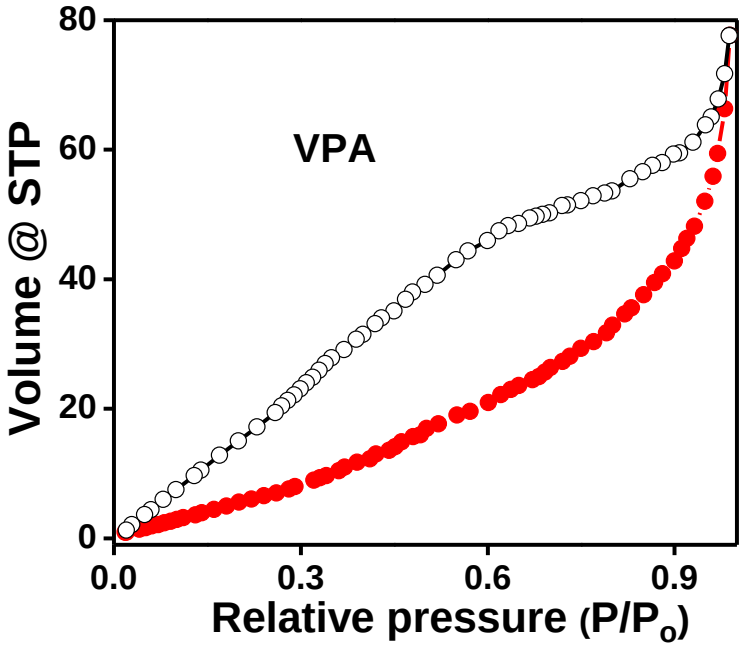

Figure 4. N_2 sorption isotherm of VPA. Closed and open circles represent adsorption and desorption respectively.

due to successive two-electron reduction of the viologen moieties in the framework. The appearance of only one weak anodic peak (-0.84 V) during reverse scan indicating a irreversible nature of the redox process. This is in contrast to methyl viologen (MV) molecules in solution which exhibits a pair of redox peaks each for cathodic (-0.73 V and -1.05 V) and anodic (-0.99 V and -0.68 V) scans **(Figure 8a)** corresponding to well-known sequential stepwise two-electron reduction and oxidation of viologen moieties. The functionalized

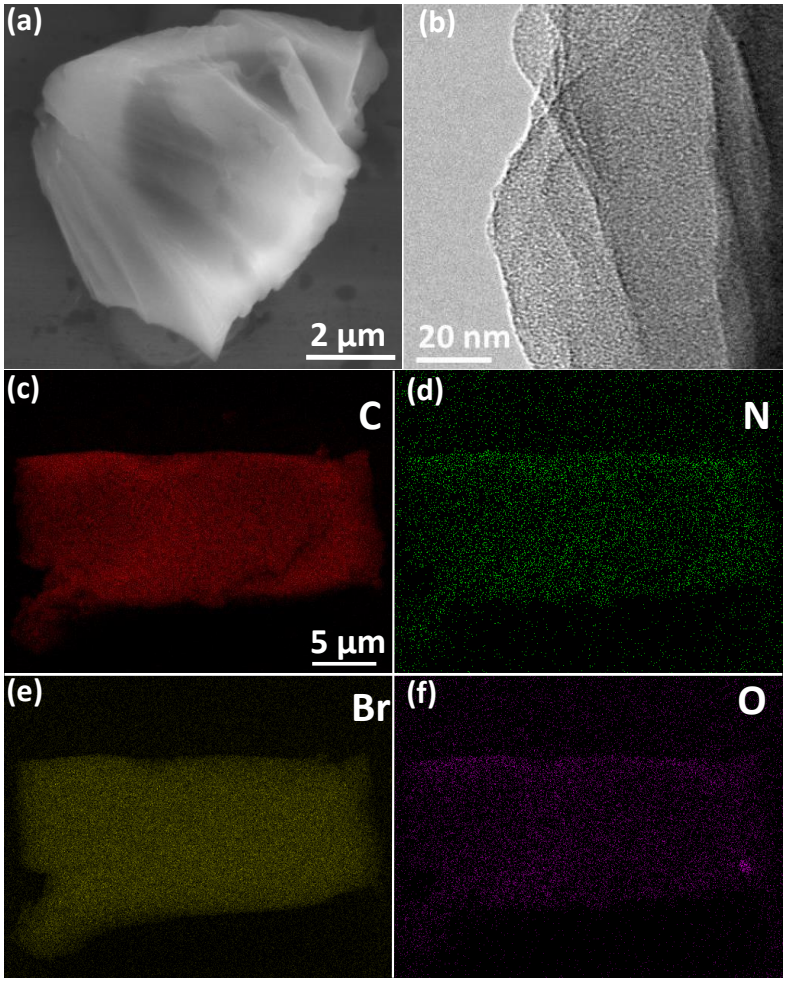

Figure 5. (a) FESEM and (b) TEM images of VPA. (c-f) EDS analyses of C, N, Br, and O respectively reveal the uniform distribution of the elements in VPA.

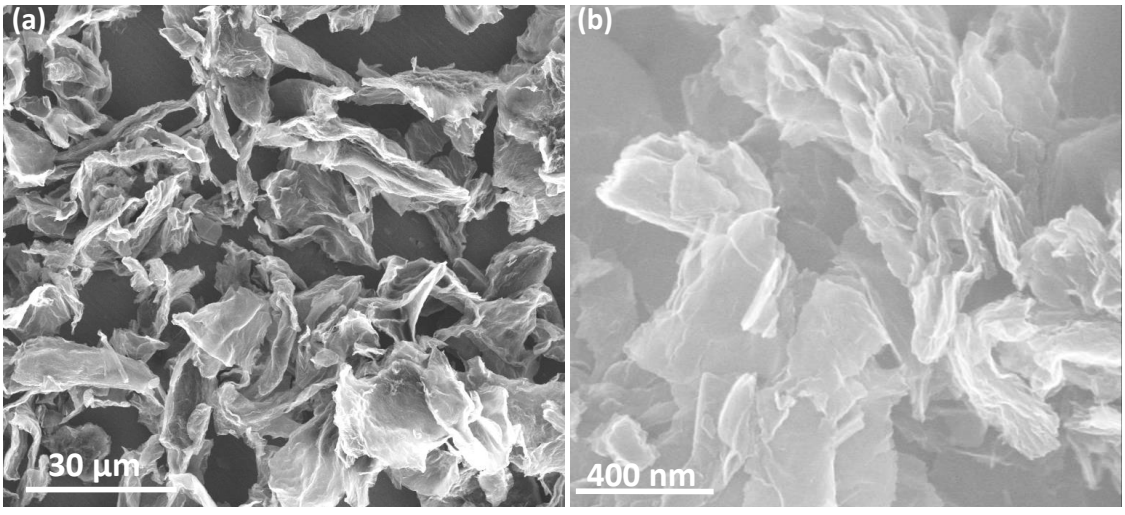

Figure 6. FESEM images of (a) graphene and (b) G-VPA indicating flaky morphology of the composite.

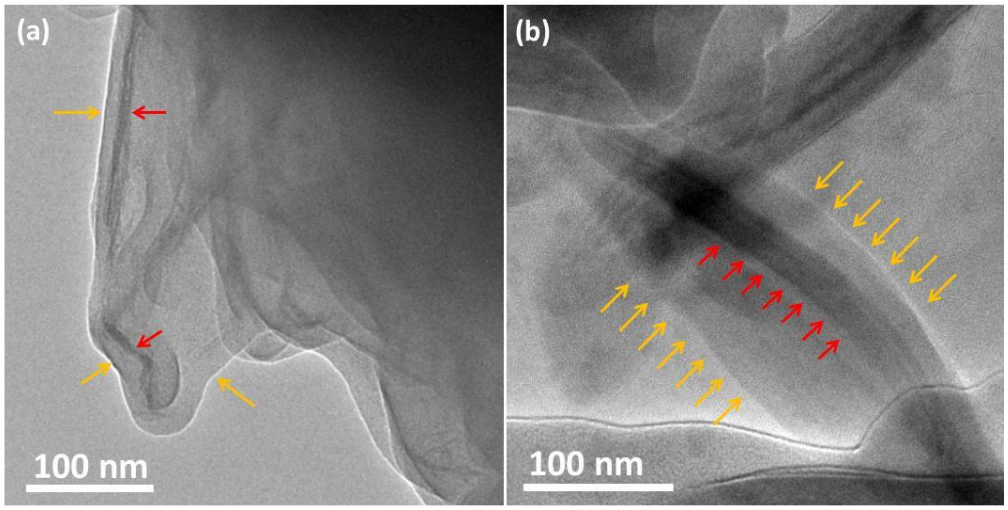

Figure 7. (a) and (b) transverse view of the TEM images of G-VPA indicating graphene backbone with overgrown covalent networks (red arrows indicate graphene layers whereas yellow ones indicate COP) with intimate contact between.

dialdehyde of viologen (VD) used to make VPA also shows similar behavior, though there is a significant shift in peak position compared to MV due to change in energy levels of the molecules upon substitution **(Figure 8a)**.(*39*) The additional oxidative peak observed for both MV and VD (at -0.87 V and -0.65 V for MV and VD respectively) are associated with well-known comproportionation reaction between the reduced species in the counter electrode and the oxidized species in the working electrode (as the CV of MV and VD were carried out in solution phase, the reduced species can migrate from the counter electrode to the working electrode resulting in the comproportionation reaction).

The low current and irreversible/pseudoreversible behavior of redox peaks for VPA in the full scan range probably results from the non-conducting nature of the framework inhibiting the two electron transfer **(Figure 8b)**. Restricting the scan range to one electron transfer regime displays reversible redox peaks, although the current is still low indicating again that the conductivity and electron transfer is an important parameter for attaining reversibility even for a single charge/electron transfer **(Figure 8b)**. For example, VPA shows both cathodic (-0.59 V) and anodic (-0.53 V) peaks with good redox reversible states (albeit shown by only a few samples) when the scan range was limited to -0.75 V instead of -1.25 V **(Figure 8b)**.

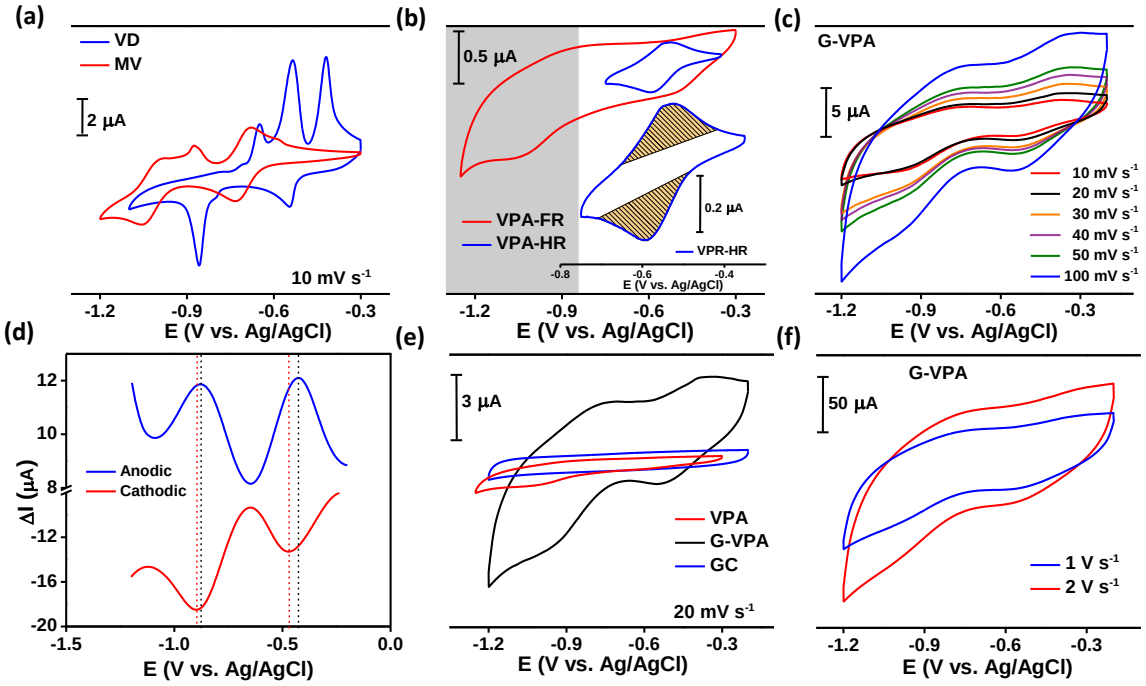

Figure 8. (a) CVs of MV and VD (solution state) at 10 mV s^{-1}. (b) CVs of VPA of over half potential scan range (VPA-HR) and full range (VPA-FR) at 10 mV s^{-1}. Also, the redox contributions are highlighted in yellow for VPA-HR indicating the good redox reversibility of the VPA for the scanned range showing the facile pseudocapacitive contribution to total capacitive energy storage. The shaded region in grey indicates the irreversible potential scanning regime. (c) CVs of G-VPA at different scan rates whereas (d) shows corresponding square wave voltammograms for cathodic and anodic scans. (e) Comparison of CVs of G-VPA and GC at 20 mV s^{-1} indicating zero pseudocapacitive contribution from glassy carbon electrode. (f) CVs of G-VPA at higher scan rates showing prominent redox peaks; indicating facile charge transfer kinetics in the former.

In order to overcome the conductivity problem which affects the full reversibility over the entire potential regime encompassing two electron transfers per viologen moiety, VPA was grown over graphene (G-VPA) to get intimate and uniform VPA-graphene interfaces **(Scheme 1 and Figure 6-7)**. Unlike the solution state study of MV, electrochemistry measurements were performed by coating the G-VPA material over the glassy carbon (GC) electrode. As opposed to VPA, CVs of G-VPA shows a pair of prominent cathodic (-0.55 V and -0.95 V) and anodic peaks (-0.76 V and -0.35 V) respectively at different scan rates **(Figure 8c)** over the entire potential range scanned (up to -1.2 V). It is important to note that the third oxidation peak

(Figure 8a) observed in the solution state CV of MV (-0.87 V) is missing for G-VPA **(Figure 8c)** as there are no comproportionation pathways due to adherence of G-VPA on to the electrode surface. This indicates that highly conducting nature of graphene at the graphene-VPA interface facilitate the efficient charge transfer between the electrode and the VPA moieties. Transmission electron microscope (TEM) images **(Figure 7)** clearly shows regions where VPA has uniformly covered the graphene layers creating effective interfaces for the facile electron transfer to and fro from VPA during the redox process. Square wave voltammograms (SWV) for G-VPA **(Figure 8d)** further indicate a pair of well-resolved faradaic peaks for both cathodic (-0.47 V and -0.89 V) and anodic (-0.88 V and -0.42) scans showing their redox origin. The effect of graphene incorporation leads to enhanced/efficient charge transfer in G-VPA as opposed to VPA as can be seen by higher current **(Figure 8e)** in the former in spite of the fact that loading in latter case (0.28 mg cm^{-2}) is greater than G-VPA (0.23 mg cm^{-2}, calculated based upon the mass of redox active component, see experimental section for details). It can be concluded that intimate and dense electron conducting pathways in G-VPA due to the presence of graphene not only resulted in reversible, step-wise two-electron redox states for VPA (over the entire potential regime) **(Figure 8b)** but also effective utilization of redox moieties for this process. The CV of blank glassy carbon (GC) under similar conditions **(Figure 8e)** did not show any significant redox peaks confirming that the pseudocapacitance purely stems from G-VPA devoid of any contribution from surface impurity. The CVs of G-VPA even at higher scan rates (1 Vs^{-1} and 2 V s^{-1} , **Figure 8f**) shows a pair of prominent redox peaks for cathodic and anodic scans separately reflecting efficient and faster charge transfer kinetics in G-VPA. The prominent effect of polarization in the absence of graphene can be clearly elucidated from **Figure 9**. The system (VPA) tends towards pseudoreversible behavior, as the second redox peak progressively shifts towards lower potential at higher scan rates **(Figure 9a-b)** indicating impeded electron transfer kinetics. Whereas, the position of redox peaks are independent of scan rates for G-VPA reflecting negligible polarization effects **(Figure 9c-d).** Stability performance of G-VPA after 1000 cycles **(Figure 10)** specifies the retention of redox peaks with a negligible shift in the redox potential which is indicative of excellent redox reversibility of the framework assisted by conducting phase (graphene).

Furthermore, in order to prove our above hypotheses, additional experiments were carried out wherein a higher amount of Vulcan carbon (60 wt. %) was

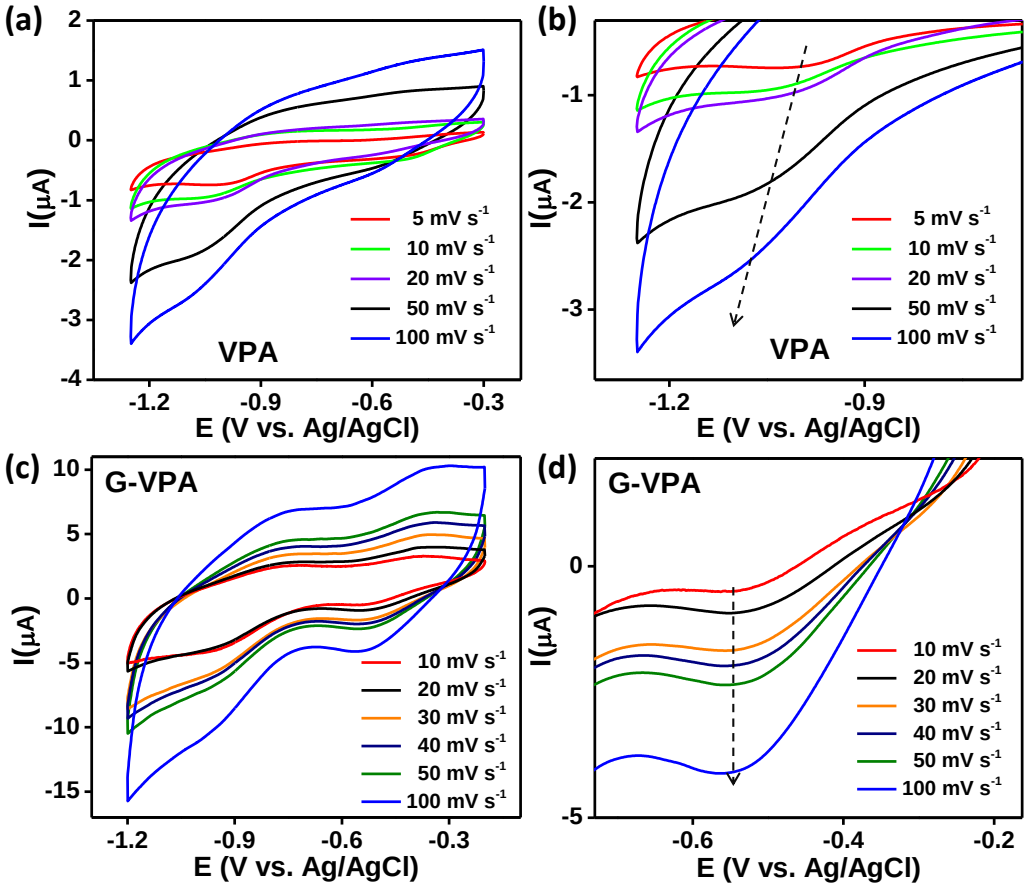

Figure 9. CVs of VPA (a) and G-VPA (c) with the corresponding polarization effect being clearly seen in (b) and (d) respectively.

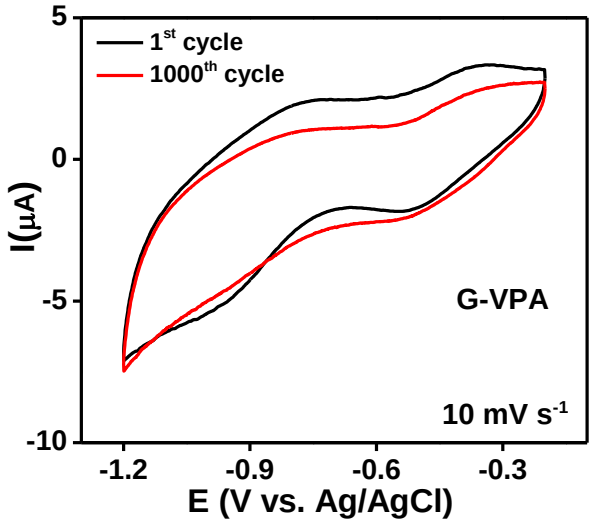

Figure 10. Cycling behavior of G-VPA at 10 mV s^{-1} indicating the presence of prominent redox peaks even after 1000 cycles.

added to VPA to ensure higher conductivity of the resultant mixture (VC-VPA). CVs of VC-VPA (**Figure 11**) indicates pseudo-rectangular behavior indicating capacitive behavior with very weak cathodic redox (-0.587 V and -0.973 V) component and absence of such peaks during the anodic scan. This

clearly indicates that even with higher loading of the conducting carbon (60 wt.%), the redox reversibility of viologen moieties in VPA is poor mainly due to the absence of intimate conducting interfaces which is further augmented by the irregular particle size of both viz. the Vulcan carbon and VPA. The above points were further corroborated by the observation that CV could not be obtained at higher scan rate (>1 V s^{-1}) for VPA-Vulcan carbon mixture due to lack facile/efficient charge transfer between Vulcan carbon and VPA.

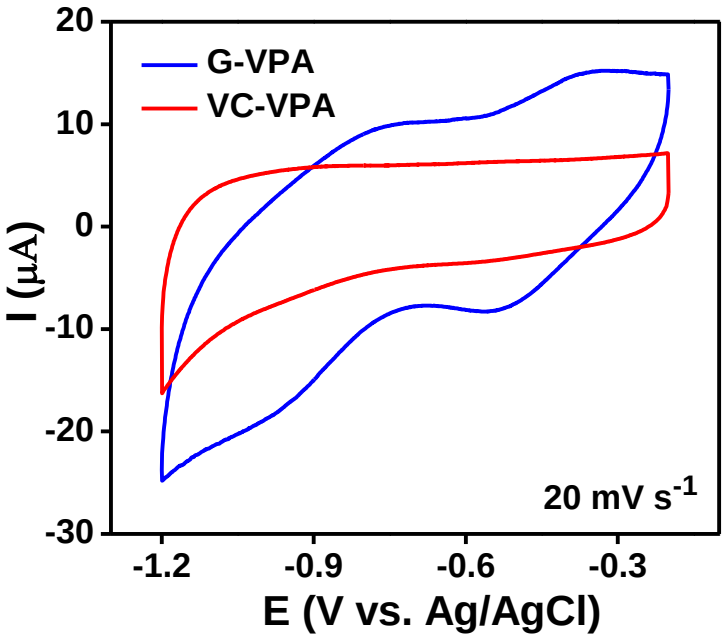

Figure 11. CV of G-VPA and 60 wt.% VC and VPA (VC-VPA) mixture.

6.5 Conclusions:

In conclusion, we have shown that by effective interface engineering between conducting (graphene) and non-conducting COP phase (containing redox active viologen moieties), the entire redox states can be reversibly attained over full potential regime without significant polarization which is not possible in simple COP. Such irreversibility in normal COP, stems from lack of uniform and intimate electron conducting pathways. The intimate and dense conducting pathways in conducting/non-conducting composites leads to efficient charge transfer across interface leading to effective and reversible participation of redox moieties over entire range. Therefore such composites holds promise for large scale production by such interfacial engineering approach which can be further amplified or boosted by tailoring conducting redox system. Although, further investigations are needed to develop and design commercially feasible systems with high reversibility and enhanced cycle life which can compete with currently available carbon based systems.

6.6 References:

1. B. E. Conway, *Electrochemical Supercapacitors: Scientific Fundamentals and Technological Applications*. (Springer US, 2013).
2. P. Simon, Y. Gogotsi, Materials for electrochemical capacitors. *Nat. Mat.* **7**, 845 (2008).
3. *Supercapacitors: Materials, Systems, and Applications*. (Wiley, 2013).
4. E. Frackowiak, F. Béguin, Carbon materials for the electrochemical storage of energy in capacitors. *Carbon* **39**, 937 (2001).
5. N.-L. Wu, Nanocrystalline oxide supercapacitors. *Mater. Chem. Phys.* **75**, 6 (2002).
6. B. Anothumakkool, R. Soni, S. N. Bhange, S. Kurungot, Novel scalable synthesis of highly conducting and robust PEDOT paper for a high performance flexible solid supercapacitor. *Energy Environ. Sci.* **8**, 1339 (2015).
7. J. Kim, J. H. Kim, K. Ariga, Redox-Active Polymers for Energy Storage Nanoarchitectonics. *Joule* **1**, 739.
8. H. Wang, J. Lin, Z. X. Shen, Polyaniline (PANi) based electrode materials for energy storage and conversion. *J. Sci. Adv. Mater. Devices* **1**, 225 (2016).
9. A. M. Bryan, L. M. Santino, Y. Lu, S. Acharya, J. M. D'Arcy, Conducting Polymers for Pseudocapacitive Energy Storage. *Chem. Mater.* **28**, 5989 (2016).
10. J. Kim *et al.*, Conductive polymers for next-generation energy storage systems: recent progress and new functions. *Mater. Horiz.* **3**, 517 (2016).
11. C. Benoit, D. Demeter, D. Bélanger, C. Cougnon, A Redox-Active Binder for Electrochemical Capacitor Electrodes. *Angew. Chem. Int. Ed.* **55**, 5318 (2016).
12. G. Pognon, T. Brousse, L. Demarconnay, D. Bélanger, Performance and stability of electrochemical capacitor based on anthraquinone modified activated carbon. *J. Power Sources* **196**, 4117 (2011).
13. C. R. DeBlase, K. E. Silberstein, T.-T. Truong, H. D. Abruña, W. R. Dichtel, β-Ketoenamine-Linked Covalent Organic Frameworks Capable of Pseudocapacitive Energy Storage. *J. Am. Chem. Soc.* **135**, 16821 (2013).
14. J. O. M. Bockris, A. K. N. Reddy, M. E. Gamboa-Aldeco, *Modern Electrochemistry 2A: Fundamentals of Electrodics*. (Springer US, 2001).

15. J. J. Gooding, Nanostructuring electrodes with carbon nanotubes: A review on electrochemistry and applications for sensing. *Electrochim. Acta* **50**, 3049 (2005).
16. D. Majdecka, R. Bilewicz, Nanostructuring carbon supports for optimal electrode performance in biofuel cells and hybrid fuel cells. *J. Solid State Electrochem.* **20**, 949 (April 01, 2016).
17. H. Sun *et al.*, Three-dimensional holey-graphene/niobia composite architectures for ultrahigh-rate energy storage. *Science* **356**, 599 (2017).
18. M. L. Jones, I. V. Kurnikov, D. N. Beratan, The Nature of Tunneling Pathway and Average Packing Density Models for Protein-Mediated Electron Transfer. *J. Phys. Chem. A* **106**, 2002 (2002).
19. W. Schmickler, J. Mohr, The rate of electrochemical electron-transfer reactions. *J. Chem. Phys.* **117**, 2867 (2002).
20. K. Fu, P. W. Bohn, Nanopore Electrochemistry: A Nexus for Molecular Control of Electron Transfer Reactions. *ACS Central Science* **4**, 20 (2018).
21. H. Chen *et al.*, Ultrafast all-climate aluminum-graphene battery with quarter-million cycle life. *Sci. Adv.* **3**, (2017).
22. A. Manthiram, A. Vadivel Murugan, A. Sarkar, T. Muraliganth, Nanostructured electrode materials for electrochemical energy storage and conversion. *Energy Environ. Science* **1**, 621 (2008).
23. J. H. Bae, J.-H. Han, T. D. Chung, Electrochemistry at nanoporous interfaces: new opportunity for electrocatalysis. *Phys. Chem. Chem. Phys.* **14**, 448 (2012).
24. Z. Xiang, D. Cao, L. Dai, Well-defined two dimensional covalent organic polymers: rational design, controlled syntheses, and potential applications. *Pol. Chem.* **6**, 1896 (2015).
25. X. Feng, X. Ding, D. Jiang, Covalent organic frameworks. *Chem. Soc. Rev.* **41**, 6010 (2012).
26. A. P. Côté *et al.*, Porous, Crystalline, Covalent Organic Frameworks. *Science* **310**, 1166 (2005).
27. Z. Xiang, D. Cao, Synthesis of Luminescent Covalent–Organic Polymers for Detecting Nitroaromatic Explosives and Small Organic Molecules. *Macromol. Rapid Commun.* **33**, 1184 (2012).
28. Z. Xiang *et al.*, Nitrogen-Doped Holey Graphitic Carbon from 2D Covalent Organic Polymers for Oxygen Reduction. *Adv. Mater.* **26**, 3315 (2014).

29. C. S. Diercks, O. M. Yaghi, The atom, the molecule, and the covalent organic framework. *Science* **355**, (2017).
30. Q. Fang *et al.*, 3D Porous Crystalline Polyimide Covalent Organic Frameworks for Drug Delivery. *J. Am. Chem. Soc.* **137**, 8352 (2015).
31. Z. Li *et al.*, A 2D azine-linked covalent organic framework for gas storage applications. *Chem. Commun.* **50**, 13825 (2014).
32. D. Mullangi *et al.*, Low-Overpotential Electrocatalytic Water Splitting with Noble-Metal-Free Nanoparticles Supported in a sp3 N-Rich Flexible COF. *Adv. Energy Mater.* **6**, 1600110 (2016).
33. X. Wang *et al.*, Homochiral 2D Porous Covalent Organic Frameworks for Heterogeneous Asymmetric Catalysis. *J. Am. Chem. Soc.* **138**, 12332 (2016).
34. F. Xu *et al.*, Electrochemically active, crystalline, mesoporous covalent organic frameworks on carbon nanotubes for synergistic lithium-ion battery energy storage. *Sci. Rep.* **5**, 8225 (2015).
35. A. J. R. Rennie, V. L. Martins, R. M. Smith, P. J. Hall, Influence of Particle Size Distribution on the Performance of Ionic Liquid-based Electrochemical Double Layer Capacitors. *Sci. Rep.* **6**, 22062 (2016).
36. J. W. Colson *et al.*, Oriented 2D Covalent Organic Framework Thin Films on Single-Layer Graphene. *Science* **332**, 228 (2011).
37. C. R. DeBlase *et al.*, Rapid and Efficient Redox Processes within 2D Covalent Organic Framework Thin Films. *ACS Nano* **9**, 3178 (2015).
38. M. J. Allen, V. C. Tung, R. B. Kaner, Honeycomb Carbon: A Review of Graphene. *Chem. Rev.* **110**, 132 (2010).
39. C. L. Bird, A. T. Kuhn, Electrochemistry of the viologens. *Chem. Soc. Rev.* **10**, 49 (1981).
40. H. A. Gemborys, B. R. Shaw, Electrochemical behavior of methyl viologen in zeolite particle films. *J. Electroanal. Chem.* **208**, 95 (1986).
41. J. R. White, A. J. Bard, Clay modified electrodes: Part IV. The electrochemistry and electron spin resonance of methyl viologen incorporated into montmorillonite films. *J J. Electroanal. Chem.* **197**, 233 (1986).
42. A. Barfidokht, S. Ciampi, E. Luais, N. Darwish, J. J. Gooding, Distance-Dependent Electron Transfer at Passivated Electrodes Decorated by Gold Nanoparticles. *Anal. Chem.* **85**, 1073 (2013).
43. F. Scholz, U. Schröder, R. Gulaboski, *Electrochemistry of Immobilized Particles and Droplets*. (Springer Berlin Heidelberg, 2005).

44. P. H. Robbs, N. V. Rees, Nanoparticle electrochemistry. *Phys. Chem. Chem. Phys.* **18**, 24812 (2016).
45. S. Chatterjee, S. Ramakrishnan, A novel photodegradable hyperbranched polymeric photoresist. *Chem. Commun.* **49**, 11041 (2013).
46. W. S. Hummers, R. E. Offeman, Preparation of Graphitic Oxide. *J. Am. Chem. Soc.* **80**, 1339 (1958).
47. C. Zhang *et al.*, Towards low temperature thermal exfoliation of graphite oxide for graphene production. *Carbon* **62**, 11 (2013).
48. H. P. Boehm, A. Clauss, G. O. Fischer, U. Hofmann, Das Adsorptionsverhalten sehr dünner Kohlenstoff-Folien. *Z. Anorg. Allg. Chem.* **316**, 119 (1962).
49. S.-Y. Ding, W. Wang, Covalent organic frameworks (COFs): from design to applications. *Chem. Soc. Rev.* **42**, 548 (2013).
50. H. M. El-Kaderi *et al.*, Designed Synthesis of 3D Covalent Organic Frameworks. *Science* **316**, 268 (2007).
51. S. Mitra *et al.*, Self-Exfoliated Guanidinium-Based Ionic Covalent Organic Nanosheets (iCONs). *J. Am. Chem. Soc.* **138**, 2823 (2016).
52. G. Das *et al.*, Viologen-Based Conjugated Covalent Organic Networks via Zincke Reaction. *J. Am. Chem. Soc.* **139**, 9558 (2017).
53. F. J. Uribe-Romo *et al.*, A Crystalline Imine-Linked 3-D Porous Covalent Organic Framework. *J. Am. Chem. Soc.* **131**, 4570 (2009).

Conclusions and Future Outlook:

The properties of carbon are much more diverse and exciting than any other element of the periodic table. Carbon offers easily tailorable exotic electronic and as well as textural properties which when combined with native ones leads to the generation of newer exciting ones. Besides, C is earth abundant, low-density etc. which makes them particularly important and interesting candidate for a plethora of applications viz. future energy material, separation, catalyst support etc. In our present investigation, we have shown that via appropriate textural engineering in carbon-based materials; remarkably enhanced electrochemical performances can be obtained. Chapter 2 and chapter 3 revealed how beneficial hierarchical micro-mesoporous structure can lead to excellent supercapacitor and battery performance. The augmented effect of mass transport effect on reaction kinetics was further proved in chapter 4 and chapter 5. It was shown that pore engineering from meso-macro scale could lead to admirable oxygen reduction, oxygen evolution and hydrogen evolution kinetics without the presence of any precious d-block element. Therefore, it opens up a newer paradigm for the development and implementation of earth abundant electrocatalysts for application in fuel cells, metal-air batteries etc. Furthermore, the conducting property of carbon was invoked to harness pseudocapacitive charge storage capacity of covalent organic polymers in chapter 6 via interface engineering.

The above examples proves that carbon based systems will be serve as future blueprint to address the energy and environmental issues of our world. The potential of carbon is immense and further research will open up newer domains with practical facets to tackle the issues of our modern times and beyond.

List of Publications:

1. **D. K. Singh**, K. S. Krishna, S. Harish, S. Sampath, M. Eswaramoorthy, No More HF: Teflon-Assisted Ultrafast Removal of Silica to Generate High-Surface-Area Mesostructured Carbon for Enhanced CO_2 Capture and Supercapacitor Performance. ***Angew. Chem. Int. Ed.*** **55**, 2032 (2016).
2. **D. K. Singh**, R. N. Jenjeti, S. Sampath, M. Eswaramoorthy, Two in one: N-doped tubular carbon nanostructure as an efficient metal-free dual electrocatalyst for hydrogen evolution and oxygen reduction reactions. ***Journal of Materials Chemistry A*** **5**, 6025 (2017).
3. S. Gope,* **D. K. Singh**,* M. Eswaramoorthy, A. J. Bhattacharyya, An Extremely High Surface Area Mesoporous-Microporous-Networked Pillared Carbon for High Stability Li-S and Intermediate Temperature Na-S Batteries. ***ChemistrySelect*** **2**, 9249 (2017).
   (* Equal contribution.)
4. **D.K. Singh**, S. Chakraborty, A. Saha, S. Sampath, M. Eswaramoorthy, Ultrafast Synthesis of Uniformly Dispersed Co_3O_4 in Highly Interconnected 3D Meso-macroporous Carbon with Enhanced Oxygen Evolution Kinetics. (Manuscript under preparation).
5. **D.K. Singh**, S. Chakraborty, S. Sampath, S. George, M. Eswaramoorthy, Harnessing Pseudocapacitive Energy of Redox Active Covalent Organic Polymer via Graphene Interface Engineering. (Manuscript under preparation.)